Computer Simulation of Dipole-Dipole Interactions Towards Understanding Nanostructure Formation

Numaan Ejaz Ahmed

Chemistry Department

A thesis submitted to University College London for the degree of Doctor of Philosophy, March 2010

I, Numaan Ejaz Ahmed, confirm the work presented in this thesis is my own. Where information has been derived from other sources, I confirm this has been indicated in the thesis.

Abstract

Chalcogenide nanocrystals, synthesised in solution, have the ability to form larger nanostructures through the association of the nanocrystals. There are a variety of structures that form which range from simple chains to more complex tripod, tetrapod and star morphologies. The association of the nanocrystals has been hypothesised to be the result of dipole-dipole interactions between nanocrystals. This results partially from the observation of the so called "pearl-necklace" type of structures visible in synthesis preceding the formation of chain structures.

The Stockmayer fluid potential, comprising a Lennard-Jones potential with additional dipole-dipole interactions, is employed to model computationally the nanocrystals in a binary mixture, where the sizes of the particles can differ. Monte Carlo simulations are performed at a range of reduced densities and various size ratios. A large range of size ratios are examined, reflecting the size distribution of nanocrystals present in synthesis. There are a number of simple models that can describe the formation of simple chain or ring nanostructures. A significant step forward in the understanding of nanoparticle self-assembly is to model the formation of the more complex tetrapod structures. In this context a modified Stockmayer fluid model is developed in which a single nanocrystal is represented by four off-centre Stockmayer fluid particles.

The Stockmayer fluid potential highlights that the formation of linear chain structures is in competition with triangular unit structures, with the energy of the triangular units becoming more favourable with increasing size ratio. The modified Stockmayer fluid model is able to produce good quality tetrapod structures over a narrow range of size ratios. There is also greater formation of tripod structures observed by using a novel analysis technique.

Acknowledgments

I would like to start by thanking my supervisor Dr. Mark Wilson for his encouragement, inspiration, guidance and assistance throughout my PhD. Like all brilliant geniuses of this world the ideas and explanations provided by Mark made impeccable sense in the presence of his great aura, for only my understanding to decrease exponentially after leaving his office!

Thanks go out to other members of the UCL Chemistry department especially Dr. Dewi Lewis, Dr. David Rowley, Dr. Wendy Brown and Prof. Karl Hale for their help and support throughout my PhD and for their entertaining, for some people excruciatingly painful, lectures during my undergraduate years at UCL.

Thanks to members of the Wilson group, Dr. Bevan Sharma, Dr. Clare Bishop and Dr Dominc Daisenberger, for their help in deciphering Dr. Wilson's comments and explanations, and most of all for their friendship during my studies at UCL.

Thanks to all members of room 105 past and present for their entertaining conversations, events and lunches over the years. In particular I would like to thank; Miguel, Keith, Alan, Fedor, Sheena, Demetrios, Tanya, Davy, Hitesh and Martine. In addition I wish to thank Billy and Nadine for proofreading parts of my thesis.

I would like to make a special mention to my former chemistry teacher Dr. C Adams, for all her encouragement, advice and belief in me, even when I got the worst GCSE chemistry mock grade in the school!

Unique debt of gratitude goes to Nasir Khan for providing exhilarating conversations regarding Manchester United, football, movies and all things Metal Gear Solid. These allowed me to stay somewhat sane during my PhD.

Finally, but not least, I am extremely grateful to my parents, Ejaz and Naheed Ahmed, and sister, Henna Ahmed, for all their love and support throughout my education. This PhD thesis is dedicated to them.

Contents

List of Figures

Chapter 1

Chapter 2

Chapter 3

Chapter 4

Chapter 5

Chapter 6

Chapter 7

List of Tables

Chapter 1 Nanomaterials

1.1 Introduction

There has been significant interest in the world of nanotechnology over the past decade. This is due to the potentially unique properties of a nanomaterial: materials which are made up of building blocks in the order of 1-10 nm in size, relative to their bulk counterparts. This difference in properties is largely attributed to the greater surface to volume ratio in nanomaterials relative to the bulk material. This essentially means there are more surface atoms as opposed to core atoms, atoms not directly exposed to external stimuli, in nanomaterials relative to bulk materials where the situation is reversed with more core atoms than surface atoms[1]. There are many changes to the physical and chemical properties of materials as a result of quantum confinement in the nano regime. One of these is a lowering of the melting/boiling temperature; there tends to be an exponential decrease in the melting temperature of nanocrystals as the volume of nanocrystals decreases due to the rapidly increasing crystal surface to volume ratio[2]. Important changes for many semiconductor materials include the increasing size of the band gap, the separation between the highest occupied molecular orbital (HOMO) and the lowest unoccupied molecular orbital (LUMO), with decreasing nanocrystal size or nanostructure size[3] (Figure 1).

There are a number of potential uses of nanomaterials. For instance, nanoparticles that luminesce are being exploited for bio-sensing and magnetic nanoparticles are used for targeted drug delivery[4,5]. Nanoparticles also have other potentially useful applications in the production of nanodevices for use as single-electron transistors (SET)[6], non-volatile memories[7] and as photovoltaic materials (solar cells) due to their inherent higher quantum yields[8]. There is also the possibility of using these nanomaterials in performing redox reactions with higher efficiency[9]. Many other fields of science are also expected to benefit from the continued development of nanomaterials such as biomedicine[10], optoelectronics[11], and many more applications are expected as new nanomaterials are developed[12].

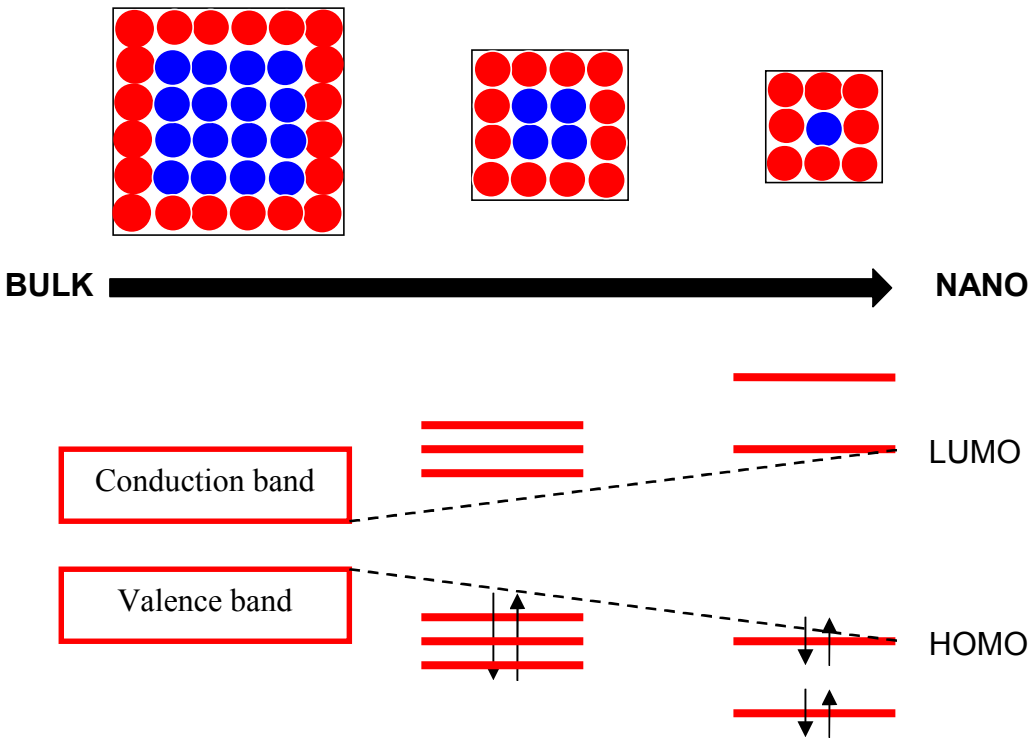

Figure 1 - *The effect of going from the bulk phase of crystals to nanocrystals, the result is an increase in the number of surface atoms (red atoms) relative to the core atoms (blue atoms). The band gap between the valence and conduction bands increases with discrete energy levels becoming more pronounced.*

There are also changes in the chemical activity of materials on reaching the nanometre scale. For instance, gold is normally thought of as an inert metal in the bulk phase. Nanoparticles of gold display catalytic activity, for example the epoxidation of alkenes[13], and there is also a change in the colour of gold nanoparticles ranging from red to blue depending on size and shape of the nanoparticles[14]. These chemical and physical changes observed in nanomaterials are not simply abrupt transitions from bulk to nano properties, but rather continuous changes in chemical and physical properties as the size of the nanocrystals decreases[15]. This is an important feature of nanomaterials and the ability of chemistry to exploit this, as subtle changes in both shape and size of nanomaterials allows fine tuning of the crystals properties for its desired purpose.

1.2 Synthesis of nanomaterials

The process of crystallization, the formation of a solid from a liquid, vapour or amorphous solid phase is in essence what gives rise to formation of nanostructures. There are two fundamental steps that lead to the formation of nanostructures through crystallization; the first is nucleation where the precursor material aggregates to form small clusters called nuclei. These aggregates serve as seeds for the second step of growth into the larger nanostructures via the Ostwald ripening process[16-18], where larger nuclei grow at the expense of smaller nuclei (Figure 2).

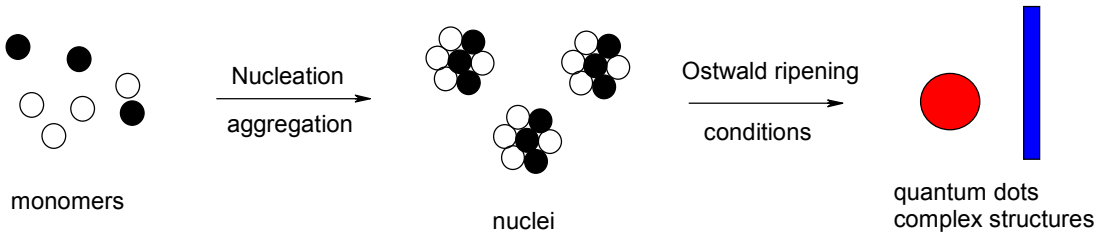

Figure 2 - *The process of crystallization in forming nanostructures. The figure shows monomers aggregating together to form nuclei seeds. The nuclei are affected by the condition of the synthesis, for example the temperature, Ostwald ripening occurs where larger nuclei grow at the expense of smaller nuclei. The final result is the formation of nanocrystals (quantum dots) and possibly more complex nanostructures such as nanorods.*

There are a number of methods for synthesising nanomaterials which allow for a degree of control in the size and shape of nanocrystals. These methods can be broadly split into two types with those involving gas phase syntheses such as vapour-liquid-solid[19,20] (vls) and thermal evaporation[21,22] and those methods which involve liquid-phase synthesis[23,24]. The liquid phase synthesis is of great interest as it allows for greater fine tuning of the nanocrystals size and shape due to the large number of parameters that can potentially be exploited to allow for absolute control over the nanocrystals[25-27]. These parameters include the monomer concentration[28], temperature[29], pH[30-32], surfactants in solution[33,34], whether synthesis occurs in aqueous and non-aqueous media, use of templates[35-37], presence of catalysts[38,39] and the presence of external fields[40-42].

The ability to alter these various conditions gives rise to many different nanostructres, which can be classified in terms of their dimensionality[43]. The nanoparticles that are initially formed in solution can be considered as essentially spherical entities, though in many cases the nanoparticles can adopt a multitude of structures from spherical to cubic resulting in faceted crystals; these structures are hence defined as zero-dimensional nanostructures. One-dimensional nanostructures are composed of nanowires and nanorods, defined as one-dimensional simply because these structures elongate in one direction[44,45]. The same analogy is applied to two-dimensional nanostructures which are growing or elongating in two directions and these include structures such as discs[46] and prisms[47]. Three-dimensional nanostructures do not strictly exist as spherical nanocrystals, defined as zero-dimensional if the crystal has stopped growing, but can be considered as three dimensional only if the crystal continues to grow in all directions. In addition to these defined nanostructures other complex nanostructures exist which do not quite fulfil the requisite requirement of being either formed in one phase of synthesis or structures being composed of different polymorphs of the same precursor material. The most commonly adopted crystal morphologies are either tetrahedral (four coordinate) or octahedral (six coordinate) structures. The tetrahedral crystals adopt either zinc blende or wurtzite morphologies. These differ only in the stacking of atoms between layers. Typical examples of complex nanostructures include stars[48], bipods, tripods and tetrapods[49,50]. These pod structures have a zinc blende nanocrystals core with additional wurtzite arms or rods attached to form tetrahedral like structures[51]. The aforementioned nanostructres are summarized in terms of a dimensional table in Figure 3.

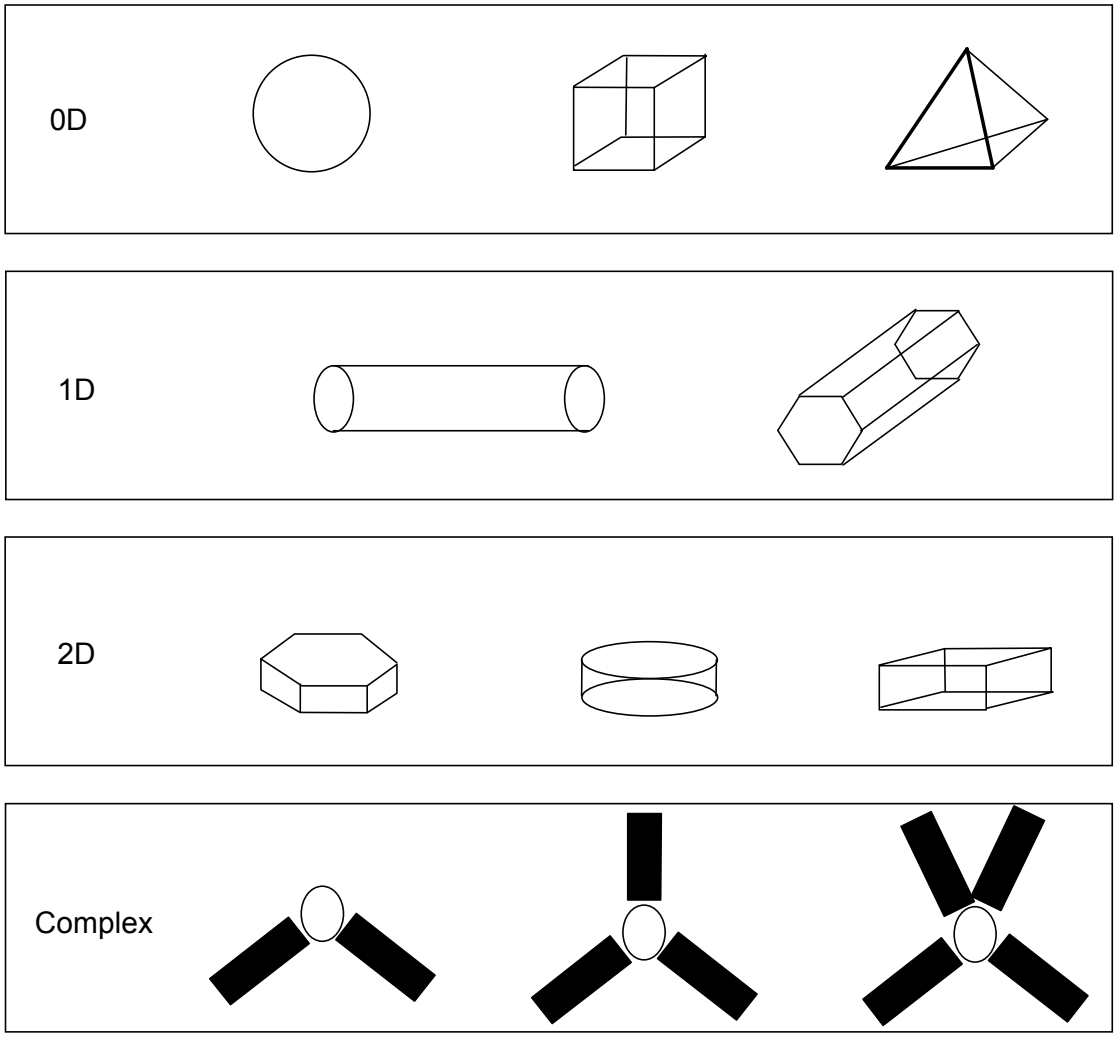

Figure 3 - *Representations of the different nanocrystals structures that are achieved by differing synthesis conditions. The top figure shows the zero-dimensional nanocrystals, the second figure down shows the one-dimensional wire and rod nanostructures and the third figure down shows the two-dimensional nanostructures composed of discs and prisms. The bottom figure shows complex structures achieved by the presence of more than one type of polymorph structure in solution. The unfilled circles represent the zinc blende phase of the nanocrystals whilst the filled arms signify the wurtzite phase of the nanocrystal.*

In the case of many semiconductor nanocrystal syntheses the most commonly applied is the non-hydrolytic method developed by Bawendi and co-workers for the formation of cadmium selenide nanocrystals[52]. The method involves injecting dimethyl cadmium and tri n-octylphosphine selenide (TOPSe) in a solution of tri n-octlyphosphine oxide (TOPO). This method offers many attractive features such as

the ability to keep the monomer concentration in solution relatively constant by applying regular injections of the precursor materials. The more important features are that the nanocrystals produced are highly crystalline and monodisperse. This method has been widely adapted by a number of groups to also yield monodisperse and highly crystalline semiconductor metal chalcogenide[53-55], metal oxide[47,56-59] and purely metal based[60-62] nanocrystals.

1.3 Chalcogenide semiconductor nanocrystals

Chalcogenide nanocrystals are nanoparticles composed of metal cations alongside sulphur, selenium or tellurium anions. These types of nanocrystals have been the focus of much research owing to their intrinsic semiconductor properties, which are observed in the bulk and hence can be further fine tuned in the nano regime by controlling both the shape and size of the nanocrystals formed. The majority of semiconductor nanocrystals such as CdSe and CdS typically adopt either the tetrahedral wurtzite (B4) or zinc blende structures (B3) (Figure 4). These structures are adopted by many III –IV and II -VI semiconductors in their ground states in the bulk material[63,64]. Many systems are seen to undergo solid-solid transitions from either the zinc blende or wurtzite structure to the octahedral rocksalt (B1) structure on the application of pressure[65-68]. This has significant implications for the system's electronic and structural properties, hence affecting the semi-conducting properties. The zinc blende and wurtzite structures are closely related, differing only in the stacking arrangement of the layers of cations and anions. The zinc blende structure adopts an ABCABC repeating sequence for each of the layers respectively; this essentially means three successive cation or anion layers will not be in equivalent positions, whilst in the wurtzite structure an ABABAB repeating sequence is adopted. Another way to describe these structures is to say that the zinc blende structure adopts a chair-chair conformation, while the wurtzite structure adopts a boat-chair conformation. Therefore by twisting the C layers of the B3 structure by 180 degrees it forms the B4 structure[69]. The rocksalt structure is symmetrical on all three faces, the successive layers being stacked on top of one another (Figure 5). Therefore it is clear why the rocksalt structure is adopted at higher pressures, as it is a denser, more compact, structure. Examples of compounds that carry out the above type of

transformations include CdS and CdSe, in which the electronic state shows a corresponding change from semiconductor to insulator[70,71]. Studies of these compounds have shown that the pressure at which this phase transition occurs varies with particle size. As the particle size decreases a corresponding respective increase in the phase transition pressure is seen. This has been related to the surface energies of the crystal structures[72-75].

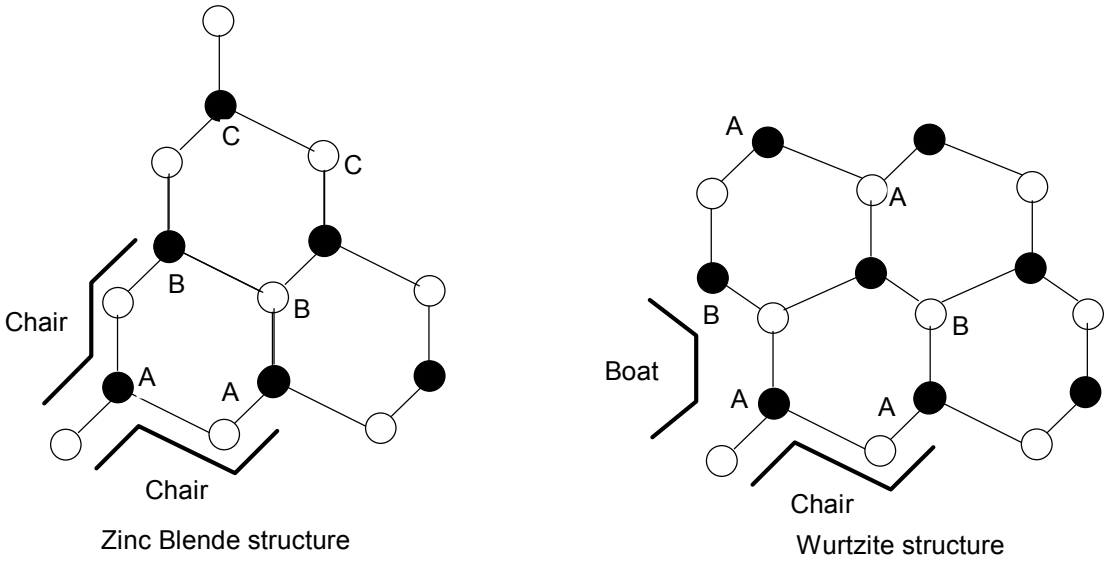

Figure 4 - *The tetrahedral structures adopted by many chalcogenide nanocrystals in solution phase synthesis. The left diagram shows the zinc blende structure with an ABC repeating stacking sequence or in another sense the structure can be considered a chair-chair conformer. The right diagram shows the wurtzite structure with an AB repeating stacking sequence or alternatively it can be considered as a chair-boat conformer.*

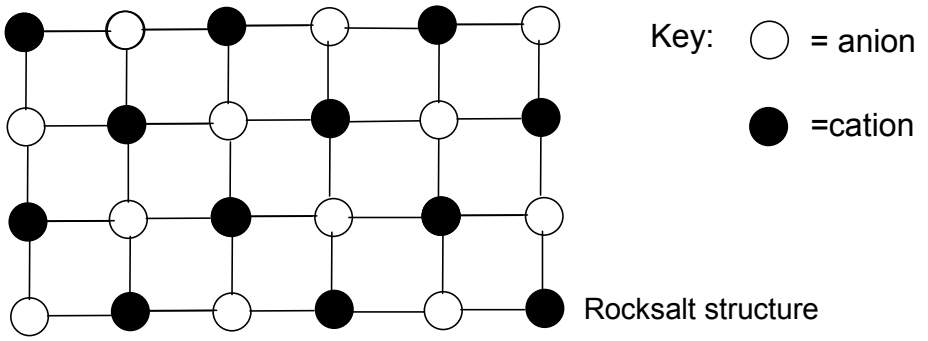

Figure 5 - *The octahedral structure adopted by some chalcogenide nanocrystals in solution phase synthesis. The structure can be considered as simply cubes stacked side by side, with edges of the cubes alternating between anions and cations.*

1.4 Hybrid nanocrystal structures

In addition to forming homogenous nanocrystals and nanostructures these chalcogenide nanoparticles are also used prevalently in the design of hybrid nanocrystals structures[76-78]. This normally involves the formation of one set of homogenous nanocrystals initially. Once formed these nanocrystals are then exposed to a second stage of synthesis whereby a new precursor material is added to the solution so that a second layer of nanocrystals form around the first set of nanocrystals. The first set of nanocrystals formed in solution hence form the core, whilst the latter introduced precursor material grown on the core nanocrystals form the shell (Figure 6). This results in the so called hybrid core-shell nanocrystals[79,80].

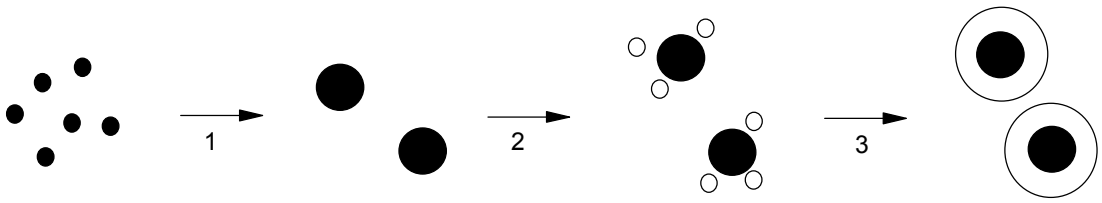

Figure 6 - *The formation of core-shell hybrid nanocrystals. The diagram describes the general process of growing hybrid nanocrystals. Intially in step 1 the precursor material that will form the core of the hybrid nanocrystals is introduced into solution under controlled conditions. Once the core nanocrystals have formed in step 2 the second precursor material is introduced, which aggregates around the core nanocrystals. The third and final step involves the formation of the core-shell hybrid nanocrystals under controlled conditions that favour formation of the shell nanocrystals.*

There are currently a number of core-shell hybrid nanocrystals that have been realised for many semiconductor nanocrystals; including CdSe/CdS[81], CdSe/ZnS[82,83], and ZnSe/ZnS[84]. The core-shell hybrid nanocrystals are potentially very useful as the addition of shell nanocrystal typically enhances the properties of the core nanocrystals such as photoluminescence and quantum yield[85]. If the two nanocrystals are carefully chosen with overlapping band gaps, classed as type 1, they can also result in highly fluorescent nanocrystals, which could be useful in biological probe processes[86]. The

photoluminescence can also be made more efficient by having the two types of nanocrystals with their band gaps staggered, classed as type 2, such that the photon emission from one nanocrystal is in the region of the band gap of the second nanocrystal. This results in an increased quantum efficiency in some hybrid core-shell nanocrystals, such as CdTe/CdSe[87-89] and CdSe/ZnTe[87], which have shown near-IR emission typically not observed for high band gap materials. These type 2 core-shell nanocrystals are particularly useful in biomedical imaging[90,91]. The technique has been extended to forming core-shell hybrid nanocrystals composed of more than two types of nanocrystals[92,93]. The core shell nanocrystals are not limited to quantum dots as nanostructures ranging from rods[94-96] to tetrapods[97] composed of CdTe/CdSe[98,99], CdS/CdTe and CdS/CdSe[100] have been produced.

1.5 Major factors affecting synthesis of nanostructures

1.5.1 Temperature

Temperature plays a crucial role in the synthesis of nanostructures such as tetrapods, which consist of a zinc blende core with the wurtzite arms[101] (Figure *7*). The temperature can control whether the nanocrystallite seeds will grow into nanorods (wurtzite only), bipods, tripods and tetrapods (zinc blende core with wurtzite arms). For example in cadmium sulfide a temperature of 300 ^{o}C produces nanorods, while lowering the temperature to 180 ^{o}C favours the formation of bipods and tripods, and further lowering of the temperature to 120 ^{o}C favours the growth of tetrapods, due to the nucleation of a greater number of zinc blende nanocrystals[102]. The adjusting of the temperature during the initial nucleation phase allows control of the crystalline phase of the seeds. In the case of manganese sulfide nanocrystals, temperatures in excess of 200 ^{o}C favours nuclei of the rocksalt phase, while temperatures below 200 ^{o}C favour the formation of nuclei in the wurtzite phase[103]. This is similar to tin sulphide which produces uncharacteristic zinc blende nanocrystals at low temperatures and its bulk orthorhombic form at higher temperatures[104]. Similarly for ZnS the most stable form under ambient conditions is considered to be the zinc blende rather than the wurtizte form[105]. However, size of crystals and conditions of growth play pivotal roles in determining which morphology is adopted[106].

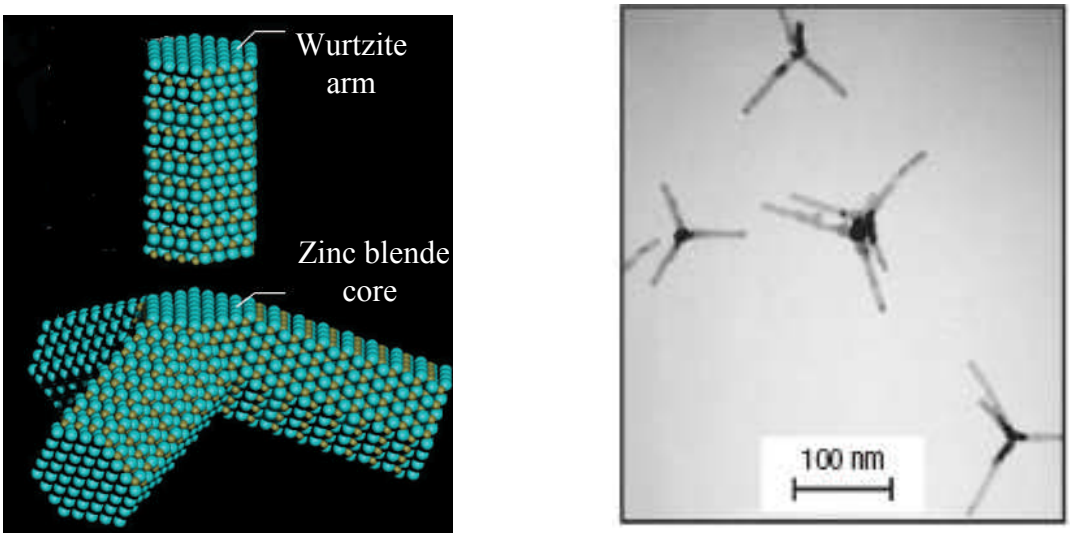

Figure *7 - The tetrapod structures formed from nanocrystals. The left figure shows a graphical depiction of the tertrapod structures, being composed of a zinc blende core and wurtzite arms. The right figure shows a transmission electron microscopy of the CdS tetrapod structures actually observed in experimental work*[101].

The nucleation of crystals is essentially dependent on two properties. The first is the free energy difference between the crystal and liquid per unit volume ΔG_v, which decreases with increasing particle radius. The second is the crystal/liquid interfacial (surface tension) energy γ which increases with increasing size of the particles radius[107]. This is summarised in Equation 1. The combination of these two properties gives rise to both the critical radius r_c and critical free energy ΔG_{crit} (Equation 2), which occurs at maximum ΔG when $dG/dr = 0$. The critical radius is the point at which nucleation will proceed and the critical free energy is essentially the activation energy required to reach the critical radius for nucleation to proceed (Figure 8).

$$\Delta G = \Delta G_{crys} + \Delta G_{surf}$$

$$\Delta G_{crys} = \frac{4}{3}\pi r^3 \Delta G_v$$

$$\Delta G_{surf} = 4\pi r^2 \gamma$$

Equation 1 - *The Gibbs free energy of nucleation. The equation shows its dependence on the the crystal/liquid free energy difference and the interfacial surface energy.*

$$r_c = -\frac{2\gamma}{G_v}$$

$$\Delta G_{crit} = \frac{16\pi\gamma^3}{3(G_v)^2}$$

Equation 2 - *The critcal radius and free energy needed to achieve crystal growth.*

The Gibbs free energy equation can be used to determine the dependence of both critical radius and free energy with temperature. The main conclusions to fall out from this are that both the critical radius and critical free energy of nucleation decrease with decreasing temperature[107]. However, the rate of decrease is greater for the critical free energy than compared to the critical radius.

$\Delta G_v = \Delta H_v - T\Delta S_v$ where H is the enthalpy, T the temperature and S the entropy.

At the equilibrium point, ΔG_v=0, at the metlting temperature T_m achieves;

$$\Delta S_v = \frac{\Delta H_v}{T_m}$$ Substituting back into the above equation;

$$\Delta G_v = \Delta H_v - T\left(\frac{\Delta H_v}{T_m}\right)$$

$$\Delta G_v = \Delta H_v\left(\frac{T_m - T}{T_m}\right)$$ Thus subsitutuing G_v back into Equation 2;

$$r_c = -\frac{2\gamma}{\Delta H_v}\left(\frac{T_m}{T_m - T}\right)$$

$$\Delta G_{crit} = \frac{16\pi\gamma^3}{3\Delta H_v{}^2}\left(\frac{T_m}{T_m - T}\right)^2$$

Equation 3 - The *Gibbs free energy used to determine the dependence of the critical radius and critical free energy with temperature.*

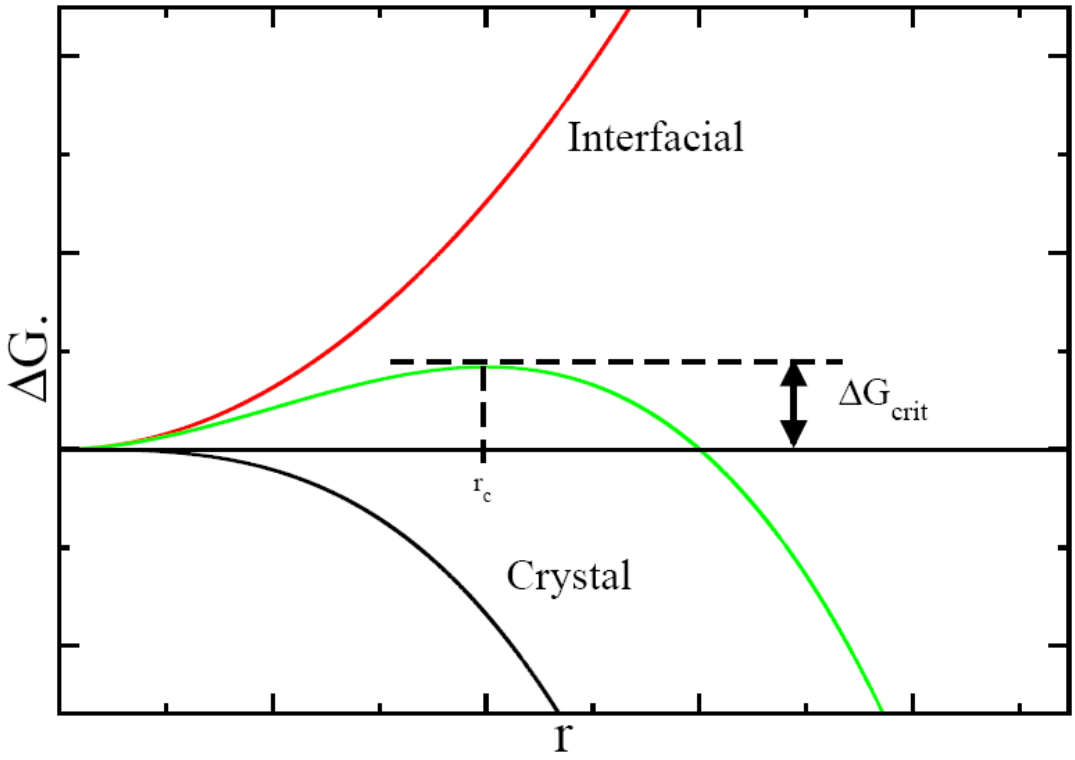

Figure 8 - *The free energy changes during the nucleation of crystals in solution. The free energy of nucleation is dependent on two quantities; the crystal/volume energy (black line) and the interfacial/surface energy (red line). The critical radius r_c is highlighted along with the critical free energy ΔG_{crit}.*

1.5.2 Monomer Concentration

The monomer concentration refers to the concentration of the building blocks of the nanocrystals, for example in the case of cadmium selenide this is the Cd and Se molecular species present that are not part of any nanostructure or nanocrystals. The formation of nanocrystals in a given solution results in the monomer concentration naturally decreasing as more nanocrystals are formed. It is found that allowing the monomer concentration to naturally decrease yields a range of structures, ranging from nanorods to tetrapods. However maintaining the monomer concentration in the solution yields the formation of nanorods with high aspect ratios, the ratio between the length and width of the nanorods,[108,109] (Figure 9). The example of cadmium sulphide also illustrates that high concentrations of the monomers in solution at low temperatures can also result in the formation of "candy corn" structures instead of tetrapod structures[110].

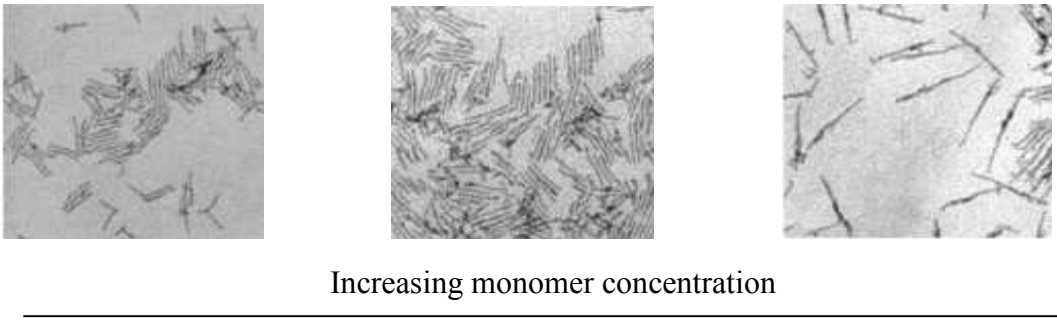

Figure 9 - *The nanostructures formed at different monomer concentrations. The left figure shows the results of having low monomer concentrations resulting in structures ranging from rods to tetrapods. The middle figure shows an increase in rod structures as the monomer concentration in solution is increased. The right figure reveals the beginnings of nanowire structures as monomer concentration is maintained*[108].

Alivisatos and co-workers also report that once tetrapod structures of CdSe have been formed and isolated, further addition of monomers yields growth of the tetrapod's wurtzite arms as well as the formation of dendritic tetrapods. The dendritic tetrapods are produced by the presence of stacking faults at the ends of the wurtzite arms which are now of an ABC stacking pattern, confirmed by high resolution transition electron microscopy, and hence a zinc blende structure. These zinc blende edges of the tetrapod arms serve as connection points for further growth of more wurtzite arms and so leading to the dendritic tetrapods[111] (Figure 10).

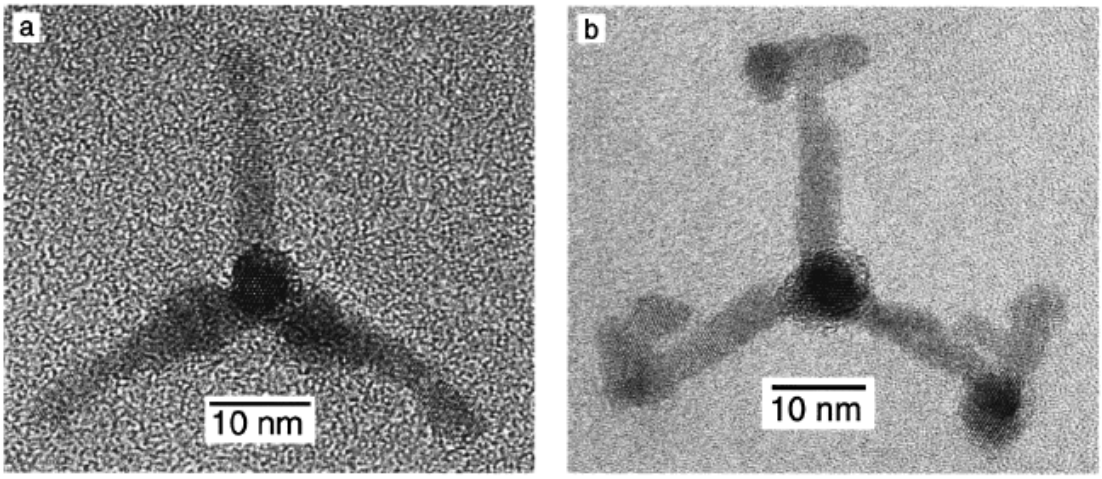

Figure 10 - *The experimental transmission electron microscopy observations of tetrapod and dendritic tetrapods. The figure inset shows; (a) tetrapods with purely wurtzite arms, and (b) dentrtic tetrapods with wurtzite arms with zinc blende edges*[111].

The formation of tetrapods can be thought of as the fusion of two different types of nanocrystals, wurtize and zinc blende, and once these nanocrystals aggregate to produce the tetrapods, the arms can continue to grow until monomers in the solution are depleted. The further application of monomers can result in the formation of new zinc blende nanocrystals which attach to the ends of the preformed tetrapods; as such these zinc blende nanocrystals act as connectors for further wurtzite nanocrystals to attach and hence growth of dentritic tetrapods. This mechanistic explanation of the formation of tetrapods and dentritic tetrapods is displayed in Figure 11.

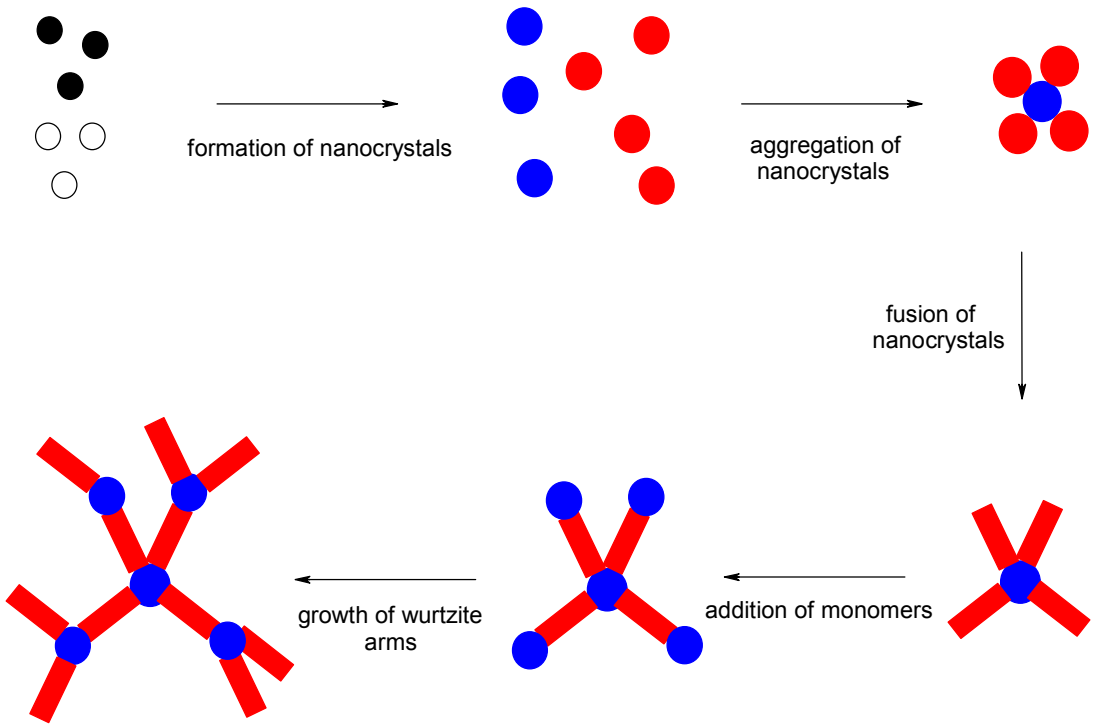

Figure 11 - *The mechanism describing the synthesis of tetrapods and dentritic tetrapods. Initially the monomers are introduced in solution (top left figure), these aggregate to form nanocrystals of wurtzite (red) and zinc blende (blue). The nanocrystals can aggregate and fuse to form tetrapod structures (bottom right figure). The addition of monomers into a solution containing tetrapods results in the formation of zinc blende nanocrystals at the edges of the tertapods. These zinc blende edges on the tetrapods act as connections points for either growth or attachment to wurtzite nanocrystals leading to the dentritic tetrapods (bottom left).*

1.5.3 Surfactant

The growth of nanostructures in the presence of surfactants relies on the fact that faceted rather than spherical seeds are nucleated, with different facets having different surface energies. This approach is successfully applied to chalcogenide semiconductor collid synthesis[111,112], for example in the case of CdSe, nanorods are obtained by growing nanocrystals in the presence of alkylphosphonic acids (surfactant). The nanorods grow along the [001] direction due to the surfactant adhering to all other facet surfaces of the nanocrystals except the [001] surface, hence growth is preferred on this face[112]. The removal of surfactants from the surface of nanocrystals also has a profound effect exemplified by the removal of oleic acid capping ligands by the addition of pyridine in lead selenide nanocrystals. The nanocrystals in the presence of oleic acid are well spaced from one another, however the addition of pyridine results in the removal of oleic acid ligands from the surface of the nanocrystals leading to the association of the nanocrystals to form chain like network structures[113] (Figure 12).

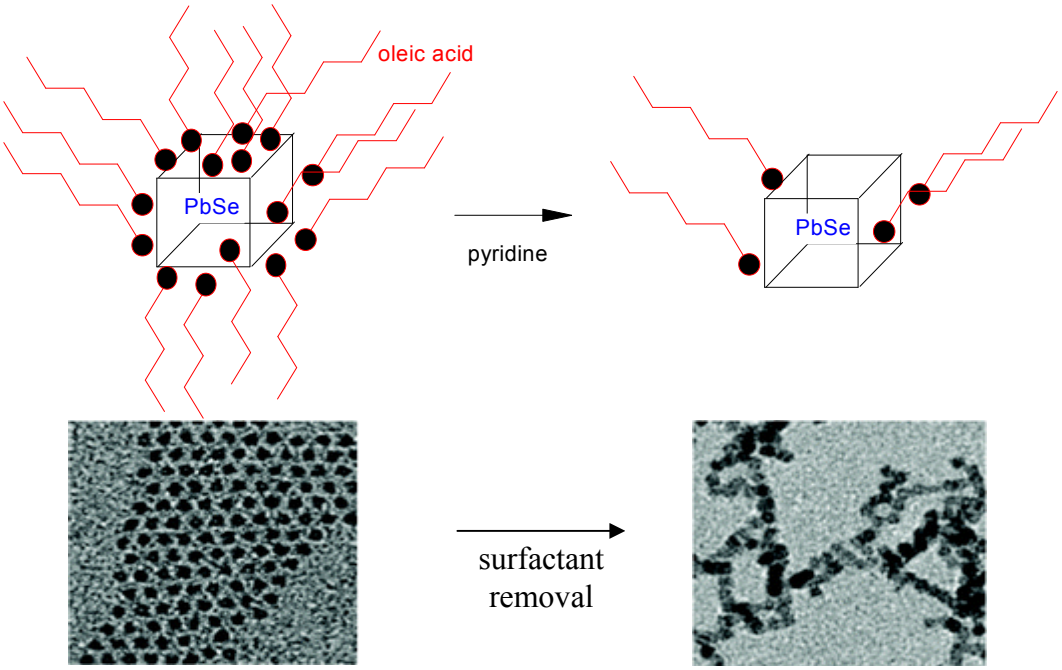

Figure 12 - *The effects of surfactant displacement on the structure of nanocrystals. The figures to the left show the lead selenide nanocrystals in the presence of oleic acid, whilst the figures to the right show the nanocrystals after treatment with pyridine. The result is removal of oleic acid from the nanocrystals and formation of a network structure*[113].

The work of Houtepen and co-workers also displays the importance of surfactants in solution phase synthesis of lead selenide in terms of the shape morphology of the nanocrystals. They find the presence of acetate, commonly used in the preparation of the lead precursor prior to injection[114], can result in a multitude of nanocrystal morphologies from spherical, star and octahedron depending on the amount of acetate present. The mechanism of these shape morphology changes is attributed to the displacement of the actual intended and used surfactant oleate by the smaller acetate molecules. This leads to a greater amount of association between the nanocrystals through certain crystal facets, the oriented attachment mechanism, resulting in the range of shape morphologies. In addition they report that temperature has no effect on the shape morphologies of the nanocrystals[115].

The importance of surfactants has been elegantly displayed by the work of Wang and co-workers. They initally found problems with reproducing synthesis of cadmium selenide nanowires to satisfactory levels. They subsequently discovered the problem lay in impurities of commercially available tri-n-octylphosphine oxide (TOPO) used in the synthesis of the nanowires[116]. It was demonstrated that by varying the surfactant combination with common impurities found in TOPO that they could control the formation of quantum dots, nanorods and nanowires simply by selecting the additional surfactants to be added to recrystalized TOPO. These variants included di-n-octylphosphine oxide (DOPO), n-octylphosphonic acid (OPA), mono-n-octylphosphinic acid (MOPA) and di-n-octylphosphinic acid (DOPA) (Figure 13). There has been further research in this area attributing the presence of impurities to the synthesis methods used to obtain commercial TOPO[117].

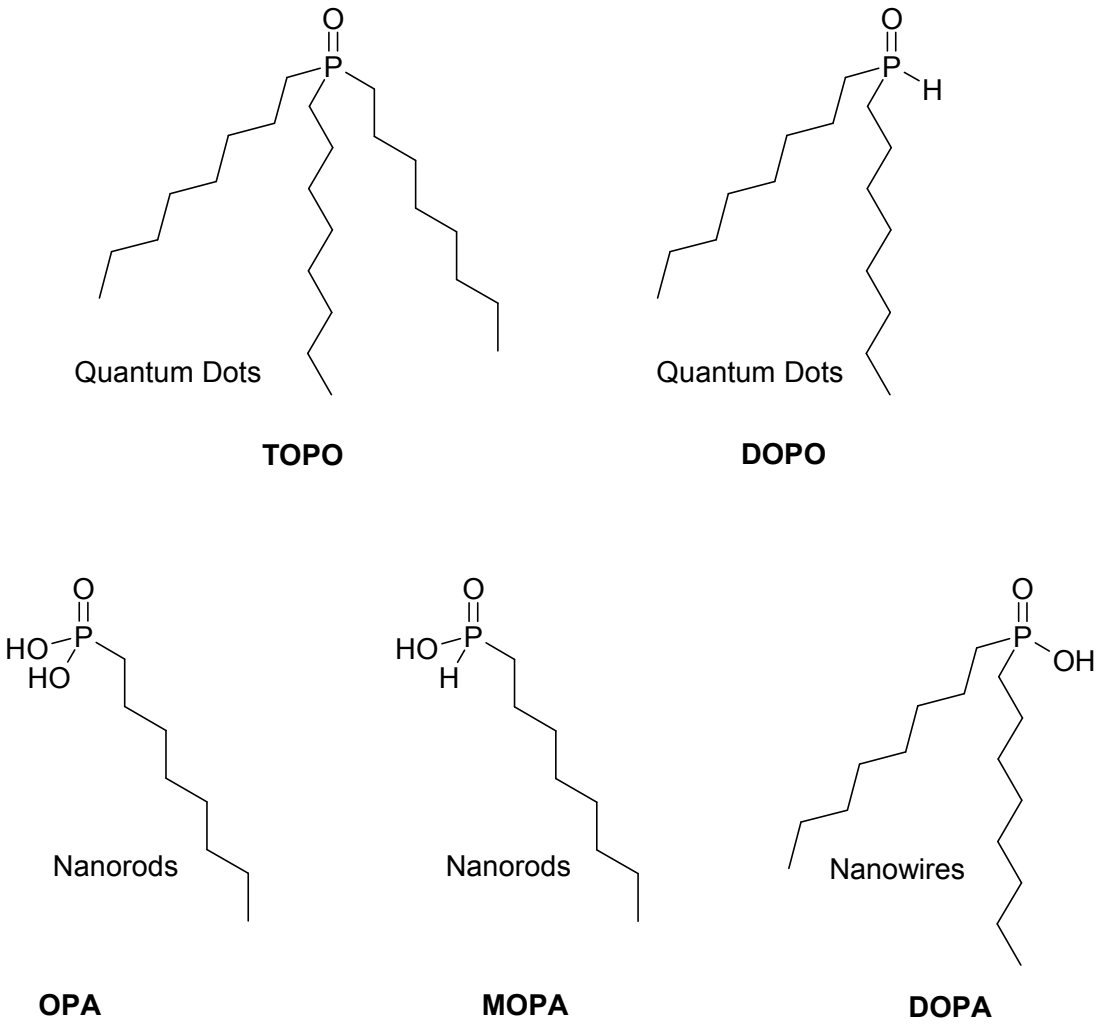

Figure 13 - *The formation of different nanostructures and their dependence on the surfactants employed during synthesis. The top figures show TOPO and DOPO, which have similar chemical structures that lead to the formation of quantum dot nanocrystals. The bottom figures show OPA, MOPA, which lead to the preferential formation of one-dimensional nanorods, and similarly DOPA which leads to the formation of one-dimensional nanowires.*

The work by Cheon and co-workers has also shown that it is possible to control the crystal phase of nanocrystals between the zinc blende and wurtzite phases for gallium phosphide[118], which is also a semiconductor. The zinc blende phase is considered to be staggered while the wurtzite phase is eclipsed; as such the former is thermodynamically favoured on steric grounds while the latter is kinetically favoured on electronic grounds due to the interactions between phosphine and gallium atoms[119] (Figure 14).

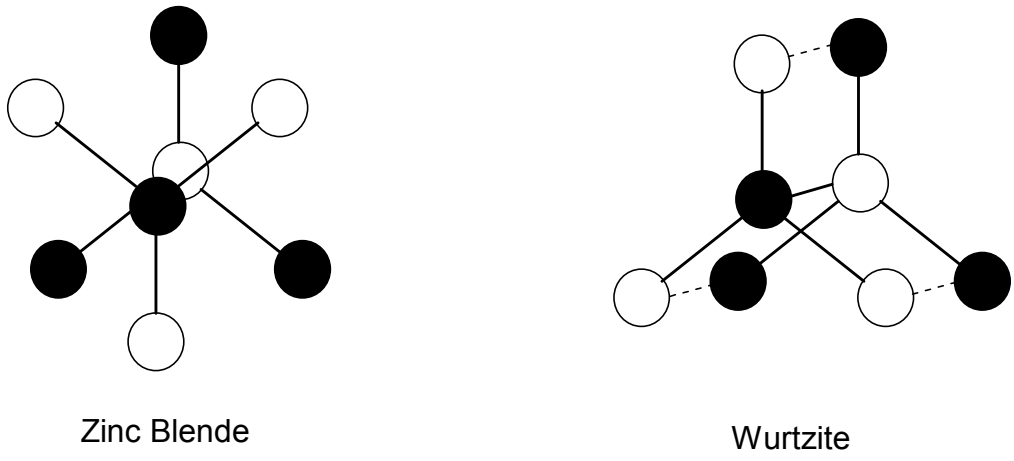

Figure 14 - *The two tetrahedral related structures that can be achieved by controlling conditions. The two structures are shown in dihedral form with the zinc blende structure in a staggered conformation, whilst the wurtzite structure is in an eclipsed conformation. The staggered conformation is the thermodynamically stable, the eclipsed conformation is kinetically stable due to favourable electrostatic interactions between geminal atoms, in this case gallium and phosphine atoms.*

The control between the two different tetrahedral structures is achieved by choosing suitable surfactants. When large sterically bulky tertiary amines are employed the staggered conformation is favoured due to the steric hindrance between the surfactant and crystal surface. Hence the zinc blende structure of gallium phosphide nanocrystals is achieved. The use of less sterically hindered surfactants such as primary amines reduce the energy difference between the two phases, due to less steric hindrance between the surfactant and crystal surface, and as such the electronic effects now play a major role leading to the formation of wurtzite structure. It should also be noted that this synthesis is considered to be the first to employ a liquid phase synthesis for III-V semiconductors resulting in anisotropic nanorods and nanowires[118]. This very same methodology has recently been applied to the synthesis of cadmium telluride tetrapods. The use of larger associating ligands with tellurium results in the first reported case of purely zinc blende tetrapods, both the core and arms[120].

Alivisatos and co-workers have also shown the importance of surfactants in the case of TiO_2 nanocrystals, where the surface selective surfactant lauric acid adheres strongly to the [001] direction of the nanocrystal seeds. Small concentrations of lauric

acid lead to the growth of nanostructures that resemble bullets or diamonds, while high concentrations of lauric acid produce branched rods[121] (Figure 15).

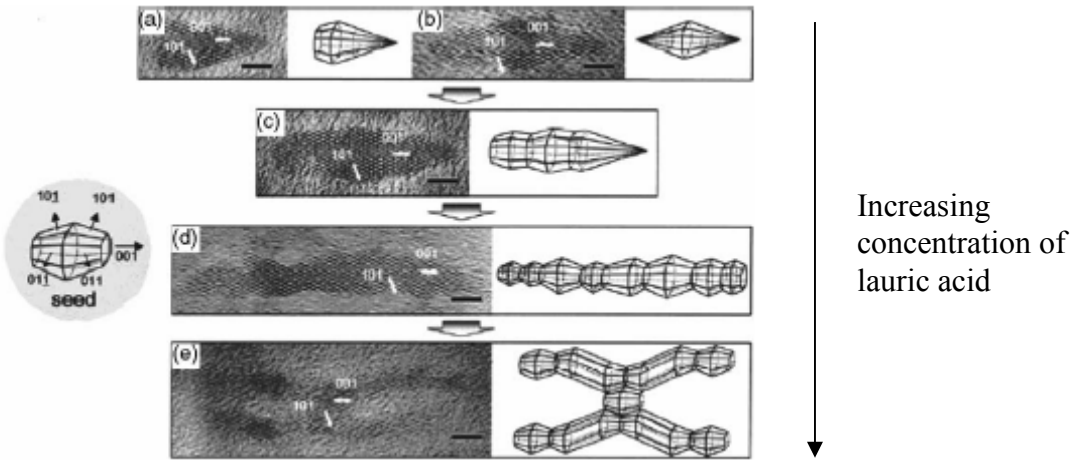

Figure 15 - *The different titanium oxide nanostructures that result with increasing surfactant concentration. The surfactant employed in this particular synthesis is lauric acid which in increasing concentrations causes branching nanostructures[121].*

1.6 Oriented attachment

The synthesis, described previously, are carried out in the solution phase without the aid of any templates and therefore involve self assembly processes[122]. For instance the formation of the zero-dimensional nanocrystals is itself a self-assembly process involving the precursor materials in solution aggregating to form these basic nanocrystal structures. These nanocrystals can be spherical or can display a multitude of faceted structures depending on the synthesis conditions. Once the formation of these zero-dimensional nanocrystals occurs the self assembly process usually continues onward to the formation of more complex structures; in essence, the zero-dimensional nanocrystals can serve as seeds themselves for producing further nanostructures. Indeed the most prevalent mechanism postulated in the literature with regards to chalcogenide nanorod and nanowire one-dimensional nanostructures is the so called oriented attachment mechanism[123]. This mechanism describes the formation of one-dimensional nanostructures from zero-dimensional nanocrystals through the alignment of common crystallographic facets of nanocrystals, which results in

minimization of the surface energy, or alternatively the surface area, of the nanocrystals (Figure 16).

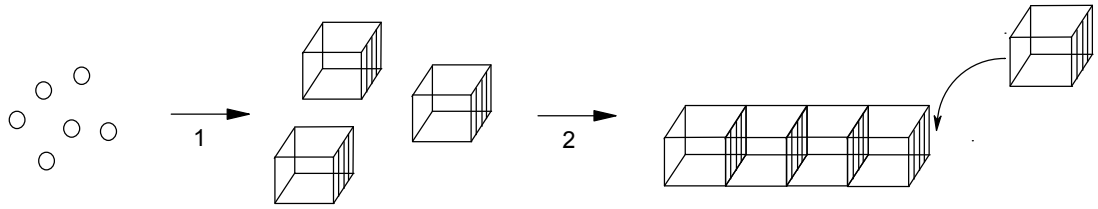

Figure 16 - *The self-assembly processes occurring to yield nanocrystals and higher dimensional nanostructures. Initially the precursor material is introduced into solution resulting in the formation of nanocrystals with faceted structures in the first step. The second step involves the formation of one dimensional nanostructures by faceted nanocrystals fusing along common crystallographic facets. The shaded face of the cubic nanocrystals depicts common crystallographic faces which results in the self-assembly.*

1.7 Oriented Attachment and dipoles

The oriented attachment mechanism was initially found to be displayed in many metal oxide systems, TiO_2[124,125], ZnO[126,127] and CuO[128], however later work showed the mechanism to be present in many metal-chalcogenide systems, including CuS[129], CdTe[130]and ZnS[131,132]. However recent work suggested that a primary reason for nanocrystals coming together in such a fashion is more fundamentally related to the presence of dipole moments in semiconductor chalcogenide nanocrystals. The mechanistic driving force therefore for the self-assembly of these nanocrystals into higher dimensional nanostructures is the dipole-dipole inter-particle interactions between nanocrystals[133]. In the early 1990's experimental work in which an electric field was applied to a sample of CdSe nanocrystals revealed, through analysis of the absorption spectra and use of the Stark effect, a dipole moment approximately 32 Debyes in magnitude present when the nanocrystals were in the first excited state[134,135]. Further research into CdSe nanocrystals led to the conclusion that the dipole moment was not only prevalent, but was in essence the result of the wurtzite

structure being adopted by the nanocrystals[136], as in the bulk structure it is known to be polar[137]. Hence this tended to support the origin of the dipole moment as being intrinsic to the wurtzite structure[138]. The evidence for this arises from the fact that the wurtzite nanocrystals of CdSe were assigned to belong to the C_{3V} point group[139]. It is typical of molecules that are assigned to this point group, such as $POCl_3$ which intrinsically have dipole moments. Similar arguments are made by Nann and co-workers in which the dipole moment in wurtzite nanocrystals is attributed to the distortion of the tetrahedral structure, such that essentially bonds in a particular direction are longer than in other directions, also resulting in a dipole moment within the nanocrystals[140] (Figure 17).

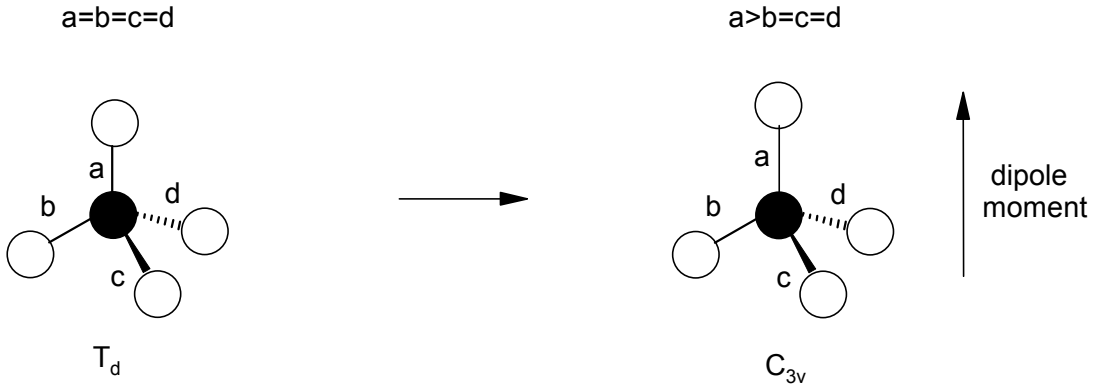

Figure 17 - *The tetrahedral structure making up the wurtzite structure. The tetrahedral structure on the left has bond lengths of equal size resulting in a dipolar neutral structure. The structure on the right is a distortion of the tetrahedral structure with one of the bond lengths greater than the others; the result is a dipole moment in the crystal with this distorted tetrahedral structure.*

1.7.1 Dipole moments in zinc blende and wurtzite crystals

It was similarly proposed by Blanton and co-workers through conductivity measurements of CdSe nanocrystals that the hexagonal wurtzite lattice was responsible for the resulting dipole moment in the nanocrystals. This meant a cubic zinc blende lattice of nanocrystals would be expected to have a zero dipole moment as these zinc blende nanocrystals are assigned to the T_d group, assuming the lattice

structure determines this apparent dipole moment[141]. This hypothesis was further investigated by Shim and co-workers, who showed that although the dipole moment of the zinc blende nanocrystals (ZnSe) is decreased relative to the wurtzite nanocrystals (CdSe), it is by no means negligible. For nanocrystals of 48 Å in diameter the observed dipole moment for the wurtzite nanocrystals is 73 Debyes, while for the zinc blende nanocrystals it is 56 Debyes. Both the lattice structures also show a dependence on nanocrystals size, with increasing nanocrystal size resulting in an increase in the dipole moment (Figure 18). This dipole moment was also shown to be thermally stable at a number of temperatures[142].

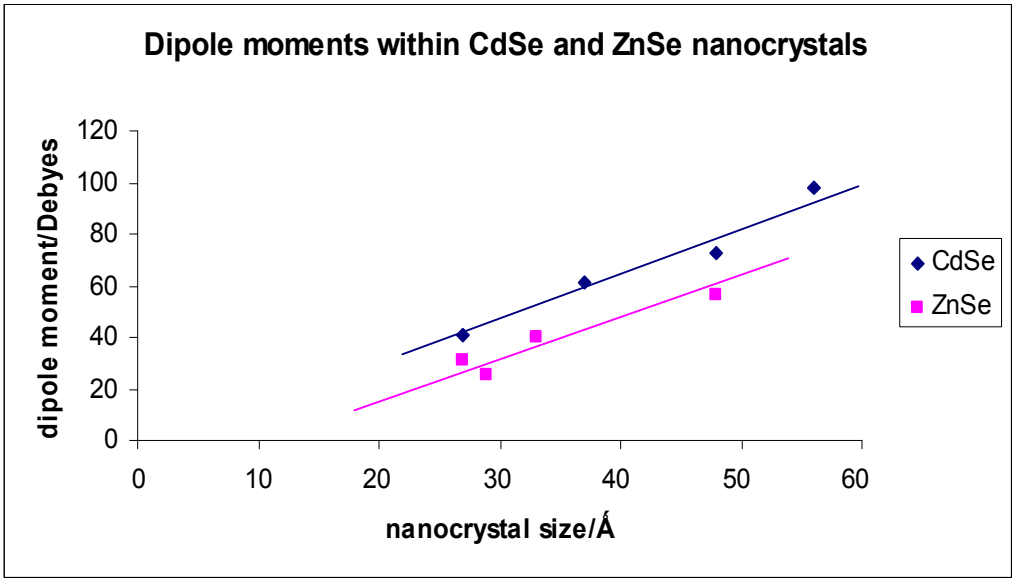

Figure 18 - *The dipole moments in different nanocrystals. The figure shows the dipole moments present for the wurtzite (CdSe) and zinc blende (ZnSe) nanocrystals of differing sizes. Lines of best fit are shown in the same colours as the data points for each respective structure as indicated by the figure legends.*

The presence of a dipole moment within these nanocrystals is accepted though the exact origin of the dipole moment has been debated. There are a number of possibilities that have been suggested which include the polar character of the hexagonal wurtzite lattice [138]. This is at odds with results of Shim and co-workers, which show that the cubic zinc blende lattice also produces a significant dipole moment[142]. A further suggestion is that, since CdSe and ZnSe are piezoelectric,

surface strain may provide a possible explanation for the presence of a dipole moment[143]. However, in the case of zinc blende structures there needs to be a distortion away from the T_d symmetry to exhibit the dipole moment. It is thought likely that surface strain in nanocrystals will be sensitive to different organic ligands and hence to temperatures, but this is not observed. The presence of surface localized charges is thought to be the primary cause of the dipole moment by Shim and co-workers[142]. This is at odds with the work of Brus and co-workers which rule out the surface charge being the cause of the dipole moment[138], as surface ligand passivation of the nanocrystals does not affect the dipole moment. Both groups do, however mention shape asymmetry or lack of inversion symmertry as being a possible explanations to the origin of the dipole moment. Indeed, small deviations of shape from a perfectly centrosymmetric nanocrystallites are likely to lead a dipole moment. However transition electron microscopy images of larger nanocrystals reveal no obvious deviations from a spheroid shape[15] (Figure 19).

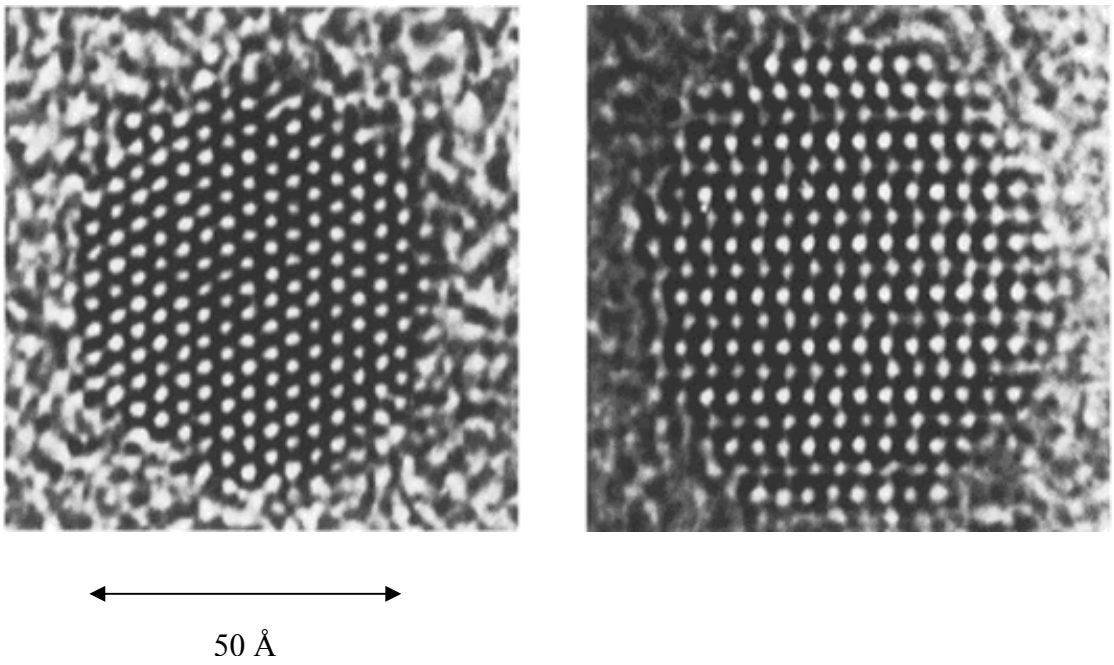

Figure 19 - *The hexagonal wurtzite cadmium selenide nanocrystallites. The figure illustrates the actual transmission electron microscopy images of cadmium selenide nanocrystals form two different angles. There are no obvious deviations of the nanocrystals from a spherical shape[15].*

1.7.2 Dipoles and crystal structure

There are a number of feasible causes for the dipole moment as outlined previously, though the most likely cause is attributed to the lack of inversion symmetry in nanocrystals. This essentially means that the nanocrystals have different terminating atoms at either side of the nanocrystals resulting in the dipole moment. This can be exemplified by imagining a CdSe nanocrystal in two dimensions terminating with cadmium atoms on the top surface of the nanocrystal, whilst the bottom of the nanocrystal surface terminates with selenium atoms (Figure 20).

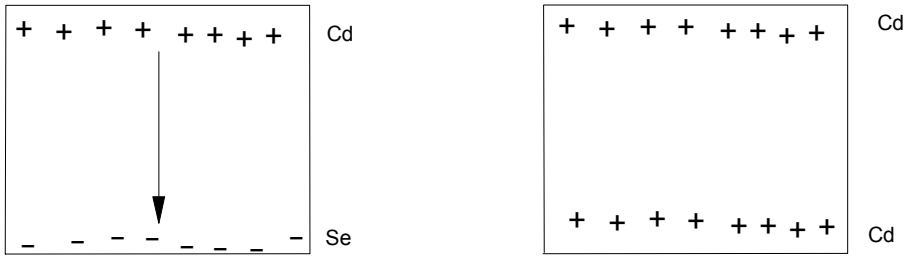

Figure 20 - *Explanation of the presence of dipole moments within nanocrystals. The figure on the left shows a depiction of 2D nanocrystals terminating with Cadmium atoms on top (positive charge) and Selenium atoms on the bottom (negative charge). The nanocrystal lacks inversion symmetry and gives rise to a dipole moment. The figure on the right shows a similar nanocrystal terminating with only Cadmium atoms on the surface; it thus has no dipole moment, and retains inversion symmetry.*

The explanation encompassing surfaces terminating with anions and cations would also provide an explanation to the oriented attachment mechanism, with certain crystal facets being exposed as cations or anions. This can potentially explain the driving force for opposing crystal facets of individual nanocrystals fusing together to form more complex nanostructures (Figure 21).

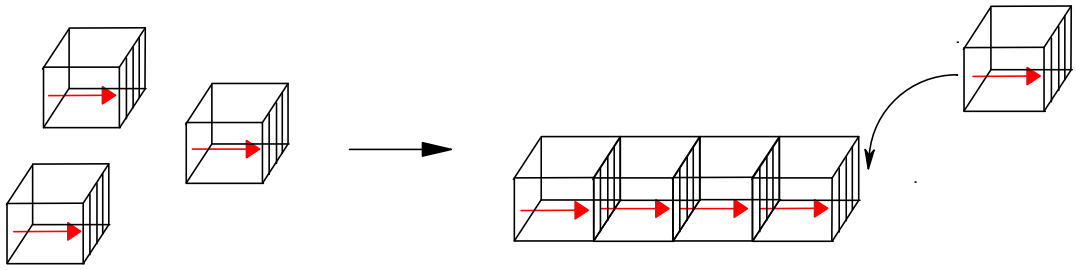

Figure 21 - *The mechanistic explanation of the oriented attachment of nanocrystals to more complex nanostructures, such as nanorods and nanowires. The figure inset shows that individual nanocrystals contain a dipole moment due to opposing crystal facets terminating with anions and cations. The presence of dipole moments in the nanocrystals means individual nanocrystals can come together in a head-tail fashion resulting in one-dimensional nanocrystals.*

The argument of different terminating atoms on opposing sides of a nanocrystal giving rise to the dipole moment in the nanocrystal implies that the dipole moment is independent of the internal structure of the nanocrystal. The previous discussion on dipole moments has focuses solely on nanocrystals with a tetrahedral structure; either the Wurtzite or Zinc blende structures. This is contrasted with the experimental work of Cho and co-workers, which highlights the formation of lead selenide cubic multifaceted nanocrystals of an octahedral morphology. These nanocrystals can self-assemble to form a number of different nanostructures depending on the conditions, giving rise to unique nanoring and zigzagging nanowires not observed in other metal chalcogenide semicondutors. The formation of these structures is attributed to the different terminating facets at the corner of the cubic lead selenide nanocrystals. There are essentially two possible combinations of terminating facets that lead to dipole moments being present in the nanocrystals. These two different dipole containing nanocrystals result in the differing pathways that produce the observed nanorings, linear nanowires and zigzag nanowires[144] (Figure 22).

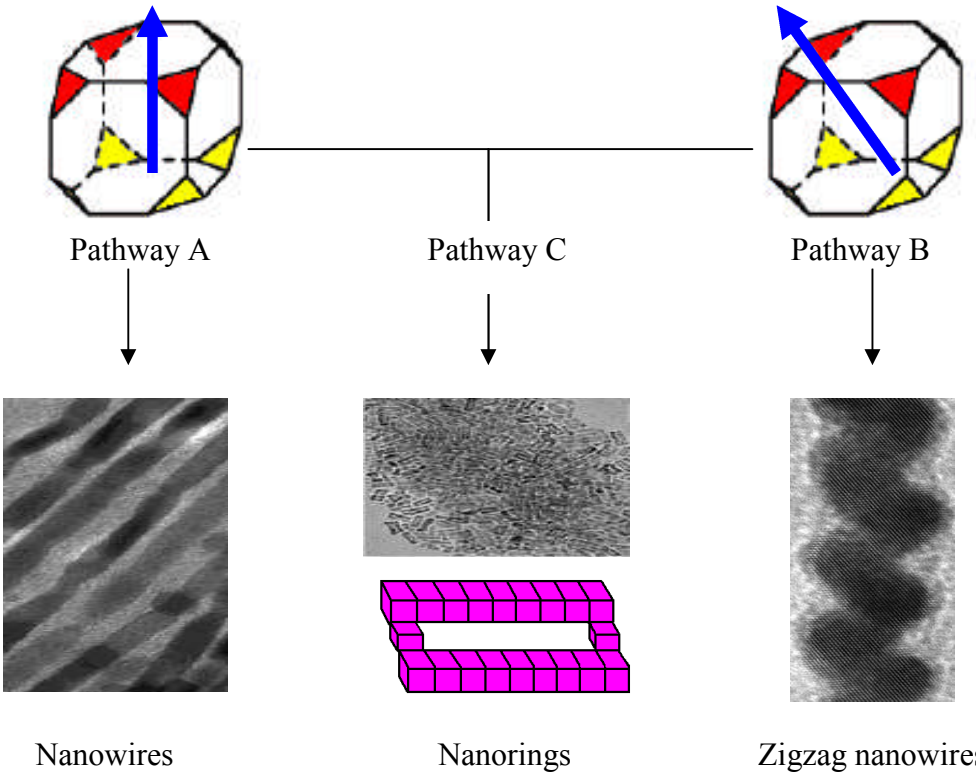

Figure 22 - *The explanation of oriented attachment in lead selenide nanoparticles producing different nanostructures. The top figure shows two possible combinations of terminating edge facets of the nanocrystals resulting in contrasting dipole moment directions. The red surfaces can be considered as selenide covered whilst the yellow as lead covered. The first pathway A produces the linear nanowires, whilst pathway B results in formation of zigzag nanowires. The combination of both types of nanocrystals results in pathway C producing unique nanorings*[144].

1.7.3 Nanorods

There has been experimental transient electric birefringence measurements carried out which confirm the existence of a permanent dipole moment along the c-crystallographic axis of one-dimensional nanorods. This observed property supports the idea of the oriented attachment being mechanistically driven by dipole moments within nanocrystal building blocks. The work also reveals there is no relationship present between the observed dipole moment relative to the length or widths of the nanorods, however there is a linear scaling for the dipole moment with the volume of the nanorods observed[145].

The synthesis of nanorods composed of CdSe and CdS by Talapin and co-workers lead to the formation of nanotracks which are composed of nanorods aligned side by side, which visually seem like large nanowires. In addition it is also observed that these nanotracks are seemingly aligning parallel to one another. The researchers comment on how very little is known about the interplay between Van der Waals and other forces affecting nanoparticle dispersions[146]. Talapin and co-workers conjecture that attractive dipolar interactions between nanorods may explain the formation of the observed nanotracks during the self assembly synthesis of nanorods, similar nanotracks are also observed in magnetic cobalt nanorods[147]. The formation of these kinds of nanorod tracks is computationally predicted from the simulations of spherocylinder hardspheres, which encompass a dipole interaction term with the Lennard-Jones potential[148] (Figure 23).

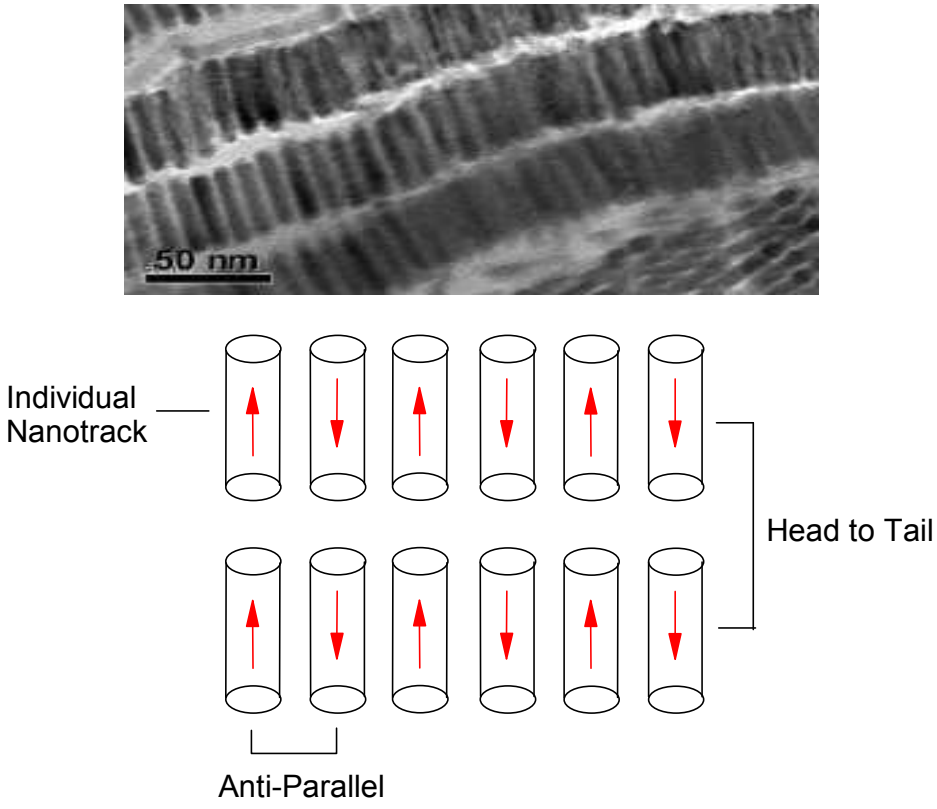

Figure 23 - *Nanorods combining to form nanowire like structures called nanotracks. The top figure inset shows the experimentally observed nanorods forming the nanotracks[147]. The bottom figure provides the possible explanation for the formation of nanotracks the nanorods align adjacent to one another with their respective dipole moments being anti-parallel. The formed nanotracks can also align parallel to one another due to head-tail dipole interactions between the tracks.*

1.7.4 Nanowires

Tang and co-workers have carried out the spontaneous synthesis of cadmium telluride nanowires, through a rather unique mechanism that is not observed in most nanowire synthesis. The cadmium and telluride precursors initially react in aqueous solution to form cadmium telluride nanocrystals possessing a zinc blende structure. These nanocrystals of cadmium telluride are left in the dark for several days, during which time the aggregation of these nanocrystals into a pearl-necklace type structure is observed (Figure 24). The pearl-necklace aggregates later rearrange themselves to form linear wires before undergoing a crystal phase transition to form nanowires of a wurtzite structure[149,150]. The formed nanowires are relatively monodisperse ranging in diameters from 2.5 to 5.4nm. These nanowires have unique properties relative to other known direct band gap semiconductors in that they show greater luminescence. The luminescence is greatest for the smaller diameter nanowires, with the smallest 2.5 nm nanowires having a luminescence maximum at 520 nm and the larger 5.4 nm nanowires having a luminescence maximum at 630 nm. The greater luminescence indicates the high crystalline nature of the formed nanowires. Tang and co-workers also believe only dipole-dipole interactions can account for the formation of these unique nanowires[130]. The mechanism of formation of these nanowires and possible nanotracks is summarised in Figure 26.

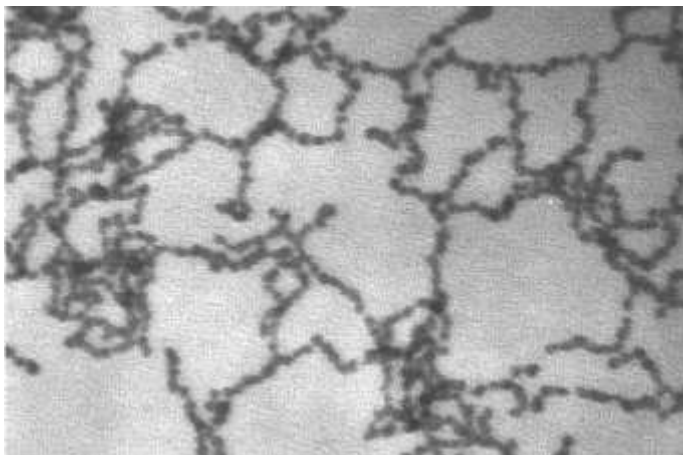

Figure 24 - *The transmission electron microscopy view of the cadmium telluride nanocrystals. The individual zinc blende nanocrystals are clearly visible in forming the larger pearl-necklace type structures*[130].

The formation of these pearl-necklace structures is not limited to metal chalogenide[151,152] nanocrystals alone as it is observed in many metals, Ag[153], Co[154],Pd[155] and Ni[156], and metal oxide, Fe_3O_4[157-159] nanocrystals prior to the formation of one-dimensional nanostructures (Figure 25). The underlying cause for the formation of these pearl-necklace structures as stated before is the dipole-dipole interaction; in the case of metals the origin is considered to be a magnetic dipole. Though the source of the dipole within these many nanocrystals varies the pearl-necklace structures present are remarkably similar and hence reinforce the idea of dipoles being important in self-assembled one-dimensional nanostructures.

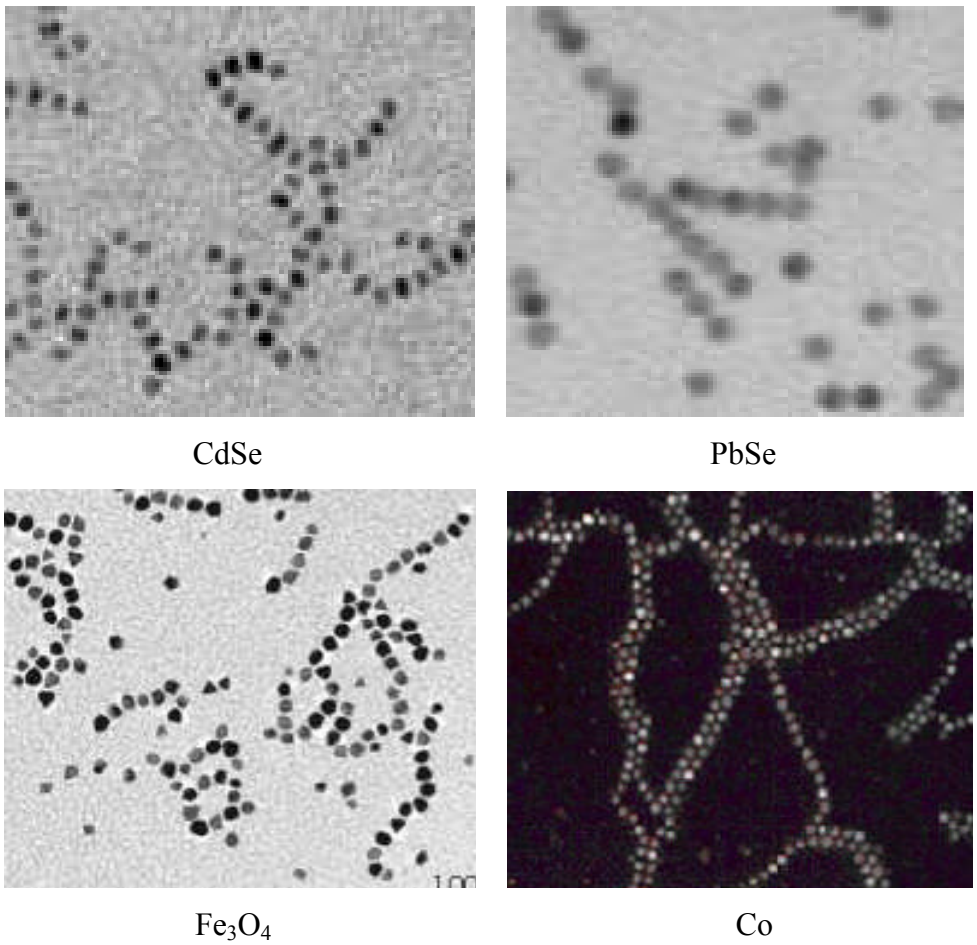

Figure 25 - *The pearl necklace structures observed in many chemical systems. The different nanocrystal systems are labelled appropriately. The structures are remarkably similar to one another even though the morphology of the nanocrystals and origin of the proposed dipole moments vary*[151,154,159].

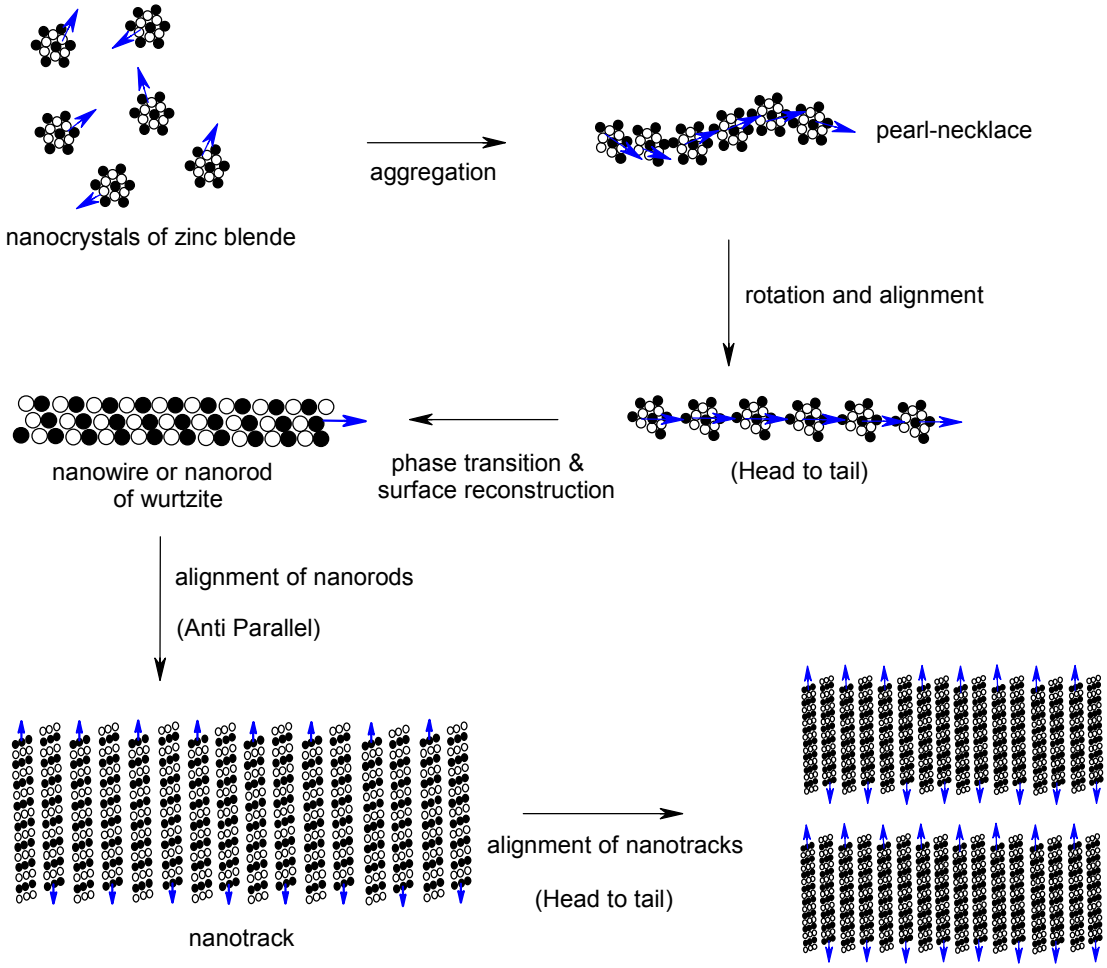

Figure 26 - *The outline of the possible mechanism leading to one dimensional nanostructures for cadmium telluride. Initially the precursor material comes together to form zinc blende nanocrystals which aggregate to form the typically observed pearl-necklace type structure due to head to tail alignment of their intrinsic dipoles. The chain structures then undergo surface reconstruction to form nanowires. The cadmium telluride nanowires uniquely also undergo a phase transition from zinc blende to wurtzite structures on their formation. The nanorods retain dipole moments from their nanocrystals constituents. This allows the nanorods to form nanotracks via anti-parallel alignment of dipoles; similarly the nanotracks can align due to head-tail dipole interactions between different nanotracks.*

1.7.5 Metal nanocrystals

Semiconductor nanocrystals are not the only nanocrystals to exhibit the self-assembly by the proposed dipole-dipole interaction between nanocrystals. Metals such as gold nanoparticles, which do not display an intrinsic electric or magnetic dipole, are also thought to self assemble through a dipole-dipole interaction between nanocrystals[160]. This is unusual as semiconductor nanocrystals which are composed of metal cations and chalcogen anions can display asymmetry in the distribution of the cations and anions on the surface, leading to the dipole moment. The gold nanoparticles are known to be surrounded by a negative charge which prevents them from aggregating in solution[161]. The negative charge is attributed to arise from partial oxidation of the gold particle surface[162]. However, it is thought an asymmetric distribution of the negative charge on the gold nanoparticle will lead to one side of the surface becoming relatively electron poor resulting in the dipole moment that drives the formation of the characteristic linear pearl necklace structures[163] (Figure 27). There are similar arguments made in the formation of palladium nanoribbons[164].

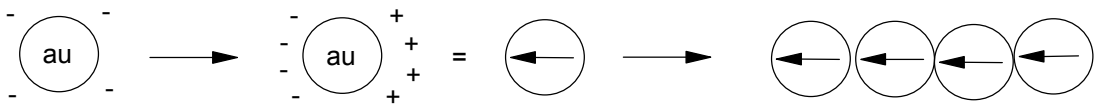

Figure 27 - *The linear aggregation of gold nanoparticles due to dipole-dipole interactions. The left figure shows a gold nanoparticle with a symmetrical distribution of negative charge on the surface. The negative charge then becomes asymmetrically distributed when changing conditions, such as the solvent in solution, resulting in a dipole moment which leads to the aggregation of gold nanoparticles forming pearl-necklace type chains.*

1.7.6 Nanotubes

One of the most unique syntheses involving the oriented attachment mechanism is in the formation of lead chalcogenide nanotubes[165]. The initial synthesis involves the formation of a complex containing lead (Pb^{2+}), cysteine ($HS\text{-}CH_2\text{-}CH(NH_2)COO^-$) and hydroxyl ($OH^-$) groups. These complex nanocrystals then self-assemble into nanowires. The mechanism accountable for this is not mentioned, though it may be

the case that the oriented attachment is responsible for this process. These precursor nanowires serve as both templates and a source of lead for the creation of the lead chalcogenide nanotubes. The desired chalcogen is then added to the precursor nanowires resulting in the formation of lead chalcogenide nanocrystals. These nanocrystals are thought to self-assemble through dipole-dipole interactions at the surface of the precursor lead nanowires to form multiple lead chalcogenide nanowires, that finally all fuse to give rise to lead chalcogenide nanotubes. This pathway to forming lead chalcogenide nanotubes is summarised in Figure 28.

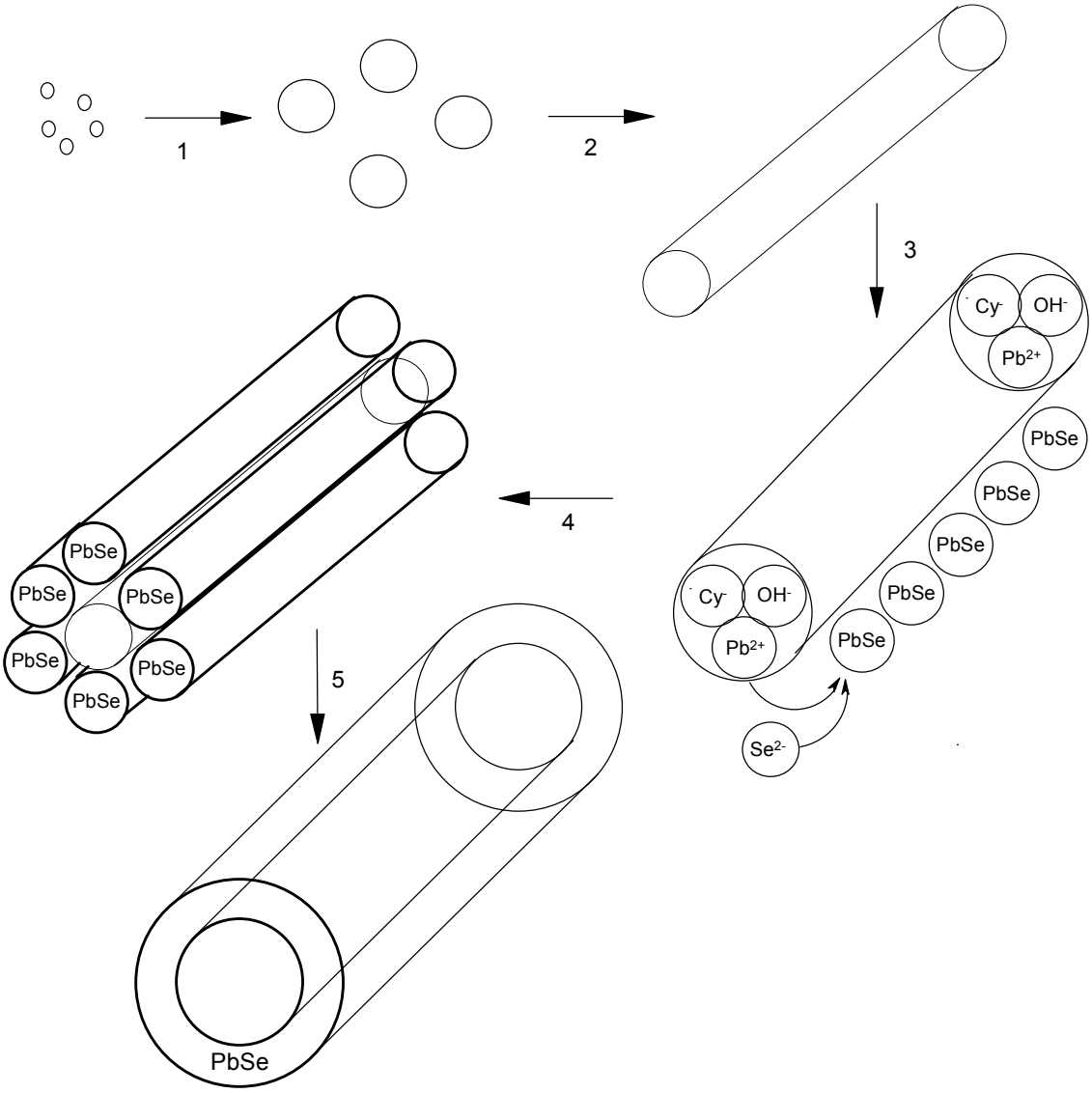

Figure 28 - *The possible pathway to formation of lead chalcogenide nanotubes from lead nanowires. In step one the precursor material is added to solution resulting in the formation of a complex lead, cytosine and hydroxyl nanocrystals. The second step involves the formation of nanowires from these nanocrystals through an oriented*

attachment process. These nanowires act as both a template and as the precursor lead source. The addition of chalcogens, in this case selenium, step three results in a reaction between chalcogen ions in solution with the surface lead ions of the preformed nanowire. This reaction produces lead chalcogenide nanocrystals at the surface of the precursor nanowires. This process continues until the lead nanowire source is depleted, the newly formed lead chalcogenide nanocrystals align via dipole-dipole interactions and fuse to form multiple nanowires (PbSe) in step four. The final step five involves the fusion of the multiple lead chalcogenide nanowires to form the nanotube.

This method has been adapted for the synthesis of PbTe nanowries with unusually small diameters[166]. The synthesis in this case involves the formation of precursor tellurium nanowires, which then combine with the lead in solution to form lead telluride nanocrystals. These nanocrystals then clearly form the pearl-necklace structure before transition into highly monodisperse lead telluride nanowires. The formation of carbon nanotubes is also seen to evolve via a particle-wire-tube mechanism similar to that presented for lead chalcogenides[167].

There are interesting questions that arise from the synthesis of nanotubes using this method, one of which is whether the nanotubes themselves contain any resultant dipole moment, similar to that observed in nanorods and nanowires, as there can be two possible routes to the formation of these nanotubes. The first method would involve the nanotubes having no resultant dipole moment due to adjacent nanowires being in an anti-parallel arrangement of dipoles. This method would involve going through steps four and five in Figure 28. The second pathway would involve the adjacent nanocrystals having an almost parallel alignment of dipoles, though this is normally repulsive. The zigzagging of adjacent nanocrystals would effectively make the arrangement an extended chain and this will help to minimize any repulsion between the many nanocrystal layers. This pathway would involve the skipping of steps four and five; instead it would involve the direct fusion of all nanocrystals post step three in Figure 28 resulting in the formation of the nanotube (Figure 29). There is also the question of morphology of the nanotube surface, for instance are the probable wurtzite, zincblende or octahedral polymorph structures usually found in semiconductor lead chalcogenide nanocrystals transferred to the formed nanotubes

using this unique method? If the morphology is not transferred then what is the phase transition mechanism for such a process? These are but a few of the unanswered questions that remain to be answered by experimentation using this unique synthesis route delivering inorganic nanotubes.

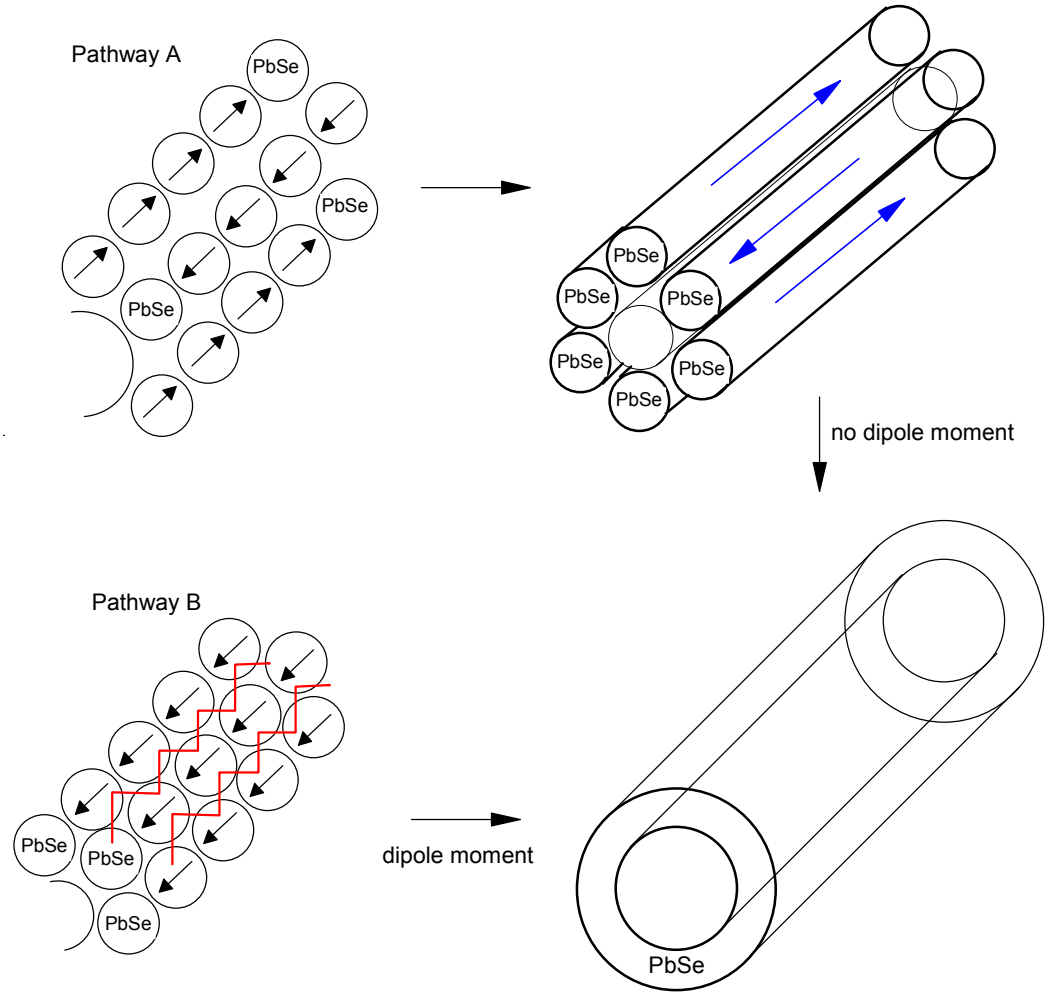

Figure 29 - *The possible dipolar pathways involved in the formation of lead chalcogenide nanotubes from nanocrystals. The top figure shows pathway A where the nanocrystals align head-tail for each layer; however each adjacent layer of nanocrystals is anti-parallel to one another. The nanocrystals then fuse to form individual nanowires which each posses large dipole moments, this dipole moment keeps the multiple nanowires together before further fusion of the nanowires produces the lead chlacogenide nanotube without a dipole moment. The bottom figure shows pathway B involving the alignment of individual nanocrystals in both a head-tail and a zigzagging fashion between different layers of nanocrystals. In this pathway the nanocrystals do not form individual nanowires, but instead direct fusion of all layers results in the final lead chalcogenide nanotube, with a large resultant dipole moment.*

1.8 Aims and Objectives

In this thesis we shall endeavour to understand the self-assembly of nanostructures from both an atomistic and mesoscale view point. The atomistic interactions between ideal tetrahedral crystal morpholgies, the zinc blende and wurtzite crystal structures, will be examined to determine if dipole-dipole interactions indeed play a pivotal role in self-assembly processes of nanocrystals. This will be complemented by mesoscale simulations by representing the nanostructures as spherical entities with net dipole moments.

1.9 Thesis structure

The following chapter 2 will highlight the computational methods used in understanding and modelling nanoparticle self-assembly. Chapters 3 and 4 will look at inter-particle interactions in nanoclusters of zinc blende and wurtzite morphologies, respectively. The primary goal of these chapters is to establish whether the atomistic interactions of clusters can be approximated to simple dipole-dipole interactions. These chapters will establish whether it is a reasonable assumption to model nanoparticles by the Stockmayer fluid. Chapter 5 will highlight the Stockmayer fluid, the model to be used in modelling nanoparticle self-assembly. Previous work in this area will be highlighted, such as the modelling of polar and non polar mixtures, and global minimum structures of dipolar fluids. The following chapter 6 will involve simulations of the Stockmayer fluid at different size ratios, a binary mixture of two different sized particles. The parameters used in these simulations are highlighted in the appendix (see section A.2) and the reduced units are listed in chapter 2 (see section 2.4). The work in chapter 7 will focus on the development of a model to account for the tetrapods and other tripod structures often observed in synthesis, but yet to be modelled in the literature. The simulations in this section will mirror those carried out in chapter 6, but with a focus on the tetrahedricity and trigonal pyramdicity of the simulation work. The final chapter 8 will summarise the findings of chapters 3-4 and chapters 6-7.

Chapter 2 Computational methods

2.1 Monte Carlo method

The simulation of the Stockmayer fluid uses the Monte Carlo method, which makes use of a random number generator to carry out the random movement of particles within the simulation cell. How the Monte Carlo routine works is briefly described. The system begins with a set of coordinates and dipoles orientations, which are stored in memory. The energy of the system in its initial state is calculated and designated U_{old}. The coordinates and dipoles are both then randomly moved and rotated respectively and the energy of the system is calculated, designated U_{new}. If the energy of the new configuration is more favourable than the old configuration, the move is accepted and the procedure is repeated this time with the new accepted coordinates and dipoles. This means U_{old} is equal to U_{new} before the subsequent move of particles. However if the move is not accepted because the new configuration is less favourable in energy than the old configuration, then the Boltzmann factor, P, is calculated (Equation 4). This is then compared to a random number, distributed 0-1. If the P value is greater than the random number the move is accepted. However, if the P value is less than the random number, the move is rejected and the loop begins again with the original coordinates and dipoles[168]. The Monte Carlo method is summarized in Figure 30.

$$P = \exp\left(\frac{-\Delta U}{k_b T}\right) \qquad \text{where; } \Delta U = U_{new} - U_{old}$$

Equation 4 - *The Boltzmann factor calculation. The equation above shows the Boltzmann factor is dependent on both the temperature and energy difference. When the energy difference ΔU is small or the temperature is high this produces values of P approaching 1, which increase the probability of higher energy configurations being accepted.*

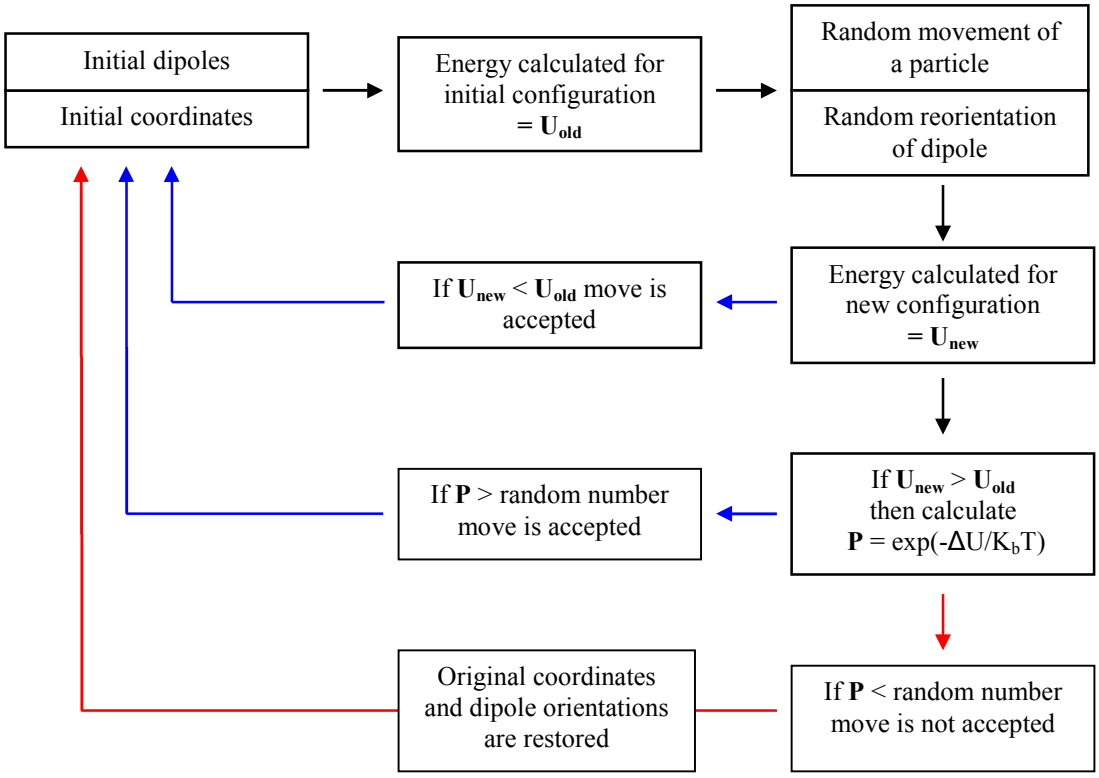

Figure 30 - *The description of how the Monte Carlo method works. The figure shows the basic components of the Monte Carlo method. The system starts with an initial configuration with energy U_{old}, a new configuration is calculated with energy U_{new}. The blue arrows indicate successfully accepted new configurations, whilst the red arrows indicate the rejected configurations.*

The Monte Carlo method works by using a random number generator, distributed between 0-1, to carry out the movement of particles. The particles are displaced relative to their previous positions, with the direction of the displacement being dependent on the random number generated for the x, y or z displacement of the particles. For example, if a particle has the initial coordinates X_1, Y_1, Z_1 the random number generator works to produce a new set of coordinates X_2, Y_2, Z_2 based on the initial position of the particle (Figure 31). It should be noted that because the random number generator produces numbers between 0 to 1 so that it would not be able to move a particle in the negative direction as such by subtracting 0.5 from the random generated number a uniform distribution occurs between -0.5 and +0.5 and so it is possible to move a particle in any direction.

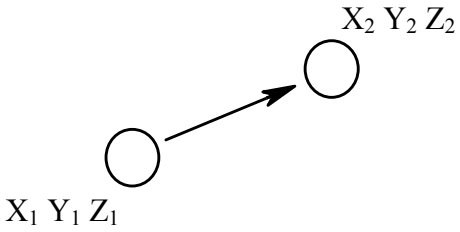

$X_2 = X_1 + ($(random number - 0.5) **x** maximum displacement$)$

$Y_2 = Y_1 + ($(random number - 0.5) **x** maximum displacement$)$

$Z_2 = Z_1 + ($(random number - 0.5) **x** maximum displacement$)$

Figure 31 - *The movement of particles in the Monte Carlo method simulations. The figure shows how new configurations, X_2 Y_2 Z_2, are generated by use of a random number (between 0 & 1). The size of the displacement from the original coordinates, X_1 Y_1 Z_1, is controlled by the variable maximum displacement.*

The maximum displacement possible at any given point in the simulation differs as the maximum displacement is a variable that changes according to the set acceptance ratio, typically between 0.2 or 0.5, of the simulation. The dynamic acceptance ratio, the ratio between the number of accepted moves over the number of steps, of the simulation is calculated throughout the simulation run. This is then compared periodically to the set acceptance ratio; if the dynamic acceptance ratio is higher than the set acceptance ratio then the maximum displacement increases. The larger displacements are usually energetically unfavourable so the number of accepted moves should decrease and as such the dynamic acceptance ratio will be lowered. Conversely if the dynamic acceptance ratio is lower than the set acceptance ratio then the maximum displacement decreases to increase the number of accepted moves and hence increase the dynamic acceptance ratio. The result of this action is to cause different size of movements through out the simulation run; for example the movement in a single plane of a particle through the simulation run is shown in Figure 32. The dashed squares indicate the possible area where the particle could move, the different sizes of the squares represent the different adjustments made to the maximum displacement in order to adhere to the set acceptance ratio. It should also be noted that the three dimensional movement of particles is cubic. The volume

that it is possible for the particle to move from its initial position is equal to the max displacement value cubed (Figure 33).

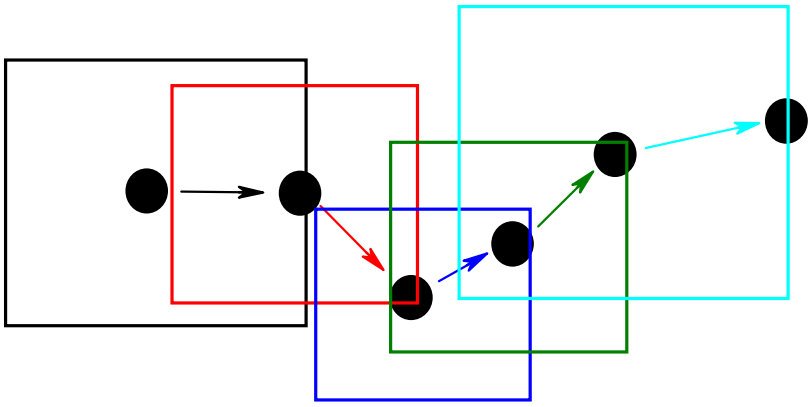

Figure 32 - *The variation of the maximum displacement throughout the simulation. The figure illustrates how the maximum displacement varies for a single particle in order for the simulation to adhere to set acceptance ratio. The larger squares indicate a higher max displacement and the different colour of the squares indicate individual moves.*

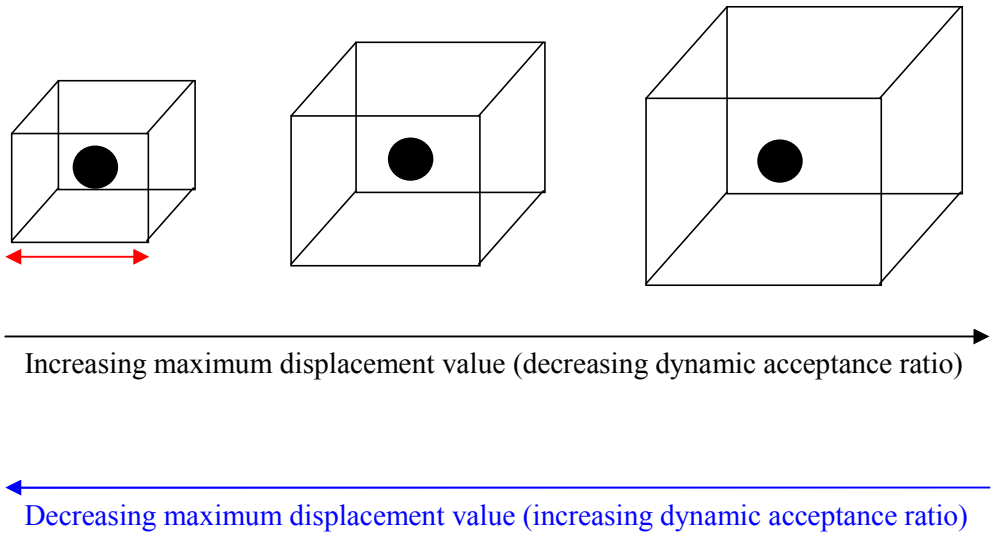

Figure 33 - *The three dimensional movement of a particle in the simulation box. The figure above shows the effect of increasing the maximum displacement leads to probable larger sized moves, which in tern leads to a lower dynamic acceptance ratio in the simulation. The situation is reversed when the maximum displacement decreases.*

2.2 Periodic boundary conditions

The periodic boundary conditions are employed so that the effects of having surface particles in the simulation box are avoided and as such the simulation mimics the bulk behaviour of the fluids. In a simple 2D example of the simulation box it can be imagined the simulation box has four boundaries. If the particles are moved towards the outside of the simulation box they are deposited to the opposing boundary of the simulation box (Figure 34).

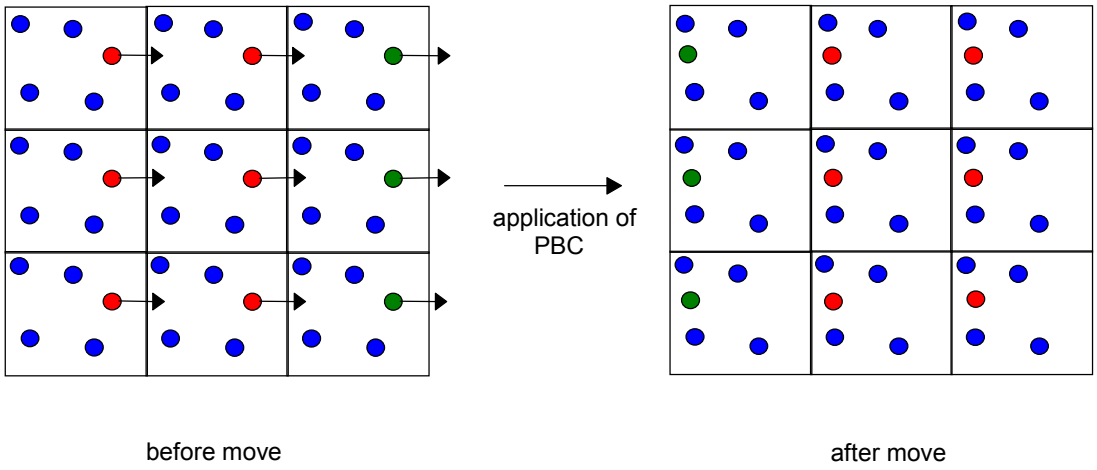

Figure 34 - *Periodic boundary conditions employed in the Monte Carlo simulations of Stockmayer fluids. The left figure shows the highlighted red particles being moved outside the simulation box. The right figure shows the use of periodic boundary conditions ensure the red particles enter the simulation box from the opposing side.*

2.3 Ewald Summation

The modelling of dipolar systems makes it necessary to perform a treatment of long range terms that arise from dipoles. Since the interaction is long range, falling away at $1/r^3$, the minimum image convention and a short range cutoff cannot be used as interactions with separations greater than half the cell length L/2 offer a significant contribution. The simulations in this work make use of the Ewald summation to calculate the long range dipole interactions[169,170]. In this method the dipole-dipole

energy in the infinitely periodic system comprised of the simulation cell and all its images is written as a sum of three terms for dipole pairs, ij (Equation 5).

$$U_{Ewald} = \frac{1}{2}\sum_{i,j,m}{}' T_{ij}^{\alpha}\mu_i^{\alpha}\mu_j^{\beta} = U_{ij}^{real} + U_{ij}^{recip} + U_i^{corr}$$

Equation 5 - *The calculation of the Ewald summation energy to account for the long range dipole-dipole interactions. The summation has three components; real, reciprocal and correction.*

The term n denotes all periodic images of the simulation cell with the prime indicating that terms where i=j if m=0 (a self interaction) are excluded. The real space term, U^{real}, is given in Equation 6.

$$U^{real} = \frac{1}{2}\sum_{i\neq j}\left(\mu_i.\mu_j\right)B\left(r_{ij}\right) - \left(\mu_i.r_{ij}\right)\left(\mu_j.r_{ij}\right)C\left(r_{ij}\right)$$

Equation 6 - *The calculation of the real contribution to the Ewald summation energy.*

The functions $B(r_{ij})$ and $C(r_{ij})$ are defined in Equation 7 , alongside the complimentary error function erfc which ensures that all the real space interactions die away to zero within the simulation cell.

$$B\left(r_{ij}\right) = \frac{\mathrm{erfc}\left(\gamma r_{ij}\right)}{r_{ij}^3} + 2\frac{\gamma}{\sqrt{\pi}}\frac{exp\left(-\gamma r_{ij}^2\right)}{r_{ij}^2}$$

$$C\left(r_{ij}\right) = 3\frac{\mathrm{erfc}\left(\gamma r_{ij}\right)}{r_{ij}^5} + 2\frac{\gamma}{\sqrt{\pi}}\left(2\gamma^2 + \frac{3}{r_{ij}^2}\right)\frac{exp\left(-\gamma r_{ij}^2\right)}{r_{ij}^2}$$

$$\mathrm{erfc}(x) = \frac{2}{\sqrt{\pi}}\int_x^{\infty} e^{-t^2}\,dt$$

Equation 7 - *The functions that make up part of the real contribution to the Ewald summation energy.*

The reciprocal term arsing from the long-range interaction in the reciprocal space is given in Equation 8. In the expression k denotes the reciprocal lattice vector with $n_x, n_y, n_z = 0..., n_{max}$ and γ is the convergence parameter.

$$U^{recip} = \frac{2\pi}{V} \sum_{k} \neq 0 \frac{exp\left(-k/4\gamma^2\right)}{k^2} \left|F(k)\right|^2$$

$$k = \left(2\pi n_x / L_x, 2\pi n_y / L_y, 2\pi n_z / L_z\right)$$

$$F(k) = \sum_{i=1}^{N} \left(\mu_i . k\right) exp\left(i \; k . r_{ij}\right)$$

Equation 8 - *The calculation of the reciprocal contribution to the Ewald summation energy.*

The correction term, U^{corr}, arising from the interaction of the particles with all their periodic images, is given in Equation 9. The parameter γ determines the rate of convergence of the real and reciprocal space parts. A value corresponding to half the cell length is used so that both terms converge reasonably quickly.

$$U^{corr} = -\frac{2\gamma^3}{3\sqrt{\pi}} \sum_{i=1}^{N} \mu_i^2$$

Equation 9 - *The calculation of the correction contribution to the Ewald summation energy.*

2.4 Reduced units

The Monte Carlo simulations of the Stockmayer fluid are carried out by using reduced units to achieve continuity with previous simulations. There are three important quantities that are represented in terms of reduced units[171]. These are the reduced dipole moment (Equation 10), the reduced density (Equation 11) and the reduced temperature (Equation 12). The Stockmayer fluid simulations carried out in chapters 5 and 6 are all parameterized such that there is a constant reduced temperature $T^* = 1.0$

and a constant reduced dipole moment $\mu^* = 3.0$ for both binary components. In the case of the reduced dipole moment each binary component (A and B) will have have the same reduced dipole, though individual components may have different diameters and hence different dipole moments. At size ratio α greater than one, the ratio between σ_A / σ_B, the dipole moments and diameters of A and B components will not be the same, though the reduced dipole will be the same for both components (Equation 13).

$$\mu^* = \sqrt{\frac{\mu^2}{\sigma^3 \varepsilon}}$$

Equation 10 - *The reduced dipole moment used in the Stockmayer fluid simulations. The equation describes the reduced dipole moment and its dependence on the actual dipole moment μ, size of the particles σ and the energy well depth ε.*

$$\rho^* = N_A \frac{\sigma_A^3}{V} + N_B \frac{\sigma_B^3}{V}$$

Equation 11 - *The binary reduced density used in the Stockmayer fluid simulations. The equation describes the reduced density of two different sized particles A and B with N number of particles of each. The volume V is that of the simulation box.*

$$T^* = \frac{k_b T}{\varepsilon}$$

Equation 12 - *The reduced temperature used in the Stockmayer fluid simulations. The reduced temperature is determined from the Boltzmann constant k_b, the temperature T and the energy well depth ε of the Lennard-Jones potential.*

$$\mu_A^* = \sqrt{\frac{\mu_A^2}{\sigma_A^3 \varepsilon}} = \mu_B^* = \sqrt{\frac{\mu_B^2}{\sigma_B^3 \varepsilon}} \qquad \text{However, } \mu_A \neq \mu_B \text{ and } \sigma_A \neq \sigma_B \text{ if } \alpha > 1.0$$

Equation 13 - *The reduced dipole moment used in the binary Stockmayer fluid simulations. The equation shows both binary components having the same reduced dipole moment, but different actual dipole moments (μ_A and μ_B) and diameters (σ_A and σ_B) when the size ratio is greater than one.*

2.5 Multipole interactions

The dipole-dipole interactions have been discussed previously with regards to the Stockmayer fluid; however other multipole interactions may be important in the self-assembly processes between nanoparticles. The higher order multipole interactions, following the dipole-dipole interactions, are the dipole-quadrupole and quadrupole-quadrupole interactions. The dipole-quadrupole interaction tensor is shown in Equation 14. The energy of interaction between two bodies i and j, with respective magnitude of dipoles μ_i and quadrupole θ_j moments, can be calculated using the dipole-quadrupole interaction tensor (Equation 15). The quadrupole-quadrupole tensor is also shown in Equation 16. The energy of interactions between two bodies i and j, with respective quadrupole moments θ_i and θ_j, can be calculated using the quadrupole-quadrupole interaction tensor (Equation 17).

When; $\alpha = \beta = \gamma$

$$T_{\alpha\beta\gamma} = \nabla_{\alpha\beta\gamma}\left(\frac{1}{r_{ij}}\right) = \frac{9r_\alpha}{r_{ij}^5} - \frac{15r_\alpha^3}{r_{ij}^7}$$

When; $\alpha = \beta \neq \gamma$

$$T_{\alpha\beta\gamma} = \nabla_{\alpha\beta\gamma}\left(\frac{1}{r_{ij}}\right) = \frac{3r_\gamma}{r_{ij}^5} - \frac{15r_\alpha^2 r_\gamma}{r_{ij}^7}$$

When; $\alpha \neq \beta \neq \gamma$

$$T_{\alpha\beta\gamma} = \nabla_{\alpha\beta\gamma}\left(\frac{1}{r_{ij}}\right) = \frac{5r_\gamma}{r_{ij}^7}$$

Equation 14 - *The dipole-quadrupole interaction tensor used in calculating the atomistic energies. The different equations are shown under the altered variables α, β and γ.*

$$U = \underline{\mu}_i \underline{\theta}_j \underline{T}_{ij}$$

Equation 15 - *The dipole-quadrupole energy calculation using the tensor. The equation describes how the dipole-quadrupole energy can be calculated using the tensor with the dipole and quadrupole moments, between two bodies i and j.*

When; $\alpha = \beta = \gamma = \delta$

$$T_{\alpha\beta\gamma\delta} = \nabla_{\alpha\beta\gamma\delta}\left(\frac{1}{r_{ij}}\right) = \frac{9}{r_{ij}^5} - \frac{90r_\alpha^2}{r_{ij}^7} + \frac{105r_\alpha^4}{r_{ij}^9}$$

When; $\alpha = \beta = \gamma \neq \delta$

$$T_{\alpha\beta\gamma\delta} = \nabla_{\alpha\beta\gamma\delta}\left(\frac{1}{r_{ij}}\right) = \frac{45r_\alpha r_\delta}{r_{ij}^7} - \frac{105r_\alpha^3 r_\delta}{r_{ij}^9}$$

When; $\alpha = \beta \neq \gamma = \delta$

$$T_{\alpha\beta\gamma\delta} = \nabla_{\alpha\beta\gamma\delta}\left(\frac{1}{r_{ij}}\right) = \frac{3}{r_{ij}^5} - \frac{15r_\alpha^2}{r_{ij}^7} - \frac{15r_\gamma^2}{r_{ij}^7} + \frac{105r_\alpha^2 r_\gamma^2}{r_{ij}^9}$$

When; $\alpha \neq \beta \neq \gamma \neq \delta$

$$T_{\alpha\beta\gamma\delta} = \nabla_{\alpha\beta\gamma\delta}\left(\frac{1}{r_{ij}}\right) = -\frac{15r_\gamma r_\delta}{r_{ij}^7} + \frac{105r_\alpha^2 r_\gamma r_\delta}{r_{ij}^9}$$

Equation 16 - *The quadrupole-quadrupole interaction tensor used to calculate the atomistic energies. The different equations are shown under the altered variables α, β and γ.*

$$U = \underline{\theta}_i \underline{\theta}_j \underline{T}_{ij}$$

Equation 17 - *The quadrupole-quadrupole energy calculation using the tensor. The equation describes how the quadrupole-quadrupole energy can be calculated using the tensor with the quadrupole moments, between two bodies i and j.*

2.6 Construction of crystal structures

The interactions between nanocrystals are of primary interest. In order to achieve understanding of these interactions between nanocrystals, nanoclusters need to be constructed with the polymorphs commonly found in nanocrystals. The unit cell allows for the construction of different morphologies of crystals structures; this is achieved by alteration of the lengths (a, b and c) and angles (α, β and γ) of the unit cell. The unit cell of the zinc blende polymorph has all three lengths of equal size and all angles are 90 degrees. The unit cell of the wurtzite polymorph has the lengths a and b of the same size, and the length c is (√8/3)a. The angles α and β are both 90 degrees, and the final angle γ is 120 degrees. The unit cell of zinc blende is considered to be cubic, whilst that of wurtizte is hexagonal[172] (Figure 35).

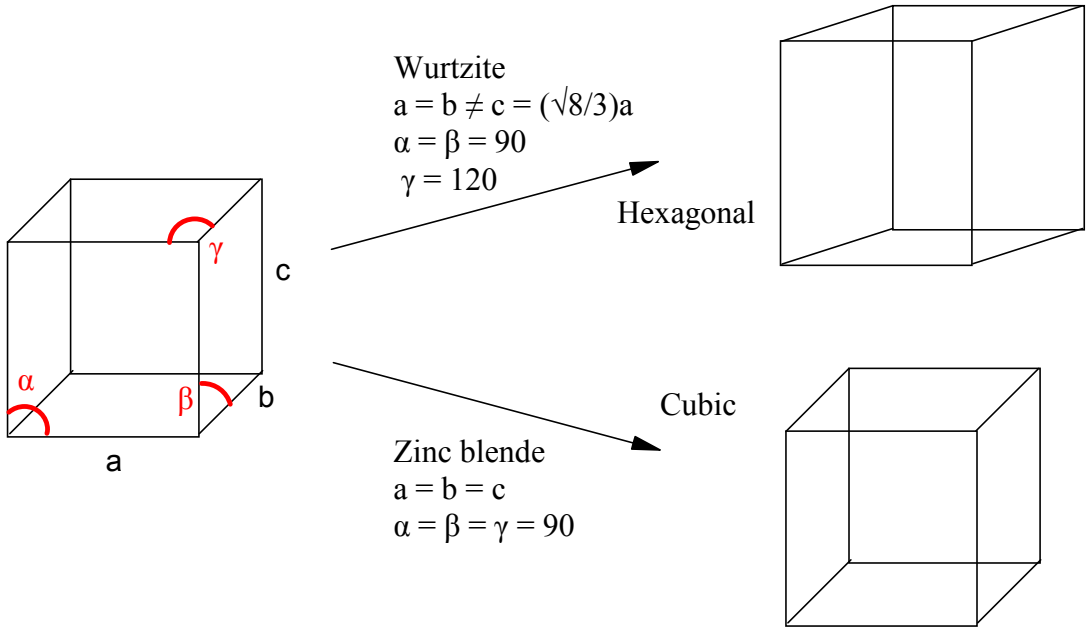

Figure 35 - *The unit cells of the zinc blende and wurtzite polymorphs. The left figure shows the archetypal unit cell with three lengths a, b & c and the three angles α, β & γ. The right figures show both the unit cells of the wurtzite (top) and of the zinc blende polymorphs (bottom).*

The fractional coordinates in a stoichiometric metal anion (MX) system of the zinc blende and wurtizte polymorphs are used to construct the crystal structures within the unit cell (Equation 18). Once this basic unit cell structure is achieved it is repeated

along x, y and z axis to achieve the construction of bulk crystal structures of the zinc blende and wurtzite polymorphs.

Wurtzite: $M \Rightarrow [0,0,0] \;\&\; \left[\frac{1}{3},\frac{2}{3},\frac{1}{2}\right]$ $X \Rightarrow \left[0,0,\frac{3}{8}\right] \;\&\; \left[\frac{1}{3},\frac{2}{3},\frac{7}{8}\right]$

Zinc Blende: $M \Rightarrow [0,0,0]\ ,\ \left[0,\frac{1}{2},\frac{1}{2}\right]\ ,\ \left[\frac{1}{2},0,\frac{1}{2}\right] \;\&\; \left[\frac{1}{2},\frac{1}{2},0\right]$

$X \Rightarrow \left[\frac{1}{4},\frac{1}{4},\frac{1}{4}\right]\ ,\ \left[\frac{1}{4},\frac{3}{4},\frac{3}{4}\right]\ ,\ \left[\frac{3}{4},\frac{1}{4},\frac{3}{4}\right] \;\&\; \left[\frac{3}{4},\frac{3}{4},\frac{1}{4}\right]$

Equation 18 - *The unit cell fractional coordinates of the zinc blende and wurtizte polymorphs. The top equations list the fractional coordinates of the wurtzite crystal structure in terms of the metal (M) and anion (X) positions. The bottom equations also list the fractional coordinates of the zinc blende crystal structure.*

2.7 Bond angle distribution

The bond angle distribution can provide valuable information on the structural form of the fluids. The bond angle distribution of the Stockmayer fluid can be built up by calculating the bond angle between three particles bonded together, which have two bonds between them of length r_i and r_j that have x, y and z components (Equation 19).

$$\theta = \cos^{-1}\left(\frac{r_{ix}r_{jx} + r_{iy}r_{jy} + r_{iz}r_{jz}}{r_i r_j}\right)$$

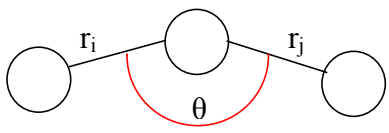

Equation 19 - *The bond angle calculation between three atoms. The equation shows the cosine function can be used to calculate the bond angle θ by knowing the bond lengths r_i, r_j and their respective x, y and z components. The right figure illustrates three atoms bonded together with the angle calculate by the equation highlighted.*

2.8 Radial distribution function

The radial distribution function (rdf) gives the probability of finding a pair of atoms or particles a distance r apart, relative to the probability expected for a completely random distribution, an ideal gas, at the same density[173] (Equation 20). The g(r) is calculated by finding the number of particles present within a separation of r and an additional constant separation dr. This is shown in Figure 36 with the particles that fall into the separation of r + dr from the particle of interest i, blue particle, highlighted in red (Figure 36).

$$g_{total}(r)dr = \frac{1}{N}\sum_{i=1}^{N} g_i(r)dr \qquad \text{Where; N = total number of particles in system}$$

$$g_{ideal}(r)dr = 4\pi\pi\rho^2 dr \qquad \text{Where; } \rho = \frac{N}{V}\text{, V = volume of simulation box}$$

$$g(r) = \frac{g_{total}}{g_{ideal}}$$

Equation 20 - *The calculation of the radial distribution function equations. The top equation highlights the calculation of the actual number of particles at each particular separation of r. The second equation calculates the number of particles expected at each particular separation in the ideal gas situation. The final equation combines the first to equations to yield the radial distribution function g(r).*

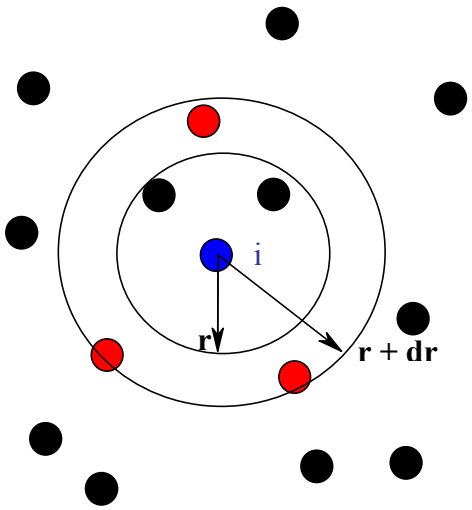

Figure 36 - *The radial distribution function. The figure shows the central particle i, in blue, of interest along with the particles that fall into the separation of r + dr represented in red. The particles in black do not fall into this volume of r + dr.*

2.9 Coordination number distributions

The coordination number distributions provide further information on the structural form of fluids by way of indicating the coordination numbers most commonly adopted in the liquid. The coordination number of particles is identified by looking for bonds or connections within a radius r_{bond} from the particle of interest. The value of r_{bond} varies depending on the binary mixture of the Stockmayer fluids and its composite A and B particles. The A and B particles have associated diameters σ_A and σ_B respectively, which are used to define the presence of connections between particles (Figure 37). The number of connections associated with individual particles is then used to construct a histogram of coordination data that can encompass all particles or its components A-A, A-B and B-B distributions only.

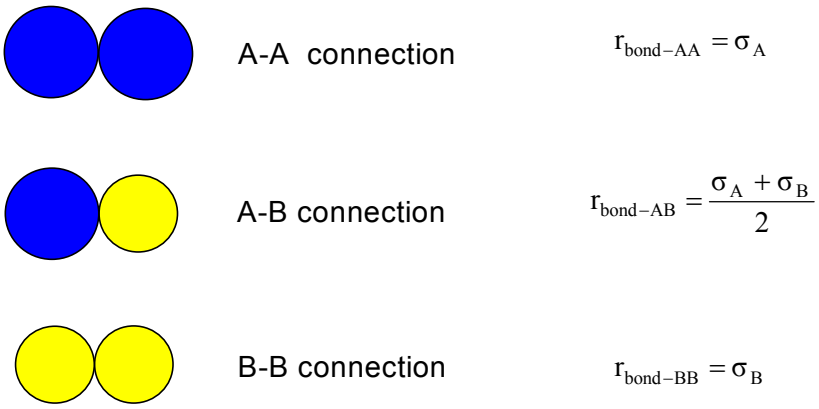

Figure 37 - *The identification of connections in the binary Stockmayer fluid. The top figure shows the A-A connection and its associated bond length based on the diameter σ_A of A particles. The middle figure shows the A-B connection and its bond length based on the diameters of both A and B particles. The bottom figure illustrates the B-B connection and its bond length based on the diameter σ_B of B particles.*

The criterion for the bond length or what constitutes a connection was determined by examining the energy profiles of the Lennard-Jones, dipole-dipole and Stockmayer fluid potential (Figure 38). Only the head-tail orientation of dipoles is examined, as this is the most favourable orientation of dipoles. In addition the reduced units and parameters used (see appendix) are consistant with the simulation work in chapters 5

and 6. Figure 38 clearly shows the Stockmayer fluid (SF) minimum occurring at less than the diameter σ of the particle, as such it was deemed appropriate to use the bond lengths highlighted in Figure 37.

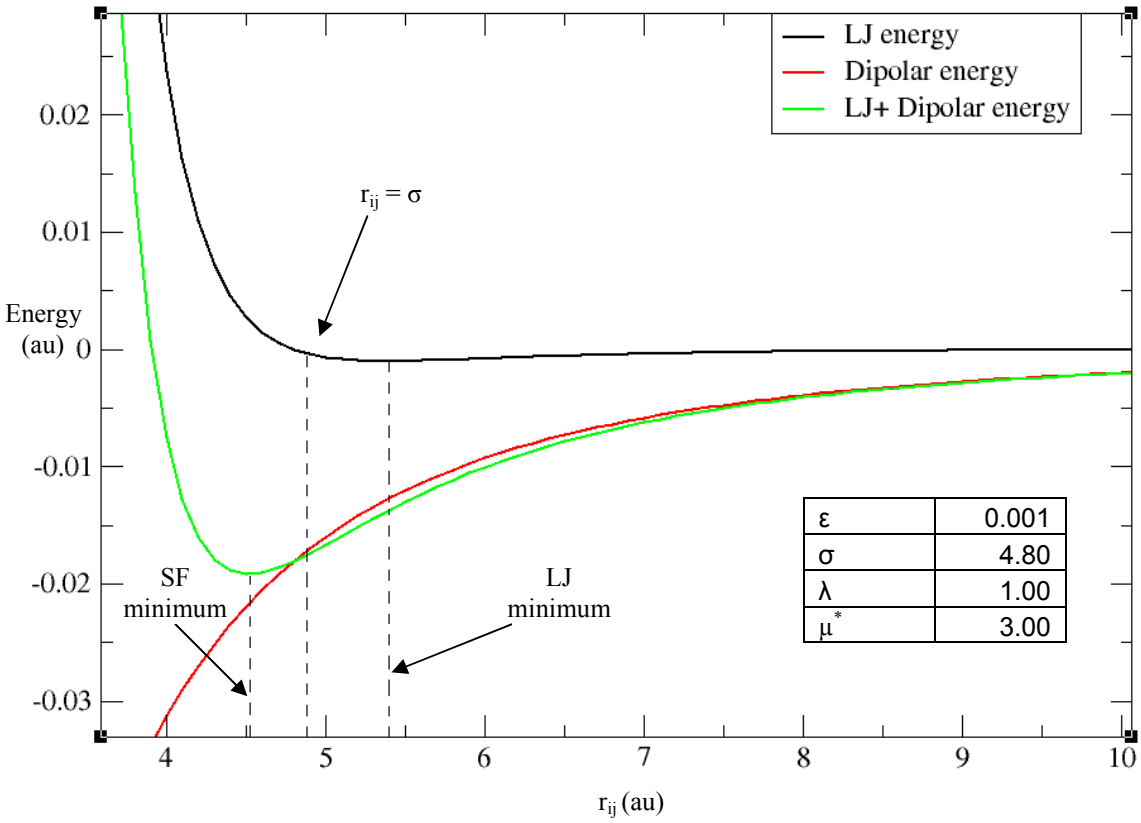

Figure 38 - *The determination of bond lengths using the Stockmayer fluid potential. The black line shows the Lennard-Jones energy only, while the red line shows the head-tail interaction of dipoles. The green line is the Stockmayer potential. The mimimum for the Stockmayer fluid is clearly less than both the Lennard-Jones minimum and diameter of the particles σ.*

2.10 Chain length distributions

The chain length distributions also provide structural information regarding the fluid of interest. The chain length data is built up similarly to the coordination data, with the connections between particles in a binary Stockmayer fluid based on the diameters as described previously. The establishment of connection data in the Stockmayer fluid is then used to find chains by finding the ends of chains, which are one coordinated particles. This is used as starting point to find the chain lengths in the fluid; these can be based on all the particles or the A-A, A-B and B-B connections only. These data can then be utilized to build up a histogram.

Chapter 3 Atomistic energies of zinc blende clusters

3.1 Introduction

This chapter will examine the possibility of dipole-dipole interactions as being the driving force for the self-assembly of zero dimensional nanocrystals into higher dimensional structures. Although the nanocrystals can form in many phases, the phases of most interest are the four coordinate wurtzite (B4) and zinc blende (B3) structures. In this chapter we will focus solely on the zinc blende nanocrystals.

3.1.1 Nanocluster pairs and Dipole pairs

In order to demonstrate how dipole interactions may be responsible for the self-assembly of nanocrystals, the interaction energies of atomistically constructed nanocluster pairs can be effectively mapped onto simple dipole pairs (Figure 39).

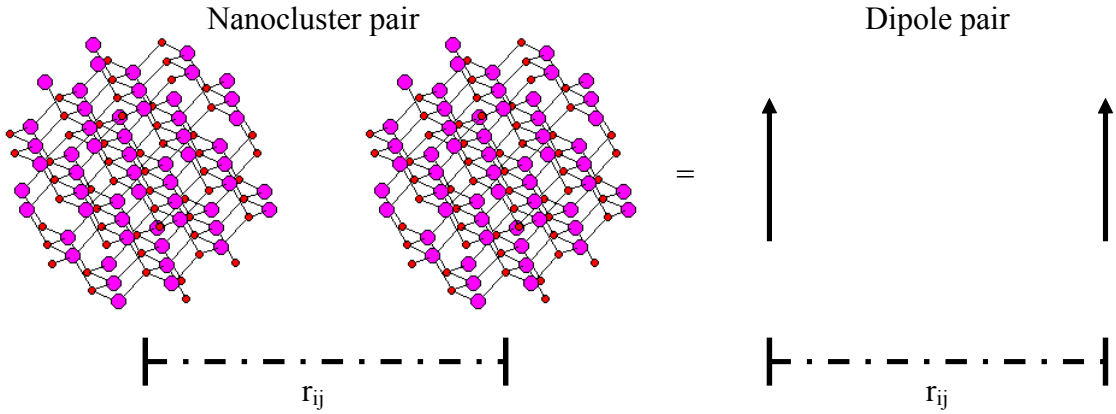

Figure 39 - *The mapping of the atomistic cluster charges onto a point dipole moment. The left hand figure shows the original cluster and its image, whilst the right hand figure shows the dipole moments resulting from the implementation of equation 1.*

Atomistic clusters of B3 have each been constructed with a bond length of 4.5 a.u (approximately 2.4 Å), which is within the range of anion-cation bond lengths encountered in many four coordinate nanocrystals. The crystals are then cut into charge neutral near-spherical clusters with diameters of approximately 30, 40 and 50 a.u. The dipole moments of the respective nanoclusters are calculated by finding the

centre of mass coordinates of the cluster and then subtracting the individual coordinates of the atoms from the centre of mass coordinates to determine the separation r_i. The sum of the charge multiplied by the separation of the atoms from the centre of mass coordinates results in the dipole moment for any given direction (Equation 21). This methodology is similarly applied to the calculation of the quadrupole moment of the clusters (Equation 22). Once the total dipole moment has been calculated the nanoclusters are oriented such that the dipole moment points along the simulation cell Y-axis. This is achieved by first rotating the cluster about the Y-axis so that the dipole moments in the X and Z directions are altered until there is only a Z dipole component remaining. Then the cluster is rotated about the X-axis till there is only a dipole component in the Y-axis (Figure 40). The coordinates of the cluster atoms are altered by rotation about each axis according to matrix operations, for example the rotation about the X-axis is shown (Equation 23). The X` Y` Z` represent the new coordinates generated when the existing coordinates X Y Z of an atom from the cluster are altered according to the angle of rotation, θ, using the cosine operations as shown in equation 2. This rotation of atoms can be exemplified by a simple diagram of a single atom being rotated by an angle θ with respect to the centre of mass of the nanocluster (Figure 41).

$$\mu = \sum_i q_i r_i$$

Equation 21 - *The equation used to determine the dipole moment of a set of atoms in a cluster. This is achieved by finding the separation from the centre of mass of each atom within the cluster and multiplying them by their respective charges.*

$$Q = \sum_i q_i \left(3x_\alpha x_\beta - r_i^2 \delta_{\alpha\beta}\right)$$

Equation 22 - *The equation used to determine the quadrupole moment of a set of atoms in a cluster. This is achieved by finding the separation from the centre of mass of each atom within the cluster, including it component separations in the x, y or z directions and multiplying them by their respective charges.*

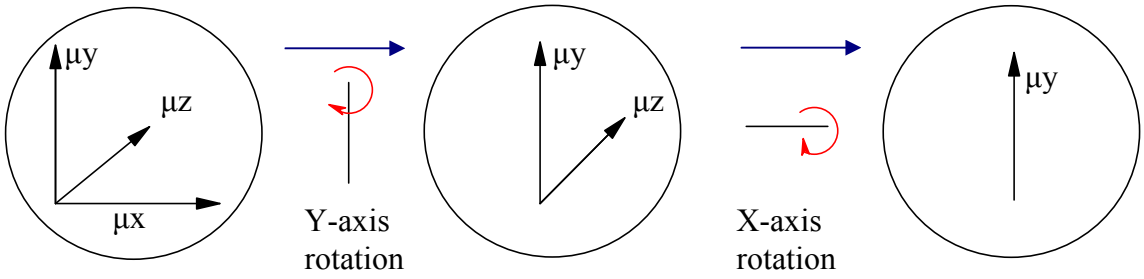

Figure 40 - *The altering of nanocluster orientations to achieve a dipole moment along the Y-axis. The left side shows the Y-axis rotation eliminating the X-axis dipole component, similarly on the right the X-axis rotation is shown to eliminate the Z-axis dipole component.*

$$\begin{pmatrix} X' \\ Y' \\ Z' \end{pmatrix} = \begin{pmatrix} 1 & 0 & 0 \\ 0 & \cos\theta & \sin\theta \\ 0 & -\sin\theta & \cos\theta \end{pmatrix} \cdot \begin{pmatrix} X \\ Y \\ Z \end{pmatrix}$$

Equation 23 - *The matrix function used to determine the new set of coordinates for atoms by rotating them about the axis by a defined angle θ.*

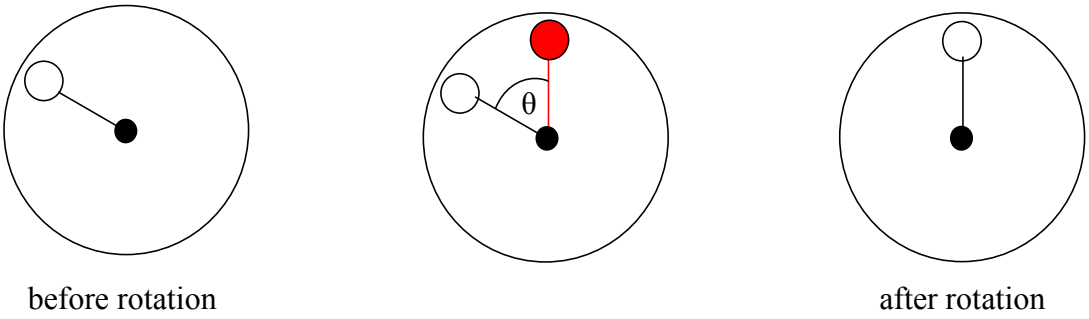

Figure 41 - *The rotation of the nanocluster exemplified by a single atom. The left figure shows the nanocluster with a single atom highlighted (white atom) and a centre of mass (black particle). The central figure shows the atom projected to be rotated by an angle θ. The right figure shows the atom finally rotated.*

The spherical clusters are then used to carry out energy calculations by producing a second image of the original cluster at a fixed separation away from the first cluster. The second cluster is rotated about the first original cluster to build up an energy profile as highlighted in Figure 41. The cluster-cluster energy is calculated by

summing all inter-particle interactions. The intra-particle energy (U_1 & U_2) contributions are removed from the total energy (U^{Total}) to leave the cluster-cluster interaction energy (U_{12}) (Equation 24).

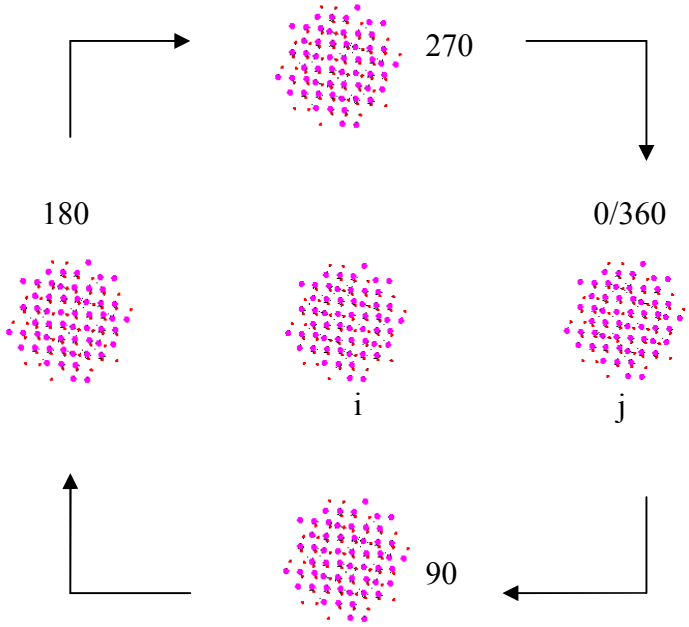

Figure 42 - *How the energy profile is built up. The original cluster lies at the centre of the figure with its image being reproduced at different angles of rotation in order to build up the energy profile of the clusters.*

$$U^{Total} = \sum \frac{q_i q_j}{r_{ij}} = U_{12} + U_1 + U_2$$

$$U_{12} = U^{Total} - U_1 - U_2$$

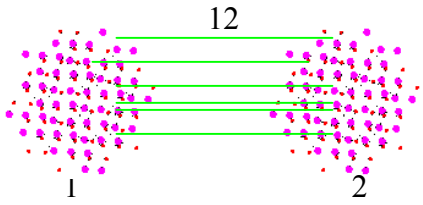

Equation 24 - *The energy between the clusters is determined by the pair wise multiplying of charges from two separate clusters and dividing them by their separations. The bottom equation shows how the inter-particle energy (U_{12}) of interest is calculated by removing the self energy of the clusters (U_1 & U_2) from the total energy (U^{Total}). The right figure shows the inter-particle interactions in green.*

3.1.2 Nomenclature

In order to understand the following analysis the notation and its meanings are represented below. The label ‘r’ means rotation refers to the rotation of the dipole in a selected plane. For the purposes of this example it is the XY plane (or rotation about the Z-axis). The number after the ‘r’ indicates the angle by which the second dipole (cluster) is rotated clockwise relative to the first dipole (cluster), which is static (Figure 43). The r0 notation, in the starting configuration, represents the parallel dipole orientation while the r180 notation represents the anti-parallel dipole orientation, any letter after the angle of rotation indicates the axis about which the second cluster is rotated. The r180x notation for example would indicate a 180 degree rotation of the second cluster about the X-axis.

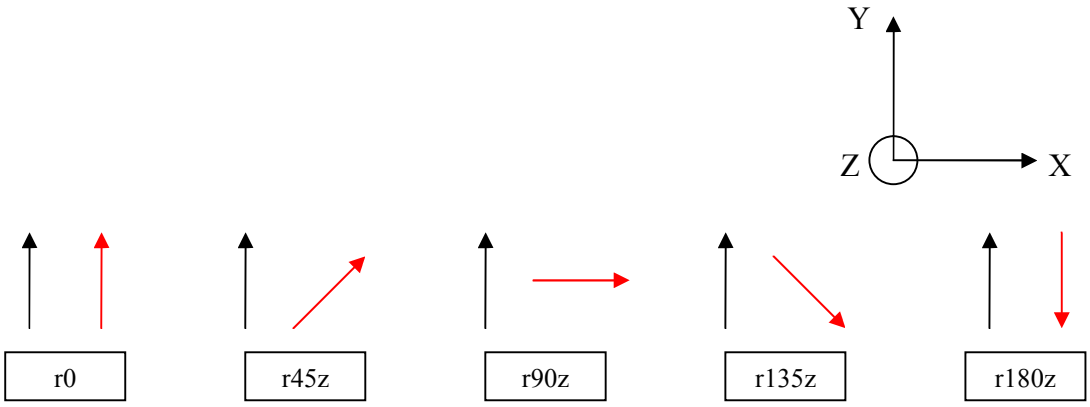

Figure 43 - *The different rotations of the clusters or dipoles. The figure on going from left to right shows the angle of clockwise rotation increasing, resulting in different dipolar configurations.*

Once the second cluster is rotated relative to the first cluster by the desired angle, there are three energy configurations that can be examined, with the second cluster being rotated anti-clockwise in the XY, XZ or YZ planes (Figure 44). This allows for an energy profile to be built up for the clusters.

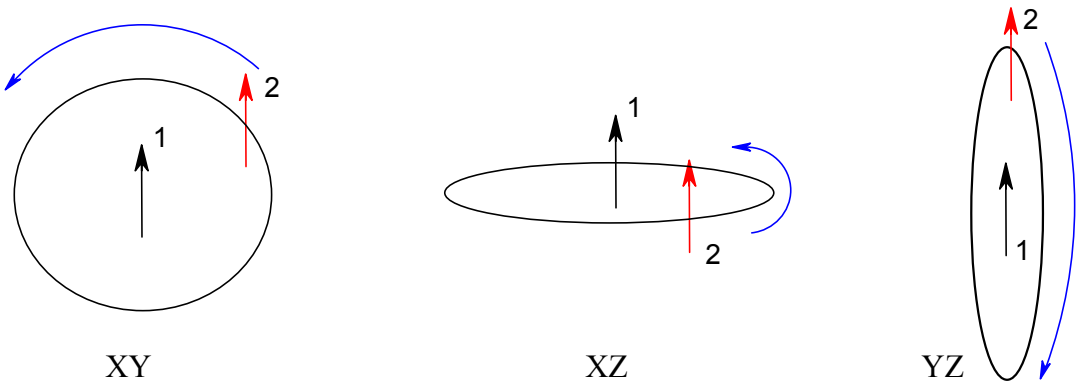

Figure 44 - *The three different planes of rotation. The left figure shows the rotation in the XY plane, the central figure shows the XZ plane rotation and the right figure shows the YZ plane rotation of the clusters/dipoles.*

In an example case of the XY plane rotation for the r0 configuration the results of this atomistic cluster energy profile will be compared to the results of the dipole pairs (Figure 45), with the magnitude of the dipole moments being determined from the nanoclusters as outlined previously (Equation 21). The r0 configuration energy profile should show maxima at 0 and 180 degrees, the head to head interaction, and minima at 90 and 270 degrees, the head to tail interaction. The atomistic cluster results, if indeed dipole moments play a pivotal role in assembly processes, should also take the form of cosine type curve. As an example the dipole pair in the r0 configuration are shown (Figure 46).

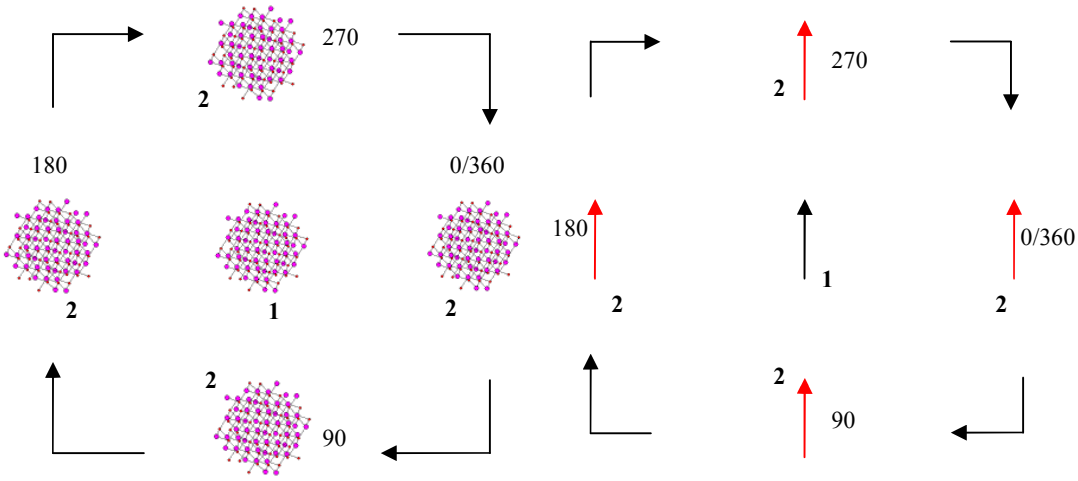

Figure 45 - *The processes of building up energy profiles. The left figure shows the atomistic energy profile built up by rotating the second cluster about the first cluster. The right figure shows the equivalent dipole pair energy profile being built up.*

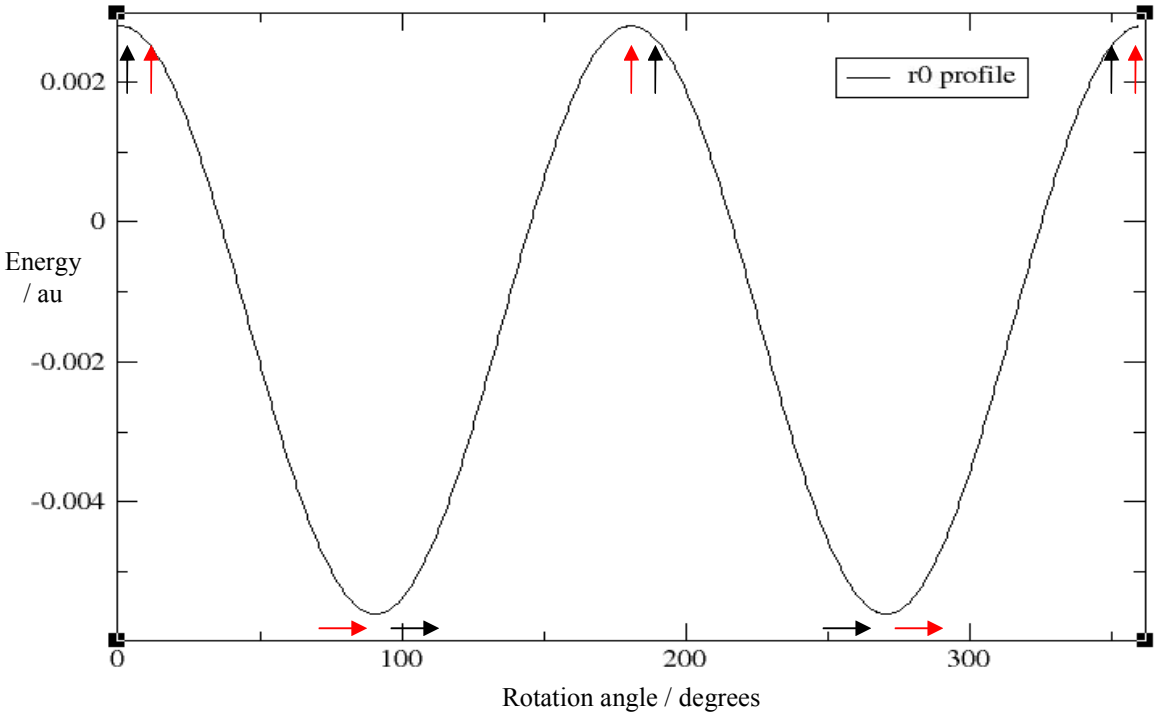

Figure 46 - *The typical energy profile produced with the dipole pairs in the r0 configuration. The r0 energy profile shows the unfavourable anti-parallel configuration occurring at 0/360 and 180 degrees. The favourable head-tail configurations occur at 90 and 270 degrees.*

Three clusters, are extracted from the ideal zinc blende structure, with approximate diameters 30, 40 and 50 au. These clusters have respective dipole moments of 53 a.u (~125 Debyes), 2.5 a.u (~7 Debyes) and 105 a.u (~250 Debyes), when the charges on the anions and cations are assumed to be -1 and +1 respectively. There are no quadrupole moments present in any of the clusters. The large differences in the resultant dipole moments in the clusters arise as a result of the extraction from the ideal crystal, where the core of the three clusters is all the same. However, the surface of each of the clusters varies and as such the resultant dipole moment also changes accordingly. Figure 47 illustrates the extraction of two different sized clusters from an ideal crystal made up of anions and cations. The different sized clusters extracted from the ideal crystal have a different combination of ions on their respective surfaces and this consequently affects the dipole moment of the clusters. The dipole moment is dependent on both the distance of ions and the charges; hence any imbalance in the composition of ions on the surface of the cluster affects it. The core atoms of the two clusters are not shown for clarity.

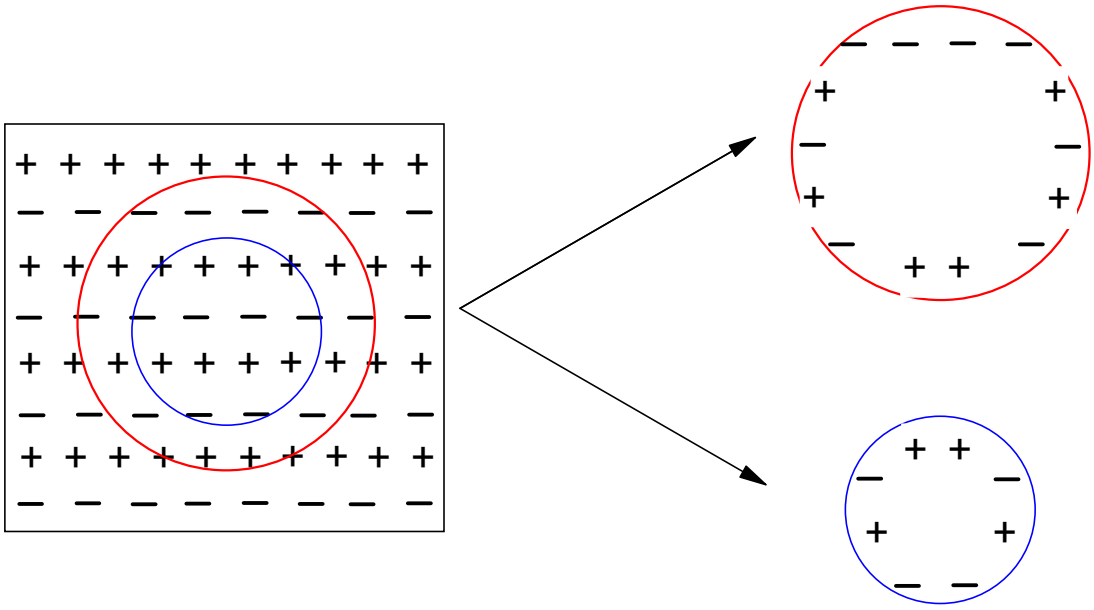

Figure 47 - *The process of cluster extraction from the ideal crystal structure. The left figure shows the ideal crystal composed of anions and cations. There are two different sized clusters, highlighted in red and blue, which are extracted from the ideal crystal. The right figure shows the two extracted clusters and their respective different surface ion composition.*

3.2 The XY Plane energy profiles

The results for the XY plane are examined for separations between clusters that are the order of 2-3 times the cluster diameter. These relatively large separations are examined first as they are less likely to be influenced by the atomistic detail of the spherical clusters. In addition only the 30 and 50 a.u clusters are analysed as the 40 a.u cluster has intentionally been constructed with a relatively small dipole moment and as such it acts as a good control comparison to highlight any differences that occur between the clusters as a result of atomistic detailing. Hence the 40 a.u cluster due to its low dipole moment is not suitable for examining the interactions of the clusters at 2-3 times the cluster diameter.

The 30 a.u and 50 a.u clusters are analyzed in tandem by looking at the energy profiles at separations of 70 a.u and 100 a.u for the smaller 30 a.u cluster and 100 a.u and 150 a.u for the larger 50 a.u cluster. These results are then contrasted by showing

the dipole pair profile, being rotated at the same separations. The r0 configuration results for both clusters are shown along with the dipole pairs (Figure 48).

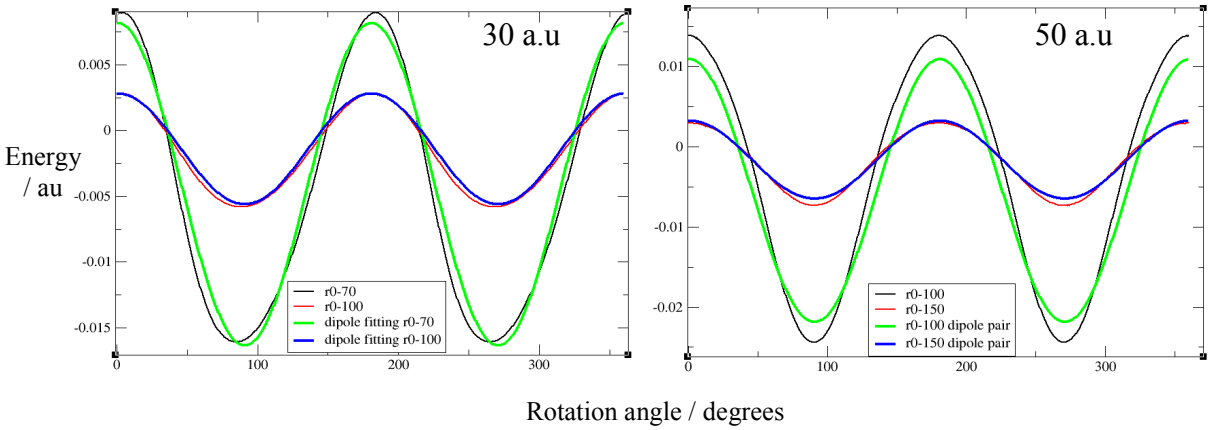

Figure 48 - *Energy profiles for the r0 configuration calculated for the clusters with diameters of 30 a.u (left hand figure) and 50 a.u (right hand figure) respectively, for the smaller 30 a.u cluster energies are calculated at separations of 70 a.u and 100 a.u as indicated in the figure legend, for the larger 50 a.u cluster these separations are 100 a.u and 150 a.u respectively. The energies of the equivalent dipole pairs are shown for comparison.*

It is reasonably clear from the data that at separations of 100 a.u for the 30 a.u cluster and 150 a.u for the 50 a.u cluster, approximately three times the diameter of the respective clusters, the energetics of the nanoclusters are agreeing well with the dipole pairs. There are some differences visible between the atomistic and dipole pair results at approximately twice the cluster diameters; for the 30 a.u cluster this is 70 a.u and for the 50 a.u cluster this is 100 a.u. These differences persist at three times the diameter of the clusters though the magnitude of the differences decreases and as such they are likely to be the result of the atomistic detailing of the clusters involved. These observations are further confirmed by viewing the r180x and r180z energy profiles as these two rotations result in the same dipolar arrangement of the second clusters (Figure 49), however different surfaces are exposed relative to the first cluster. There are implications for different surfaces being exposed between the clusters in terms of energies as one surface may contain more or less atoms firstly and secondly the surface may have more cations or anions showing, which will result in different energies. The r180z and r180x configurations are used to show how different surfaces

can be exposed in dipolar equivalent environments using a simple 2D box example (Figure 50).

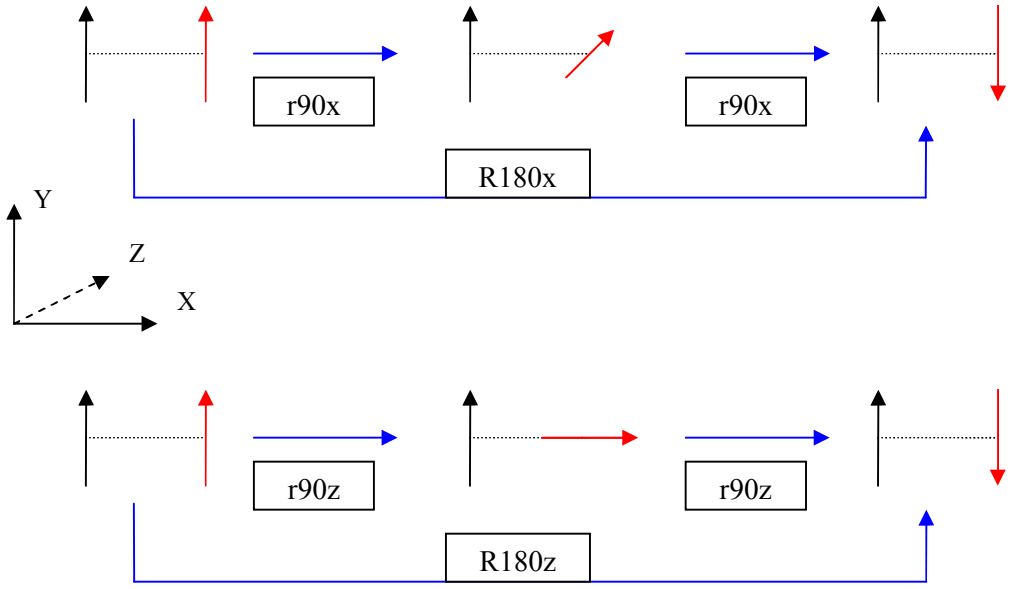

Figure 49 - *The r180x and r180z rotations of clusters produce the same dipolar arrangements via different routes. The top figures show the rotations carried out in order to achieve the r180x configuration. The bottom figures show the rotations carried out to achieve the r180z configuration.*

As can be seen from Figure 49 the rotation of the second cluster (dipole) about the X-axis or the z-axis will result in the dipole moments of the clusters pointing in the same direction. The dipolar equivalent configurations r180z and r180x are represented in Figure 50 as a central dipole with four quadrants, labelled A to D, to depict the different surfaces of the cluster. Starting from the same configurations it is clearly visible how the two orientations r180x and r180z result in the same dipolar position, but the quadrants exposed to original image are C and A for the r180x orientation and B and D for the r180z orientation. This potentially highlights how any difference in energies for dipolar equivalent configurations may arise. The results for r180x and r180z for the 30 a.u cluster, at separations of 70 a.u and 100 a.u, and 50 a.u cluster, at separations of 100 a.u and 150 a.u, are shown along with the respective dipole pairs (Figure 51).

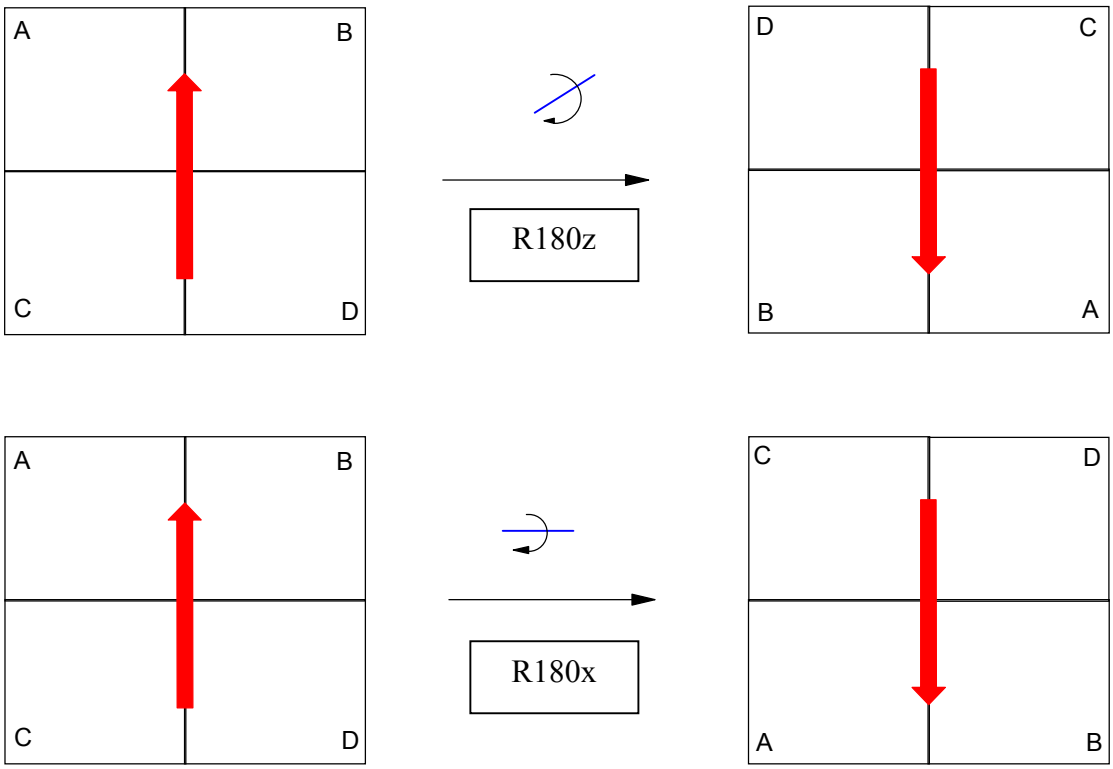

Figure 50 - *A simple 2D illustration of the nano clusters in terms of a dipole moment with quadrants (A-D) to represent surfaces of the clusters. The quadrants are transformed by the r180x (bottom) and r180z (top) orientations such that different quadrants are exposed to the original boxes (left).*

The atomistic results for the 30 a.u clusters in both the r180x and r180z configurations at separations of 70 and 100 a.u compare very favourably with the dipole pairs. The larger 50 a.u clusters show good agreement with the dipole pair profiles at a separation of 150 a.u for both r180x and r180z, though at 100 a.u of separation the r180x compares well to the dipole pairs profile, but the r180z does not. The minima in the r180z are smaller than that of r180x and the dipole pairs, this is most likely due to the surface atoms of the clusters still playing a significant role in the interaction. The r180z configuration does however have the minima and maxima occurring in the expected profile rotation angles according to the dipole pair profile. This discrepancy in the minima of the r180z also occurs at the larger separation of 150 a.u, however the difference between the r180z and dipole pair is far smaller when compared to the r180z and dipole pair at 100 a.u of separation.

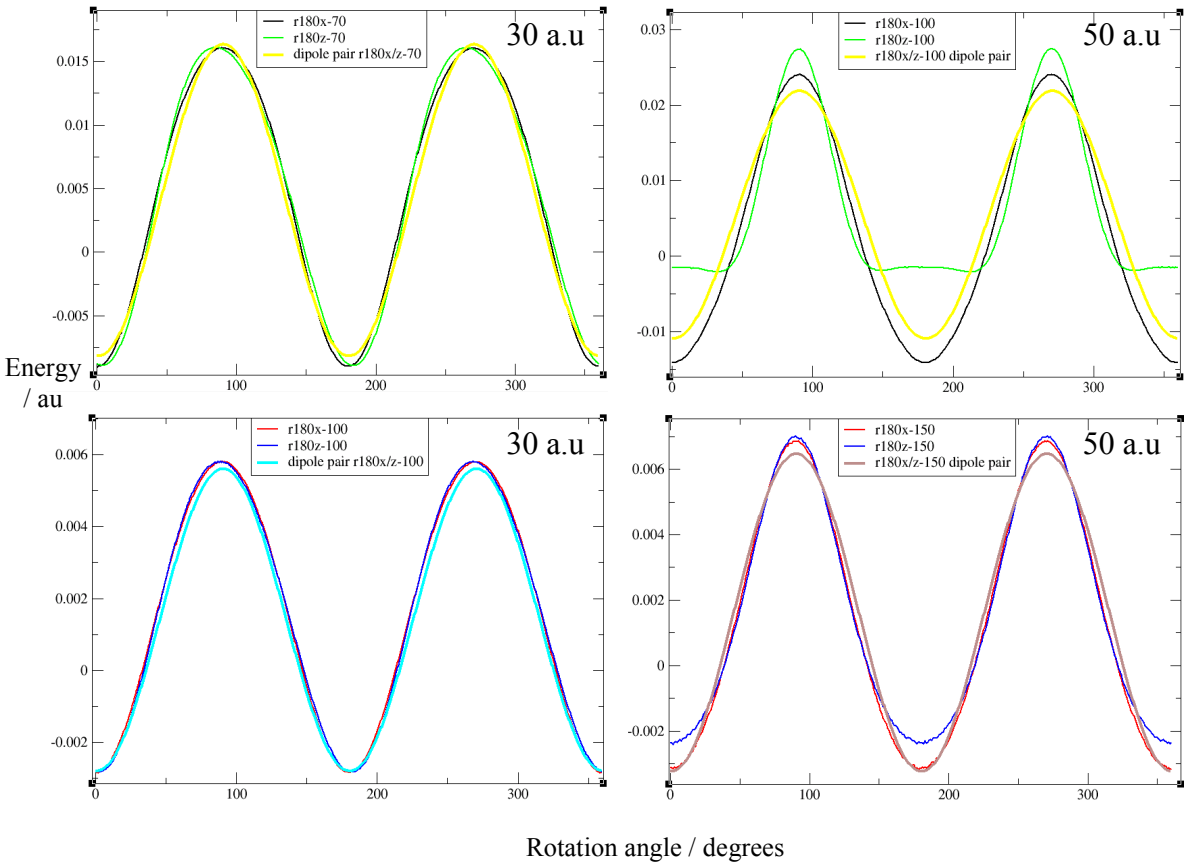

Figure 51 - *Energy profiles of the dipolar equivalent r180x and r180z configurations calculated for the 30 a.u (left hand figures) and 50 a.u (right hand figures) clusters respectively. The 30 a.u cluster energies are calculated at separations of 70 a.u (top left) and 100 a.u (bottom left). The 50 a.u cluster energies are calculated at separations of 100 a.u (top right) and 150 a.u (bottom right). The energies of the equivalent dipole pairs are shown for comparison as indicated by the respective legends.*

3.2.1 Repulsive starting configurations

The repulsive starting profiles, in terms of dipoles this is approximately the parallel configuration, for all three cluster sizes which include the r0, r45y, r90y, r135y, r180y, r45x and r45z dipolar configurations are represented concurrently with their respective dipole pair profiles. In order to avoid confusion only the r0 orientation calculation is carried out for the dipole pairs (Figure 52). The individual configuration energy profiles are not particularly of interest. The pattern the configurations collectively adopt and whether they are more generally in agreement with the dipole

pair pattern is more important. This also applies to subsequent energy profiles at short separations.

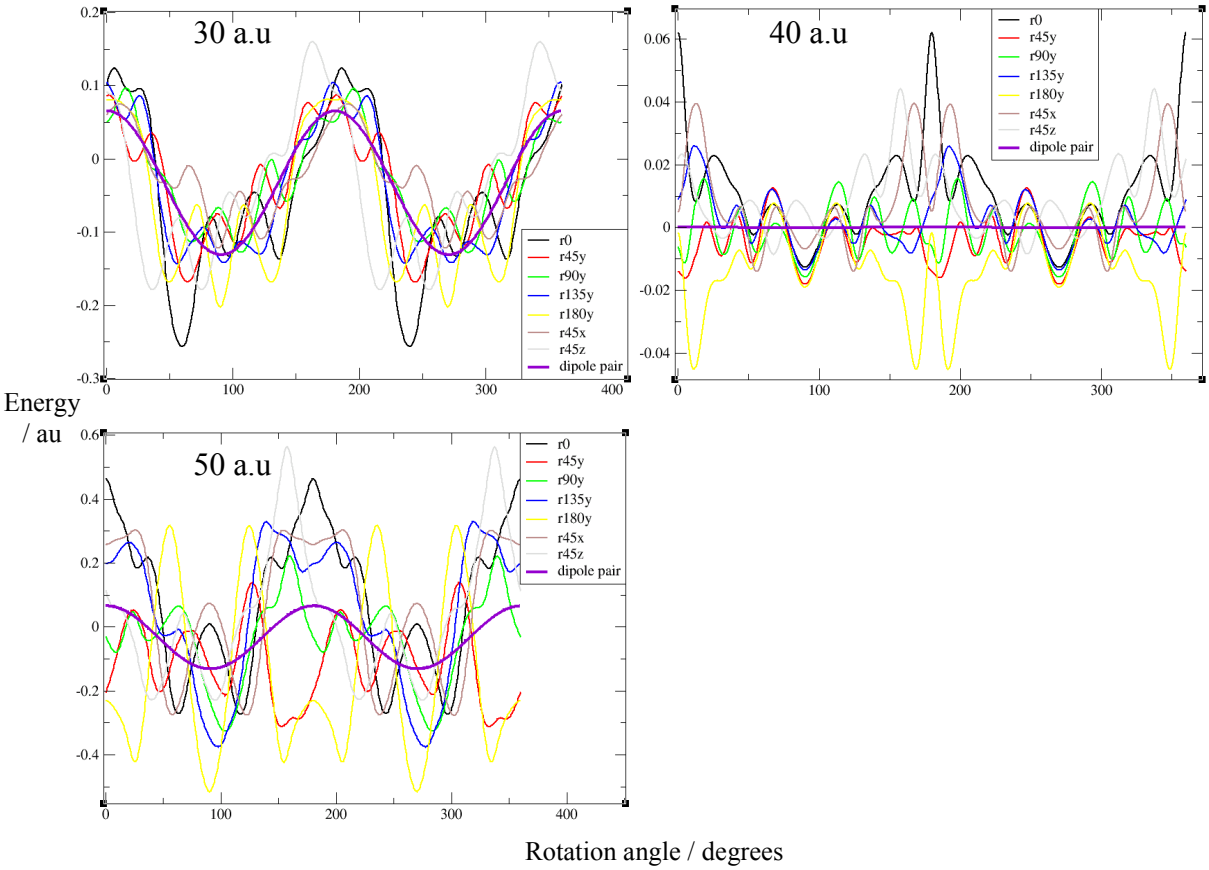

Figure 52 - *Energy profiles, starting configurations starting in a repulsive orientation, for the 30 a.u cluster (top left), 40 a.u cluster (top right) and 50 a.u cluster (bottom left) at separations of 35 a.u, 45 a.u and 55 a.u respectively. The dipole pair energies are calculated for the r0 configurations only, to act as a marker for comparison.*

The results of these short separation interactions provide intriguing results; the smaller 30 a.u cluster provides clear evidence that interactions at short separations, 35 a.u, are in part strongly governed by the dipole moment of the nano clusters as there are cosine type curves visible for all the indicated configurations, which compare favourably with the r0 dipole pair energy profile. All the clusters start in the same position, and so the dipole pair and atomistic results should show troughs and peaks in similar positions in each of the three cluster profiles. However, as discussed previously the 40 a.u cluster unlike the other two clusters has a relatively small dipole

moment. The dipole pair results for the 40 a.u cluster clearly illustrate that the dipole energy is negligible when compared to the actual atomistic results. The atomistic results for the 40 a.u cluster in general show a similar pattern to that of the 30 a.u cluster, except for the 180y profile, even though the dipole moment of the cluster is having a minimal effect according to the dipole pair energy profile. The energy scale of the figures should also be looked at closely as this reveals there is an energy difference in the scale of the order of five between the 30 a.u and 40 a.u clusters; similarly the 50 a.u cluster has energies that are ten times greater than that of the 40 a.u cluster. The 50 a.u cluster also tends to conform to the dipole pair energy profile, though the atomistic results here look exaggerated in terms of the peaks and troughs. When the 50 a.u cluster is compared to the 30 a.u cluster there is clear contrast between the two clusters as all of the atomistic results are very closely following the r0 dipole pair profile in the 30 a.u cluster, whilst in the 50 a.u cluster the atomistic results are only loosely following the r0 dipole pair configuration. There are also some results present for the 50 a.u cluster, such as the r180y and r45y, which do not conform to the dipole pair result. This maybe down to the fact the number of surface atoms is increasing as the size of the cluster increases, the implication being that the atomistic detailing of the cluster begins to have a greater contribution than the dipole moment of the cluster hence affecting the atomistic energy profile.

3.2.2 Attractive starting configurations

The attractive starting energy profiles, in terms of dipoles this is approximately the anti-parallel configuration, for each of the three clusters which include the r135x, r135z, r180x and r180z dipolar configurations are represented along with the associated dipole pair energy profiles. To avoid confusion the dipole pair calculation is carried out for the r180x/z profile only (Figure 53).

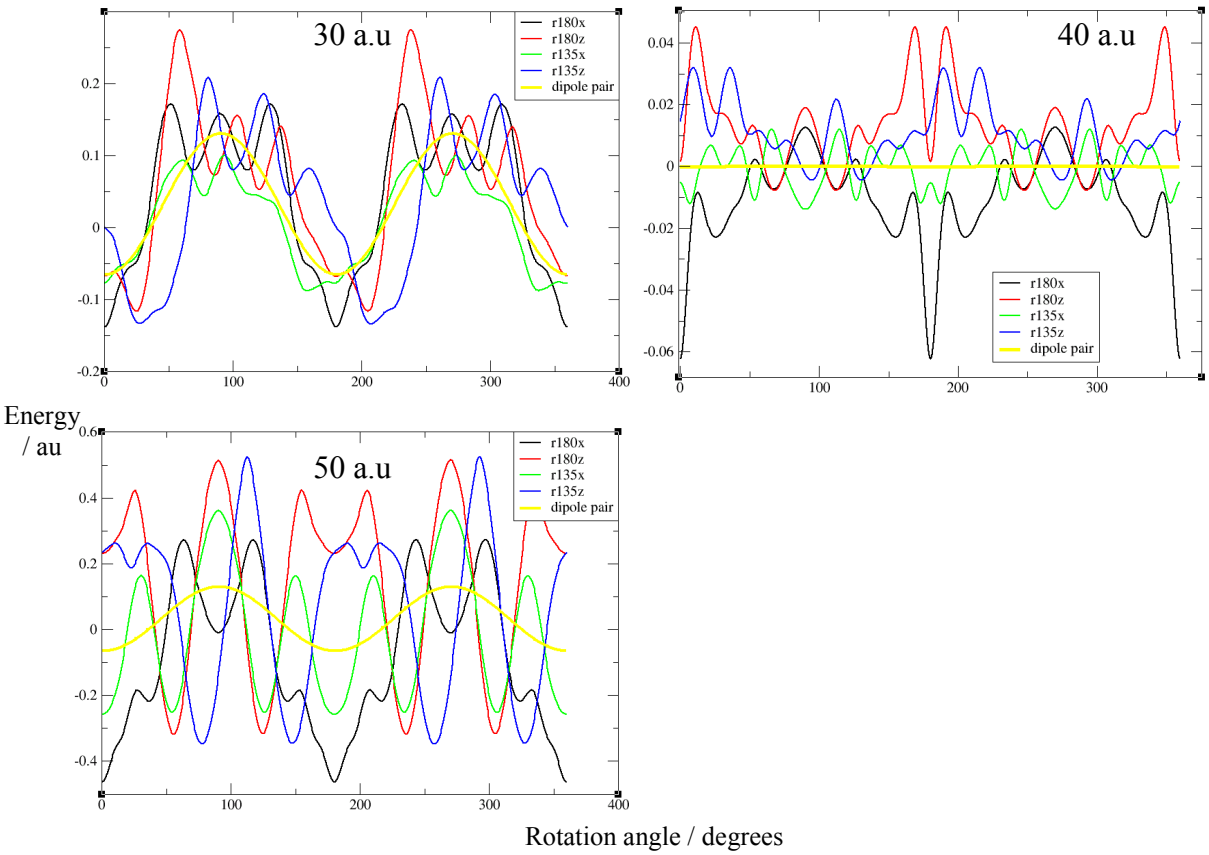

Figure 53 - *Energy profiles, starting configurations starting in an attractive orientation, for the 30 a.u cluster (top left), 40 a.u cluster (top right) and 50 a.u cluster (bottom left) at separations of 35 a.u, 45 a.u and 55 a.u respectively. The dipole pair energies are calculated for the r180z/r180x configurations only, to act as a marker for comparison.*

The atomistic data for the attractive starting profiles very much mirror the results for the previous repulsive starting profiles whereby the smallest cluster, 30 a.u cluster, shows the greatest agreement with the dipole pair profile. The 40 a.u cluster is essentially showing the effects of the atomistic detailing as previously stated. The 50 a.u cluster shows some elements of being correct especially for the r135x and 180x profiles, there are some clear ambiguities for the r135z and r180z profiles, but again they show some consistency with the dipole pair energy profile in general terms. As before there is a difference in the energy scales between the 40 a.u cluster and 30 cluster of the order of five and similarly between the 40 a.u cluster and 50 a.u cluster of approximately ten.

3.2.3 Neutral starting configurations

The results for the neutral starting configurations (r90x & r90z) with their respective dipole pair energy profiles are shown (Figure 54).

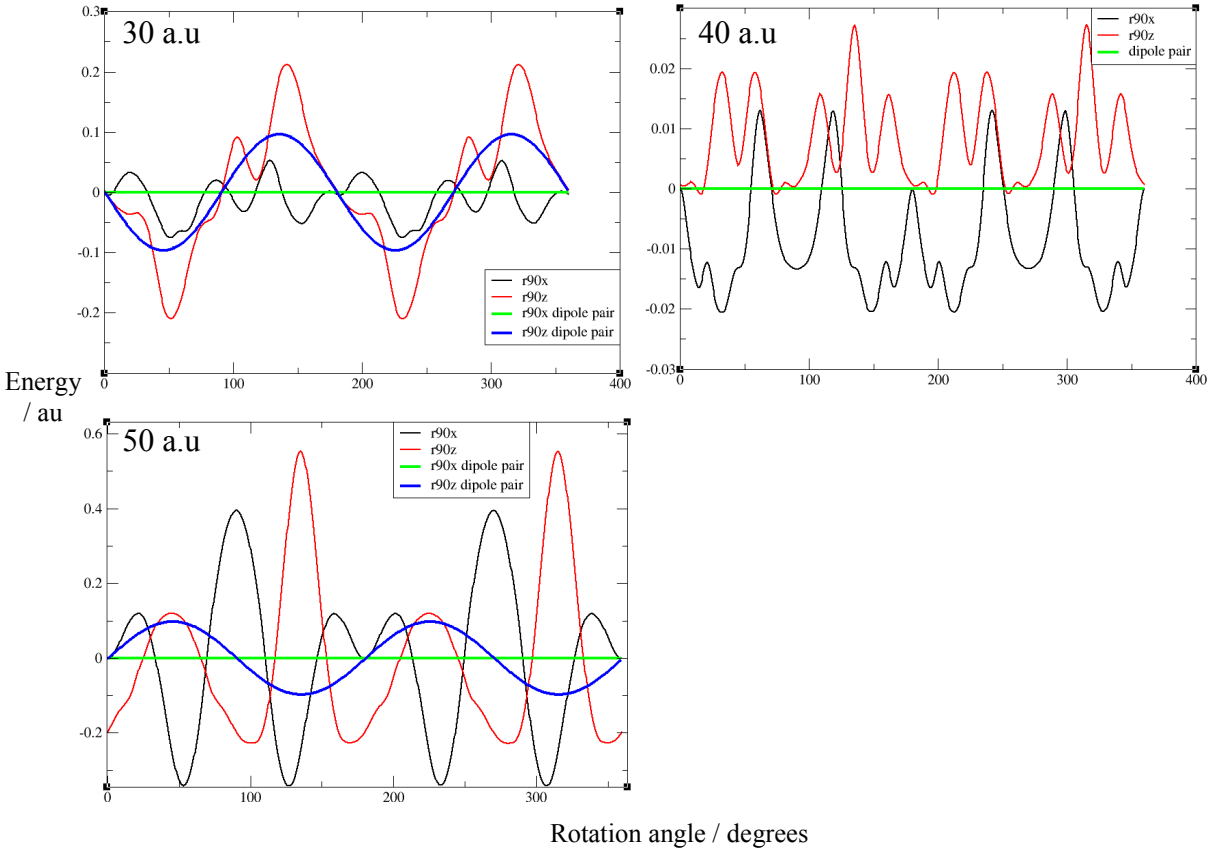

Figure 54 - *Energy profiles, starting configurations starting in a neutral orientation, for the 30 a.u cluster (top left), 40 a.u cluster (top right) and 50 a.u cluster (bottom left) at separations of 35 a.u, 45 a.u and 55 a.u respectively. The dipole pair energies are calculated for the r90x and r90z configurations for comparison.*

The 30 a.u cluster, like previous results, shows good agreement with the dipole pair energy profiles. The r90z atomistic data has enhanced peaks and troughs in almost the same positions as the r90z dipole pair profile. The r90x atomistic profile tends to oscillate about zero energy and also has minima and maxima that are higher and lower respectively than the r90z configuration suggesting it is also conforming to the r90x dipole pair profile. The 40 a.u cluster shows rather an odd result whereby the r90x configuration is basically in an attractive state throughout the energy profile while the

opposite is true for the r90z configuration as this is in an unattractive state throughout the energy profile. The 50 a.u cluster shows little conformity to the dipole pair profiles, the energy scale also reveals how large an effect the atomistic detailing of the cluster is now having over the energy profile, this point is nicely illustrated by the atomistic r90x profile which according to the associated dipole pair result should be zero. However as is clearly visible rather large oscillations are occurring, which are comparable in energy to the maxima and minima observed in the previous repulsive and attractive starting profiles. This implies the energy profile at short range is mostly governed by the atomistic detailing, though the dipolar energy of the cluster acts to modify the atomistic energy, such that those orientations that are dipolar favourable help to bias the overall energy of the cluster to those favourable configurations.

3.3 The XZ plane energy profiles

The results for the XZ plane are now examined. In this configuration the different dipole orientations of the cluster should result in constant dipolar energy as the cluster dipole orientations are fixed for the duration of the rotation about the XZ plane. The larger separation results, 2-3 times the cluster diameter, are first examined for the the 30 a.u and 50 a.u clusters, as previously stated and observed the 40 a.u cluster has a relatively small dipole moment and as such is not included for this analysis. The r0 configurations for the two clusters of interest are shown at separations of 70 a.u and 100 a.u for the 30 a.u cluster and 100 a.u and 150 a.u for the 50 a.u cluster (Figure 55).

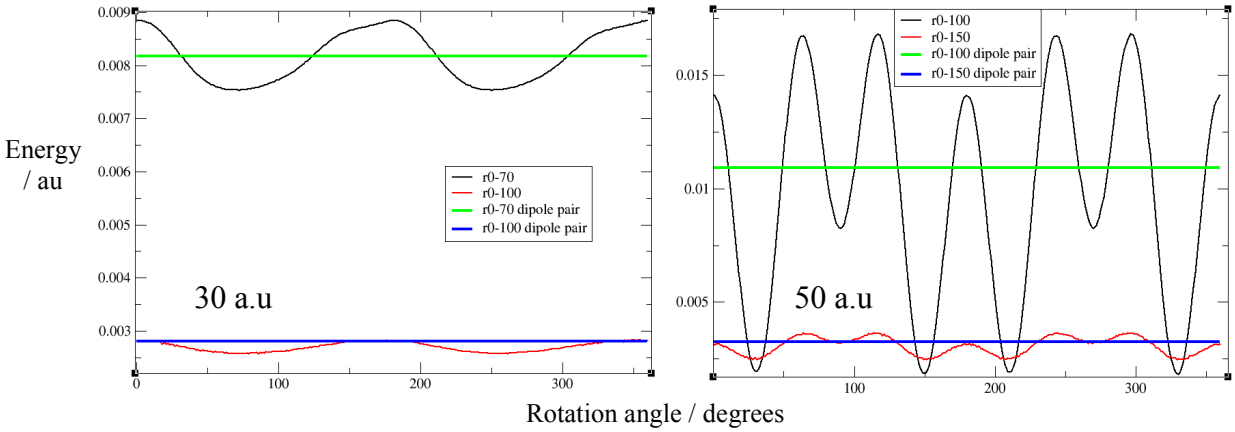

Figure 55 - *Energy profiles for the r0 configuration calculated for the clusters with diameters of 30 a.u (left hand figure) and 50 a.u (right hand figure) respectively, for the smaller 30 a.u cluster energies are calculated at separations of 70 a.u and 100 a.u as indicated in the figure legend, for the larger 50 a.u cluster these separations are 100 a.u and 150 a.u respectively. The energies of the equivalent dipole pairs are shown for comparison.*

The dipole pair results for both the 30 and 50 a.u clusters clearly show the roughly constant dipolar energy that would be expected as a result of having the dipole configurations stuck in their respective starting positions throughout the profile rotation. The first thing to note is that in both clusters the atomistic energy profiles are oscillating about their respective dipole pair profiles; these are of course simply linear lines indicating a constant dipolar energy. Secondly these atomistic energy oscillations are proportional to the separation between the clusters as the magnitude of these oscillations decays from approximately twice the cluster diameter separation to three times the cluster diameter separation in both cases. It is clearly visible that though the magnitude of the oscillations decreases on going from twice to three times the cluster diameter separation, for both the 30 a.u and 50 a.u clusters respectively, that the peaks and troughs are still occurring at the same profile angle rotations. This highlights how the atomistic detailing of the cluster can still have significant effects at large separations. The dipolar equivalent r180x and r180z cluster profiles are examined at large separations for the two clusters (Figure 56).

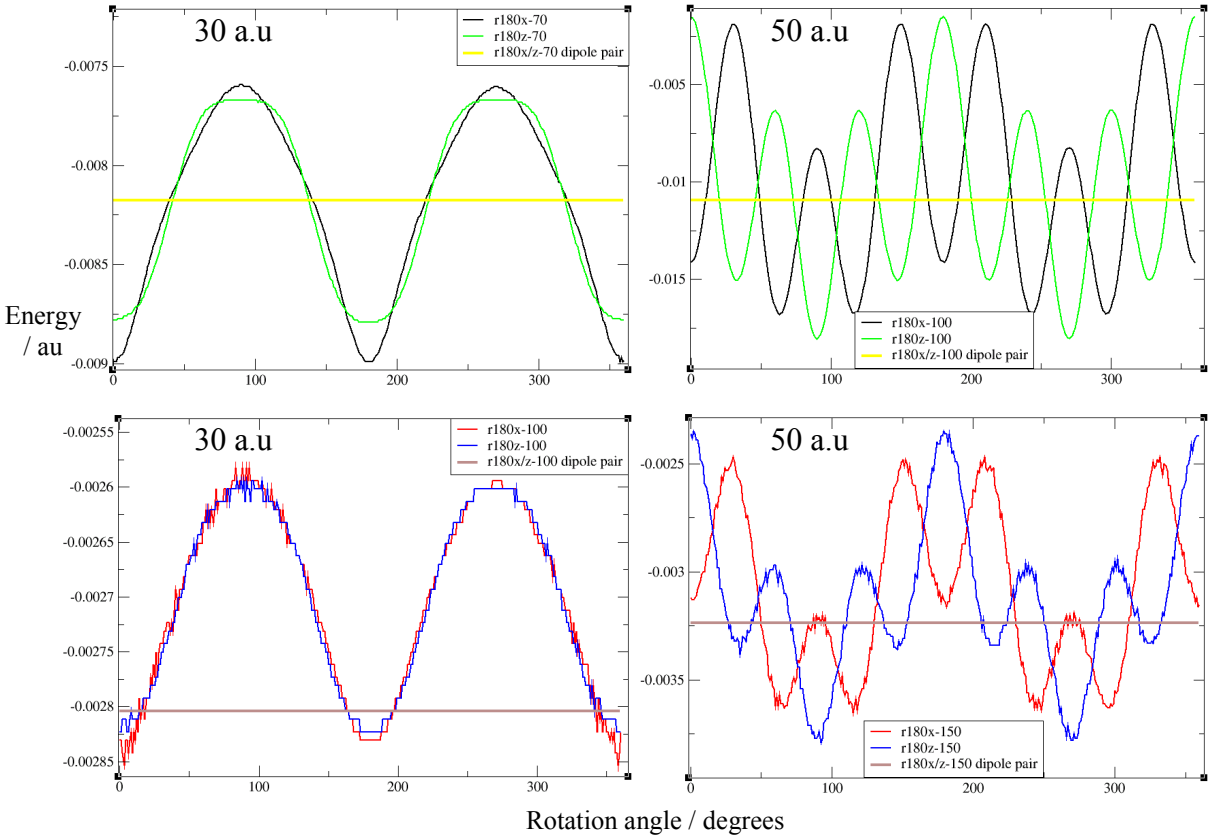

Figure 56 - *Energy profiles of the dipolar equivalent r180x and r180z configurations calculated for the 30 a.u (left hand figures) and 50 a.u (right hand figures) clusters respectively. The 30 a.u cluster energies are calculated at separations of 70 a.u (top left) and 100 a.u (bottom left). The 50 a.u cluster energies are calculated at separations of 100 a.u (top right) and 150 a.u (bottom right). The energies of the equivalent dipole pairs are shown for comparison as indicated by the respective legends.*

The results here show the same pattern as the r0 configurations observed previously with regard to the atomistic oscillations about the dipole pair energy profile, though there are some differences visible between the two clusters. The 30 a.u cluster has both the r180x and r180z profiles in phase with one another and overlapping rather well at both the separations of 70 a.u and 100 a.u shown. There are slight differences visible between the r180x and r180z at 70 a.u of separation whereby the former shows slightly greater oscillations about the dipole pair energy relative to the later. In the case of the 50 a.u cluster the r180x and r180z profiles are out of phase with one another, in fact if looked at closely the r180x and r180z look like mirrored images of one another, when there are peaks for the r180x profile there are troughs for the r180z

profile and vice versa. This further reinforces the idea of atomistic detailing being an important component of interactions between nanocrystals.

3.3.1 Repulsive starting configurations

The energy profiles at small separations of the clusters are now examined, as has previously been done the energy profiles are separated into three categories determined by the starting dipolar configurations of the cluster, these being the repulsive (r0, r45y, r90y, r135y, r180y, r45x & r45z), attractive (r135x, r180x, r135z & r180z) and neutral (r90x & r90z) configurations. The repulsive starting configurations are shown for all three clusters (Figure 57), at separations of 35 a.u, 45 a.u and 55 a.u for the 30 a.u, 40 a.u and 50 a.u clusters respectively. It should be noted that the dipole pair energy is not shown for the 40 a.u cluster as previously seen the energy is negligible compared to the atomistic energies of the cluster.

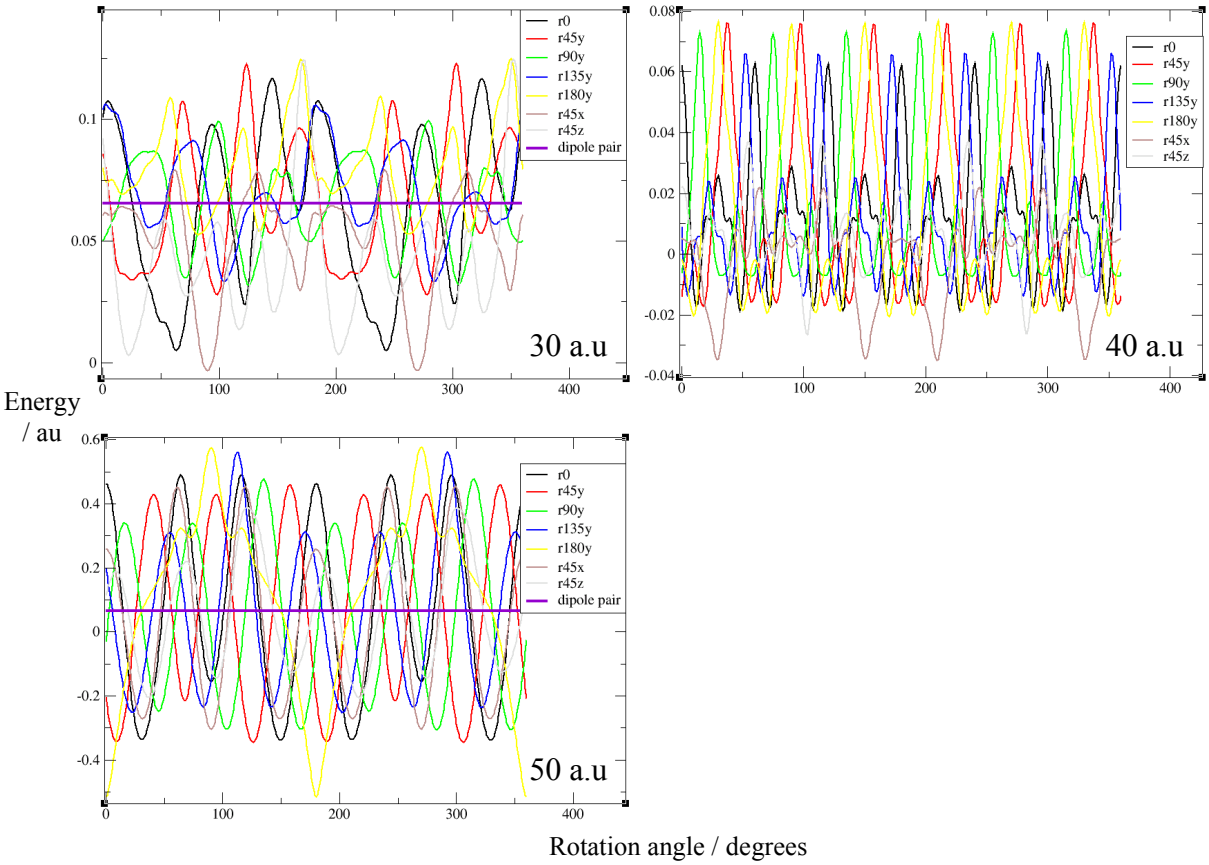

Figure 57 - *Energy profiles, starting configurations starting in a repulsive orientation, for the 30 a.u cluster (top left), 40 a.u cluster (top right) and 50 a.u*

cluster (bottom left) at separations of 35 a.u, 45 a.u and 55 a.u respectively. The dipole pair energies are calculated for the r0 configurations only, to act as a marker for comparison. The dipolar energy for the 40 a.u cluster is zero; as such it is not shown.

The 30 and 50 a.u clusters clearly show consistency with the large separation results, there are oscillations about the dipole pair profile. The 30 a.u cluster does show greater conformity as all the configurations here should be repulsive and hence should have positive energies and this is confirmed from the energy scale of the graph. The 40 a.u cluster also tends to comply with this as most of the configurations are positive in energy, with most prominent exception being the r45x configuration. In the case of the 50 a.u cluster there are clearly large oscillations, which result in the energy of the profiles regularly falling into favourable negative energies.

3.3.2 Attractive starting configurations

The results for the attractive starting dipolar configurations (r135x, r180x, r135z & r180z) of the clusters are shown (Figure 58). Again to avoid confusion only the r180x/z dipolar pair profiles are shown for comparison.

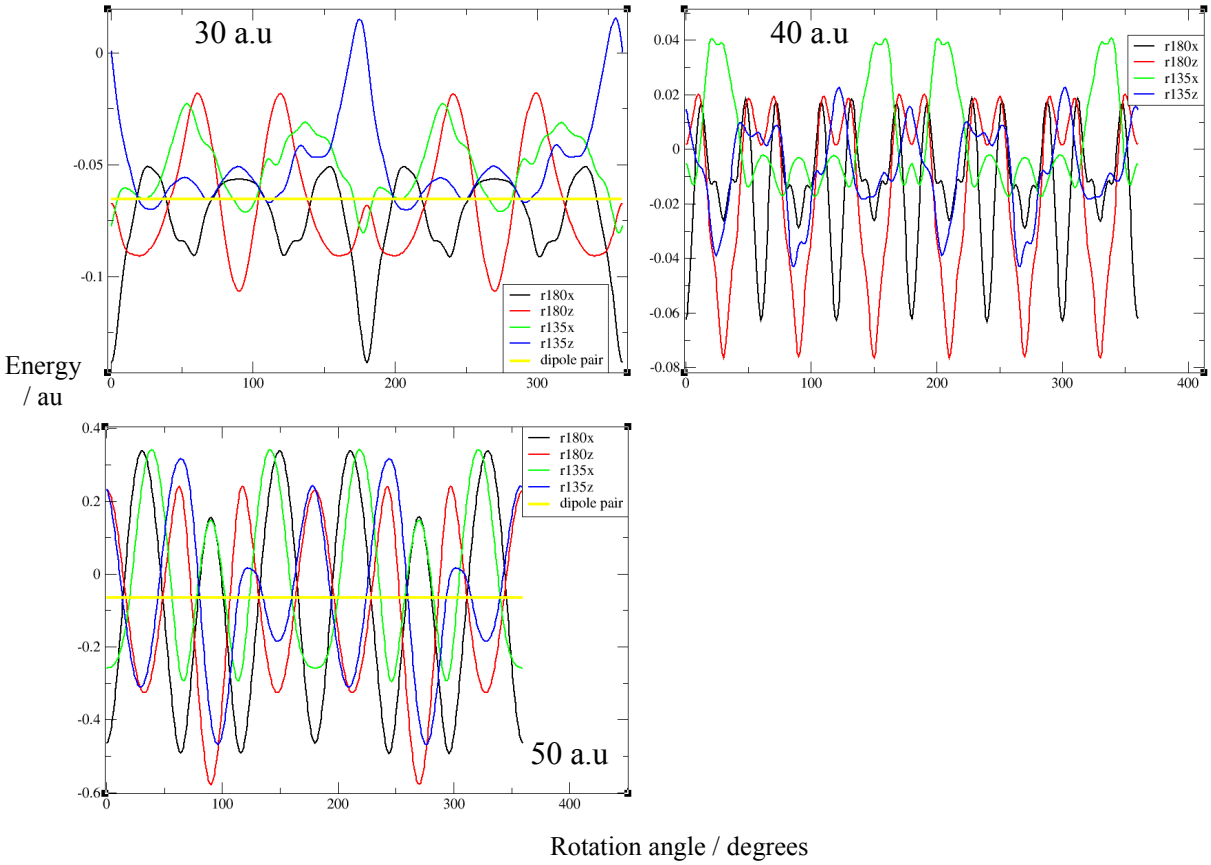

Figure 58 - *Energy profiles, starting configurations starting in an attractive orientation, for the 30 a.u cluster (top left), 40 a.u cluster (top right) and 50 a.u cluster (bottom left) at separations of 35 a.u, 45 a.u and 55 a.u respectively. The dipole pair energies are calculated for the r180z/r180x configurations only, to act as a marker for comparison. The dipolar energy for the 40 a.u cluster is zero, this is not shown.*

The attractive results are again similar to that of the repulsive data, the smaller 30 a.u cluster shows greatest agreement with the dipole pair results, as the oscillations of the energy profiles on the whole remain in negative energies signifying an attractive energy. The larger 50 a.u cluster does show agreement to the dipole pair profile; however, the oscillations of the energy profiles have regularly entered into repulsive and positive energies. The 40 a.u cluster also has the majority of the energy profiles drifting into negative energies like the other two clusters; it is interesting to also note the energy scales of the three different clusters as they tend to follow the pattern of increasing energy scales with increasing dipole moments of the clusters.

3.3.3 Neutral starting configurations

The neutral starting dipolar configurations (r90x & r90z) of the clusters are represented for the 30 a.u, 40 a.u and 50 a.u clusters (Figure 59).

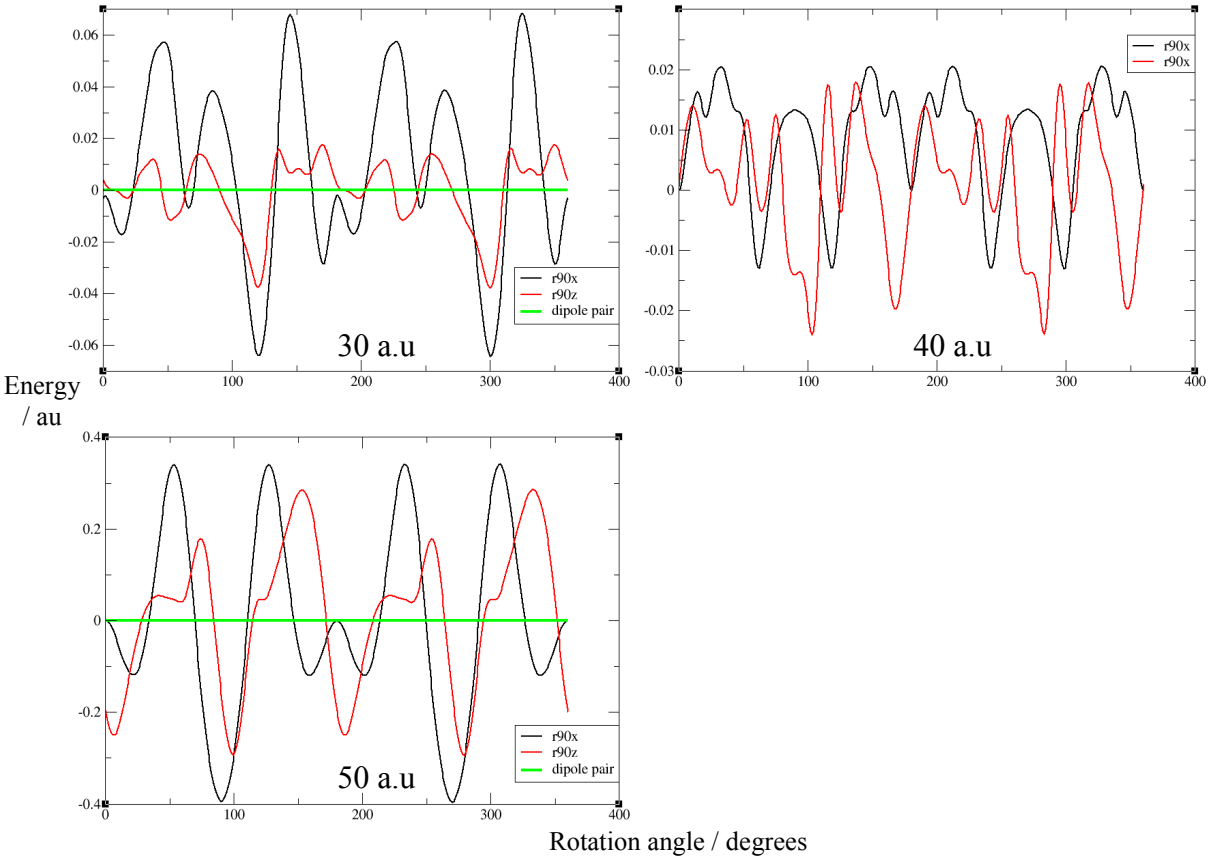

Figure 59 - *Energy profiles, starting configurations starting in a neutral orientation, for the 30 a.u cluster (top left), 40 a.u cluster (top right) and 50 a.u cluster (bottom left) at separations of 35 a.u, 45 a.u and 55 a.u respectively. The dipole pair energies are calculated for the r90x/r90z configurations for comparison.*

The result for the neutral starting dipole configurations shows harmony with the previous results for the repulsive and attractive cluster configurations. All the clusters show oscillations of the profile energies about zero energy and the extent of these oscillations increases from the 30 a.u to the 50 a.u cluster, pointing to the increase in atomistic detailing contribution to the overall energy. The 40 a.u cluster interestingly shows smaller oscillations than the 30 a.u cluster and this would tend to indicate that

the dipole-dipole contribution between the clusters has an effect at small separations even when the dipolar energy should be zero for the interaction between clusters.

3.4 The YZ plane energy profiles

The following analysis of the clusters is for the YZ plane; these results should be similar to those observed for the XY plane as the clusters will go through a range of configurations for the duration of the profile rotation. The larger separation between the clusters for the 30 a.u cluster (separations of 70 a.u and 100 a.u) and the 50 a.u cluster (separations of 100 a.u and 150 a.u) are examined first for the r0 configuration (Figure 60), again the 40 a.u cluster is not analysed in this section.

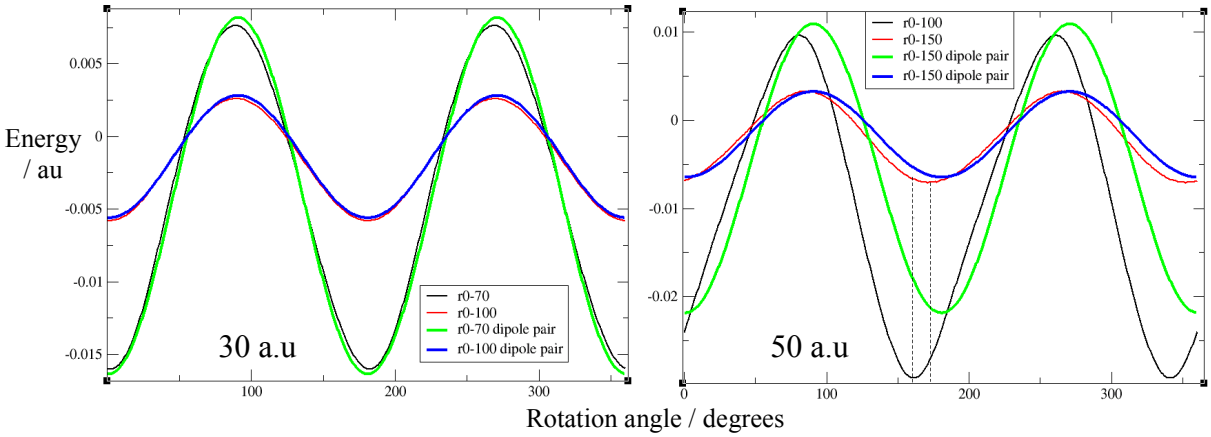

Figure 60 - *Energy profiles for the r0 configuration calculated for the clusters with diameters of 30 a.u (left hand figure) and 50 a.u (right hand figure) respectively, for the smaller 30 a.u cluster energies are calculated at separations of 70 a.u and 100 a.u, for the larger 50 a.u cluster these separations are 100 a.u and 150 a.u respectively. The energies of the equivalent dipole pairs are shown for comparison.*

The results for the 30 a.u cluster show very good agreement between the dipole pair profile and the atomistic profiles at both approximately twice and three times the diameter of the cluster. The larger 50 a.u cluster shows a discrepancy between the dipole pair profile results and the actual atomistic profile results for both the separations shown. The atomistic result are out of phase with the dipole pair result, the magnitude of which varies according to the separation that is looked at. For

instance at a cluster separation of 100 a.u they are approximately 20 degrees out of phase while the same curves at a separation of 150 a.u are out of phase by approximately 10 degrees. The consequence of this is that the curves at 150 a.u are in better agreement than those at 100 a.u of cluster separation; this also again highlights how the atomistic detailing of the cluster can affect the energy profile at short separations and how its effects begin to dissipate at larger separations. The results for the dipolar equivalent r180x and r180z profiles are shown along with the dipole pair profiles (Figure 61).

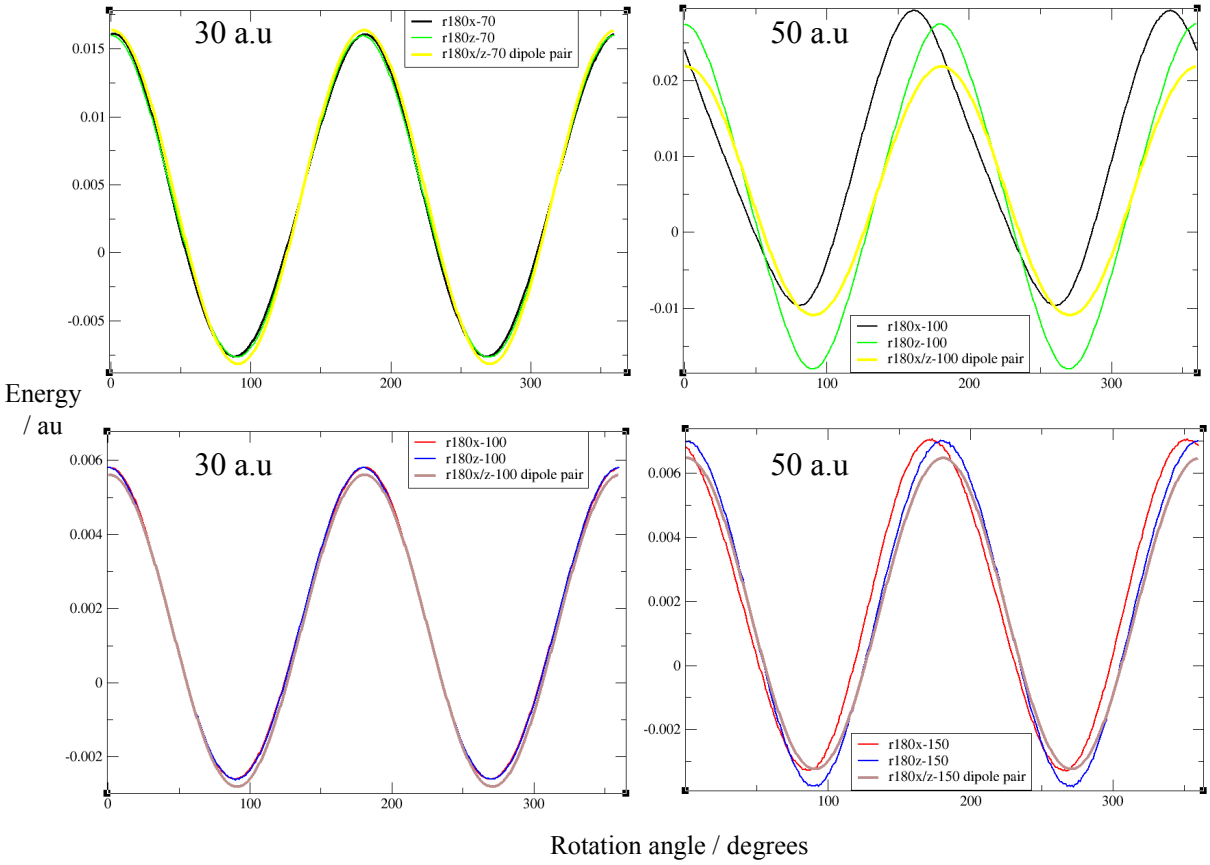

Figure 61 - *Energy profiles of the dipolar equivalent r180x and r180z configurations calculated for the 30 a.u (left hand figures) and 50 a.u (right hand figures) clusters respectively. The 30 a.u cluster energies are calculated at separations of 70 a.u (top left) and 100 a.u (bottom left). The 50 a.u cluster energies are calculated at separations of 100 a.u (top right) and 150 a.u (bottom right). The energies of the equivalent dipole pairs are shown for comparison as indicated by the respective legends.*

The results for the 30 a.u cluster are similar to those of the r0 configuration in showing very good agreement between the atomistic and dipole pair profiles at both the separations of 70 a.u and 100 a.u. The 50 a.u cluster shows good conformity between the dipole pair results and the r180z configuration at both the separations shown, 100 a.u and 150 a.u, though the peaks are subtly higher and troughs lower than dipole pair profile at 100 a.u of separation. The r180x configuration shows a phase shift of approximately 20 degrees at 100 a.u of separations and of roughly 10 degrees when the separation is increased to 150 a.u, this phase shift has already been observed in the previous r0 configurations. The persistent phase shift presents a problem initially as some configurations seem not to be affect while other are. This problem can be rationalized if one considers the cluster as three-dimensional crystal that is separated into two compartments A and B (Figure 62). The starting cluster (i) is in the r0 configuration and different rotations of the second cluster (j) will result in different surfaces between the clusters being exposed. The results so far indicate that the r0 and r180x configurations produce divergence from the expected energy profiles, whilst the r180z configuration is unaffected as it shows good agreement with the expected dipole pair profile. The three dimensional representation of the nanocluster clearly shows the r0 and r180x configurations having the same surfaces exposed to the static starting nanocluster through out the YZ profile rotation. This essentially means surface A in the static starting cluster and surface A of the second rotating cluster (r0 or r180x) are exposed to one another; this similarly applies to the B surfaces. The r180z configuration plainly shows it has opposing surfaces exposed relative to both the r0 and r180x configurations. This means surface A in the static starting cluster will be exposed to the B surface of the second rotating r180z cluster (Figure 63).

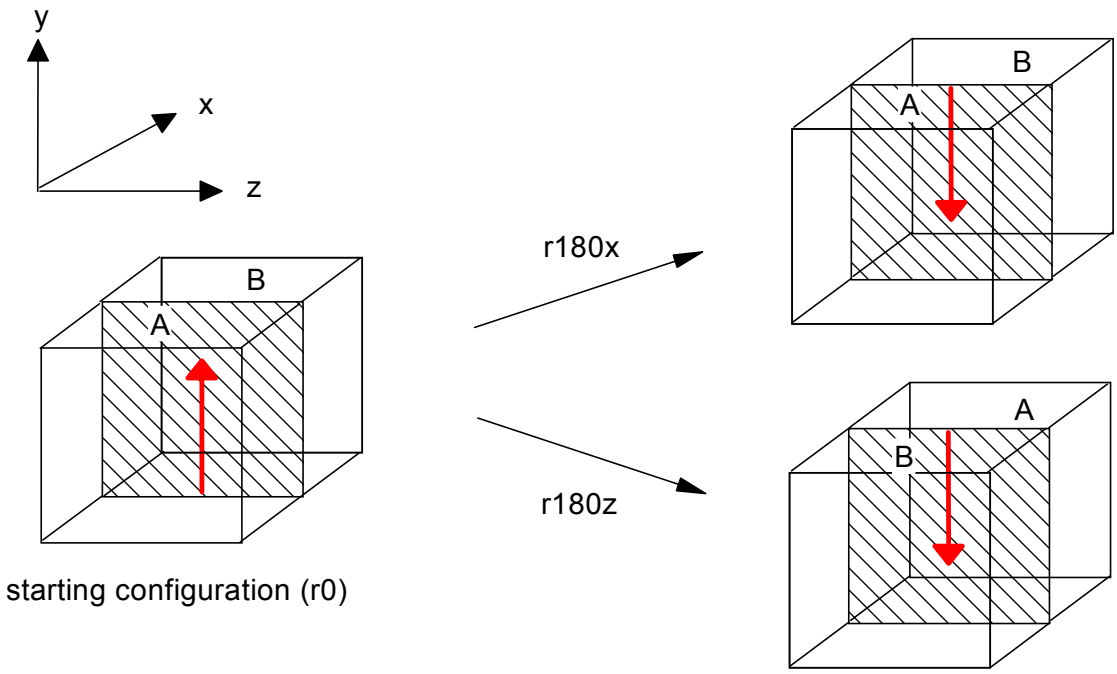

Figure 62 - *The nanoclusters represented as three dimensional entities with two compartments. The left figure shows both the starting cluster and the r0 configuration with cluster having two surfaces A and B. The right figures show the r180x and r180z rotations of the starting cluster. The r180z has relatively different surfaces exposed compared to the r0 and r180x configurations. The dipole moments of the respective clusters are shown with red arrows.*

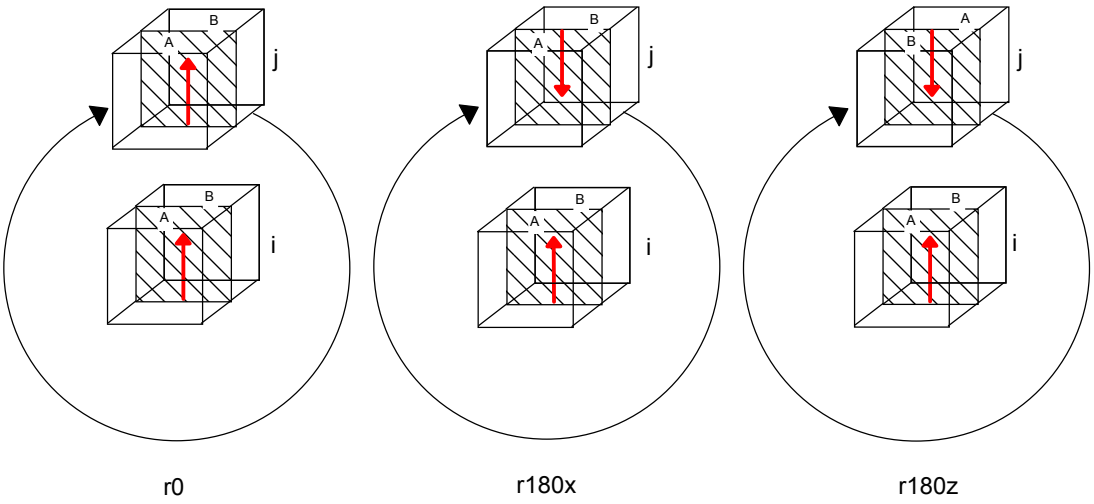

Figure 63 - *The energy profile being built up for different configurations. The left figure highlights the r0 configuration profile and the surfaces of the two clusters i and*

j exposed to one another. The central figure shows the r180x configuration profile with the same surfaces exposed as the r0 configuration. The right figure shows the r180z configuration profile with different surfaces between the clusters i and j exposed relative to the r0 and r180x configurations.

One method of confirming the explanation of shifted energy profiles being the result of particular surface interactions between clusters is to look at another configuration not previously examined for longer separations. The r180y configuration should have no shifted energy profiles as it has the same surfaces as the r180z configuration exposed (Figure 64). However the r180y configuration in dipole terms is the same as the r0 configuration and hence at a separation of 100 a.u the energy profile of the r180y configuration should be in phase with the r0 dipole pair profile for the 50 a.u cluster (Figure 65). The energy profile graph evidently shows the r180y configuration to be completely in phase with the dipole pair profile, though the peaks are higher and the troughs are lower. This result confirms the importance of the surface make-up of the clusters and their bearing on the interaction between clusters.

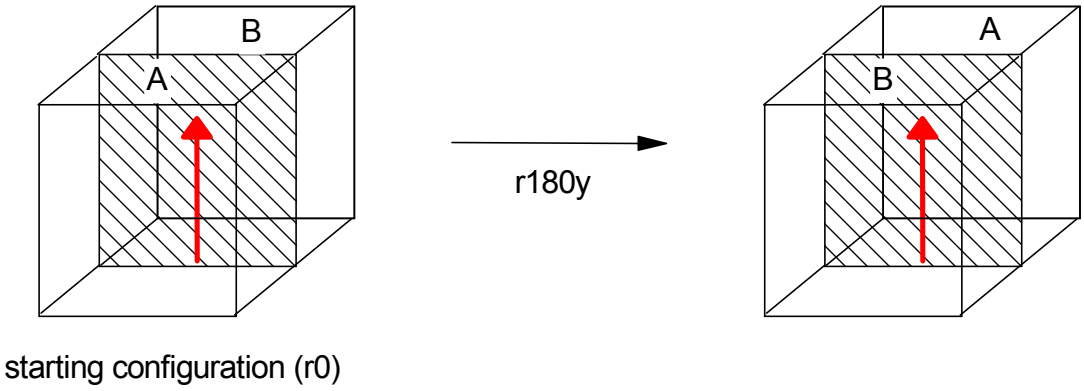

Figure 64 - *The rotation of the starting nanocluster representation to yield the r180y configuration. The figure illustrated the rotation of the starting configuration to obtain the r180y configuration with surfaces A and B exposed in exactly the same way as the previous r180z configuration. The red arrows show the dipole moments of the respective clusters.*

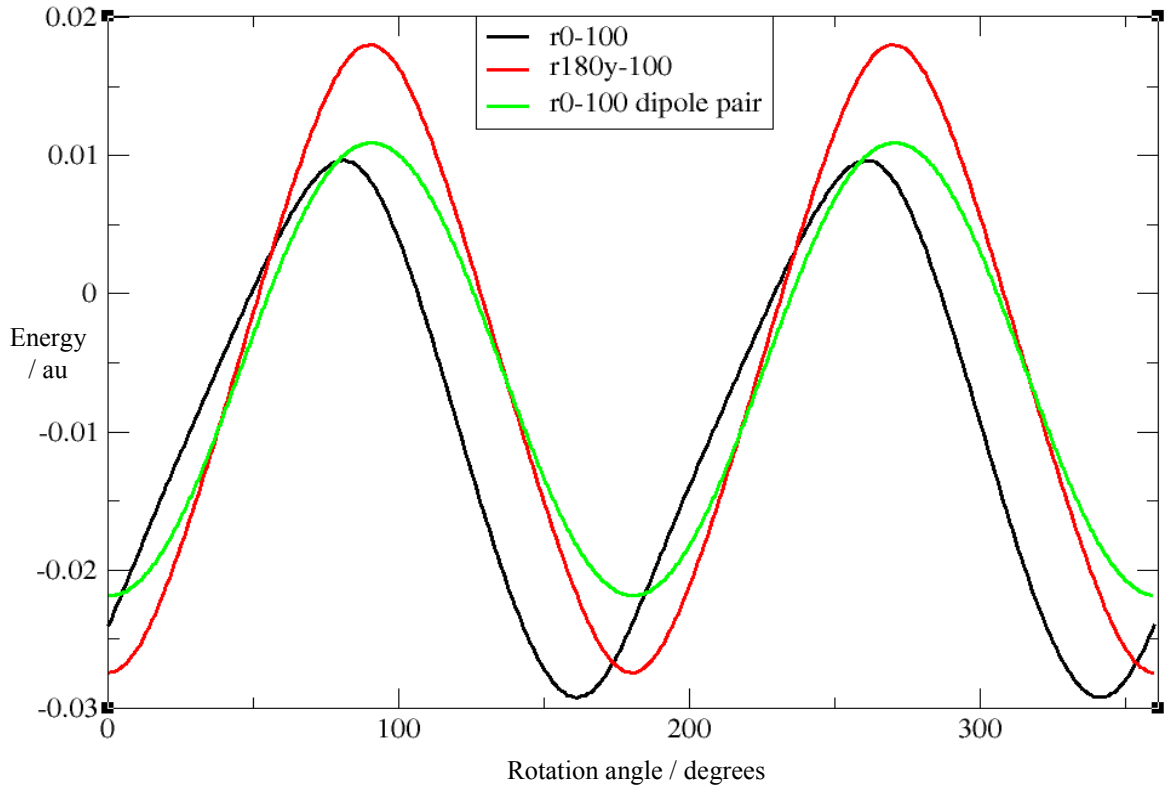

Figure 65 - *The energy profiles of the dipolar equivalent r0 and r180y configurations. The r0 configuration is out of phase with the expectant dipole pair profile. The r180y configuration is in phase with the expectant dipole pair profile.*

3.4.1 The attractive starting profiles

The results for the clusters at short separations are examined; the results here are separated in terms of whether the starting configurations are attractive (r0, r45x, r45y, r90y, r135y, r180y & r45z), repulsive (r135x, r180x, r135z & r180z) or neutral (r90x & r90z). The attractive data is illustrated first (Figure 66). The general pattern adopted by the different energy configurations at short separation and their comparison to the dipole pair profile is most important, not the individual energy configurations.

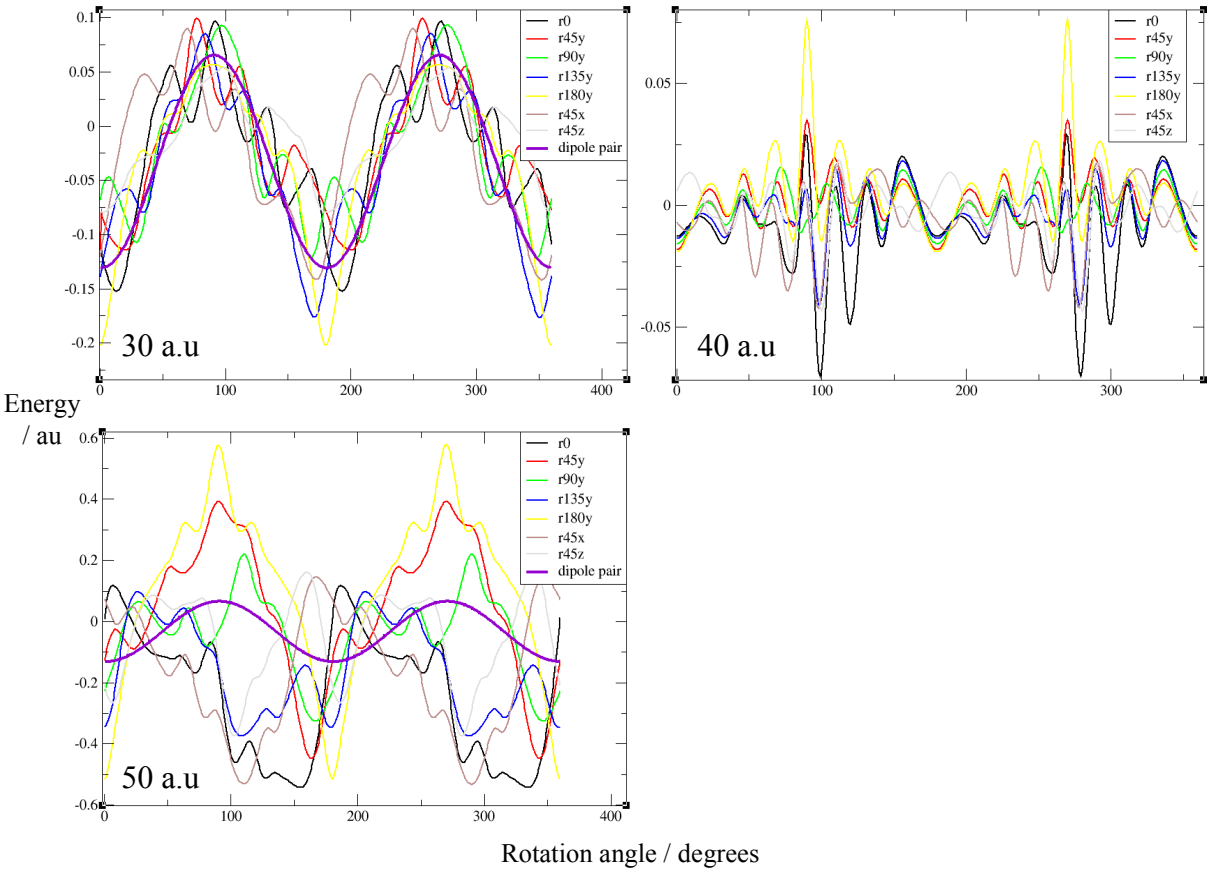

Figure 66 - *Energy profiles, starting configurations starting in a attractive orientation, for the 30 a.u cluster (top left), 40 a.u cluster (top right) and 50 a.u cluster (bottom left) at separations of 35 a.u, 45 a.u and 55 a.u respectively. The dipole pair energies are calculated for the r0 configurations only, to act as a marker for comparison. The dipolar energy for the 40 a.u cluster is zero; as such it is not shown.*

There are similarities with the repulsive results observed for the XY plane as the smaller 30 a.u cluster show good continuity between the atomistic and dipole pair profiles. The 50 a.u cluster has some atomistic profiles that are comparable to the dipole pair profile result, such as the r180y, r45y and r90y. The remaining configurations seem to be phase shifted, a possible explanation for this occurring has already been outlined in figure 23, by approximately 60 degrees from the dipole pair profile; this is illustrated by the r0, r135y, r45x and r45z configurations. The 40 a.u cluster had previously showed elements of following the dipolar profiles of the 30 and 50 a.u cluster in the XY plane, in terms of the placement of the peaks; however in this YZ plane the results actually do not tend to follow the pattern observed in the 30 and

50 a.u cluster dipole pair results. The dipole pair results for the 30 a.u and 50 a.u clusters show peaks at 90 and 270 degrees while the in the case of the 40 a.u cluster the atomistic results in general terms show no conformity to this. The results for the repulsive starting cluster dipole configurations are shown (Figure 67).

3.4.2 The repulsive starting profiles

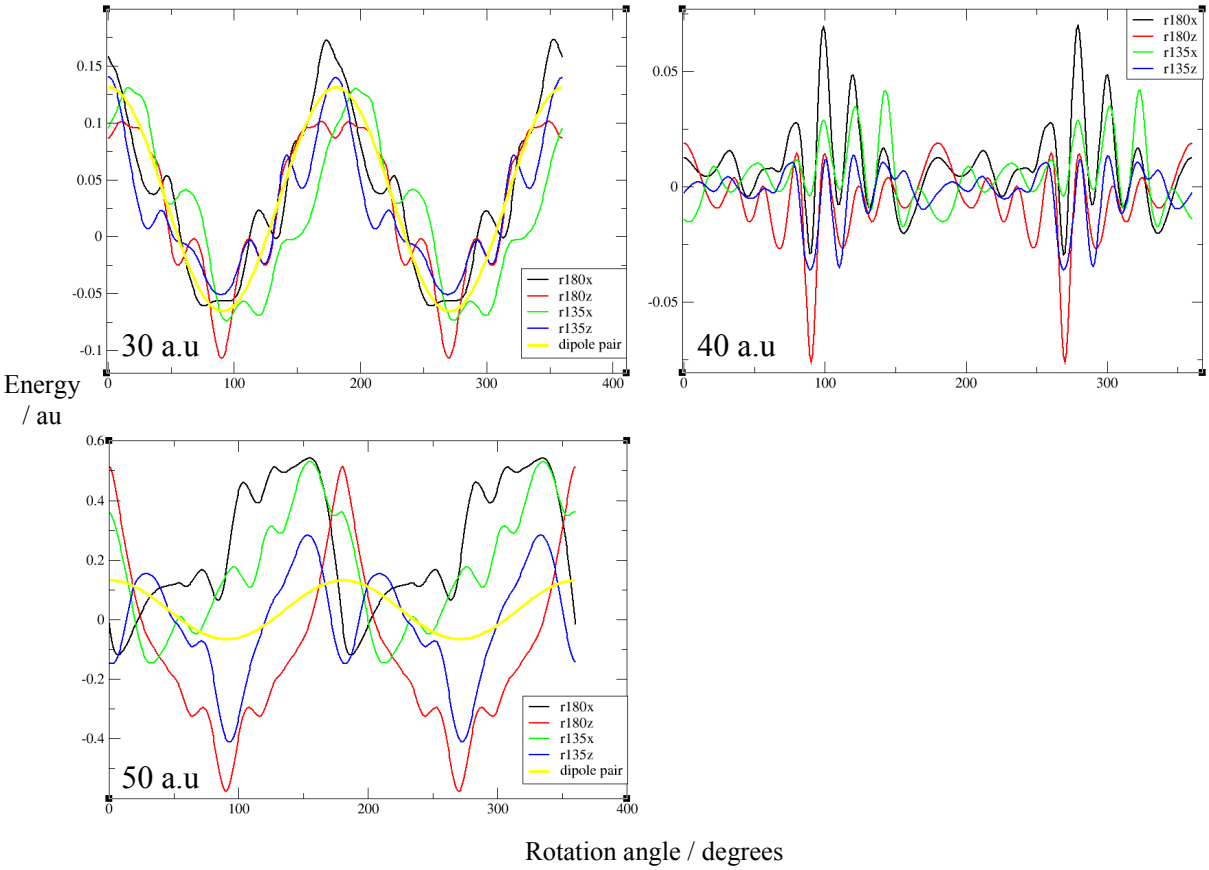

Figure 67 - *Energy profiles, starting configurations starting in repulsive orientations, for the 30 a.u cluster (top left), 40 a.u cluster (top right) and 50 a.u cluster (bottom left) at separations of 35 a.u, 45 a.u and 55 a.u respectively. The dipole pair energies are calculated for the r180z/r180x configurations only, to act as a marker for comparison. The dipolar energy for the 40 a.u cluster is zero, this is not shown.*

The same pattern emerges in the repulsive starting configurations as those seen in the attractive starting configurations. The 30 a.u clusters atomistic profiles compare favourably with the dipole pair profiles. The 40 a.u cluster does not follow the pattern of the dipole pair profiles from the 30 and 50 a.u clusters. There are phase shifts

visible for the 50 a.u cluster in the r180x and r135x configurations similar in magnitude to those observed in the attractive starting profiles. Finally the neutral starting dipole cluster configurations are shown (Figure 68).

3.4.3 Neutral starting configurations

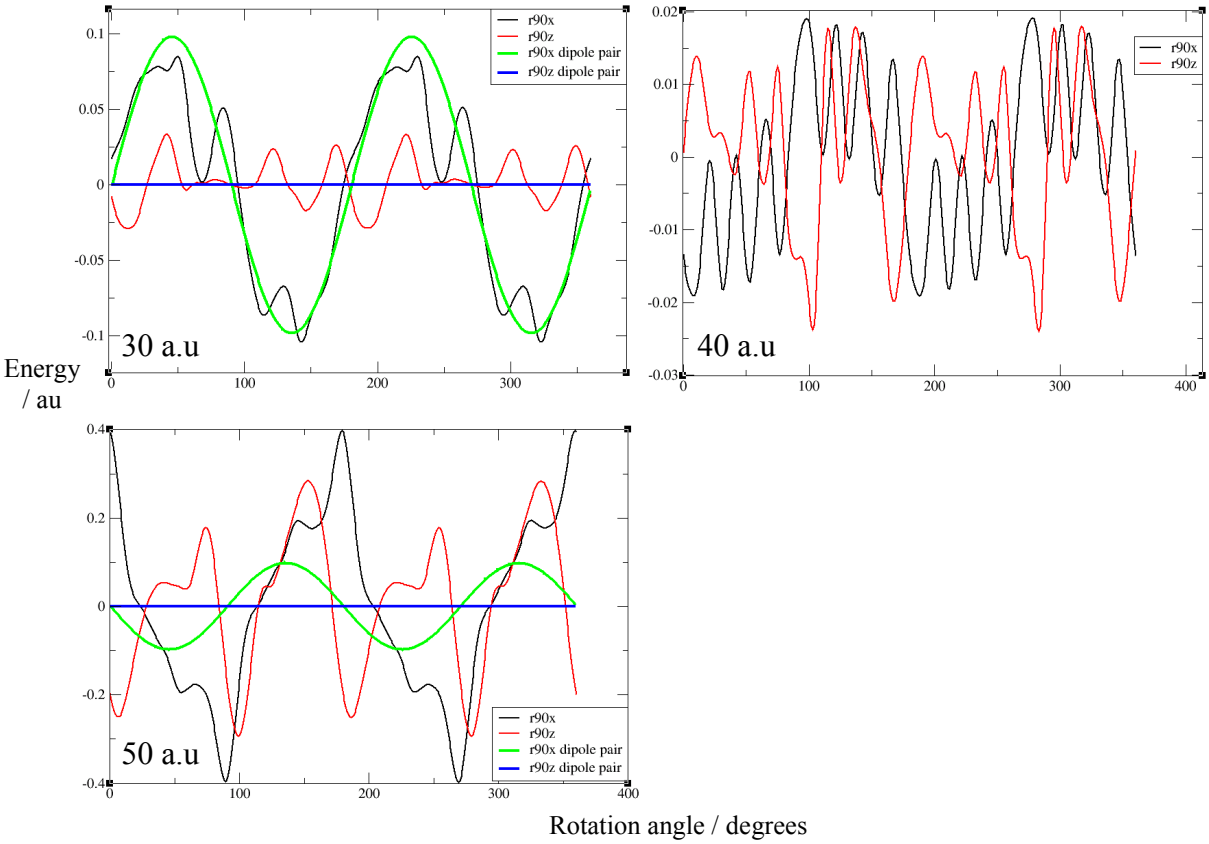

Figure 68 - *Energy profiles, starting configurations starting in a neutral orientation, for the 30 a.u cluster (top left), 40 a.u cluster (top right) and 50 a.u cluster (bottom left) at separations of 35 a.u, 45 a.u and 55 a.u respectively. The dipole pair energies are calculated for the r90x/r90z configurations for comparison.*

The 30 a.u cluster shows excellent agreement between the r90x and r90z with their respective dipole pair profiles. The 50 a.u cluster as seen before has rather larger oscillations in the atomistic profiles and like previous results the r90x is tending to the follow the r90x dipole pair profile, albeit that it seems phase shifted by approximately 40 degrees. The 40 a.u cluster also shows both the r90x and r90z oscillating about zero energy as one would expect in the absence of dipole-dipole interactions.

3.5 Summary

In summary the zinc blende cluster energy profiles have shown that dipole-dipole interactions may indeed play a significant role in the self-assembly processes of nanocrystals. The dipole-dipole interactions between the clusters may not however be the only contributing factor to the self-assembly processes as the atomistic detailing of the cluster itself plays a significant role in determining the most favourable orientations of attachment between the clusters, in particular at short separations. The atomistic detailing has less of an effect as the size of the cluster decreases as there are fewer surface atoms and also fewer atoms in total. This observation is backed up by the larger 50 a.u cluster, which shows phase shifts in the energy profiles as a result of the surface atoms or atomistic detailing have a significant effect.

Chapter 4 Atomistic energies of wurtzite clusters

4.1 Introduction

In the previous chapter nanoclusters composed of a zinc blende structure were examined. In this chapter nanoclusters of a wurtzite structure will be considered. There are three clusters to be examined, as previously observed, having diameters of 30, 40 and 50 a.u. However unlike the zinc blende clusters the wurtzite clusters have additional quadrupole moments, which give rise to possible multipole interactions between the clusters in the form of dipole-dipole, dipole-quadrupole and quadrupole-quadrupole terms. Therefore the atomistic cluster profiles are additionally compared to multipole pair profiles, which will highlight the total effect of these multipole interactions between the clusters. This is simply illustrated using the square net arrangement of the quadrupole to describe the construction of the multipole pair profile (Figure 69).

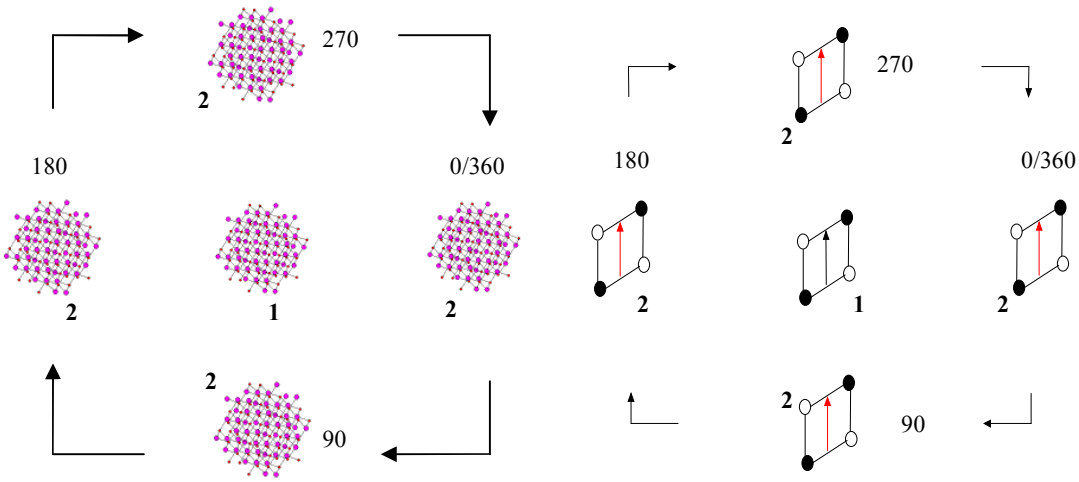

Figure 69 -*The processes of building up energy profiles. The left figure shows the atomistic energy profile built up by rotating the second cluster about the first cluster. The right figure shows the equivalent multipole pair energy profile being built up.*

The process of building up the atomistic energy profiles is the same as that for the zinc blende clusters in chapter 3 with the starting configuration of the original cluster such that their respective dipole moments all point along the laboratory y-axis. Three clusters are extracted from the ideal wurtzite structure with approximate diameters of 30, 40 and 50 a.u, which have respective dipole moments of 59 a.u (~148 Debyes), 19 a.u (~48 Debyes) and 67 a.u (~168 Debyes). In addition to the dipole moments these 30, 40 and 50 a.u wurtzite clusters also have quadrupole moments of magnitudes 1170 a.u (1566 Debye Å), 2030 a.u (2740 Debye Å) and 3070 a.u (4144 Debye Å) respectively. These moments are calculated on the basis of the anions and cations of the wurtzite structure having -1 and +1 charges, respectively.

The results for the XY plane are examined for separations between clusters that are the order of 2-3 times the cluster diameter. These relatively large separations are examined first as they are less likely to be influenced by the atomistic detail of the spherical clusters as has been seen previously. However, unlike the preceding zinc blende cluster all clusters are analysed, though the 40 a.u cluster has intentionally been constructed with a relatively small dipole moment compared with the 30 and 50 a.u clusters and as such it acts as a good control comparison to highlight any differences that occur between the clusters as a result of multipole interactions other than the dipole-dipole interactions.

4.2 The XY Plane energy profiles

The 30 a.u, 40 a.u and 50 a.u clusters are analyzed simultaneously by looking at the energy profiles at separations of 70 a.u and 100 a.u for the smaller 30 a.u cluster, 90 a.u and 135 a.u for the 40 a.u cluster and 100 a.u and 150 a.u for the larger 50 a.u cluster. These results are then contrasted by showing the dipole pair profile, being rotated at the same separations. The r0 configuration results for all the clusters are shown along with the dipole pairs (Figure 70).

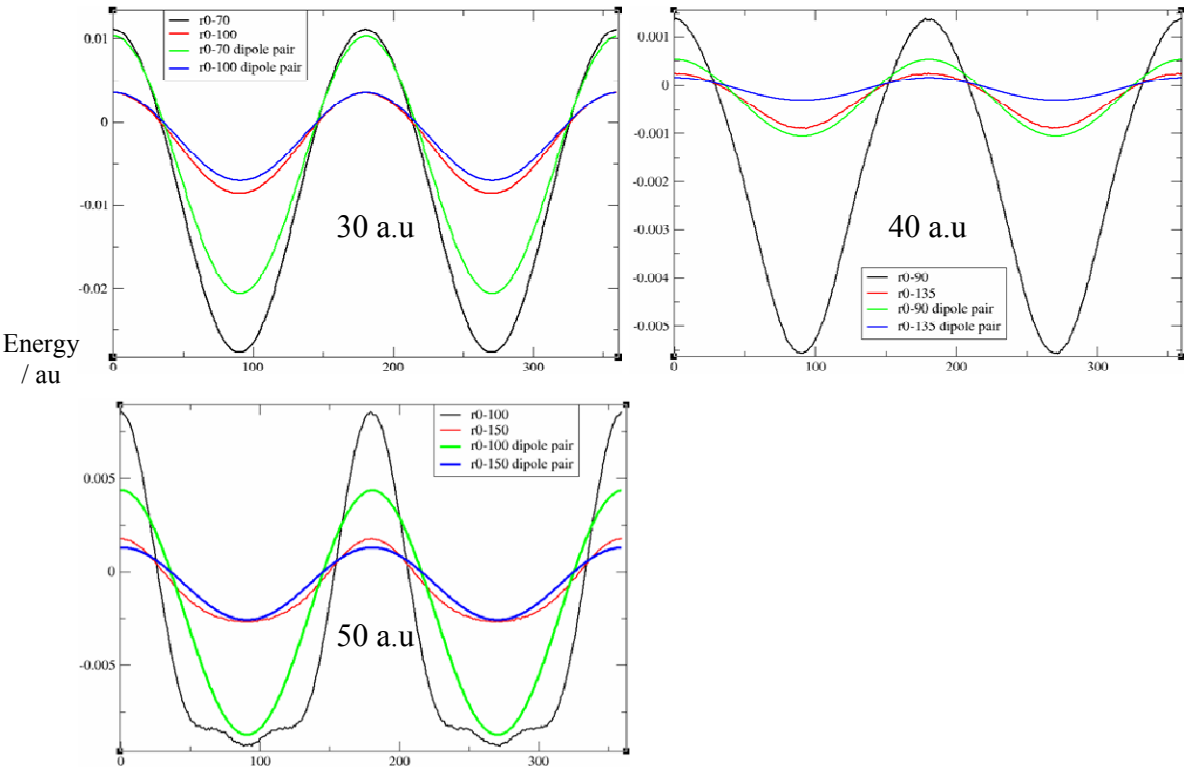

Figure 70 - *Energy profiles for the r0 configuration calculated for the clusters with diameters of 30 a.u (top left), 40 a.u (top right) and 50 a.u (bottom left) respectively, for the smaller 30 a.u cluster energies are calculated at separations of 70 a.u and 100 a.u as indicated in the figure legend, for the 40 a.u unit cluster it is at 90 a.u and 135 a.u and the larger 50 a.u cluster these separations are 100 a.u and 150 a.u respectively. The energies of the equivalent dipole pairs are shown for each cluster for comparison as indicated by the figure legends.*

It is clear from the data at separations that are approximately three times the cluster diameters for the 30 a.u and 50 a.u clusters (100 a.u and 150 a.u of separation respectively). There is very favourable comparison between the atomistic data and the dipoles pairs. However in the case of the 40 a.u cluster at a separation of 135 a.u this is not true as there is a relatively large discrepancy between the two sets of data. Though the 40 a.u cluster is the odd one out again here, it should be noted that the peaks and troughs of the atomistic data all coincide perfectly with the dipole pair data. When the 30 a.u, 40 a.u and 50 a.u clusters are observed at approximately twice their respective diameter separations (70 a.u, 90a.u and 100 a.u respectively) there are now larger differences visible between atomistic and dipole pair data, though this is more

pronounced in the 40 a.u cluster and 50 a.u cluster. In order to understand whether these differences are the result of atomistic detailing of the individual clusters or if multipole interactions are playing a role, the multipole pair breakdown is shown (Figure 71).

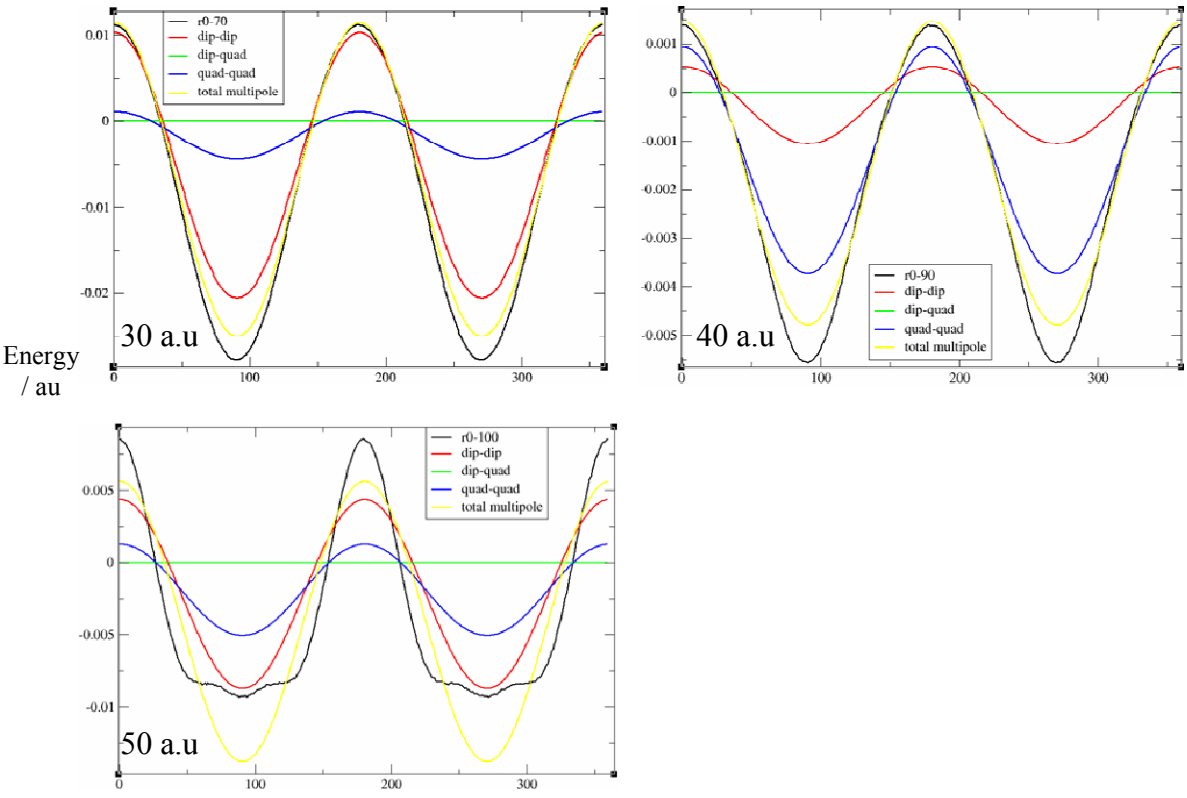

Figure 71 - *Multipole pair profiles for the r0 configuration calculated for the clusters with diameters of 30 a.u (top left), 40 a.u (top right) and 50 a.u (bottom left) at separations of 70 a.u, 90 a.u & 100 a.u respectively. Each figure inset contains the dipole-dipole, dipole-quadrupole and quadrupole-quadrupole interactions energies, as well as the total sum of these forces the total multipole interaction energy. This is directly compared to the atomistic profiles as highlighted by the figure legends.*

The results in Figure 71 show that, in the case of the 30 a.u cluster, the dominating energy contribution comes from the dipole-dipole energy and there is a smaller quadrupole-quadrupole energy component. The 40 a.u cluster is the converse of the 30 a.u cluster, as there is a larger quadrupole-quadrupole contribution relative to the dipole-dipole contribution. The 50 a.u cluster shows the dipole and quadrupole

energies to be similar and hence almost equally contributing in forming the atomistic profiles. The total multipole energies for each individual cluster compare very favourably with the atomistic results in each cluster case and it should be noted that though the dipole and quadrupole contributions vary between the three different clusters they effectively work to augment the dipole energy profile. This simply means these two multipole interactions are in phase with one another and hence the peaks and troughs expected from the parallel and head to tail dipole interactions respectively are in fact supplemented by the quadrupole energies. This increase in the peaks of the troughs has the effect of a bigger energy gap between the repulsive and attractive dipolar configurations; from a self assembly point of view this will increase the probability of forming the head to tail orientations of the nanocrystals in solution as other configurations become energetically less favourable.

The results for the dipolar equivalent r180x and r180z energy profiles alongside the dipolar pair profiles are represented for the 30 a.u (separations of 70 a.u & 100 a.u), 40 a.u (separations of 90 a.u & 135 a.u) and 50 a.u (separations of 100 a.u & 150 a.u) (Figure 72).

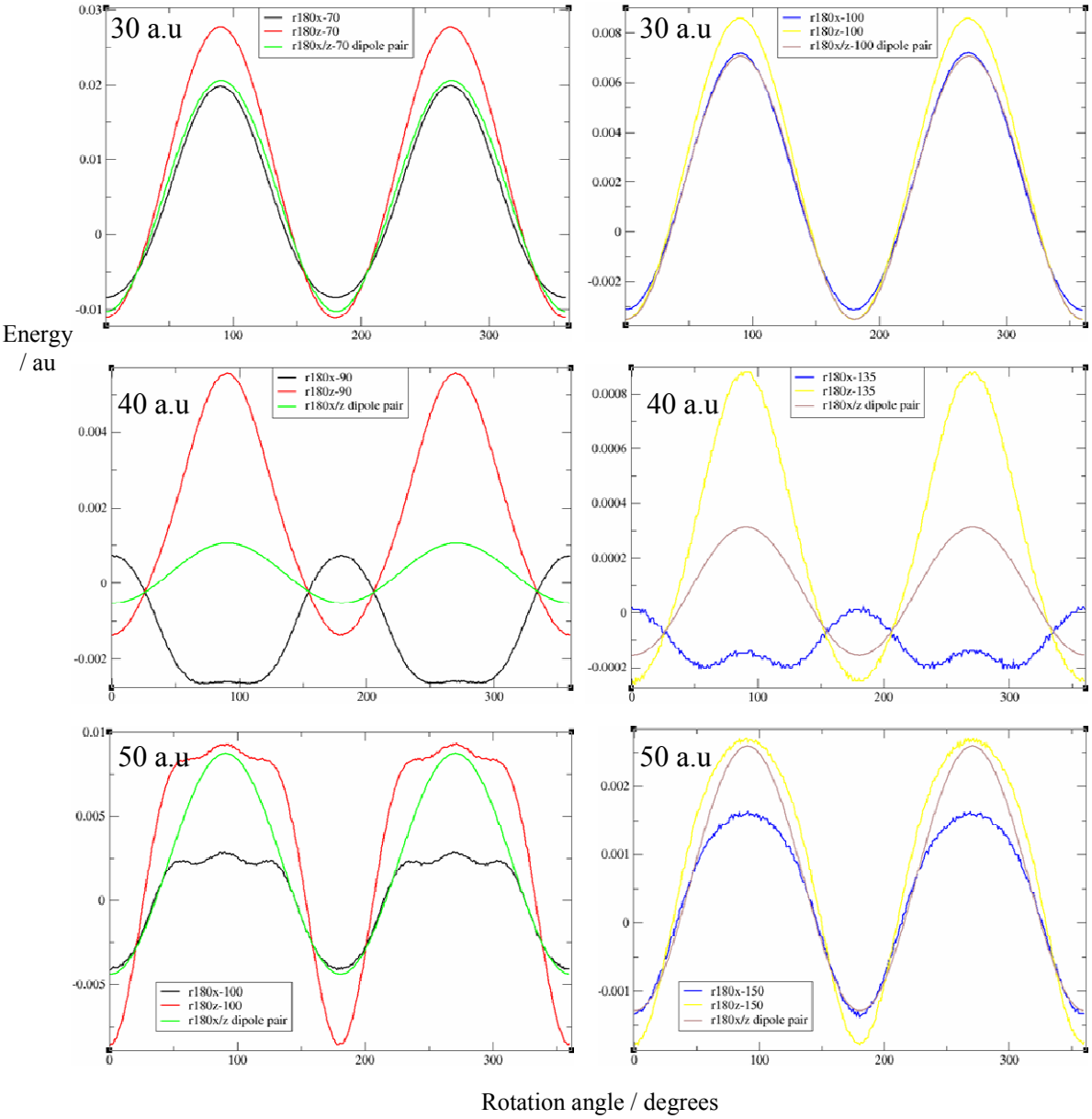

Figure 72 - *Energy profiles for the r180x and r180z configurations calculated for the clusters with diameters of 30 a.u (top), 40 a.u (middle) and 50 a.u (bottom) respectively. Energy profiles are calculated at separations of 70 a.u, 90 a.u and 100 a.u for the 30 a.u, 40 a.u and 50 a.u clusters respectively (left hand figures top to bottom) as well as at separations of 100 a.u, 135 a.u and 150 a.u (right hand figures top to bottom). The energies of the equivalent dipole pairs are shown for each cluster for comparison as indicated by the figure legends.*

Starting with the 30 a.u cluster the data shows very good agreement between the atomistic cluster profiles, the r180x and r180z configurations, and the dipole pairs at both separations of 70 a.u and 100 a.u shown in Figure 72. The r180z configuration tends to have subtly higher peaks and lower troughs relative to the dipole pair and r180x configuration for both separations of 70 a.u and 100 a.u. The 40 a.u cluster shows that the r180x configuration does not compare well to the dipole pairs at either separations of 90 a.u and 135 a.u. These results points to other multipole interactions dominating here; however, there is also a subtle difference between the two separations. There are large flat troughs at 90 degrees and 270 degrees of profile rotation at a separation of 90 a.u, but these troughs at a separation of 135 a.u are altered by the emergence of small peaks. This occurs as a result of the dipole-dipole interaction beginning to dominate at large separations over other multipole interactions. The r180z configuration for the 40 a.u cluster shows peaks and troughs in the expected place relative to the dipole pair profiles, though in both cases they are exaggerated and this is true for both separations of 90a.u and 135 a.u. The relative energy difference between the r180z results and the dipole pair profiles decrease as the separations are increased from 90 a.u to 135 a.u; this again points to the dipole-dipole interaction component becoming more prominent at the larger separation. In the 50 a.u cluster both the r180x and r180z results tend to follow the dipole pair profiles in terms of peaks and troughs, they both show good conformity at the larger separation of 150 a.u. The r180z tends to compare better with the dipole pair relative to the r180x at both separations of 100 a.u and 150 a.u. In general terms it is rather interesting to note how the two clusters with the larger dipole moments, the 30 a.u and 50 a.u clusters, do indeed tend to follow their respective dipole pair profiles quite well, whilst the 40 a.u cluster with the lowest dipole moment is showing obvious signs of other multipole interactions dominating. To determine which multipole interactions are contributing to the atomistic energy profiles here, the multipole breakdown for the r180x and r180z profiles are shown for the 30 a.u cluster (separation of 70 a.u), 40 a.u cluster (separation of 90a.u) and 50 a.u cluster (separation of 100 a.u) (Figure 73).

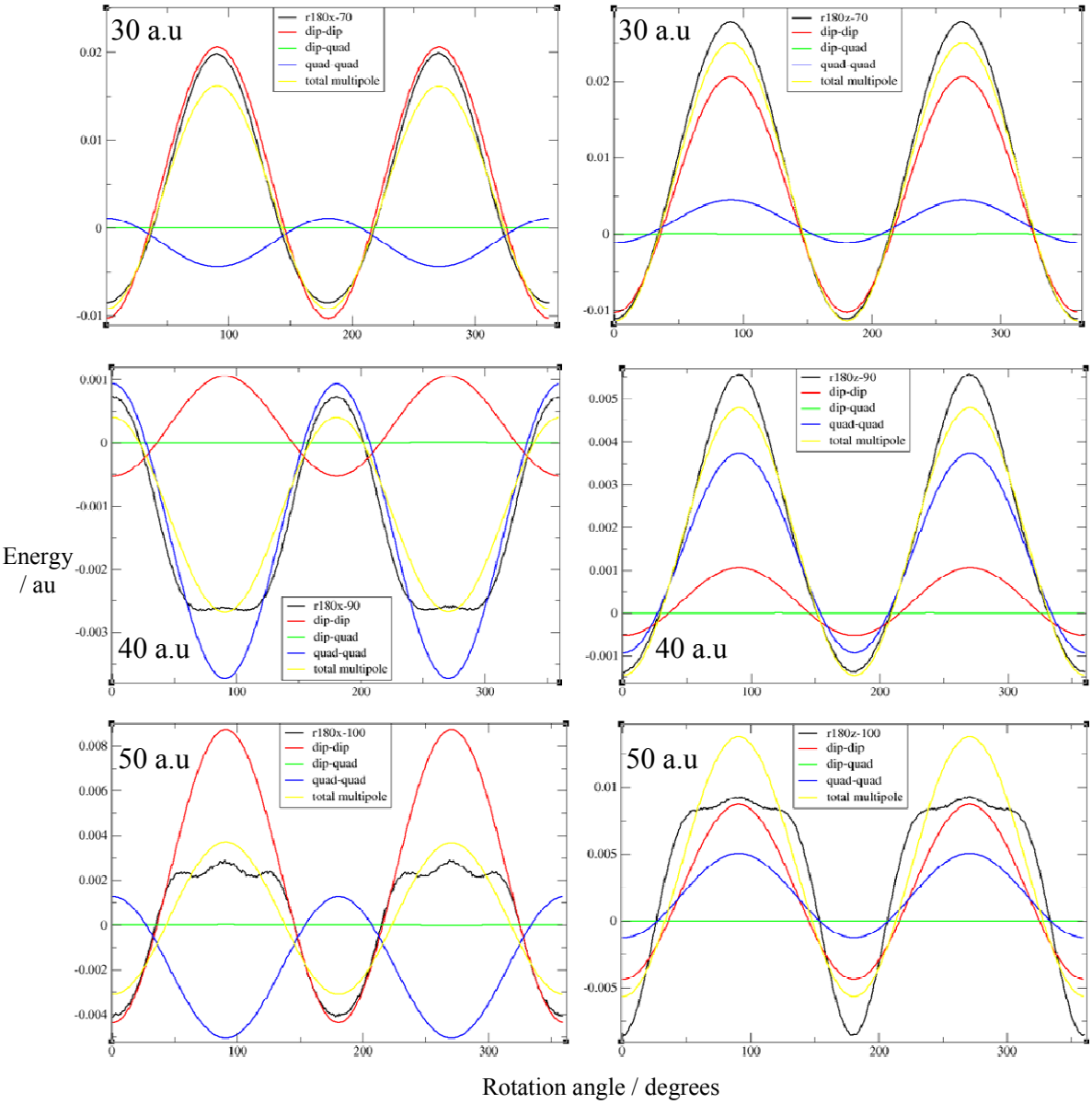

Figure 73 - *Multipole pair profiles for the r180x and r180z configurations calculated for the clusters with diameters of 30 a.u (top), 40 a.u (middle) and 50 a.u (bottom) respectively. Energy profiles are calculated at separations of 70 a.u, 90 a.u and 100 a.u for the 30 a.u, 40 a.u and 50 a.u clusters respectively. The r180x (left hand figures top to bottom) and r180z (right hand figures top to bottom) multipole breakdowns are shown, each figure inset contains the dipole-dipole, dipole-quadrupole and quadrupole-quadrupole interactions energies, as well as the total sum of these forces the total multipole interaction energy. This is directly compared to the atomistic profiles as highlighted by the figure legends.*

The results for the r180z profiles for all three clusters show how the dipole-dipole and quadrupole-quadrupole interactions work to augment one another, leading to the overall profile energy following the expected dipole pair results in terms of peaks and troughs. The r180x multipole breakdown for the three clusters reveals how in fact the dipole and quadrupole interactions are working against one another. The resulting overall multipole energies are dependent on the relative size of the dipole and quadrupole energy interactions in order to determine which force dominates. The 40 a.u cluster has a low a dipole moment relative to the 30 a.u and 50 a.u clusters and this can be seen in Figure 73, where the quadrupole interaction dominates the dipole interaction leading to the overall multipole interaction essentially follow the quadrupole interaction for the 40 a.u cluster. The 30 a.u and 50 a.u clusters have dipole interactions that outweigh quadrupole interactions and hence the overall energy still follows the dipole pair profile.

4.2.1 Repulsive starting configurations

The results at short separations for clusters starting in dipolar repulsive orientations (r0, r45x, r45y, r45z, r90y, r135y & r180y) are shown for the 30 a.u cluster, 40 a.u cluster and 50 a.u cluster at separations of 35 a.u, 45a.u and 55 a.u respectively alongside r0 configuration dipole/multipole pair profiles (Figure 74). The individual energy profiles of different configurations are not the main focus here, it is more important to see in general terms if the energy profiles compare favourably with the dipole and multipole pair profiles. This is true for all subsequent energy profiles at short separations.

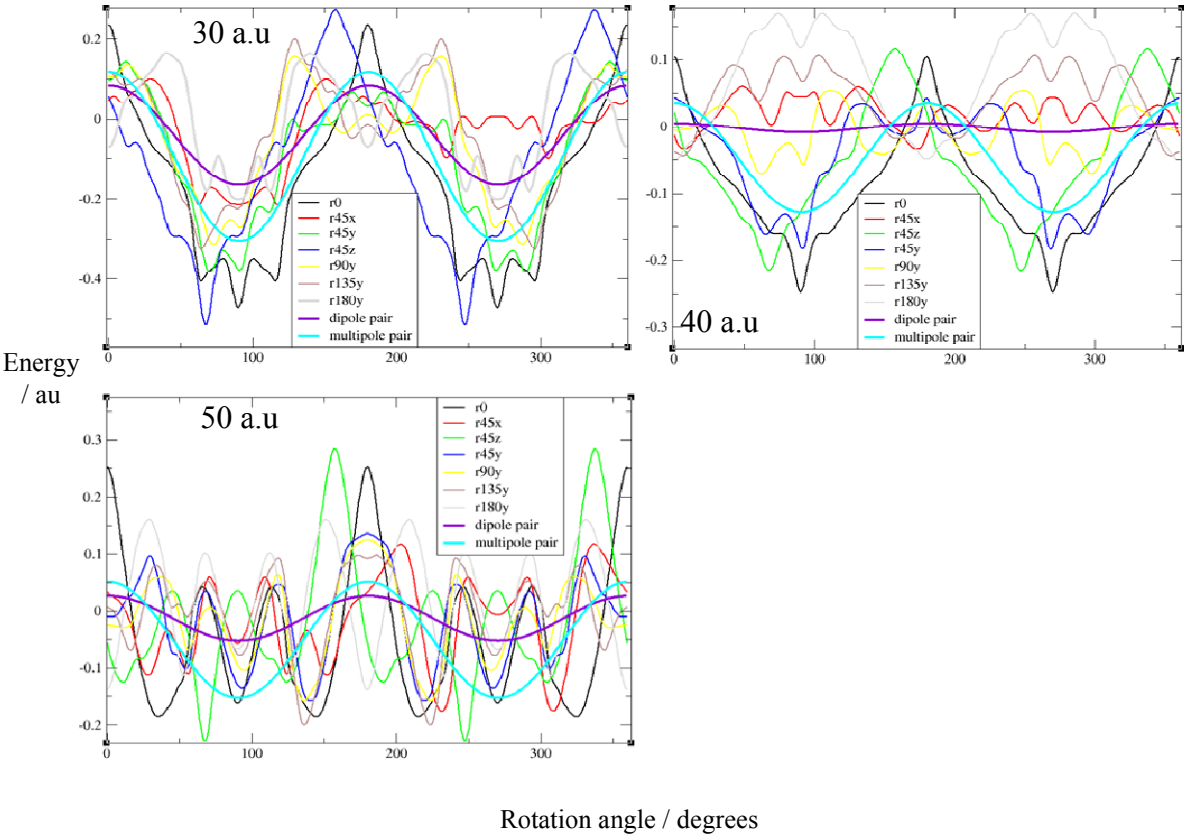

Figure 74 - *Energy profiles, starting configurations beginning in a repulsive dipolar orientation, for the 30 a.u cluster (top left), 40 a.u cluster (top right) and 50 a.u cluster (bottom left) at separations of 35 a.u, 45 a.u and 55 a.u respectively. The dipole pair and multipole energies are calculated for the r0 configurations only, to act as markers for comparison, as indicated by the figure legends.*

The data for the clusters at short separations provide evidence that in general terms the three clusters are following their respective multipole and dipole pair profiles quite well. The 30 a.u cluster tends to show the greatest conformity between the atomistic profiles and the multipole pair profile, with the peak and troughs of the cluster being well defined for all the configurations shown in the figure. The 50 a.u cluster displays similar attributes to the 30 a.u cluster in terms of well defined peaks, however the troughs are not as well defined, none the less in general terms there is good agreement between the atomistic and multipole pair profiles for the 50 a.u cluster. The 40 a.u cluster firstly shows how the dipole pair profile energy is so much smaller than the total multipole pair energy, as a result of the quadrupole energy contribution, but it is also markedly lower relative to the dipole pair profile energies of the 30 a.u and 50 a.u clusters. There is good agreement between the r0, r45y and

r45z atomistic profiles with multipole pair profiles, however as can be seen in the figure as the second atomistic cluster is rotated about the y-axis (r45y, r90y, r135y, & r180y configurations), the energies of the atomistic profile increase on going from the 45y to the r180y configuration and they consequently no longer follow the dipole pair energy profile. These different energy profiles can be explained in terms of quadrupole-quadrupole interactions between the clusters using a simplified model, in which the quadrupole within a cluster is represented as a square net made up of two cations and two anions. The quadrupole interactions are shown at 90 or 270 degrees of profiles rotation, as this is where the greatest change is visible for the 40 a.u cluster in Figure 74, for the r0, r90y and r180y configurations (Figure 75).

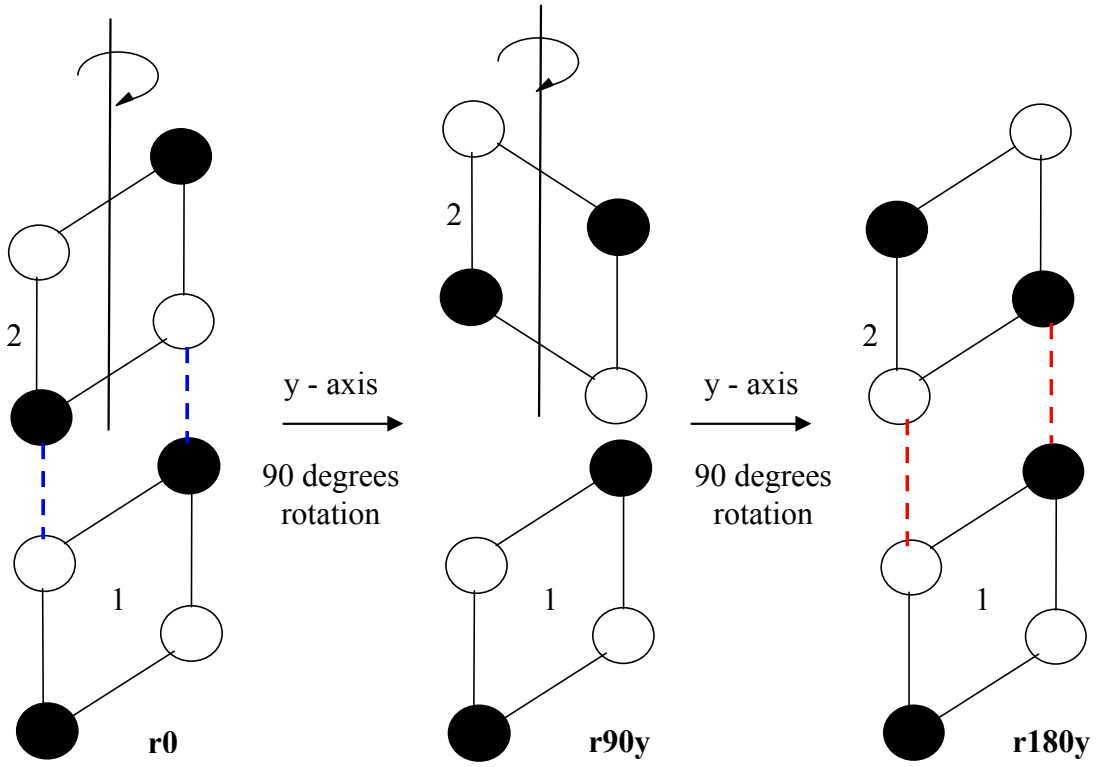

Figure 75 - *Simple quadrupole profiles for the 40 a.u cluster, depicting the effects of a y-axis rotation of the second cluster at 90 or the equivalent 270 degrees of profile rotation. On going from left to right in figure the second quadrupole, representing the cluster, is rotated about the y-axis resulting in the energy going from attractive for the r0 configuration to neutral for the r90y configuration to finally repulsive as the r180y configuration is reached. The blue dashed lines indicate attractive interactions, while the red dashed lines indicate repulsive interactions.*

The figure above of two clusters, in terms of a square net quadrupole, shows how the energy of the clusters can be affected by rotations of the second cluster about the y-axis. The important thing to note is that the r0 configuration is attractive whilst the r180y configuration is repulsive; this helps to explain the stepwise increases in energy seen in Figure 74 for the 40 a.u cluster on going from the r0 to the r180y configuration. The red and blue dashed lines help to indicate the dominating atomistic repulsive and attractive interactions respectively that determine the overall quadrupole energy. The r90y configuration falls between the r0 and r180y configuration and hence it is neutral in energy terms as proved by Figure 74, where the r90y profile oscillates about zero energy.

4.2.2 Attractive starting configurations

The results at short separations for clusters starting in dipolar attractive orientations (r135x, r180x, r135z & r180z) are shown for the 30 a.u cluster, 40 a.u cluster and 50 a.u cluster at separations of 35 a.u, 45a.u and 55 a.u respectively alongside dipole/multipole pair profiles (Figure 76).

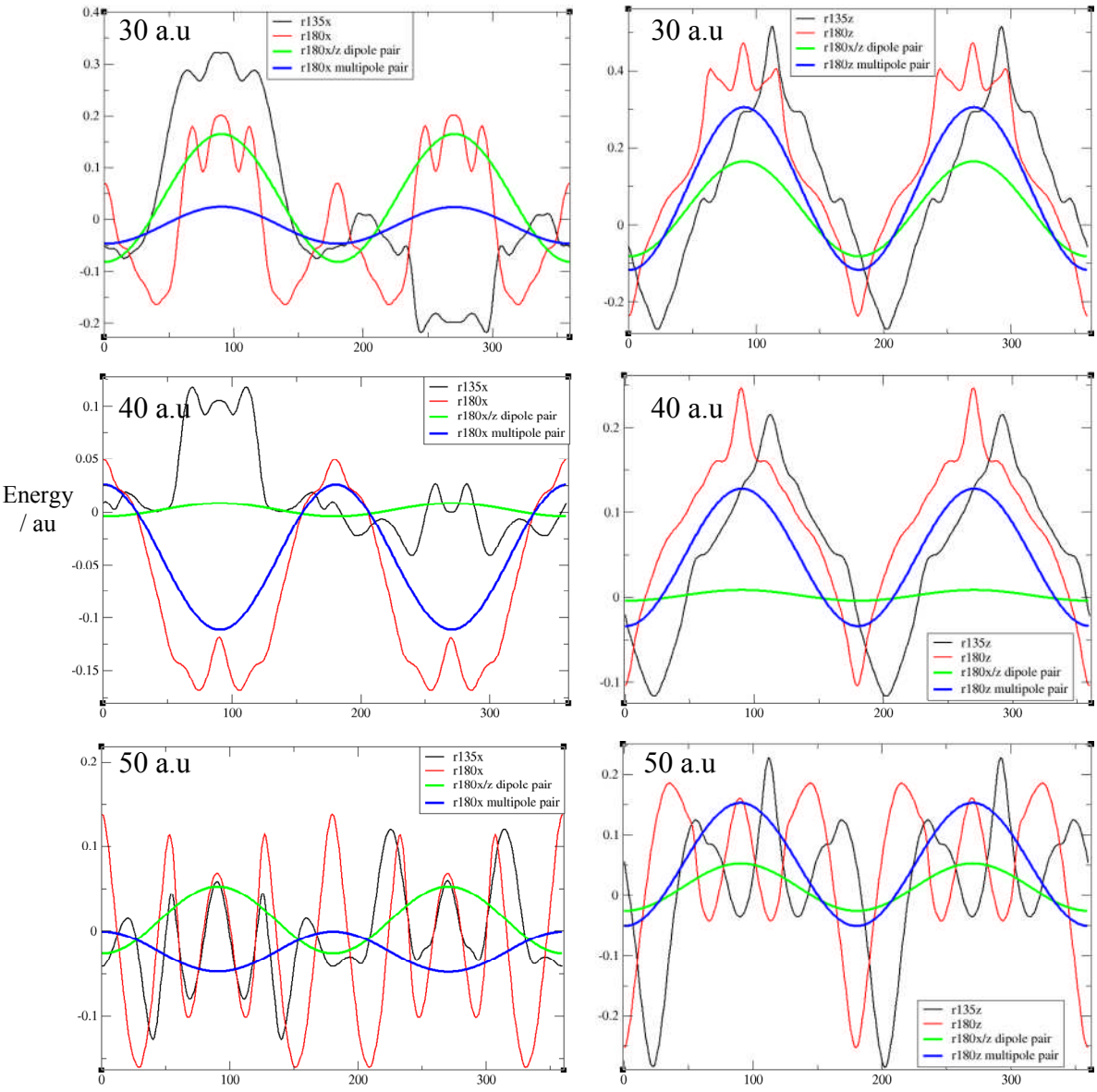

Figure 76 - *Energy profiles, starting configurations beginning in an attractive dipolar orientation, for the 30 a.u cluster (top row), 40 a.u cluster (middle row) and 50 a.u cluster (bottom row) at separations of 35 a.u, 45 a.u and 55 a.u respectively. The atomistic profiles for the dipolar equivalent r135x, r180x (all left hand figures), r135z and r180z (all right hand figures) are shown, the dipole pair and multipole pair energies are calculated for the r180x configuration (left figures) and the r180z configuration (right figures) only, to act as markers for comparison, as indicated by the figure legends.*

The results for the r135z and r180z configurations show very good agreement between atomistic profiles and the multipole pair profiles, as has previously been shown in Figure 73 the multipole pair profile is the sum of the dipole and quadrupole energies; however the same is not quite true for the r135x and r180x atomistic profiles. The results for the r135x and r180x configurations show a range of results in terms of the peaks or troughs that occur at 90 and 270 degrees or profile rotation. For the 30 a.u cluster the results are conforming in general terms to the multipole and dipole pair profiles and as a result there are atomistic peaks at 90 and 270 degrees of profile rotation. The 40 a.u cluster with its low dipole moment shows that the quadrupole moment is essentially dominating the total multipole energy profile and as such there are now troughs at 90 and 270 degrees of profile rotation. The 50 a.u cluster in contrast to the 40 a.u and 30 a.u clusters only shows a slight preference to the quadrupole-quadrupole interaction as the overall multipole energy oscillates close to zero and as such the atomistic profile shows no real adherence to either the dipole or multipole pair profiles. The r135z and r180z configuration results all show peaks occurring, indicating strongly repulsive interactions, at 90 and 270 degrees of profile rotations for all three clusters at these short separations. Though the 50 a.u cluster shows a greater degree of oscillation, due to a larger number of surface atoms relative to the two smaller clusters and hence greater atomistic energy contribution, in relative terms the oscillations about 90/270 degrees can be considered peaks when compared to the large toughs that occur at 0/180 degrees of profile rotation. The good agreement between the atomistic and multipole pair profiles result from the effects of the dipole-dipole and quadrupole-quadrupole interactions working together to augment each others interactions unlike the results for the r135x and r180x configurations where the two interactions are opposing one another, these results can be explained via simple square net dipole model of the clusters for the r180x and r180z configurations at 90/270 degrees of profile rotation (Figure 77).

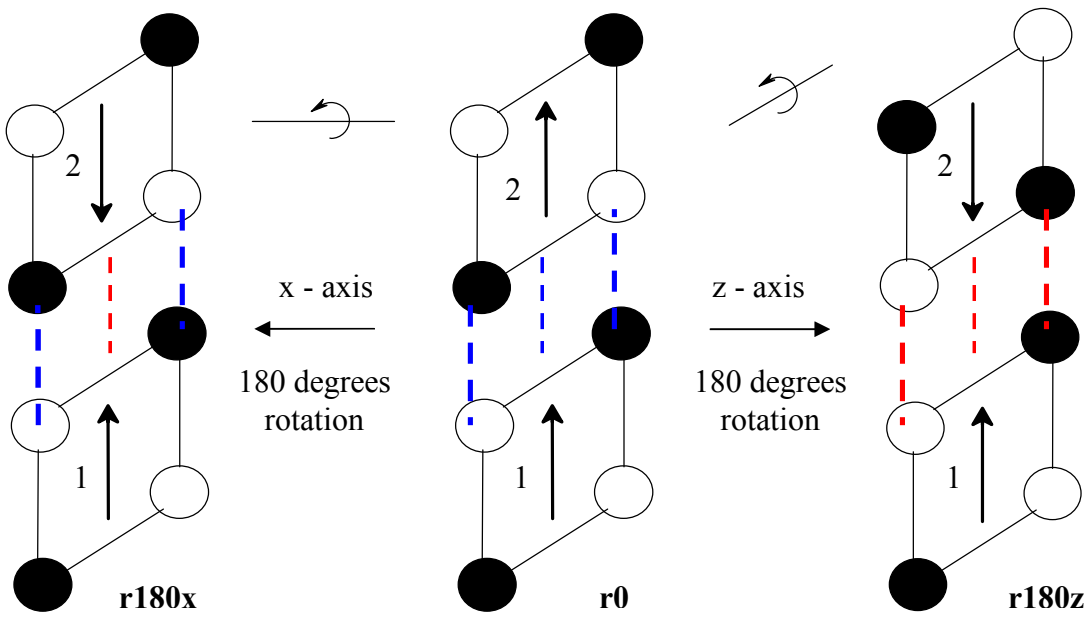

Figure 77 - *Simple dipole and quadrupole profiles for the r180x and r180z configurations, depicting the effects of the different configurations at 90 or the equivalent 270 degrees of profile rotation. The central figure shows the r0 configuration, which acts to highlight the difference between the r180x (left figure) and r180z (right figure) configurations. The blue dashed lines indicate attractive interactions, while the red dashed lines indicate repulsive interactions.*

The simplified depiction of the clusters in terms of a dipole and square net quadrupole, show how the r180x configuration results in a repulsive interaction between the dipoles of the two clusters yet the quadrupole interactions between the two are attractive. The overall effect of these two interactions depends on the relative strength of each interaction, with the dominant of the two being able to determine the overall energy profile of the cluster. In the case of the 30 a.u cluster the dipole interaction dominates and hence large repulsive peaks are seen at 90/270 degrees of profile rotation, similarly the 40 a.u cluster has large troughs at the same angle of profile rotation as in this case the quadrupole interaction out weighs the dipole interaction. The 50 a.u cluster shows the effects of approximately equal dipole and quadrupole interactions. This can be contrasted with the r180z profile depicted in figure 9, as it clearly shows the dipole and quadrupole interactions working together to result in repulsive interactions at 90/270 degree of profile rotation.

4.2.3 Neutral starting configurations

The results at short separations for clusters starting in dipolar neutral orientations (r90x & r90z) are shown for the 30 a.u cluster, 40 a.u cluster and 50 a.u cluster at separations of 35 a.u, 45a.u and 55 a.u respectively, additionally multipole pair profiles are also shown (Figure 78).

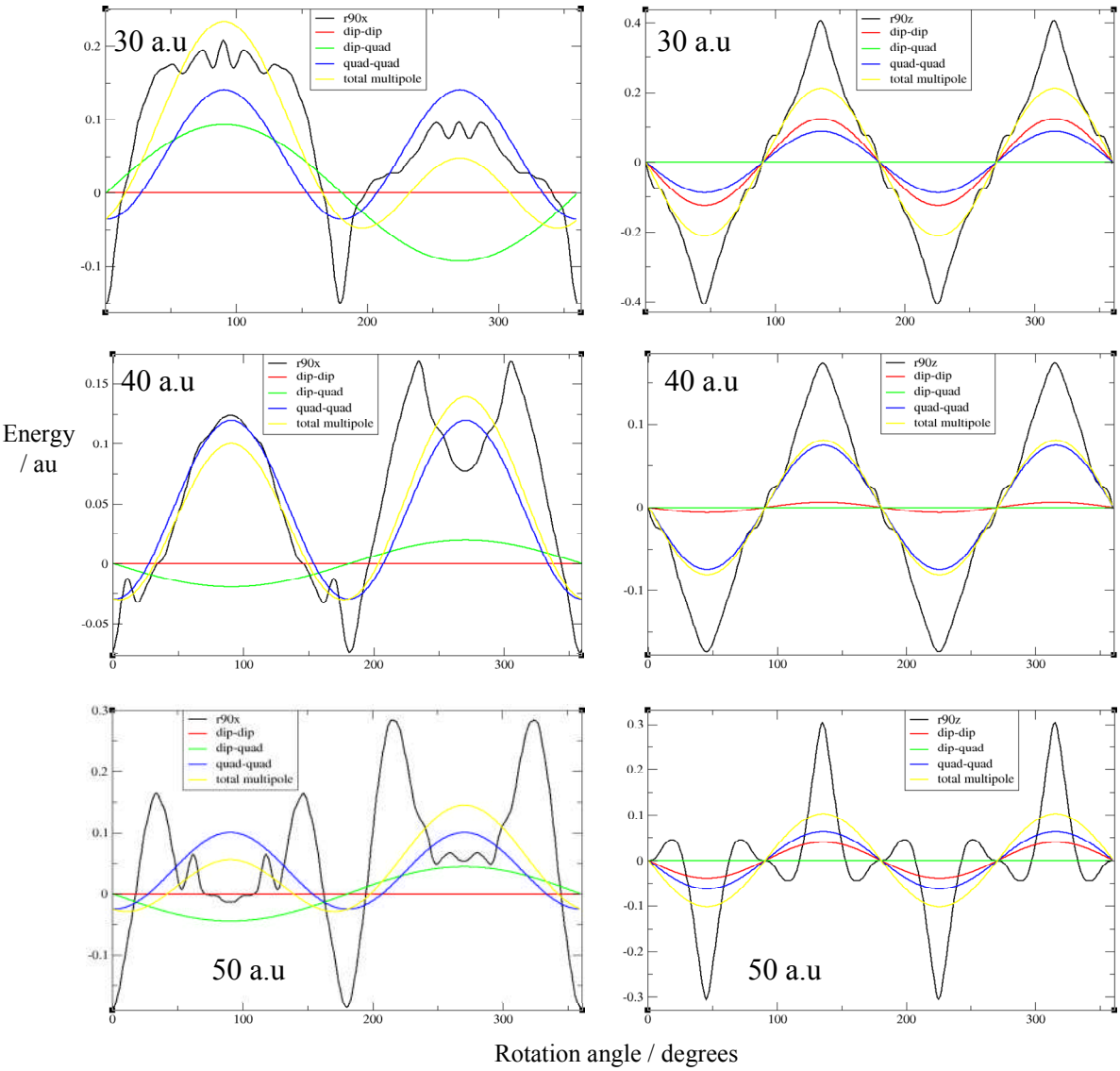

Figure 78 - *Energy profiles, starting configurations beginning in a neutral dipolar orientation, for the 30 a.u cluster (top row), 40 a.u cluster (middle row) and 50 a.u cluster (bottom row) at separations of 35 a.u, 45 a.u and 55 a.u respectively. The atomistic profiles for the r90x (left hand figures) and r90z (right hand figures) configurations are shown, the dipole pair and multipole pair profiles are calculated for each of the configurations as highlighted by the figure legends.*

The results for the neutral starting configurations shows, in the case of the r90z configurations, how the dipole-dipole and quadrupole-quadrupole interactions work concurrently to form peaks at 135/315 degrees of profile rotation and troughs at 45/225 degrees of profile rotation. The atomistic profile of the r90z compares favourably with total multipole pair profile in terms of the position of peaks and troughs, though the magnitude of the troughs and peaks are lower and higher respectively. This holds true for all three sized clusters and this can once again be attributed to the atomistic surfaces of the clusters being closer together than the indicated separations for the profiles and as such this results in enhanced responses in the atomistic energy profiles. There are also subtly more oscillations visible in the larger 50 a.u cluster relative to the smaller 30 a.u and 40 a.u clusters, this would be expected as there are more surface atoms on the larger cluster and this translates to greater oscillations in the atomistic energy profiles as it is essentially also mapping the surface of the cluster. The r90x configuration results generally show good agreement with multipole pair profiles and unlike the r90z profile there is no dipole-dipole contribution, though there is an additional dipole-quadrupole interaction between the clusters. The additional interaction can be seen to be identical in shape for the 40 a.u and 50 a.u clusters, but this is opposite to the 30 a.u cluster. This can be simply explained as the consequence of the starting r0 configuration of the clusters and the direction of dipole moments either being positive or negative (Figure 79). The diagram shows the first cluster in terms of a central dipole surrounded by a square net, which represents the quadrupole moment, the second cluster is represented as an atomistic dipole moment for simplicity to highlight the dipole-quadrupole interaction clearly between the clusters. The starting r0 configurations show how the clusters can have either a positive (arrows pointing upwards) or negative (arrows pointing downwards) dipole moment. The r90x configurations that result are dependent on the starting configurations and as such the atomistic profiles that are formed consequently will differ only at the points where the dipole quadrupole interaction energies are repulsive or attractive at profile angles of 90 and 270 degrees. The left hand diagrams depict the 30 a.u cluster, whilst the right hand diagrams in figure 10 portray the 40 a.u and 50 a.u clusters.

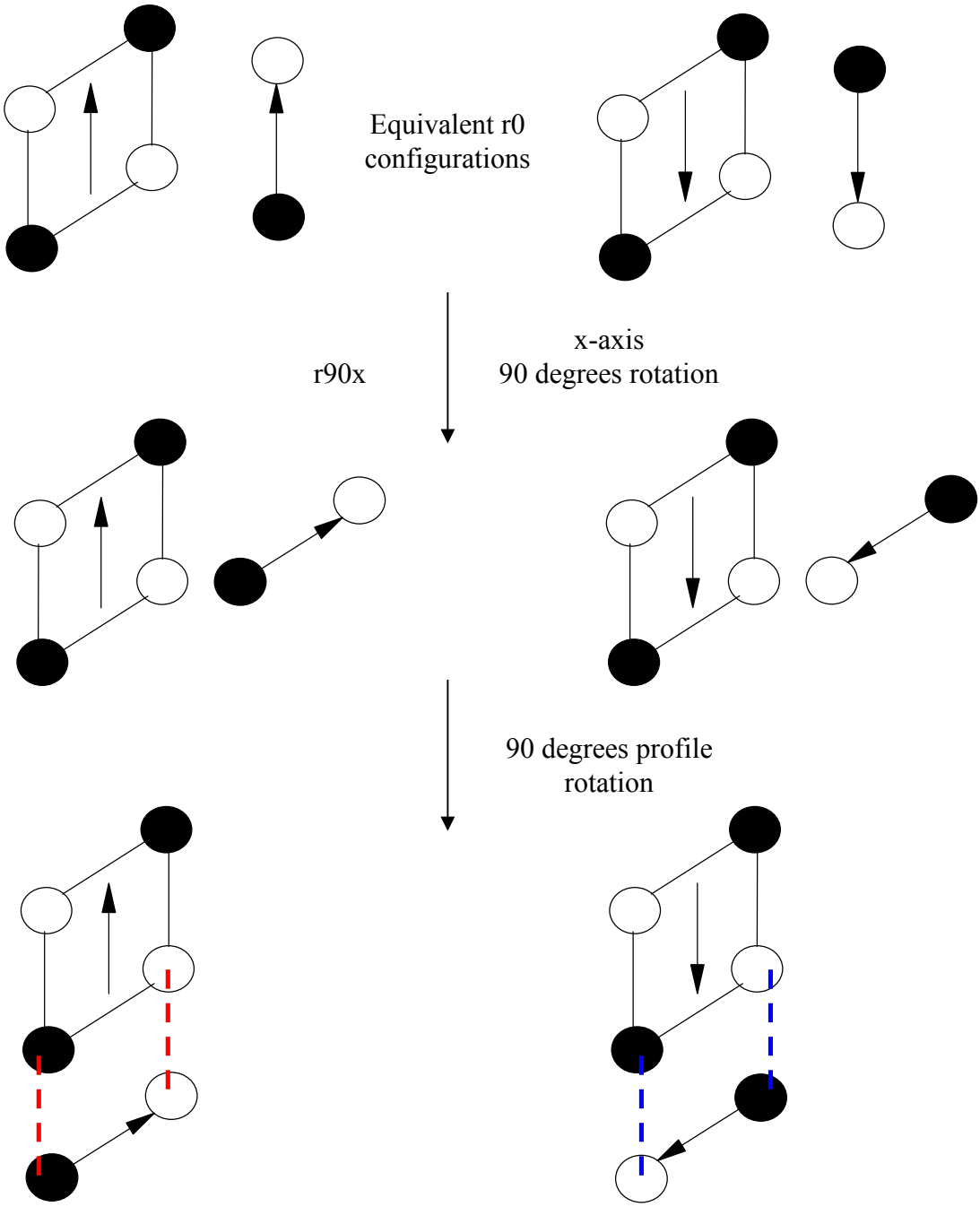

Figure 79 - *Equivalent dipole and quadrupole profiles for the r90x configuration, depicting the effects of the subtly different starting r0 configurations on the resulting energy profiles at 90 degrees of profile rotation in terms of the dipole-quadrupole interaction only. The top figures shows the energy equivalent r0 configurations, which acts to highlight the difference between the resulting r90x (middle figures) configurations. The resulting energy profiles at 90 degrees of rotation have either blue dashed lines to indicate attractive interactions or red dashed lines indicate repulsive interactions.*

4.3 The XZ plane energy profiles

The results for the XZ plane are now examined. In this configuration, the different dipole orientations of the cluster should result in constant dipolar energy as the cluster dipole orientations are fixed for the duration of the rotation about the XZ plane. The larger separation results, 2-3 times the cluster diameter, are first examined for the different clusters. The r0 configurations for the three clusters of interest are shown for the 30 a.u (separations of 70 & 100 a.u), 40 a.u (separations of 90 & 135 a.u) and 50 a.u (separations of 100 a.u & 150 a.u) clusters (Figure 80).

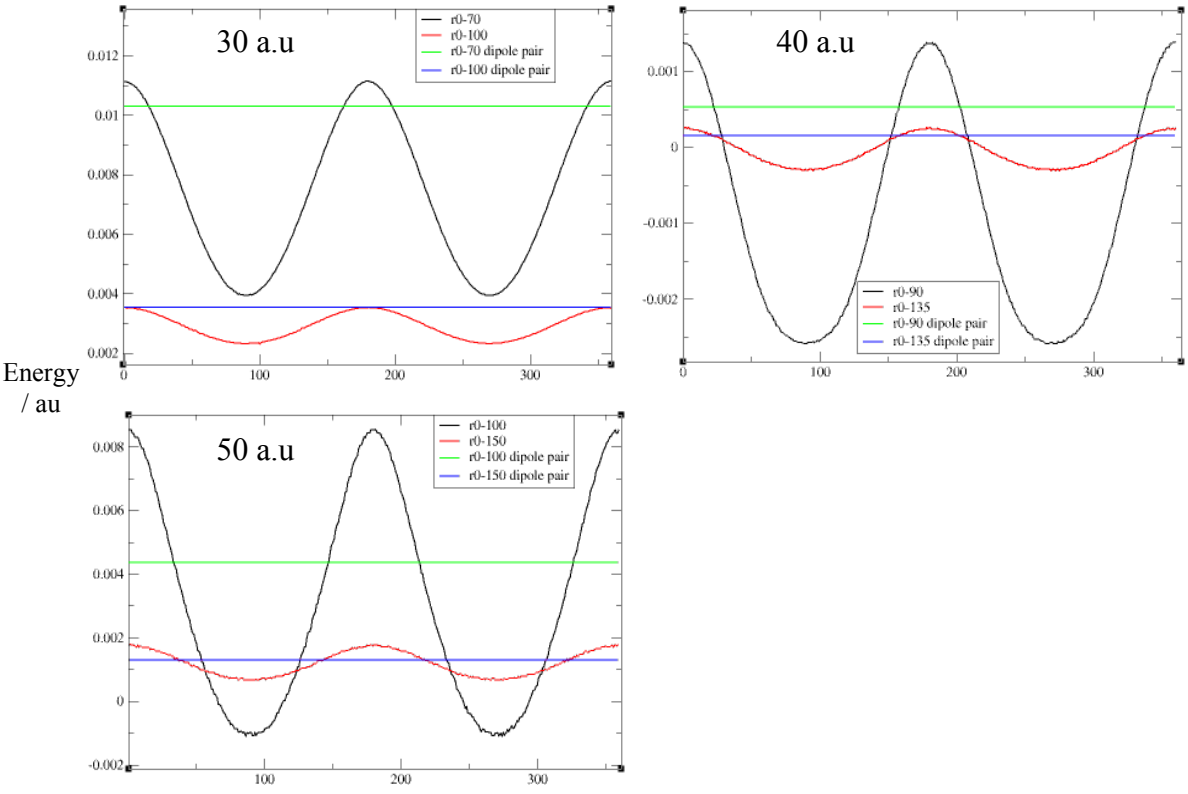

Figure 80 - *Energy profiles for the r0 configuration calculated for the clusters with diameters of 30 a.u (top left figure), 40 a.u (top right figure) and 50 a.u (bottom left figure) respectively, for the smaller 30 a.u cluster energies are calculated at separations of 70 a.u and 100 a.u as indicated in the figure legend, for the 40 a.u cluster these separations are 90 a.u and 135 a.u respectively and for the 50 a.u cluster the separations are 100 a.u and 150 a.u. The energies of the equivalent dipole pairs are shown for comparison as indicated by the figure legends.*

The r0 configuration results show firstly that the atomistic profiles are oscillating close to the anticipated dipole pair profiles for all the clusters at both the separations shown for each individual cluster. These atomistic oscillations tend to decrease in magnitude for all the clusters when the separations increase from approximately twice the cluster diameter (black lines in Figure 80) to three times the cluster diameters (red lines in Figure 80), though the positions of the peaks and troughs in terms of profile rotation angles remain the same. These relatively large oscillations are not random in nature and are most likely the result of the quadrupole-quadrupole interactions between the clusters, this is confirmed by examining the multipole interaction breakdown for the 30 a.u (separation of 70 a.u), 40 a.u (separation of 90 a.u) and 50 a.u (separation of 100 a.u) clusters (Figure 81).

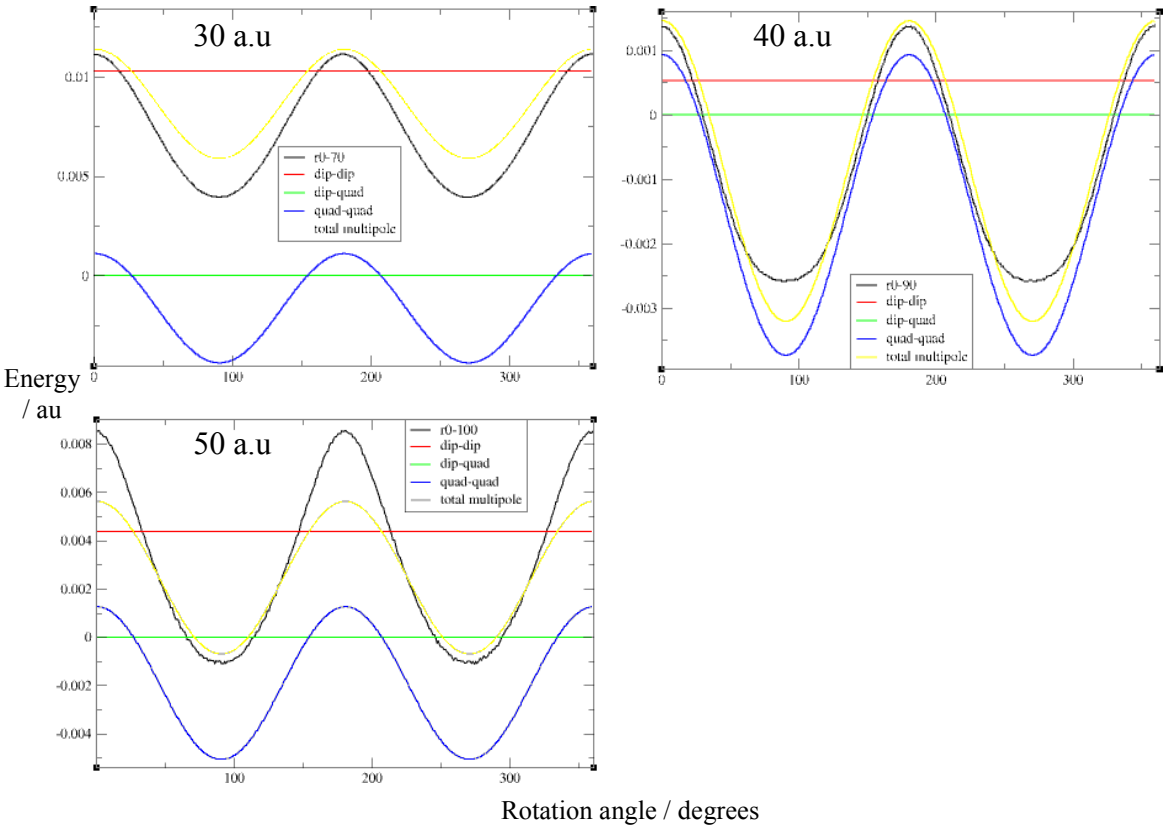

Figure 81 - *Multipole pair profiles for the r0 configuration calculated for the clusters with diameters of 30 a.u (top left), 40 a.u (top right) and 50 a.u (bottom left) at separations of 70 a.u, 90 a.u & 100 a.u respectively. Each figure inset contains the dipole-dipole, dipole-quadrupole and quadrupole-quadrupole interactions energies, as well as the total sum of these forces the total multipole interaction energy. This is directly compared to the atomistic profiles as highlighted by the figure legends.*

The multipole breakdown energies do indeed illustrate that the atomistic profiles of the three clusters is the result of quadrupole-quadrupole interactions between clusters. There is however subtle discrepancies between the atomistic and multipole pair profiles and these can be attributed to the atomistic detailing of the clusters as has been the case previously for the zinc blende clusters. There is no dipole-quadrupole interaction between any of the clusters according to the multipole pair profiles for all three sized clusters. This can be attributed to attractive and repulsive dipole-quadrupole interactions between clusters in equal measure, such that the two interactions cancel one another out. This is illustrated with a simple depiction of the clusters as dipoles surrounded by a square net quadrupole (Figure 82).

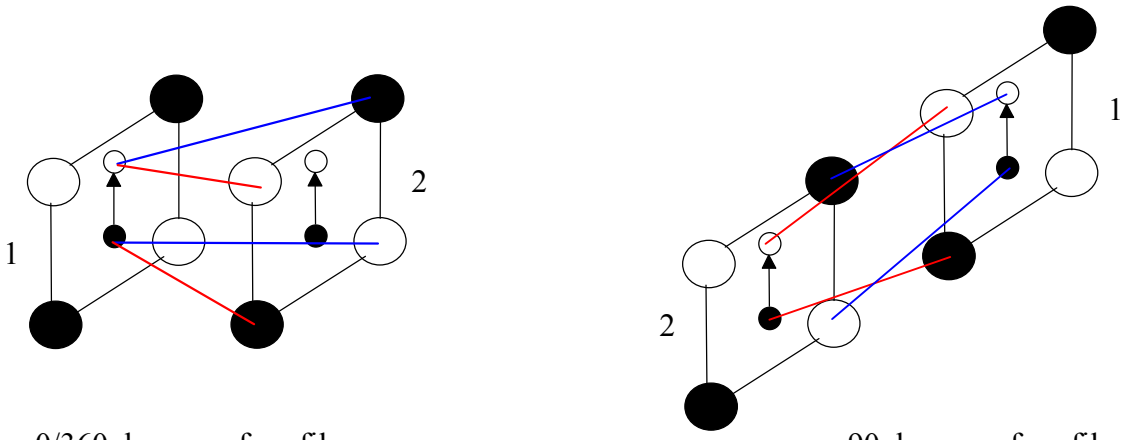

0/360 degrees of profile rotation

90 degrees of profile rotation

Figure 82 - *The depiction of dipole-quadrupole interactions between clusters in the r0 configuration. The left figure shows the two clusters in the starting configuration. The dipole-quadrupole interaction between cluster 1 and cluster 2 is highlighted and there are equally attractive and repulsive interactions that cancel one another out. The right figure highlights the same clusters, but this time at a profile rotation of 90 degrees. There are again attractive and repulsive interactions in equal measure between the two clusters leading to a cancellation of energies. The attractive interactions are highlighted in blue and repulsive interactions in red.*

The dipolar equivalent r180x and r180z profiles are examined concurrently for the 30 a.u (separations of 70 & 100 a.u), 40 a.u (separations of 90 & 135 a.u) and 50 a.u (separations of 100 a.u & 150 a.u) clusters (Figure 83).

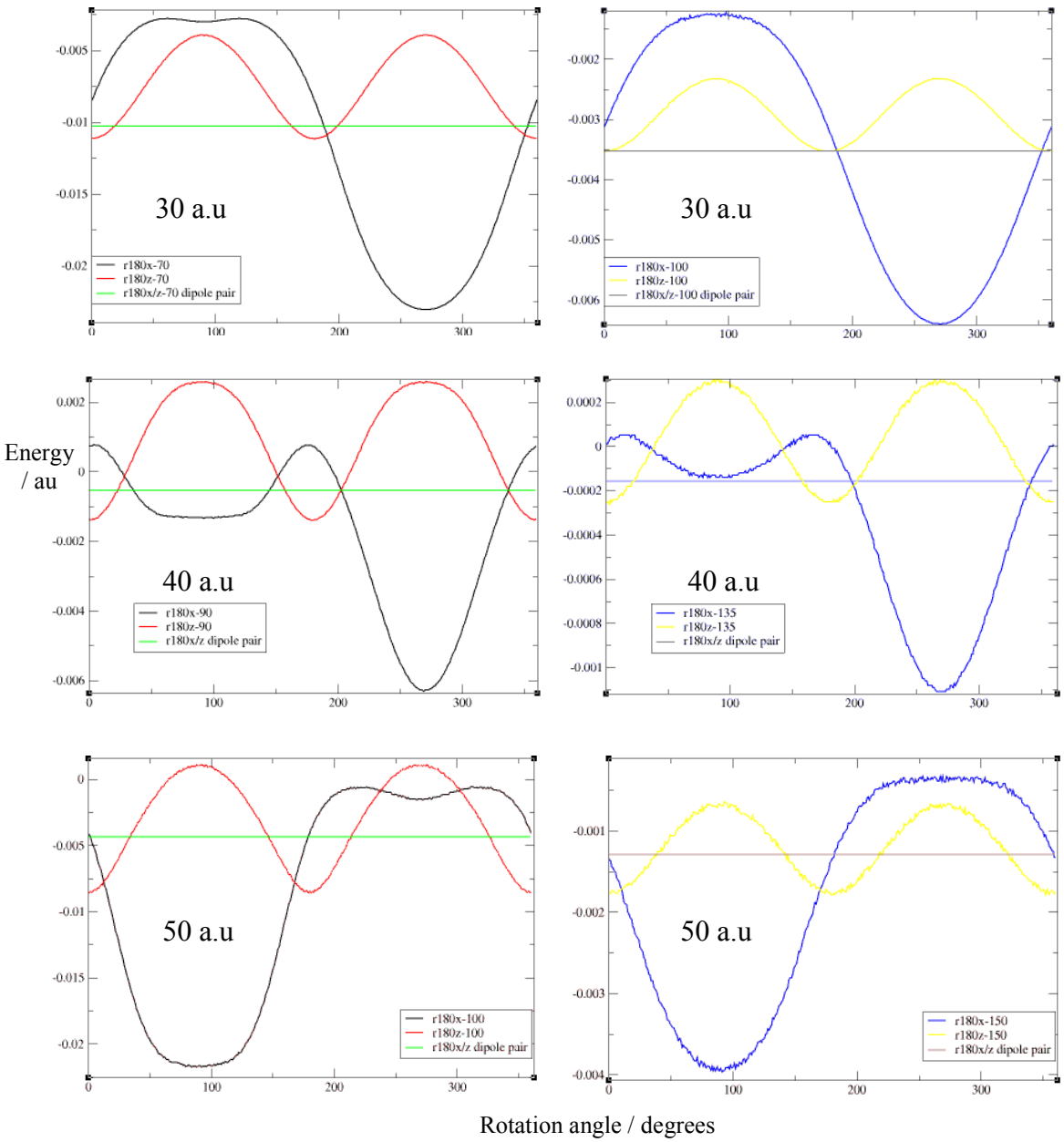

Figure 83 - *Energy profiles for the r180x and r180z configurations calculated for the clusters with diameters of 30 a.u (top), 40 a.u (middle) and 50 a.u (bottom) respectively. Energy profiles are calculated at separations of 70 a.u, 90 a.u and 100 a.u for the 30 a.u, 40 a.u and 50 a.u clusters respectively (left hand figures top to bottom) as well as at separations of 100 a.u, 135 a.u and 150 a.u (right hand figures top to bottom). The energies of the equivalent dipole pairs are shown for each cluster for comparison as indicated by the figure legends.*

The data reveals that the two dipolar equivalent orientations do not result in the same atomistic profiles for all three clusters as the r180z profiles are symmetric in shape whilst the r180x profiles are asymmetric in shape, though both the r180x and r180z

atomistic profiles are oscillating close to their respective dipole pair profiles. These asymmetric shapes in atomistic profiles are an indication of the presence of dipole-quadrupole interactions, whilst the symmetric shapes in the atomistic profiles indicate the existence of quadrupole-quadrupole interactions in the clusters. The multipole breakdown for the 30, 40 and 50 a.u clusters, at separations of 70 a.u, 90 a.u and 100 a.u respectively, are revealed (Figure 84).

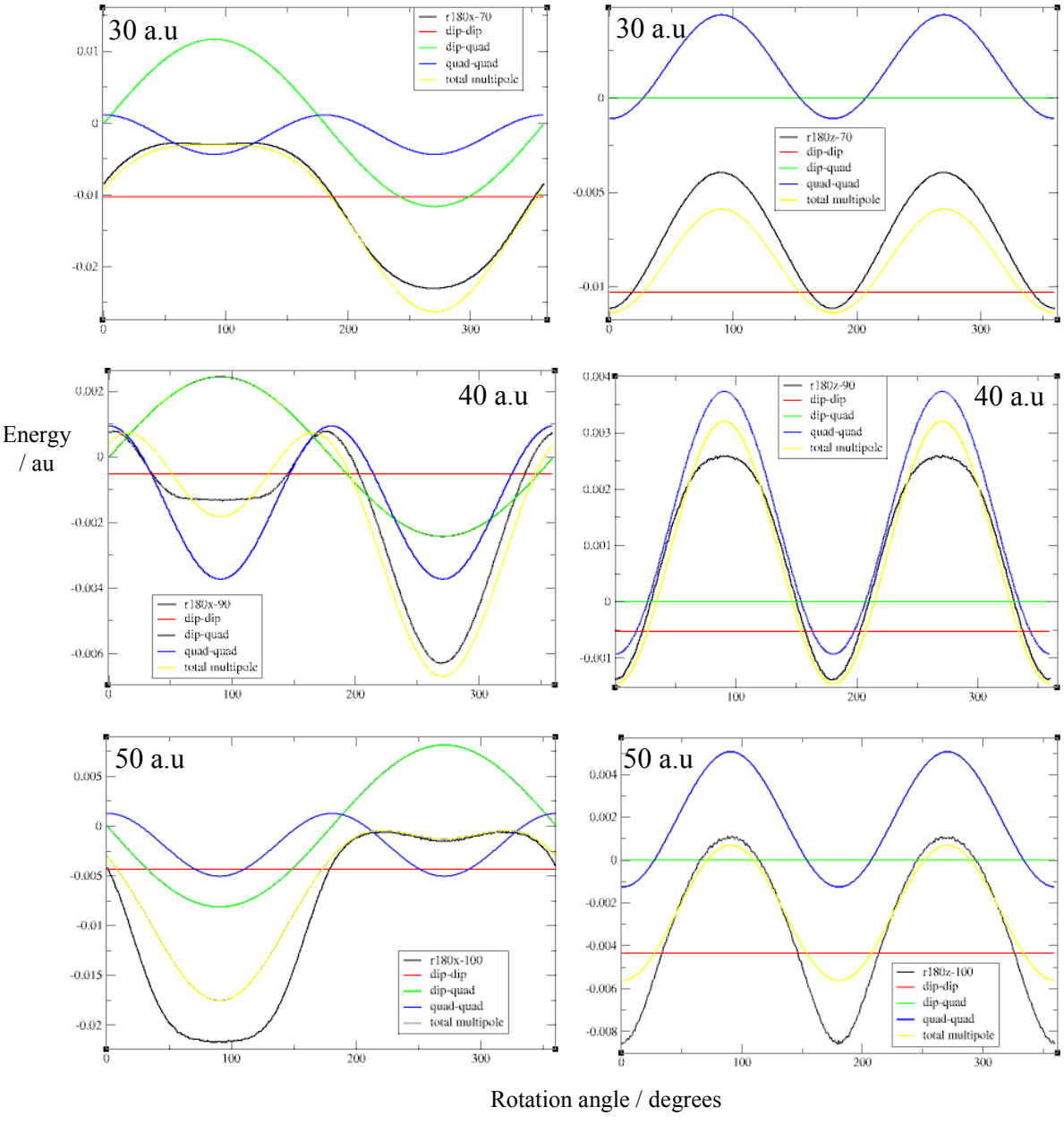

Figure 84 - *Multipole pair profiles for the r180x and r180z configurations calculated for the clusters with diameters of 30 a.u (top), 40 a.u (middle) and 50 a.u (bottom) respectively. Energy profiles are calculated at separations of 70 a.u, 90 a.u and 100 a.u for the 30 a.u, 40 a.u and 50 a.u clusters respectively. The r180x (left hand figures*

top to bottom) and r180z (right hand figures top to bottom) multipole breakdowns are shown, each figure inset contains the dipole-dipole, dipole-quadrupole and quadrupole-quadrupole interactions energies, as well as the total sum of these forces the total multipole interaction energy. This is directly compared to the atomistic profiles as highlighted by the figure legends.

The multipole pair profiles for the r180x configuration clearly show the presence of both dipole-quadrupole and quadrupole-quadrupole interactions for all the clusters. The 40 a.u cluster has a larger quadrupole-quadrupole interaction component relative to the 30 and 50 a.u clusters and this can be seen at 270 degrees of profile angle rotation where the quadrupole-quadrupole minima is less than the dipole-quadrupole component. The total multipole pair energies for each of the three clusters have favourable comparisons with the atomsitc data, though the largest 50 a.u cluster shows some difference between the atomistic data and the multipole pair energies at approximately 90 degrees of profile rotation and this can be largely attributed to atomistic detailing of the cluster. The r180z data shows only the presence of quadrupole interactions for all the clusters with the multipole data matching up to the atomistic data well, though again small discrepancies in terms of peak and trough heights exist and likely to be the result of atomistic detailing of the clusters.

4.3.1 Repulsive starting configurations

The results at short separations for clusters starting in dipolar repulsive orientations (r0, r45x, r45y, r45z, r90y, r135y & r180y) are shown for the 30 a.u , 40 a.u and 50 a.u cluster at separations of 35 a.u, 45a.u and 55 a.u respectively alongside r0 configuration dipole/multipole pair profiles (Figure 85). Once again the analyses of the short separation energy profiles is to establish whether in general terms that the varying energy profiles show conformity to the dipole and multipole pair profiles. This is also true for subsequent short separation energy profiles examined.

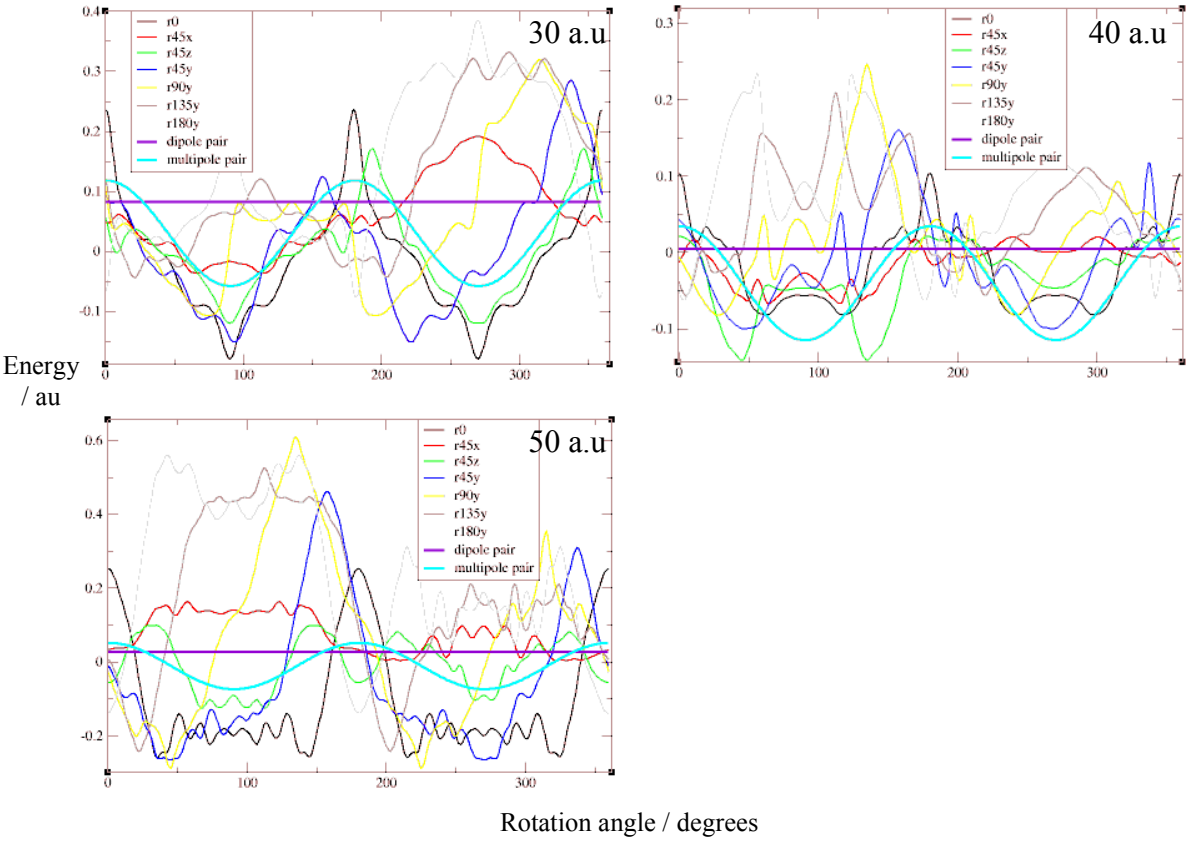

Figure 85 - *Energy profiles, starting configurations beginning in a repulsive dipolar orientation, for the 30 a.u cluster (top left), 40 a.u cluster (top right) and 50 a.u cluster (bottom left) at separations of 35 a.u, 45 a.u and 55 a.u respectively. The dipole pair and multipole pair energies are calculated for the r0 configurations only, to act as markers for comparison, as indicated by the figure legends.*

The atomistic data of all three clusters indicates a good comparison with their respective dipole pair profiles as all atomistic results oscillate about this energy marker. The multipole pair profiles for the r0 configuration in all three clusters also fit well with the atomistic r0, r45y and r45z data. The remaining configurations do not conform to the multipole pair r0 profiles as these only contain dipole-dipole and quadrupole-quadrupole components, whereas on going from the r0 to the r180y there is also a dipole-quadrupole interaction which causes asymmetry in the atomistic data in relation to the results between angles of 0-180 degrees and 180-360 degrees. The 30 a.u cluster can be seen to have peaks for the r0 configuration at 0/360 and 180 degrees of profile rotation angle, as the entire atomistic configuration involving a y axis rotation (r45y, r90y, r135y & r180y) show there is a sequential shift of the peak at 360 degrees in the r0 configuration to 270 degrees in the r180y configuration and

similarly there is a sequential shift of the peak at 180 degrees in the r0 configuration to 90 degrees in the r180y configuration. The two peaks of the r180y configuration are asymmetric due to the dipole-quadrupole interaction. These effects are also visible in both the 40 a.u and 50 a.u clusters, the 50 a.u cluster also shows far more oscillations in each curve as a result of greater number of surface atoms relative to the other two clusters. These dipole-quadrupole interactions are explained using a simple dipole moment surrounded by a square net, to depict the quadrupole moment, to represent the clusters in the r0 and r180y configuration (Figure 86).

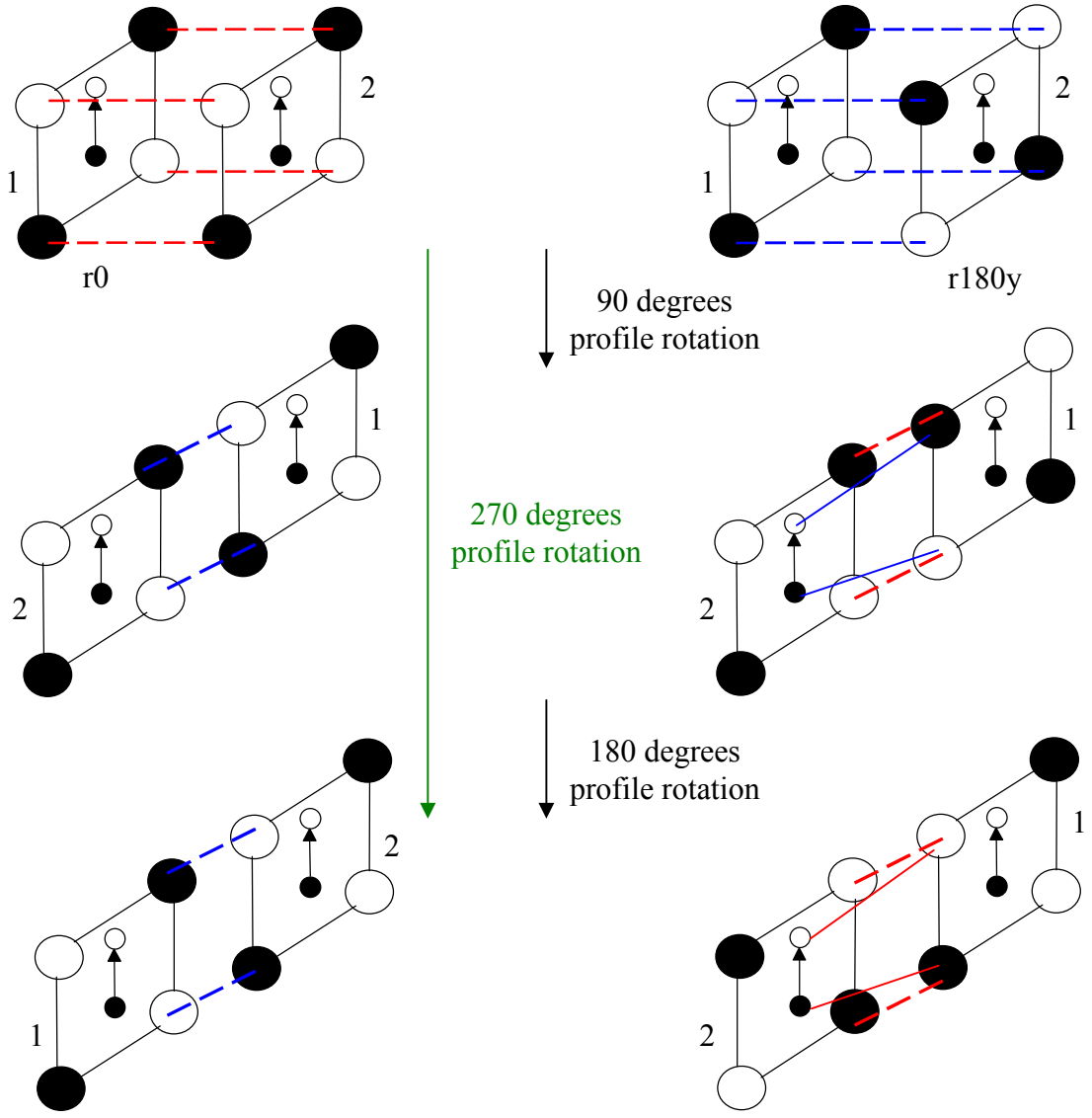

Figure 86 - *Simple dipole and quadrupole profiles for the r0 and r180y configurations, depicting the effects of the different configurations at 90 and the equivalent 270 degrees of profile rotation. The left sided figures show the r0*

configuration and the various orientations, whilst the right sided figures show the r180y configuration and the various orientations that result. The blue dashed lines indicate attractive interactions, while the red dashed lines indicate repulsive interactions.

The figure illustrates how the r0 configuration begins in a repulsive configuration with respect to the quadrupole interaction, the profile rotation of the second cluster by 90 degrees results in an attractive configuration with respect to the quadrupole interactions. It has previously been stated that there is no dipole-quadrupole interaction in this configuration, however there are two dipole-quadrupole interactions in this configuration that in fact cancel one another's effects resulting in zero energy contribution so in essence the earlier statement of no interaction energy contribution is true. These dipole-quadrupole interactions have not been highlighted in order to avoid confusion, though one can simply look at the comparable r180y figures to see the overall cancellation of this force. The r180y configuration at 90 and 270 degrees of profile rotation shows the quadrupole-quadrupole interaction energy to be repulsive. The dipole-quadrupole interaction between the clusters at 90 degrees profile rotation is attractive, but this interaction is repulsive at 270 degrees of profile rotation and as such this explains the asymmetry in the atomistic data peaks. There is only one dipole-quadrupole interaction shown in both the cluster orientations at 90 and 270 degrees of profile rotation; however, the remaining dipole-quadrupole interactions are exactly the same in magnitude as the ones already shown.

4.3.2 Attractive Starting Configurations

The results at short separations for clusters starting in dipolar attractive orientations (r135x, r180x, r135z & r180z) are shown for the 30 a.u cluster, 40 a.u cluster and 50 a.u cluster at separations of 35 a.u, 45a.u and 55 a.u respectively, additionally the dipole/multipole pair profiles are also shown (Figure 87).

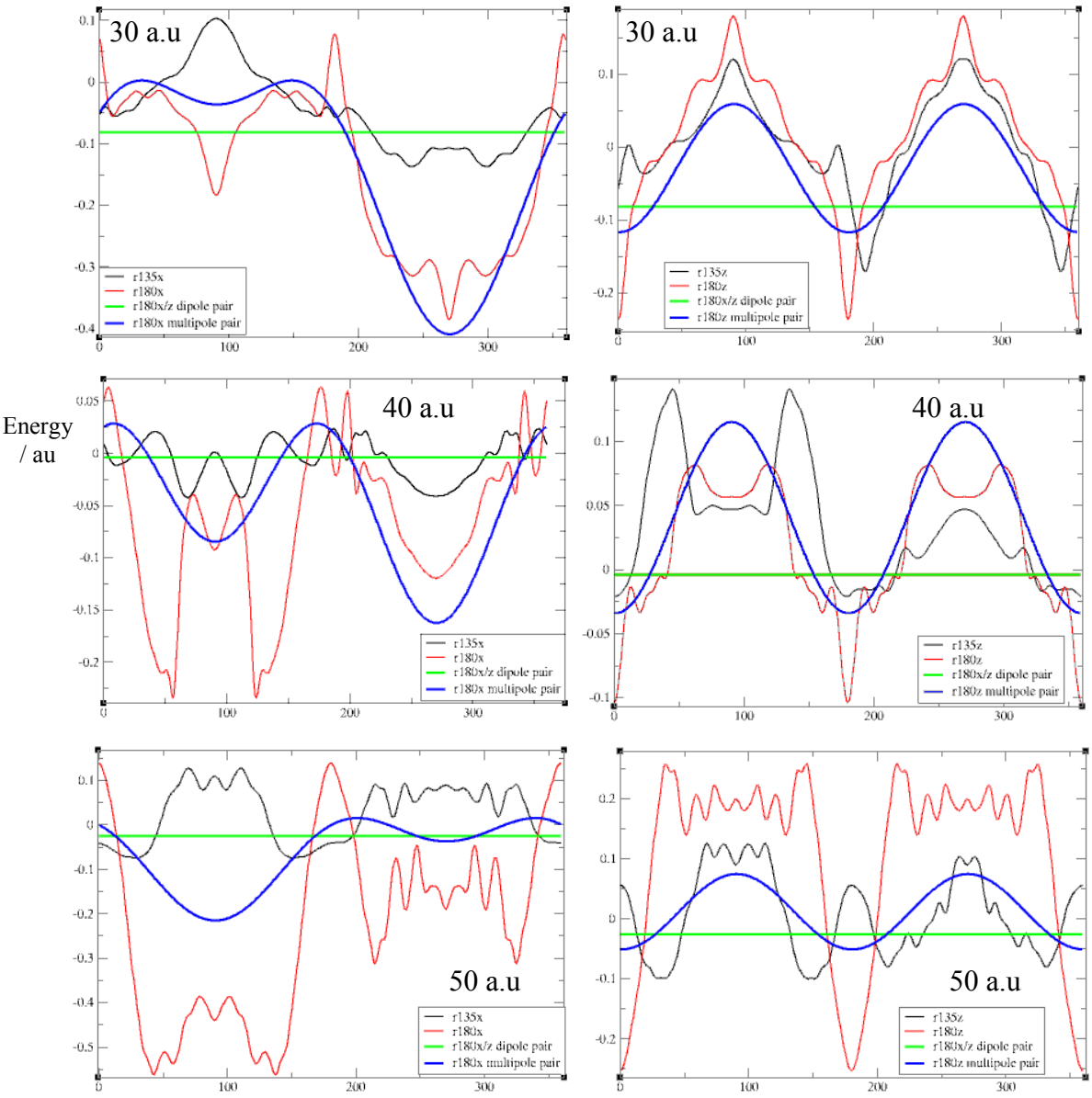

Figure 87 - *Energy profiles, starting configurations beginning in an attractive dipolar orientation, for the 30 a.u cluster (top row), 40 a.u cluster (middle row) and 50 a.u cluster (bottom row) at separations of 35 a.u, 45 a.u and 55 a.u respectively. The atomistic profiles for the dipolar equivalent r135x, r180x (all left hand figures), r135z and r180z (all right hand figures) are shown, the dipole pair and multipole energies are calculated for the r180x configuration (left figures) and the r180z configuration (right figures) only, to act as markers for comparison, as indicated by the figure legends.*

The atomistic data for the r135x and r180x for all three clusters compares reasonably well with the dipole pairs and multipole pairs. There is asymmetry in the troughs of

the graphs at 90 and 270 degrees of profile rotation due to the dipole-quadrupole interactions between the clusters, though these are not shown as a detailed breakdown of the multipole interactions involved have already been shown in Figure 84. There are some oscillations in all the clusters as a result of the close distance between the surfaces of the clusters. These oscillations increase on going from the 30 a.u to the 40 a.u and 50 a.u clusters as the number of atoms on the surfaces increases and hence this results in the observed increased frequency of oscillations in the atomistic data. The atomistic results for the r135z and r180z also show good agreement with the dipole and multipole pair profiles for all three clusters, there is no assymtery in the peaks at 90 and 270 degrees of profile rotation for the r180z as there are only quadrupole interactions involved in this configuration. There is however dipole-quadrupole interactions in the r135z profile which result in some asymmetry in the peaks, but relative to the r135x and r180x data these are small for all three clusters.

4.3.3 Neutral starting configurations

The results at short separations for clusters starting in dipolar neutral orientations (r90x & r90z) are shown for the 30 a.u cluster, 40 a.u cluster and 50 a.u cluster at separations of 35 a.u, 45a.u and 55 a.u respectively alongside the multipole pair profiles (Figure 88).

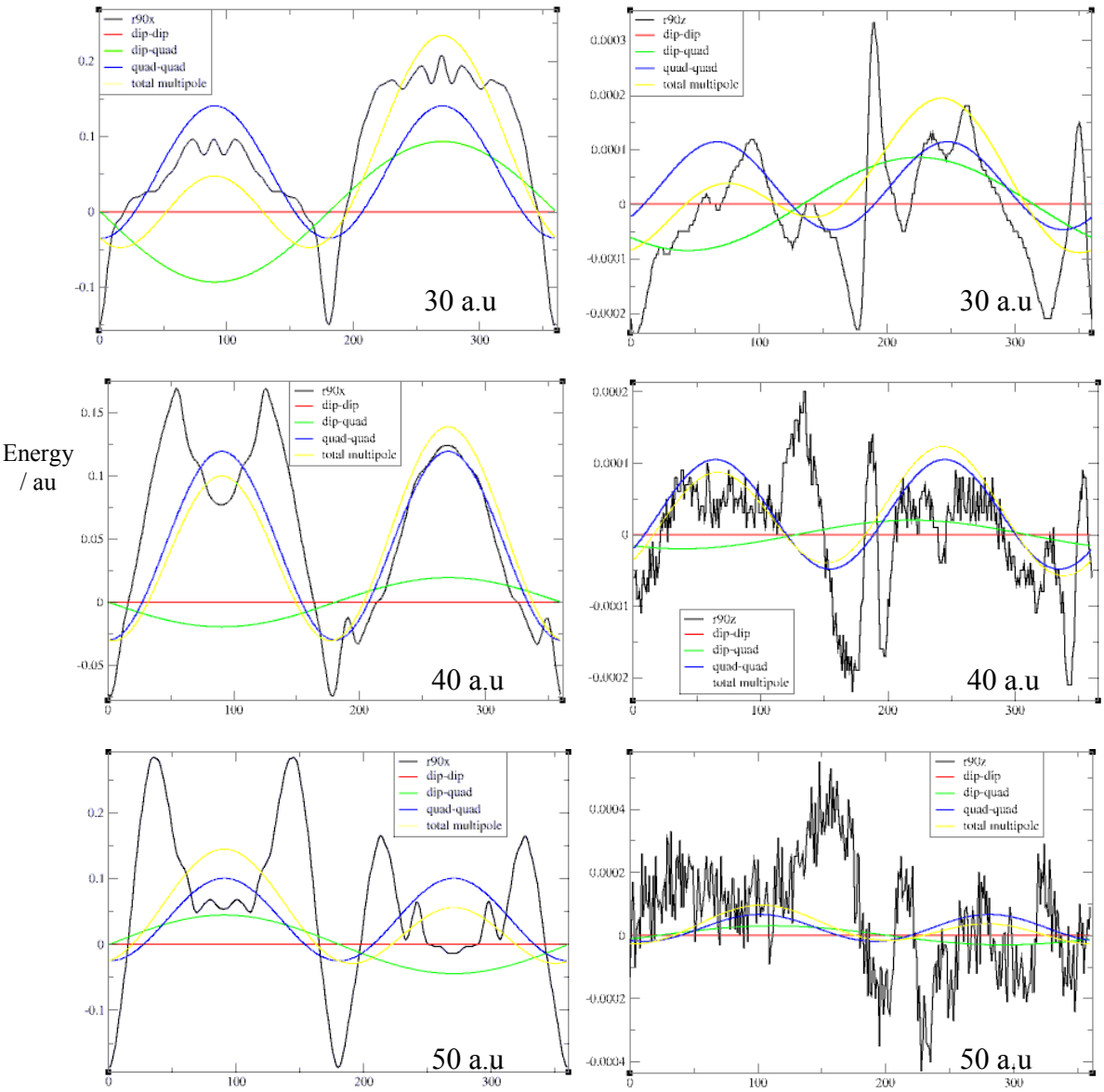

Figure 88 - *Energy profiles, starting configurations beginning in a neutral dipolar orientation, for the 30 a.u cluster (top row), 40 a.u cluster (middle row) and 50 a.u cluster (bottom row) at separations of 35 a.u, 45 a.u and 55 a.u respectively. The atomistic profiles for the r90x (left hand figures) and r90z (right hand figures) configurations are shown, the dipole pair and multipole pair profiles are calculated for each of the configurations as highlighted by the figure legends.*

The atomistic data for the r90x configuration for all three clusters generally agrees with the multipole pair profiles, the major component contributing to the atomistic data is the quadrupole-quadrupole interaction followed by the dipole-quadrupole interaction. There is no dipole-dipole interaction for the r90x configuration and as

seen before there is asymmetry in the atomistic data peaks at 90 and 270 degrees of profiles rotation for all three clusters as a result of dipole-quadrupole interactions. The dipole-quadrupole interactions have either troughs or peaks at 90 or 270 degrees of profile rotation and this depends on the initial starting configurations of the quadrupoles in the clusters, these different interactions are shown via dipole square net model representing the clusters (Figure 89).

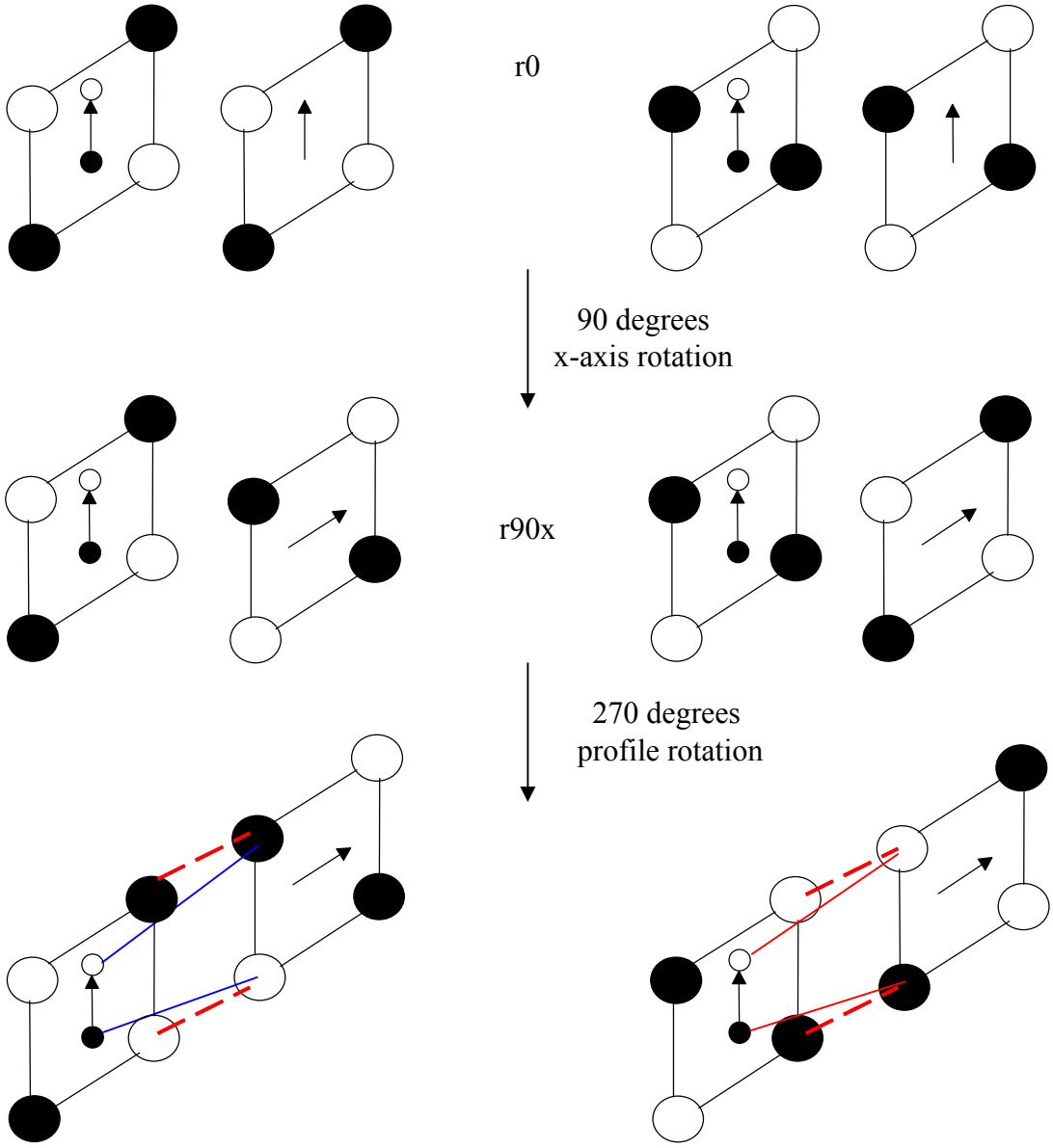

Figure 89 - *Equivalent profiles for the r90x configuration, depicting the effects of the subtly different starting r0 configurations on the resulting energy profiles at 270 degrees of profile. The top figures shows the energy equivalent r0 configurations, which acts to highlight the difference between the resulting r90x (middle figures) configurations. The resulting energy profiles at 270 degrees of rotation (bottom*

figures) have either blue dashed lines to indicate attractive interactions or red dashed lines indicate repulsive interactions.

The simple depiction of the forces between the clusters in the r90x configuration at 270 degrees profile rotation illustrate how the starting configuration can have the effect of producing different peak sizes at 90 and 270 dgerees of profile rotation. There can either be the case of the quadrupole-quadrupole and dipole-quadrupole both being repulsive, hence producing the highest peak with greatest energy, or the quadrupole-quadrupole interaction is repulsive with the dipole-quadrupole interaction being attractive resulting in the second peak which is less in energy than the former higher peak. It should also be noted that unlike previous examples of the dipole-quadrupole interactions in Figure 86, where there are in fact two dipole-quadrupole interactions between the clusters, there is only one dipole-quadrupole interaction for the r90x configuration in the XZ plane. The atomistic data for the r90z configuration in Figure 88 has an extremely low energy scale; it is approximately 100 times smaller than the r90x configurations energy scale. This arises as the r90z configuration of the clusters means no multipole interaction between the clusters for the duration of the profile, there is equally repulsive and attractive interactions (Figure 90). Any small multipole forces present are merely the result of either small errors in rotating the clusters into the desired configurations and atomistic detailing between the clusters. The interesting thing to note is pronounced increase in the frequency of oscillations in the atomistic data on going from the 30 a.u cluster to the 40 a.u and finally 50 a.u cluster, this nicely illustrates the effect of the increasing number of surface atoms on the clusters and how this produces greater fluctuations in atomistic data.

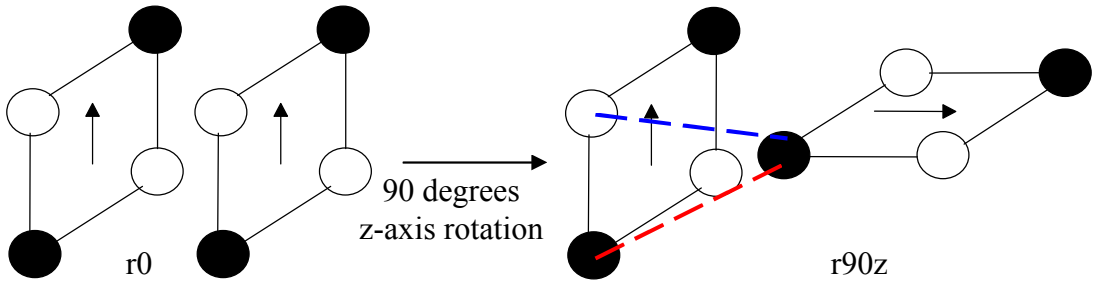

Figure 90 - *Simple depiction of the r90z configuration showing that there are equally repulsive and attractive interactions between the clusters throughout the duration of the energy profile construction. There is no dipole-dipole, dipole-quadrupole or*

quadrupole-quadrupole interaction as the dipoles and quadrupoles are orthogonal to one another. The blue dashed lines shows attractive interactions while the red dashed lines show repulsive interactions.

4.4 The YZ plane energy profiles

The following analysis of the clusters is for the YZ plane; these results should be similar to those observed for the XY plane as the clusters will go through a range of configurations for the duration of the profile rotation. The larger separation results, 2-3 times the cluster diameter, are first examined for the different clusters. The r0 configurations for the three clusters of interest are shown for the 30 a.u (separations of 70 & 100 a.u), 40 a.u (separations of 90 & 135 a.u) and 50 a.u (separations of 100 a.u & 150 a.u) clusters (Figure 91).

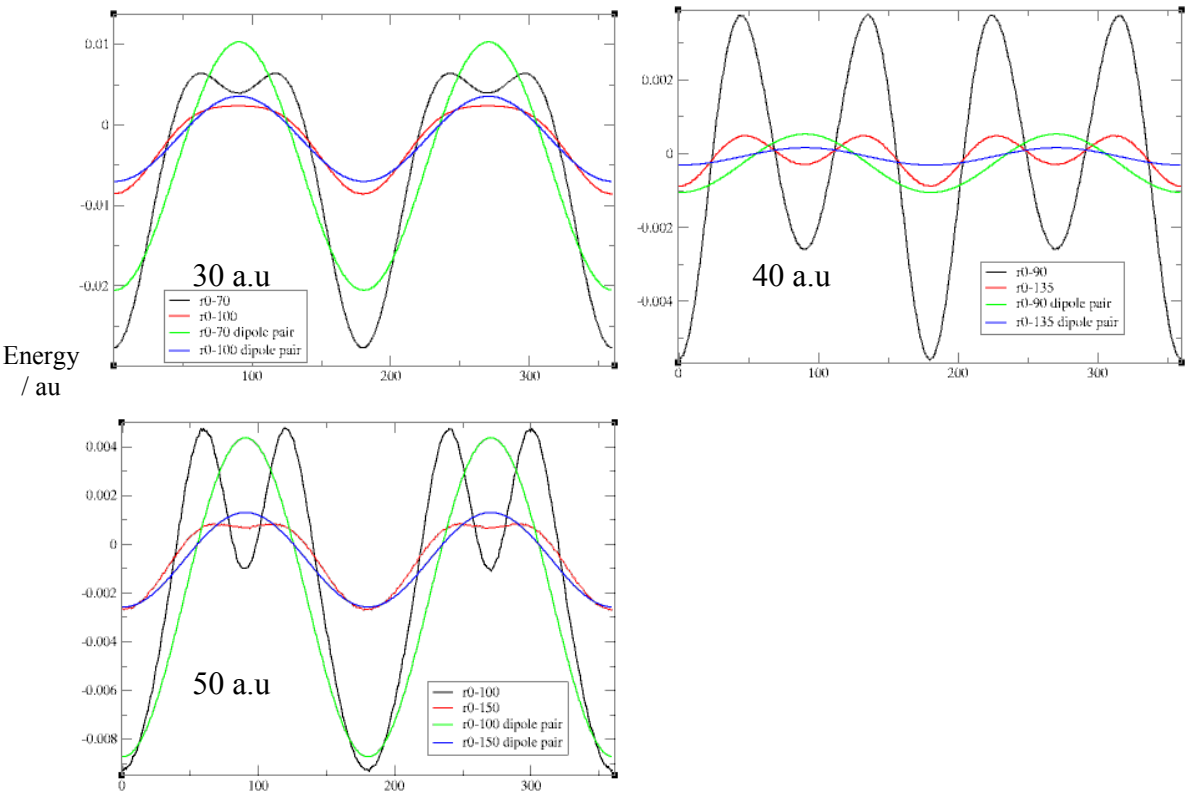

Figure 91 - *Energy profiles for the r0 configuration calculated for the clusters with diameters of 30 a.u (top left figure), 40 a.u (top right figure) and 50 a.u (bottom left figure) respectively, for the smaller 30 a.u cluster energies are calculated at*

separations of 70 a.u and 100 a.u as indicated in the figure legend, for the 40 a.u cluster these separations are 90 a.u and 135 a.u respectively and for the 50 a.u cluster the separations are 100 a.u and 150 a.u. The energies of the equivalent dipole pairs are shown for comparison as indicated by the figure legends.

The atomistic r0 configurations for the 30 a.u and 50 a.u clusters seem to agree with their respective dipole pair profiles, though both these clusters display double peaks at either side of the profile rotations angles of 90 and 270 degrees with subtle troughs occurring at exactly 90 and 270 degrees of profile rotation within the larger peaks. These subtle troughs at 90 and 270 degrees of profile rotation are particularly large in the 40 a.u cluster results. The 40 a.u atomistic data as a result compares rather poorly with the dipole pair profiles at both 90 a.u and 135 a.u of separation, as the dipole pair profiles indicates that peaks should occur at 90 and 270 degrees of profile rotation rather than the actual troughs. The obvious difference between the 30 a.u, 50 a.u and 40 a.u clusters is the larger quadrupole moment in the 40 a.u cluster. The 30 a.u cluster also has these subtle troughs at 90 and 270 degrees of profile rotation disappearing on going from the 70 a.u to 100 a.u separations between the clusters, there is also a better comparison between the atomistic data at 100 a.u of separation with the relevant dipole pair profile compared to the same results at 70 a.u. The disappearing troughs at larger separations also occur in the 50 a.u cluster on going from 100 a.u to 150 a.u and these can be attributed to the fact that dipole interactions are longer range in contrast to quadrupole interactions. This can be further examined by looking at the multipole interaction breakdown for the 30 a.u, 40 a.u and 50 a.u cluster at separations of 70 a.u, 90 a.u and 100 a.u respectively (Figure 92).

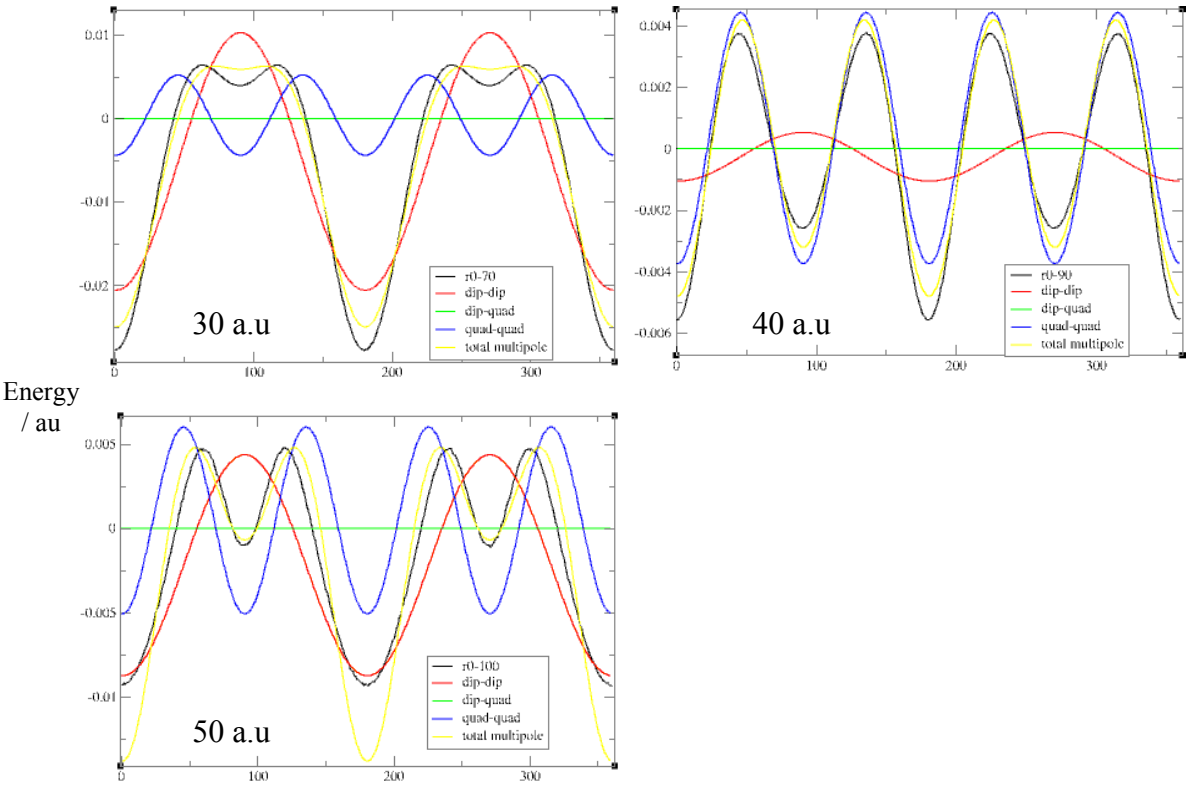

Figure 92 - *Multipole pair profiles for the r0 configuration calculated for the clusters with diameters of 30 a.u (top left), 40 a.u (top right) and 50 a.u (bottom left) at separations of 70 a.u, 90 a.u & 100 a.u respectively. Each figure inset contains the dipole-dipole, dipole-quadrupole and quadrupole-quadrupole interactions energies, as well as the total sum of these forces the total multipole interaction energy. This is directly compared to the atomistic profiles as highlighted by the figure legends.*

The multipole breakdown of the three clusters conveys that the quadrupole-quadrupole interaction is indeed responsible for the subtle troughs within the larger peaks at 90 and 270 degrees of profile rotation for both the 30 a.u and 50 a.u cluster. In the case of the 40 a.u cluster the quadrupole-quadrupole interaction is more dominant relative to the dipole-dipole interaction and as such there are true troughs at 90 and 270 degrees of profile rotation. The sinusoidal shape of the quadrupole interactions for each of three clusters is the same with regard to shape and with minima and maxima alternating every 45 degrees, though the magnitude for each cluster varies due differences in quadrupole moments. These results are explained by a simple dipole square net quadrupole model (Figure 93).

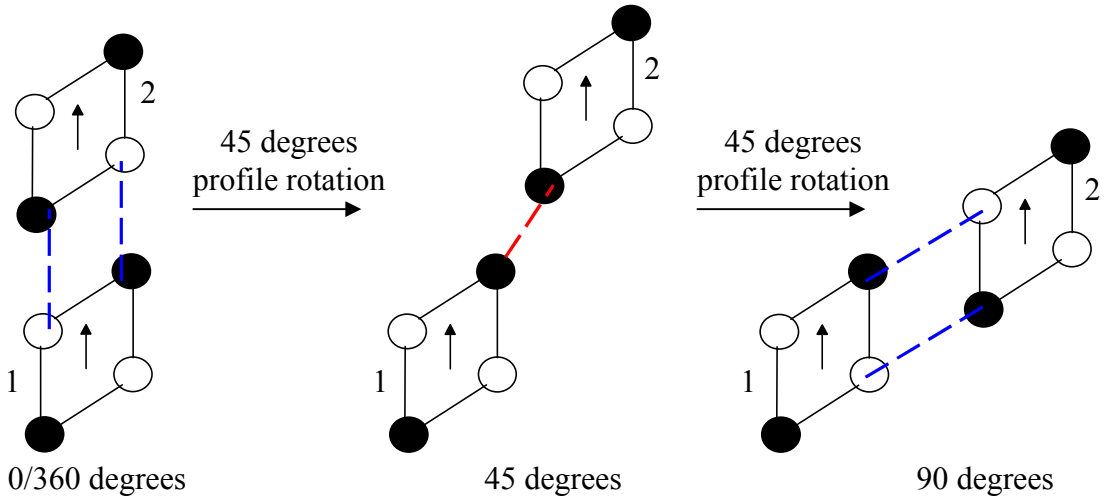

Figure 93 - *The simple representation of the clusters as dipoles surrounded by a square net quadrupole show the dominant quadrupole interactions between the clusters at 45 degree intervals in the YZ plane for the r0 configuration.*

The diagram in Figure 93 shows the dominating quadrupole interactions between the clusters at different angles of rotation. The starting r0 configuration has both attractive dipole (head to tail interaction) and quadrupole interactions resulting in the minima for all clusters at 0 and 180 degrees of profiles rotation in Figure 92. When the second cluster is rotated about the first in the YZ plane there is clearly a repulsive interaction dominating between the two quadrupoles. Further rotation of the cluster by 45 degrees, to the 90 degree profile, results in the same attractive interaction observed for the starting configuration, though on this occasion the dipoles are in the repulsive parallel orientation. The relative strength of these interactions leads to the different atomistic profiles in Figure 92. In the case of the 30 a.u cluster the dipole interaction dominates at 90 degrees of profile rotation, as the energy is repulsive. The 50 a.u cluster shows the same shape of the atomistic data as that of the 30 a.u cluster, though on this occasion the energy at 90 degrees profile rotation is slightly attractive hence the quadrupole interaction dominates. The 40 a.u cluster clearly has a dominating quadrupole interaction due to a low dipole moment in this cluster relative to the 30 and 50 a.u clusters. The dipolar equivalent r180x and r180z profiles are examined concurrently for the 30 a.u (separations of 70 & 100 a.u), 40 a.u (separations of 90 & 135 a.u) and 50 a.u (separations of 100 a.u & 150 a.u) clusters (Figure 94).

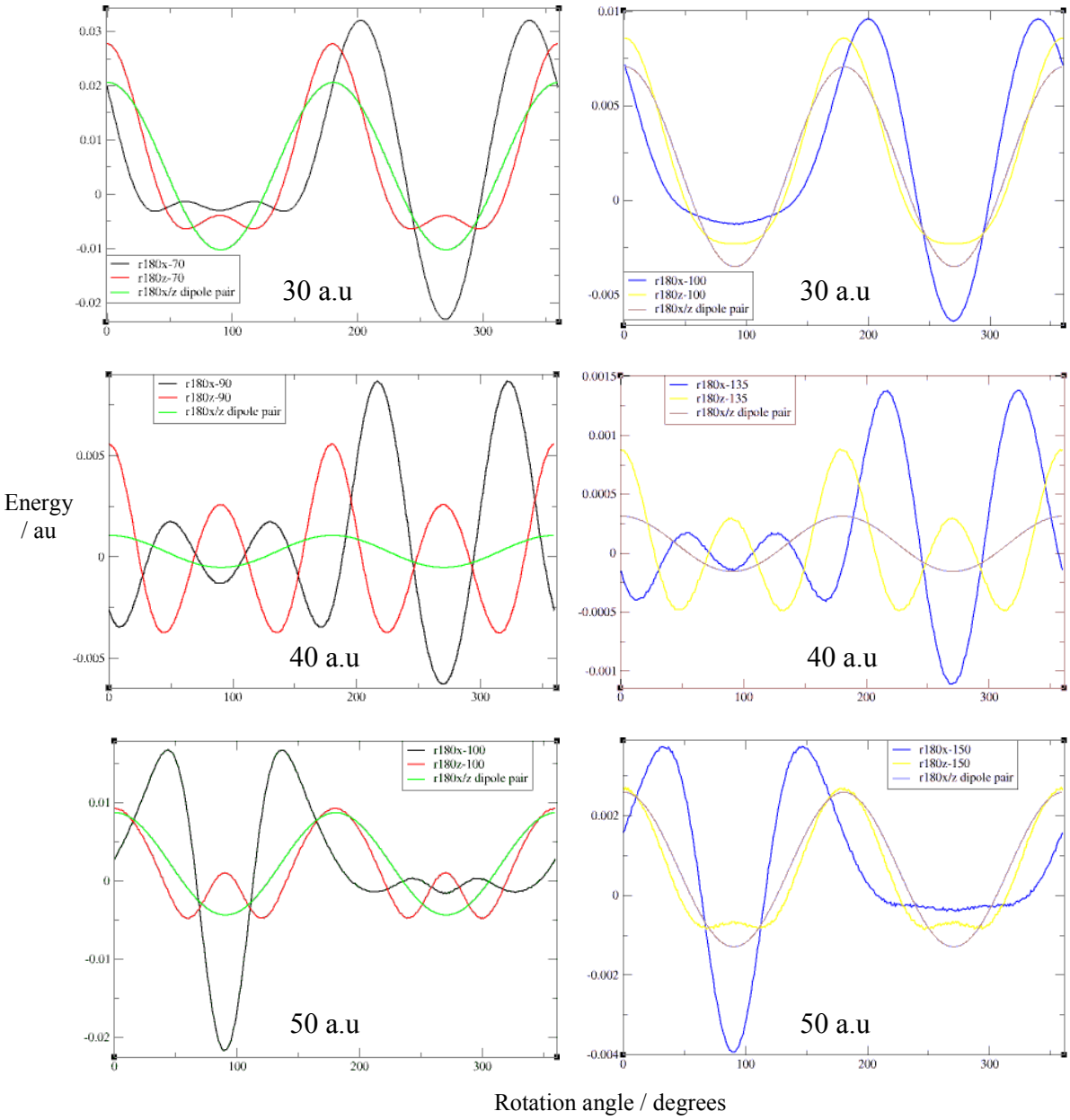

Figure 94 - *Energy profiles for the r180x and r180z configurations calculated for the clusters with diameters of 30 a.u (top), 40 a.u (middle) and 50 a.u (bottom) respectively. Energy profiles are calculated at separations of 70 a.u, 90 a.u and 100 a.u for the 30 a.u, 40 a.u and 50 a.u clusters respectively (left hand figures top to bottom) as well as at separations of 100 a.u, 135 a.u and 150 a.u (right hand figures top to bottom). The energies of the equivalent dipole pairs are shown for each cluster for comparison as indicated by the figure legends.*

The smaller 30 a.u cluster shows reasonably good agreement between the atomistic r180z data at separations of 70 a.u and 100 a.u with the respective dipole pair profiles. There are minima's that occur at approximately 90 and 270 degrees of profile rotation

at separation of 70 a.u that bare striking resemblance to the peaks observed in Figure 91 at the same angles, there are subtle peaks within these minima and due to the similarities to Figure 91 can be attributed to quadrupole interaction. There is also similarly a softening of these smaller peaks with increasing separation as observed at 100 a.u of separation between the clusters. The r180x atomistic data for the 30 a.u cluster shows mimima's at the expectant angles of rotation, 90 and 270 degrees, however these minima are not symmetrical and they persist on going from the 70 a.u to the 100 a.u atomistic data. The asymmetry as previously observed and stated in synonymous with the dipole-quadrupole interaction. The 40 a.u cluster shows no agreement at all between the atomistic data for the r180x and r180z at both separations of 70 and 100 a.u with the dipole pair profiles; this is mostly attributed to the low dipole moment of the cluster relative to the other clusters and a larger quadrupole moment. The results for the 50 a.u cluster are almost identical to those observed for the 30 a.u clusters, whereby the r180z shows good agreement with the dipole pairs at both separations (100 a.u & 150 a.u) except for these subtle peaks that occur within the overall minima's at 90 and 270 degrees of profile rotation. There is also a softening of these subtle peaks as the separation is increased from 100 a.u to 150 a.u, though they are still present. The atomistic r180x profiles also have troughs in the expectant angles of 90 and 270 degrees of profile rotation, but again there is asymmetry in the result indicating the presence of dipole-quadrupole interactions. These results and whether in fact the dipole-quadrupole interactions do play a pivotal role in the asymmetrical atomistic data are examined further by viewing the multipole interaction breakdown of the three clusters, 30 a.u, 40 a.u and 50 a.u, at separations of 70 a.u, 90 a.u and 100 a.u respectively (Figure 95).

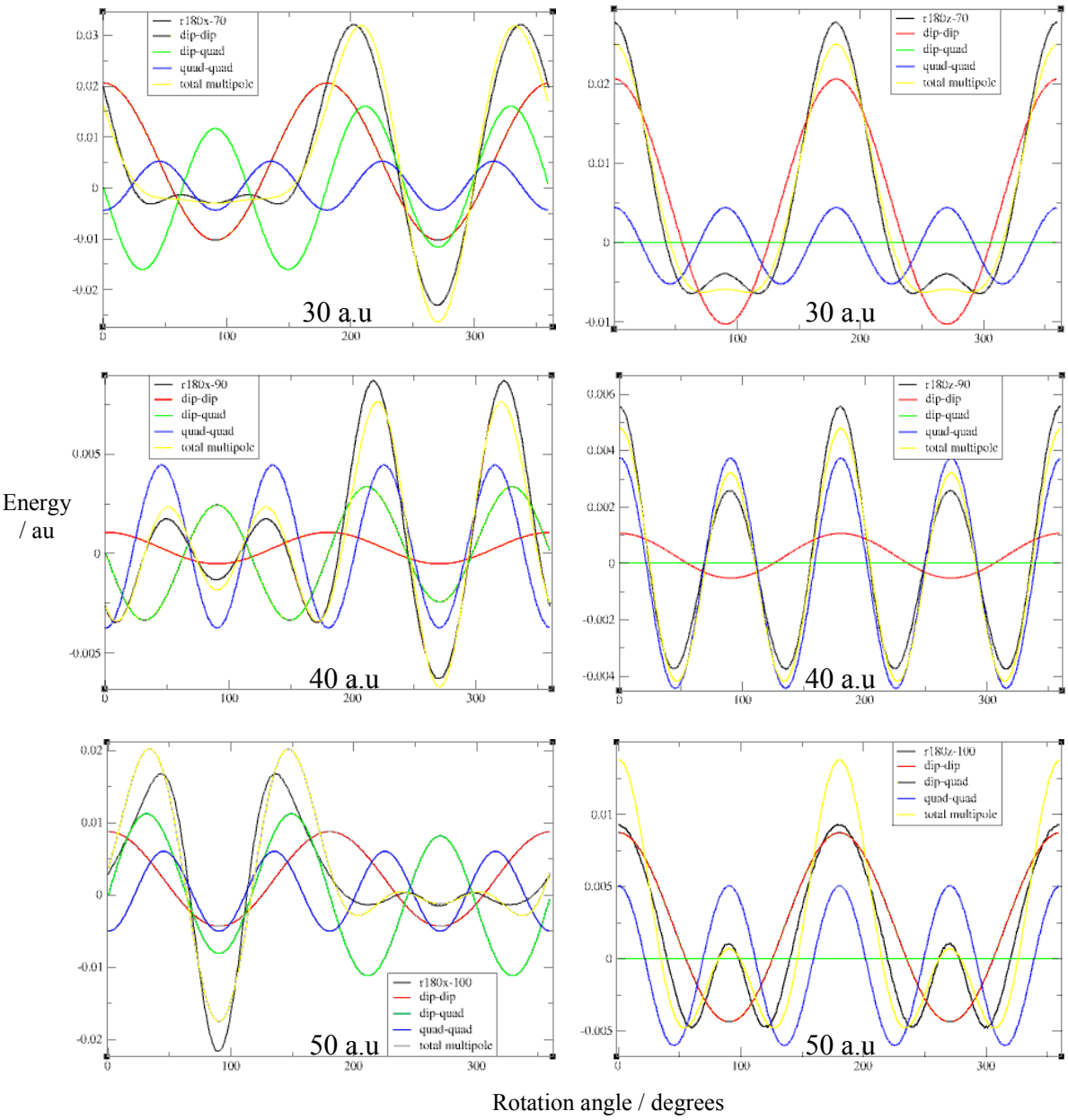

Figure 95 - *Multipole pair profiles for the r180x and r180z configurations calculated for the clusters with diameters of 30 a.u (top), 40 a.u (middle) and 50 a.u (bottom) respectively. Energy profiles are calculated at separations of 70 a.u, 90 a.u and 100 a.u for the 30 a.u, 40 a.u and 50 a.u clusters respectively. The r180x (left hand figures top to bottom) and r180z (right hand figures top to bottom) multipole breakdowns are shown, each figure inset contains the dipole-dipole, dipole-quadrupole and quadrupole-quadrupole interactions energies, as well as the total sum of these forces the total multipole interaction energy. This is directly compared to the atomistic profiles as highlighted by the figure legends.*

The multipole breakdown reveals that for the r180x configuration in each cluster there are indeed dipole-quadrupole interactions present, however unlike previous examples the dipole-quadrupole interaction itself is unsymmetrical. This is not usually the case as it's the combination of the dipole and quadrupole interactions combined together that give asymmetrical shape in the total of the multipole interactions. The dipole-quadrupole interaction is not present in the r180z configuration for all three clusters, there is only the dipole-dipole interaction and the quadrupole interaction, which has alternating minima and maxima 45 degrees apart, observed previously in Figure 92. The total multipole interactions for both the r180x and r180z configuration do compare rather well with their respective atomistic data. The r180x configuration for the 30 a.u cluster has rather odd looking minima at 90 and 270 degrees of profile rotation, the multipole breakdown explains the large almost flat minima at 90 degrees occurs due to the cancellation of the forces between the attractive, dipole-dipole and quadrupole-quadrupole interactions, and repulsive dipole quadrupole interaction. The sharper minima at 270 degrees of profile rotation results from the in phase augmentative effect of the dipole-dipole, dipole-quadrupole and quadrupole-quadrupole interactions at this angle resulting in much lower minima than would be expected with dipole interactions alone. The 50 a.u cluster follows the same pattern as the 30 a.u cluster except for the flat and sharp minima swapping positions between 90 and 270 degrees of profile rotation. The 40 a.u cluster is also very similar to the former clusters even though the dipole moment of the cluster is low. The assymetrical dipole-quadrupole interaction in the 30 a.u cluster for the r180x configuration seems to have alternating minima and maxima occurring at angles of 30, 90, 150, 210, 270, 330 degrees, the troughs and peaks are switching constantly every 60 degrees. There are also two distinct types of energies for the maxima or minima and can be classed as either being ±0.16 a.u (occurring at 30, 150, 210 & 330) or ±0.12 a.u (occurring at 90 & 270). The differing results of the two r180x and r180z configurations are explained using a simple dipole surrounded by a square net quadrupole model (Figure 96).

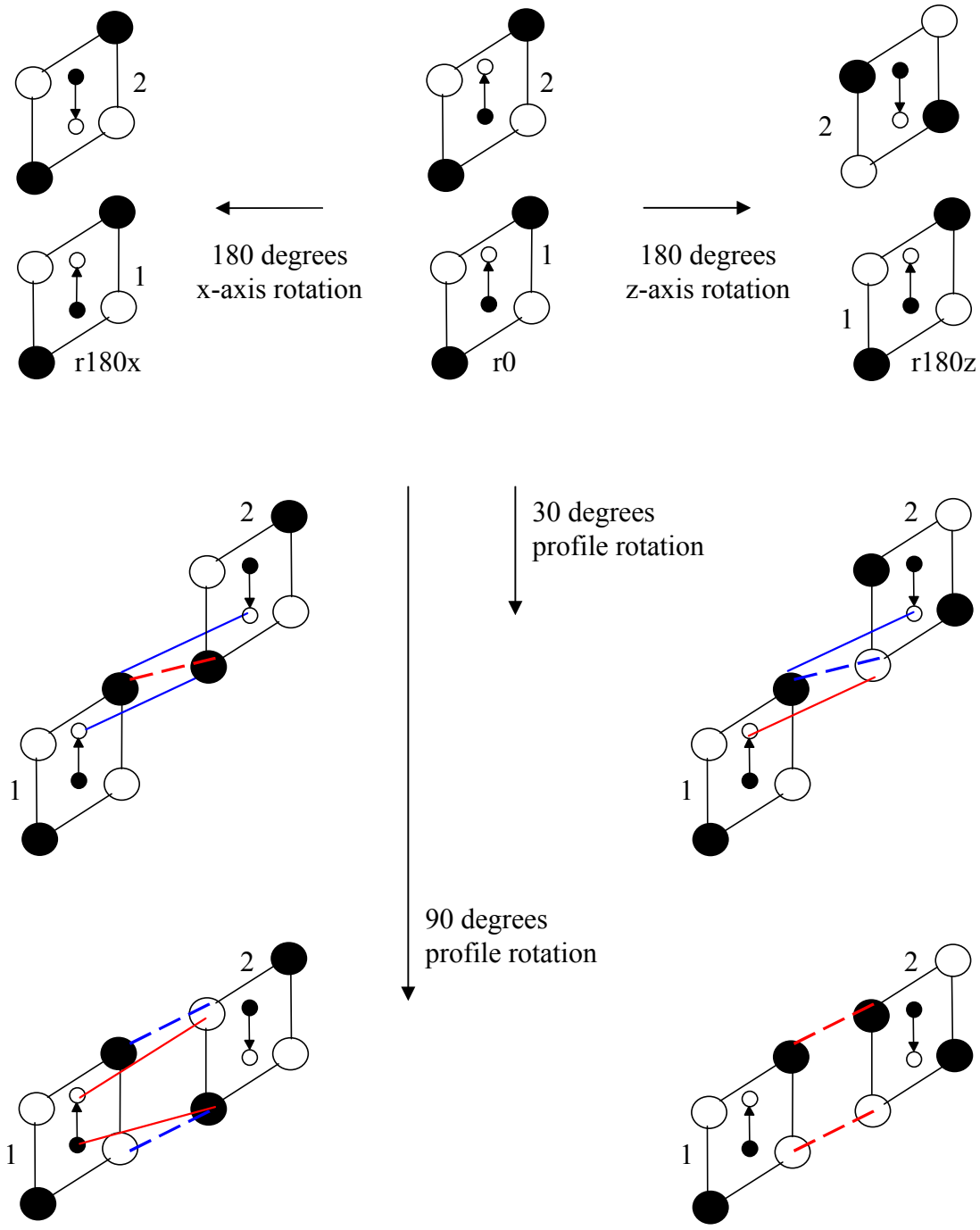

Figure 96 - *The simple representation of the clusters as dipoles surrounded by a square net quadrupole. The top figures show how the two r180x (left) and r180z (right) configurations arise through different axis rotations; the middle figures show the dominant quadrupole interactions between the clusters at 30 degrees of profile rotation. The bottom figures show the dominant quadrupole interactions at 90 degrees of profile rotation. The blue dashed lines indicate attractive interactions, whilst red lines indicate repulsive interactions between clusters.*

The only difference that arises between the r180x and r180z configurations is a subtle change in the quadrupole moment direction. This difference then results in contrasting dipole-quadrupole interactions between the clusters as indicated in Figure 96 at 30 degrees of profile rotation. The r180x configuration has attractive dipole-quadrupole interactions between cluster 1 and cluster 2 and similarly between cluster 2 and cluster 1, in other words the two dipole quadrpole interactions between the clusters work together to achieve an overall attractive dipole-quadrupole component. In contrast the r180z configuration at the same angle results in two dipole-quadrupole interactions that works against one another to achieve an overall zero dipole-quadrupole component. These effects persist throughout the energy profile cycle of these configurations and to further highlight this the orientations of the dipole equivalent r180x and r180z configurations at 90 degrees of profile rotation show that the r180x has a dipole-quadrupole interaction in addition to a quadrupole-quadrupole interaction, whilst the r180z configuration has only a quadrupole-quadrupole interaction as the dipole-quadrupole forces cancel each other out. The two different orientations at 30 and 90 degrees of profile rotation also highlight the difference in energy that arises between those configurations that are ±0.16 a.u (occurring at 30, 150, 210 & 330) and ±0.12 a.u (occurring at 90 & 270) is simply the result of the dipole-quadrupole separations between the clusters being closer at 30 degrees than 90 degrees.

4.4.1 Attractive starting configurations

The results at short separations for clusters starting in dipolar attractive orientations (r0, r45x, r45y, r45z, r90y, r135y & r180y) are shown for the 30 a.u, 40 a.u and 50 a.u cluster at separations of 35 a.u, 45 a.u and 55 a.u respectively alongside the r0 configuration dipole/multipole pair profiles (Figure 97). The analyses of the short separation energy profiles is to establish whether in general terms that the varying energy profiles show conformity to the dipole and multipole pair profiles. This is true for subsequent short separation energy profiles examined.

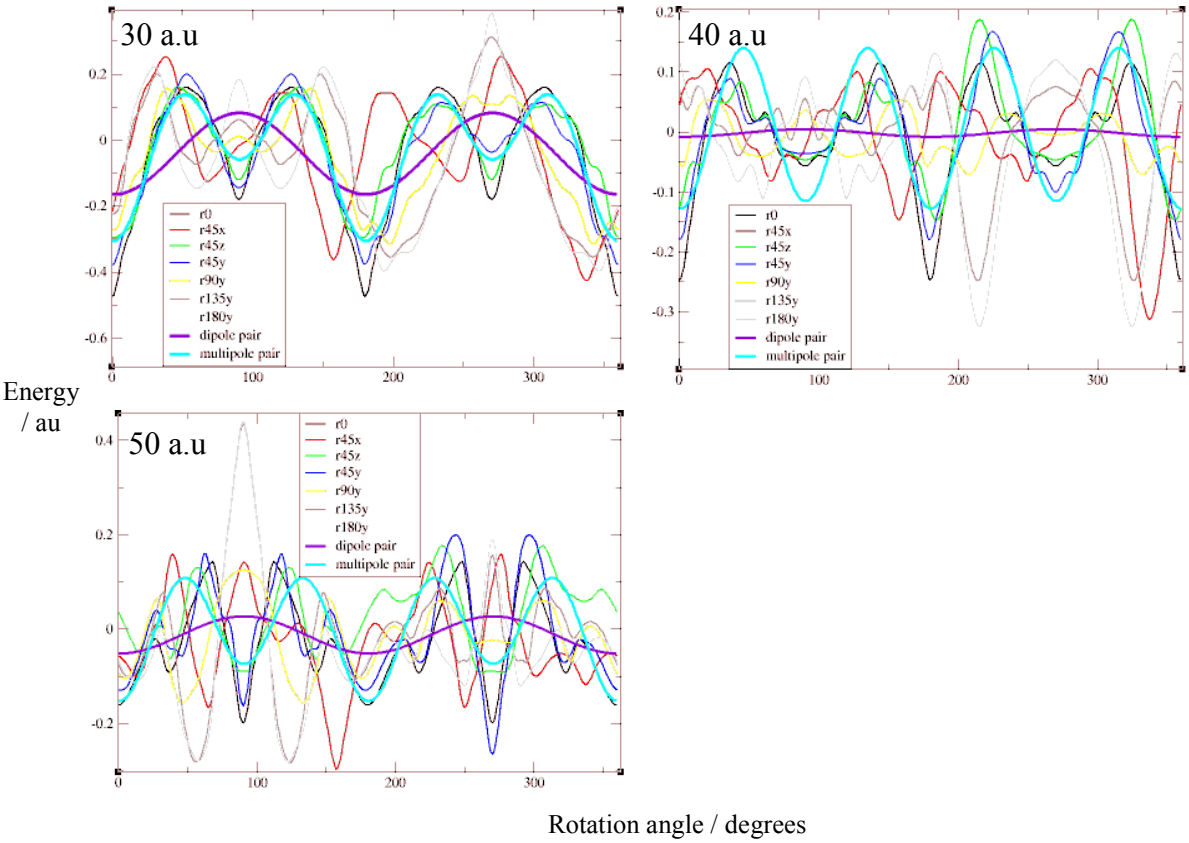

Figure 97 - *Energy profiles, starting configurations beginning in a attractive dipolar orientation, for the 30 a.u cluster (top left), 40 a.u cluster (top right) and 50 a.u cluster (bottom left) at separations of 35 a.u, 45 a.u and 55 a.u respectively. The dipole pair and multipole pair energies are calculated for the r0 configurations only, to act as markers for comparison, as indicated by the figure legends.*

The data for the attractive starting configurations reveals that for all three clusters in general terms the atomistic data follows the expectant r0 multipole pair profiles reasonably well. In essence the atomistic data also follows the r0 dipole pair profiles as these have common minima with the multipole pair profiles at 0/360 and 180 degrees of profile rotation. The smaller 30 a.u cluster has the greatest conformity between all atomistic data configurations and the r0 dipole/multipole pair profiles. The 40 a.u cluster has a small dipole moment and hence a small dipole interaction component, the r0 multipole pair profile is mostly made up of the quadrupole-quadrupole interactions between clusters. The atomistic data for all the configurations shown in Figure 97 compare well with the multipole pair profile. The larger 50 a.u cluster also has reasonably good agreement between the atomistic data and the dipole/multipole pair profiles, however there is certainly more oscillations in the

atomistic data when compared directly with the 30 a.u and 40 a.u clusters. This has previously been attributed to the fact the larger the cluster the greater the number of surface atoms and hence the greater the surface energy contribution will be, resulting in greater oscillations in the atomistic data.

4.4.2 Repulsive starting configurations

The results at short separations for clusters starting in dipolar repulsive orientations (r135x, r180x, r135z & r180z) are shown for the 30 a.u cluster, 40 a.u cluster and 50 a.u cluster at separations of 35 a.u, 45 a.u and 55 a.u respectively alongside dipole/multipole pair profiles (Figure 98).

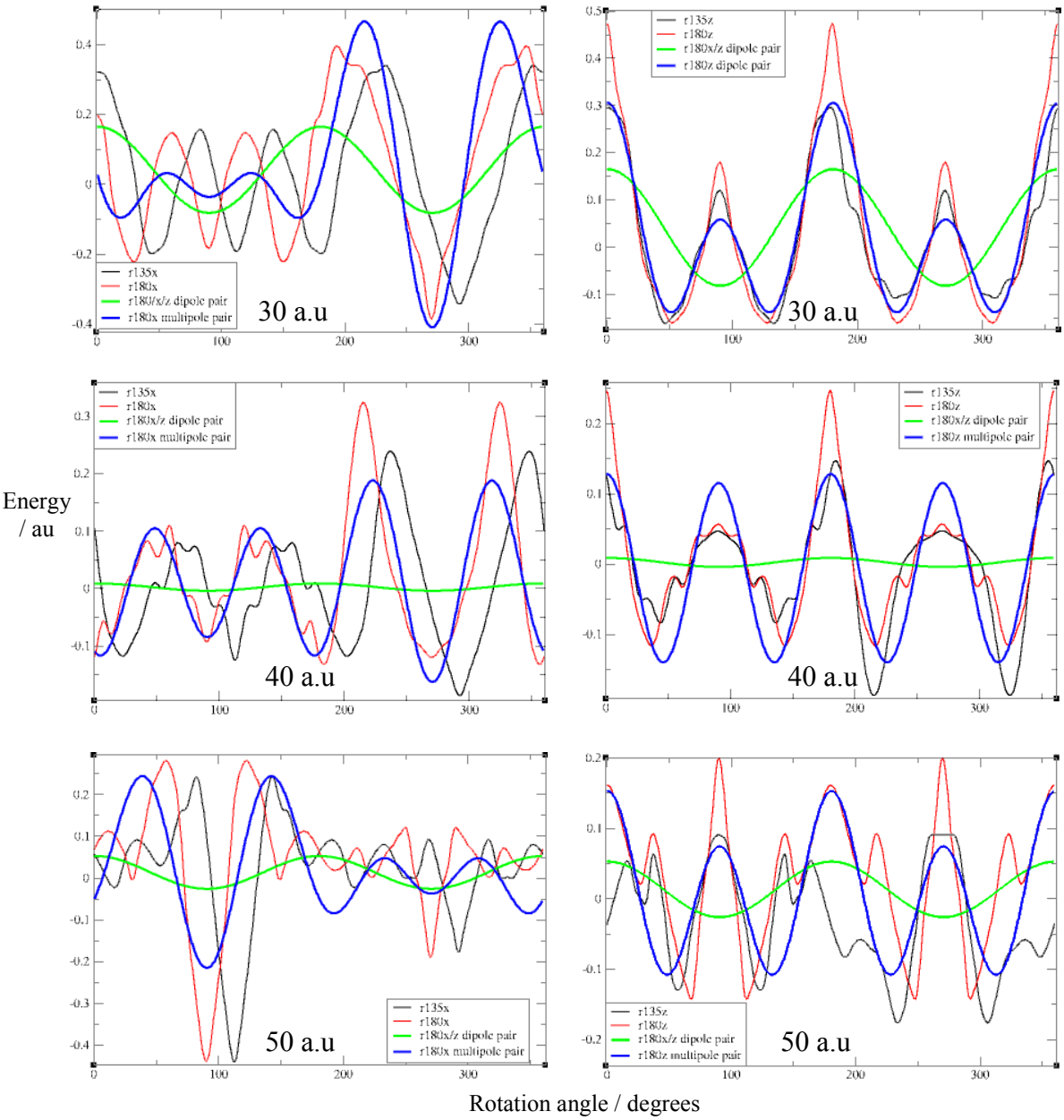

Figure 98 - *Energy profiles, starting configurations beginning in a repulsive dipolar orientation, for the 30 a.u cluster (top row), 40 a.u cluster (middle row) and 50 a.u cluster (bottom row) at separations of 35 a.u, 45 a.u and 55 a.u respectively. The atomistic profiles for the dipolar equivalent r135x, r180x (all left hand figures), r135z and r180z (all right hand figures) are shown, the dipole pair and multipole energies are calculated for the r180x configuration (left figures) and the r180z configuration (right figures) only, to act as markers for comparison, as indicated by the figure legends.*

The atomistic data for the r180x configurations for all three clusters compares very favourably with their repesctive r180x multipole pair profiles. The atomsitc r135x profiles in all three clusters is very similar to the r180x atomistic data except for the fact the data seems phase shifted by approximately 20 degrees relative to the r180x data for all three clusters. In the case of the atomisitc r180z configuration data for all three clusters there is also good comparisons between these and their respective multipole pair profiles. There is no phase shifting observed between any of the r180z and r135z configurations observed, however there is clearly reduced maxima for the r135z configuration data relative to the r180z configuration at profile angles of 0/360, 90, 180 and 270 degrees. In all three clusters the atomistic data shows extremely good agreement with the expectant multipole pair profiles. The asymmetry of the r135x and r180x atomistic data arises from the dipole-quadrupole interactions, which have already been discussed in Figure 95 and Figure 96.

4.4.3 Neutral starting configurations

The results at short separations for clusters starting in dipolar neutral orientations (r90x & r90z) are shown for the 30 a.u cluster, 40 a.u cluster and 50 a.u cluster at separations of 35 a.u, 45a.u and 55 a.u respectively alongside the multipole pair profiles (Figure 99).

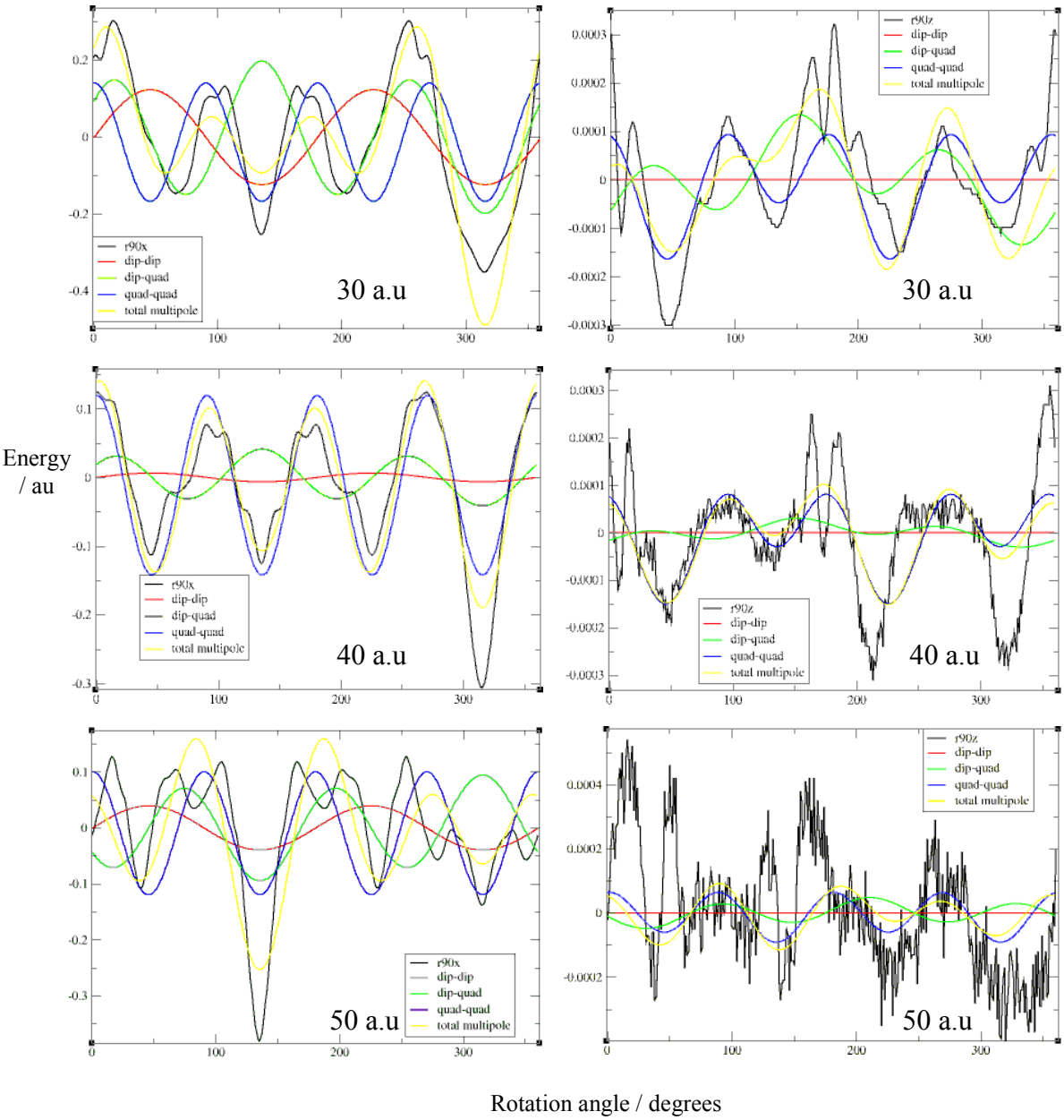

Figure 99 - *Energy profiles, starting configurations beginning in a neutral dipolar orientation, for the 30 a.u cluster (top row), 40 a.u cluster (middle row) and 50 a.u cluster (bottom row) at separations of 35 a.u, 45 a.u and 55 a.u respectively. The atomistic profiles for the r90x (left hand figures) and r90z (right hand figures) configurations are shown, the multipole pair breakdown profiles are calculated for each of the configurations as highlighted by the figure legends.*

The r90x configurations for all three clusters show the presence of dipole-dipole, dipole-quadrupole and quadrupole-quadrupole interactions between the clusters. There is some assymetery in the atomistic data that take the form of lower minima,

occurring at approximately 310 degrees of profile rotation for the 30 a.u and 50 a.u cluster and at approximately 135 degrees of profile rotation for the 50 a.u cluster. This lower minima occurs due to the in phase augmentation of dipole-dipole, dipole-quadrupole and quadrupole-quadrupole interactions between the clusters. The angle at which the minima materialises depends on the starting orientation of the quadrupole and dipole moments in the clusters, as it can be seen from the data the minima and maxima between clusters for the dipole-dipole and quadrupole-quadrupole interactions does not change for different size clusters. The only change that occurs between the different sized clusters is the position of the maxima and minima of the dipole-quadrupole interaction, in the case of the 30 a.u and 40 a.u clusters the cycle begins with a peak at 20 degrees and ultimately leads to trough at 310 degrees. The larger 50 a.u cluster in contrast begins with a trough at 20 degrees and ultimately leads to a peak at 310 degrees. The dominant forces that occur for the larger 50 a.u cluster at 135 degrees of profile rotation are highlighted using a simple dipole surrounded by a quadrupole square net (Figure 100).

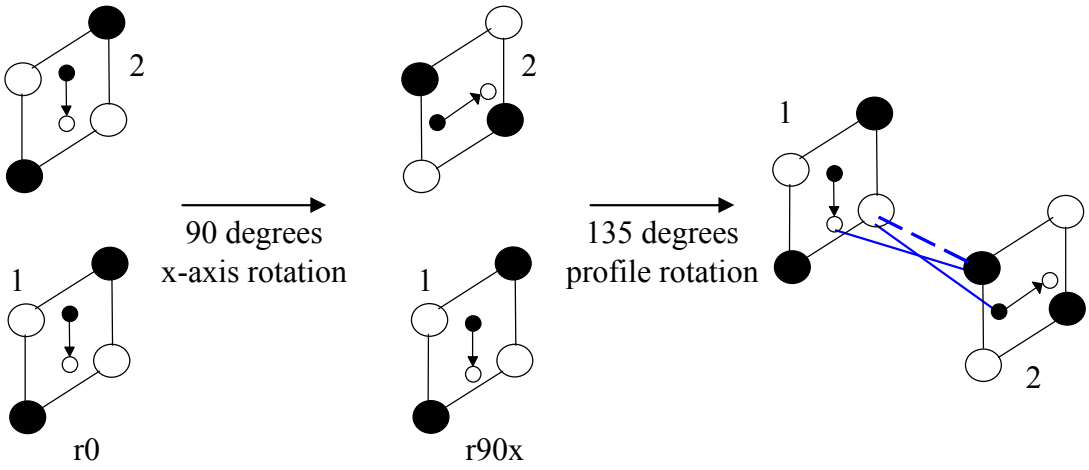

Figure 100 - *The simple representation of the clusters as dipoles surrounded by a square net quadrupole. The left figures show the r0 configuration, the central figures shows the r90x configuration and the right figures show the r90x configuration at 135 degrees of profile rotation. The blue dashed lines indicate attractive interactions, the heavy dashed lines are for quadrupole interactions only and the lighter dashed lines are for dipole-quadrupolre interactions only.*

The simple diagram of the forces between the clusters in the r90x configuration at 135 degrees profile rotation illustrates how the dipole-quadrupole and quadrupole-quadrupole forces augment one another to result in the odd minima observed at 310 or 135 degrees of profile rotation in all of the three clusters. The r90z configuration data in Figure 99 for all three clusters has energies 100 times smaller than the r90x configuration results, this is due to the fact that all the multipole forces are orthogonal to one another during the building of energy profile and as such there is essentially no energy interaction between the clusters except for subtle errors in rotating the second cluster in order to obtain the desired r90z configuration. This can be simply explained using a dipole surrounded by a square net quadrupole (Figure 101), there are no energies of interactions as both the attractive and repulsive interactions cancel one another's effects.

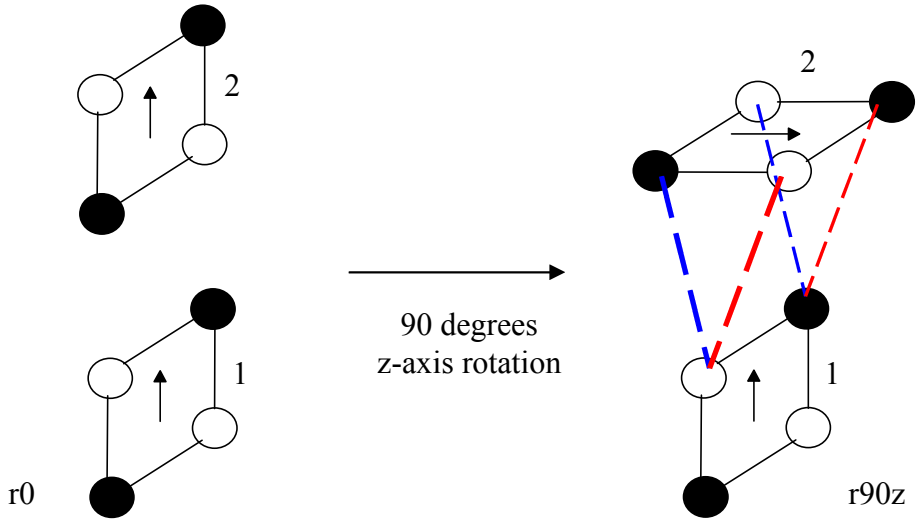

Figure 101 - *Simple depiction of the r90z configuration showing that there are equally repulsive and attractive interactions between the clusters throughout the duration of the energy profile construction. There is no dipole-dipole, dipole-quadrupole or quadrupole-quadrupole interaction as the dipoles and quadrupoles are orthogonal to one another. The blue dashed lines shows attractive interactions whilst the red dashed lines show repulsive interactions.*

4.5 Summary

The results for the wurtzite nanoclusters indicate that there are a number of odd orientations of the clusters with respect to the dipole moment that are possible due to the presence of the other multipole forces, these being the dipole-quadrupole and quadrupole-quadrupole interactions. The most favourable orientation of the clusters with respect to the dipole and quadrupole interactions between the clusters is similar to the head to tail interaction observed in the zinc blende clusters. In contrast, the presence of the quadrupole interactions in the wurtzite cluster also aids the ability of clusters to come together to form nanowires. The mechanism for the self-assembly of nanocrystals can be formulated from the nanocluster data by means of simple scenario in Figure 102. Initially nanocrystals in solution are dispersed evenly and the long range dipolar forces between the nanocrystals guide them to form a loosely bound chain (pearl necklace) with dipoles oriented head-tail. Overtime the nanocrystals rotate about the chain or dipole axis, but this has no effect on the dipole-dipole energy between nanocrystals. It does, however, strongly affect the quadrupole interactions between the nanocrystals. The nanocrystals can be imagined to continue rotating about the chain or dipole axis until a favourable quadrupole interaction is found; this then acts to loosely lock the nanocrystals in position like pieces of Lego. At longer times surface reconstruction and Ostwald ripening result in the elimination of gaps between the nanocrystals and the formation of nanowires.

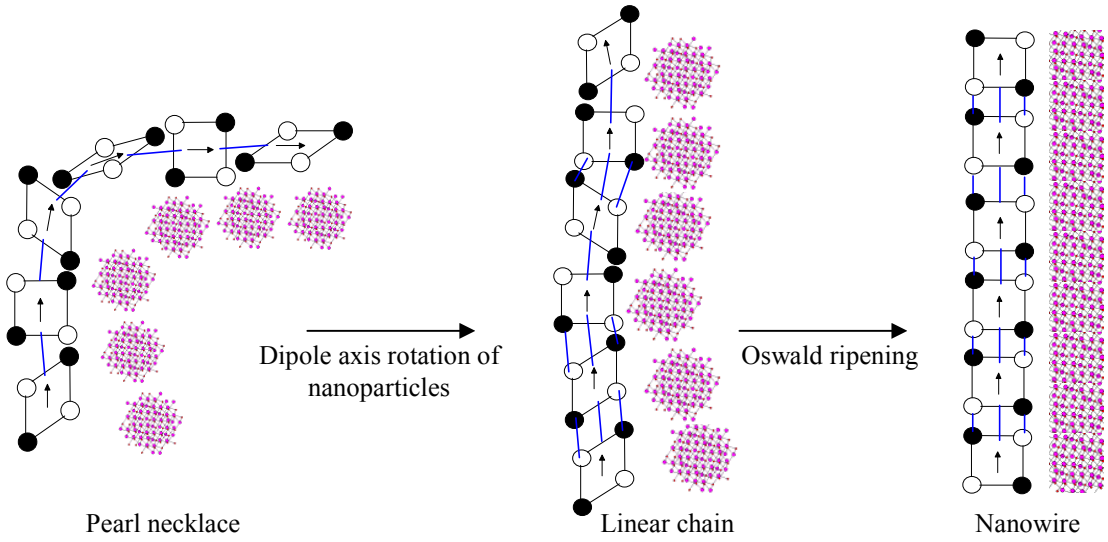

Figure 102 - *Mechanism depicting the self-assembly of random nanoparticles from initial pearl necklace chain formations, via dipole-dipole interactions, followed by*

dipole axis rotation of nanoparticles resulting in the formation of liner chain due to quadrupole-quadrupole interactions. The final step involves Ostwald ripening and surface reconstruction to yield wurtzite nanowires.

Chapter 5 Stockmayer fluid

5.1 Introduction to Stockmayer fluid

In order to understand the evolution of nanostructures a computational model needs to be used that could possibly describe their formation, such as the one-dimensional nanowires observed. A significant motivation is to choose a model which is both relatively simple in terms of its parameterisation, and hence is computationally tractable and well understood. One possible computational model fitting the criteria is the Stockmayer fluid[174]. This model in part contains a more familiar function, the Lennard-Jones 6-12 potential[175], which describes the interaction between two neutral spherical bodies i and j with diameters σ and well depth ε (Equation 25).

$$U_{ij}(LJ) = 4\varepsilon\left[\left(\frac{\sigma}{r_{ij}}\right)^{12} - \lambda\left(\frac{\sigma}{r_{ij}}\right)^{6}\right]$$

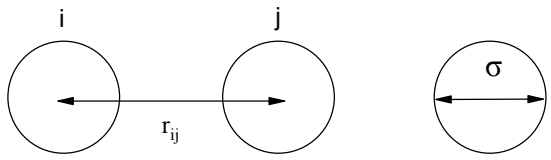

Equation 25 - *The Lennard-Jones 6-12 potential equation. This describes the energy interaction, $U_{ij}(LJ)$, between two spherical neutral bodies i and j. The r_{ij} term is the separation between the two bodies i and j. The σ term is the diameter of the bodies, whilst the ε term is the well depth. The λ term is a variable that can be adjusted to any value between zero and one.*

The Lennard-Jones 6-12 potential contains essentially two terms, a long-range attractive term, $(1/r_{ij})^6$, and a short-range repulsive term, $(1/r_{ij})^{12}$, to calculate the energy of interaction between particles. The well depth ε simply determines the energy value of the minimum in this potential, whilst the minimum in the Lennard-Jones 6-12 potential always occurs at $2^{1/6}$ σ (if λ=1). This is exemplified by using set values for all these parameters, with the resultant Lennard Jones potential plotted in Figure 103. The Lennard-Jones potential graph is clearly shown to have the well depth ε and minima at the expected positions.

The Lennard-Jones potential described contains an adjustable parameter λ, which can be changed from any value from zero to one. When this parameter is set to one then the typical Lennard-Jones 6-12 potential is achieved, however when set to zero the attractive component of the Lennard-Jones potential is removed and only the repulsive components remains. This results in a transition from the Lennard-Jones potential to the soft sphere potential as the value of λ decreases from 1 to zero[176] (Equation 26).

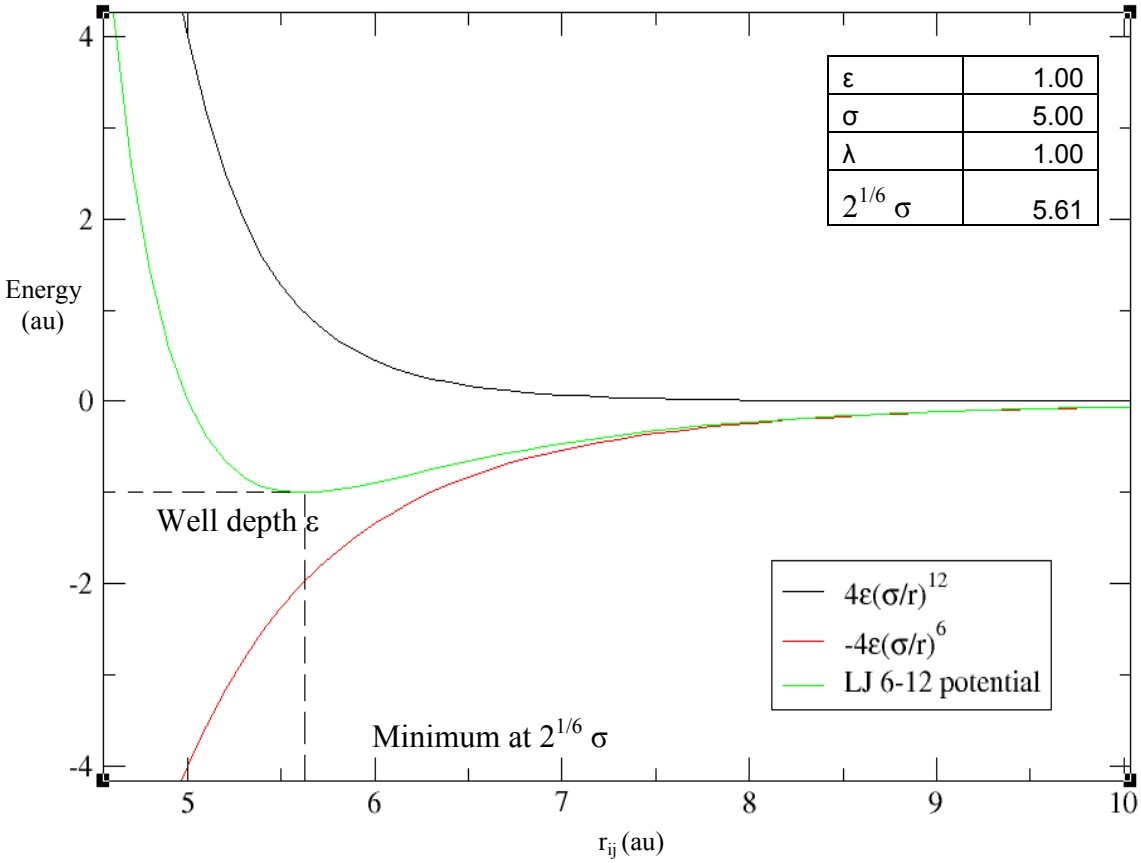

Figure 103 - *The Lennard-Jones 6-12 potential graph. The Lennard-Jones (LJ) potential (green line) is made up of a repulsive component (black line) and an attractive component (red line). The parameters used to construct the Lennard-Jones potential are listed in the top right hand corner of the figure. The graph shows the minima for the Lennard-Jones potential to be at 5.61 a.u, which is $2^{1/6}$ σ, and the well depth to be the value of ε.*

$$U_{ij}(ss) = 4\varepsilon\left(\frac{\sigma}{r_{ij}}\right)^{12}$$

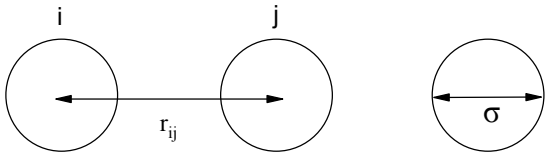

Equation 26 - *The soft sphere potential equation. This describes the energy interaction, $U_{ij}(SS)$, between two spherical neutral bodies i and j. The r_{ij} term is the separation between the two bodies i and j. The σ term is the diameter of the bodies, whislt the ε term is the well depth.*

The Stockmayer fluid potential in addition to the Lennard-Jones potential contains a dipole-dipole energy interaction term between two bodies i and j, the magnitude of the dipole moments on each body are represented as μ_i and μ_j respectively (Equation 27).

$$U_{ij}(dd) = \frac{1}{4\pi\varepsilon_o\varepsilon_r}\frac{\mu_i\mu_j}{r_{ij}^{\,3}} - \frac{3(\mu_i r_{ij})(\mu_j r_{ij})}{r_{ij}^{\,5}}$$

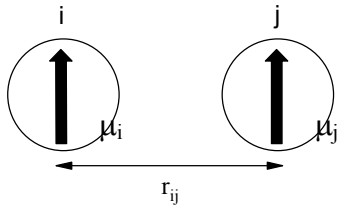

Equation 27 - *The dipole-dipole interaction energy equation. This describes the dipole-dipole interaction energy, $U_{ij}(dd)$, between two bodies i and j each with dipole moments μ_i and μ_j respectively at different separations, r_{ij}, between the two bodies.*

The Stockmayer fluid, for which λ =1, encompasses the $U_{ij}(LJ)$ + $U_{ij}(DD)$ term to give the total energy of the system, U_{ij} = $U_{ij}(LJ)$ + $U_{ij}(dd)$. The dipole-dipole interaction energy can be derived by considering the fact that dipole moments in a neutral body arise from an imbalance of charges, the interaction energy of two charges vary according to $1/r_{ij}$ and are represented in terms of a tensor (Equation 28).

$$T = \left(\frac{1}{r_{ij}}\right) \qquad \text{where;} \quad r_{ij} = \sqrt{r_x^{\,2} + r_y^{\,2} + r_z^{\,2}}$$

$$T_\alpha = \nabla_\alpha\left(\frac{1}{r_{ij}}\right) = -\frac{r_\alpha}{r_{ij}^{\,3}}$$

$$T_{\alpha\beta} = \nabla_{\alpha\beta}\left(\frac{1}{r_{ij}}\right) = \frac{3r_\alpha r_\beta - {r_{ij}}^2 \delta_{\alpha\beta}}{{r_{ij}}^5}$$

Equation 28 - *The dipole tensor derivation. The first statement describes the variation of energy between two charges is $1/r_{ij}$, when this is differentiated with respect to distance the result is the variation of the energy with respect to a charge and dipole T_α . The second derivative $T_{\alpha\beta}$ describe the variation of energy between two dipoles. The $\delta_{\alpha\beta}$ is equal to one when $\alpha = \beta$ and zero when $\alpha \neq \beta$.*

The final result in Equation 28 becomes equivalent to the dipole-dipole interaction energy term encountered in Equation 27, when multiplied by the dipole moments, in the same plane as one another such that $\alpha = \beta$ and $\delta_{\alpha\beta} = 1$, on the two respective particles, i and j, (Equation 29).

$$U = \mu_{i\alpha}\mu_{j\beta}T_{\alpha\beta}$$

$$U = -\mu_{i\alpha}\mu_{j\beta}\frac{3r_\alpha r_\beta - {r_{ij}}^2\delta_{\alpha\beta}}{{r_{ij}}^5}$$

$$U = \mu_{i\alpha}\mu_{j\beta}\frac{{r_{ij}}^2\delta_{\alpha\beta} - 3r_\alpha r_\beta}{{r_{ij}}^5}$$

$$U = \mu_{i\alpha}\mu_{j\beta}\left(\frac{{r_{ij}}^2\delta_{\alpha\beta}}{{r_{ij}}^5} - \frac{3r_\alpha r_\beta}{{r_{ij}}^5}\right)$$

$$U = \frac{\mu_{i\alpha}\mu_{j\beta}\delta_{\alpha\beta}}{{r_{ij}}^3} - \frac{3r_\alpha r_\beta \mu_{i\alpha}\mu_{j\beta}}{{r_{ij}}^5}$$

where; $\alpha = \beta$ then $\delta_{\alpha\beta} = 1$

where; $\alpha \neq \beta$ then $\delta_{\alpha\beta} = 0$

$$U = \frac{\mu_{i\alpha}\mu_{j\beta}}{{r_{ij}}^3} - \frac{3(r_\alpha\mu_{i\alpha})(r_\beta\mu_{j\beta})}{{r_{ij}}^5}$$

Equation 29 - *The rearrangement of the dipole-dipole interaction energy equation. The dipole-dipole interaction energy derived from the tensor is shown to be*

equivalent to the form of that encountered in Equation 27, when α=β and as such δαβ=1.

In order to understand the presence of dipole interactions between two bodies one can imagine a simple example in two dimensions (X and Y), where two dipoles i and j a fixed distance, r_{ij}, apart and with the angle θ between the centres of the two dipoles (Figure 104). In this example the dipoles are both pointing in the Y direction for ease of showing how the dipole tensor works.

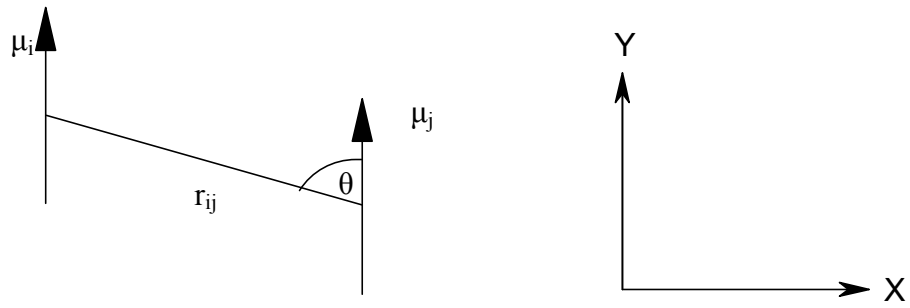

Figure 104 - *Two interacting dipoles in a single plane. The figure shows the two dipoles μ_i and μ_j that are a constant distance r_{ij} apart from one another at a variable angle θ between the two centres. The dipoles in this depiction only have a Y component.*

There are only Y components to the dipoles in this 2D depiction ($\mu_i = \mu_{iy}$ and $\mu_j = \mu_{jy}$), which means the energy of this interaction can be evaluated using the dipole tensor term for the T_{yy} component as it is equal to the T_{ij} (Equation 30). It is then possible to calculate the separation between the two centres of the dipoles with respect to the Y direction, r_{yy}, in terms of the separation r_{ij} between the two dipoles, when there is angle θ between the two centres (Figure 105).

$$U_{ij}(dd) = -\mu_i \mu_j T_{ij}$$ as; $\mu_i \mu_j = \mu_{iy} \mu_{jy}$, then

$$U_{ij}(dd) = -\mu_i \mu_j T_{yy}$$

$$U(dd) = -\mu_i \mu_j \frac{3r_y r_y - r_{ij}^2}{r_{ij}^5}$$

Equation 30 - *The dipole-dipole interaction energy for two dipoles i and j pointing in the same direction at a fixed separation r_{ij}. The dipole-dipole energy simplifies to evaluation of the Y component as the dipoles μ_i and μ_j point only in the Y direction.*

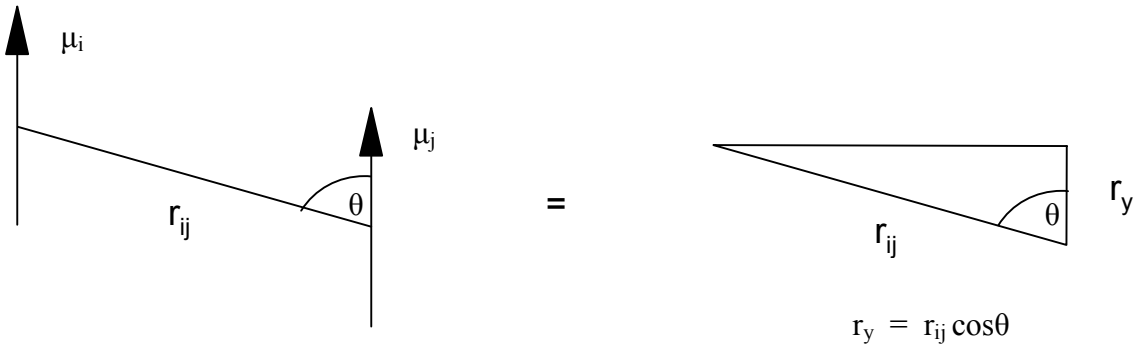

Figure 105 - *The separation between two dipoles in the Y direction. The separation between the two dipoles in the Y direction r_y can be in terms of the actual separation between the dipoles r_{ij} and an angle θ between the centres of the two dipoles.*

The separation of the dipoles in terms of r_{ij} and an angle θ can be used to determine the dipole-dipole energy interaction when this is substituted into the final equation of Equation 30 to obtain another common form of the dipole-dipole interaction energy (Equation 31).

$$U_{ij}(dd) = -\mu_i \mu_j \frac{3r_y^2 - r_{ij}^2}{r_{ij}^5} \qquad \text{as;} \quad r_y = r_{ij}\cos\theta \text{ , then}$$

$$U(dd) = -\mu_i \mu_j \frac{3r_{ij}^2\cos^2\theta - r_{ij}^2}{r_{ij}^5}$$

$$U(dd) = -\mu_i \mu_j \frac{3\cos^2\theta - 1}{r_{ij}^3}$$

$$U(dd) = \mu_i \mu_j \frac{1 - 3\cos^2\theta}{r_{ij}^3}$$

Equation 31 - *The derivation of the dipole-dipole energy between two linear dipoles. The dipole-dipole energy between to linear dipoles, i and j, with magnitudes of μ_i and μ_j respectively can be determined, when an angle θ and the separation r_{ij} is known.*

This form of the dipole interaction can be used to show the range of attractive and repulsive configurations between dipoles a fixed distance apart, by varying the angle θ between the dipoles so that a plot of $1\text{-}3\cos^2\theta$ vs. θ can be made (Figure 106).

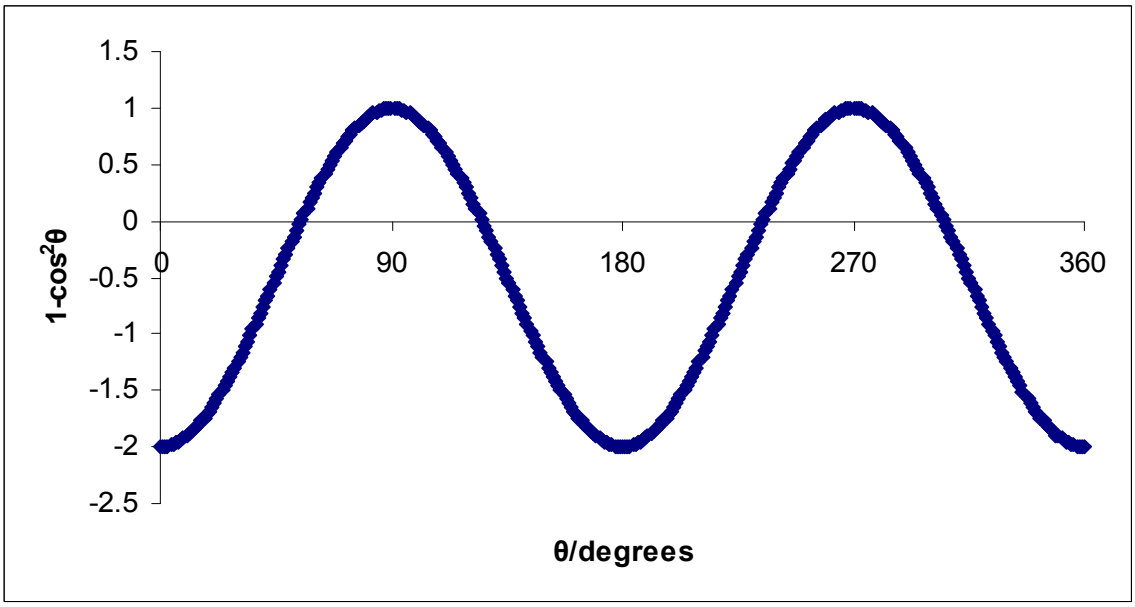

Figure 106 - *The plot of $1\text{-}3\cos^2\theta$ vs. θ. This graph essentially shows the variation of energy independent of the dipole moments on the bodies and separation between them. There are minima at 0 and 180 degrees, the result of the head-tail orientation. There are maxima at 90 and 270 degrees, which are attributed to the parallel orientation of dipoles.*

The graph illustrates there are minima at 0 and 180 degrees of the angle θ and similarly there are maxima at 90 and 270 degrees of the angle θ. These minima and maxima are the result of two configurations for the dipoles, the head-tail and parallel orientations respectively. These configurations are shown with their respective

energies independent of the fixed separation r_{ij} and dipole moments on each body (Figure 107).

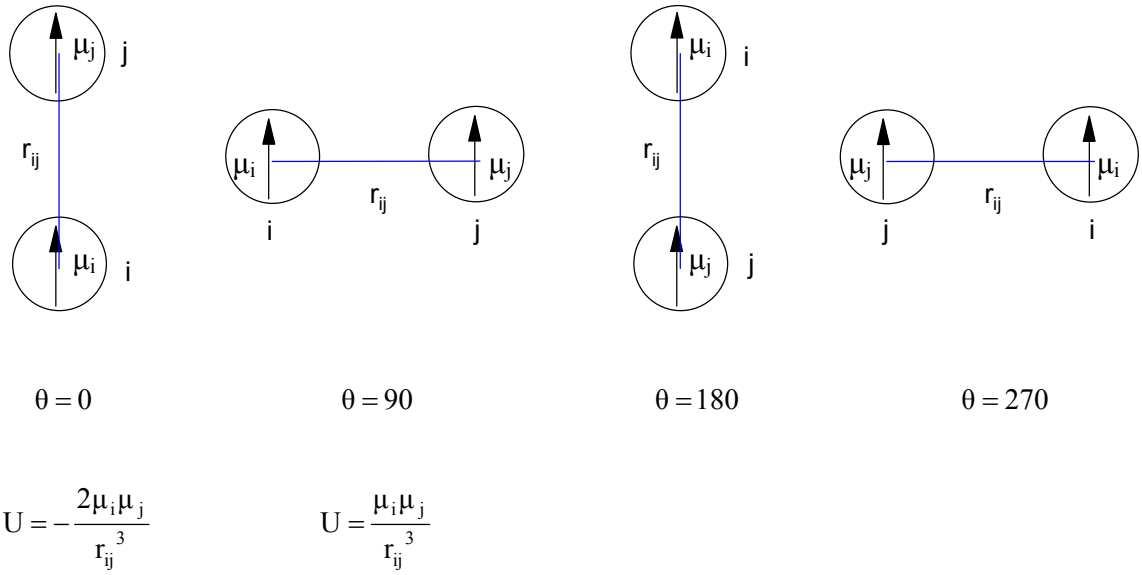

Figure 107 - *The different orientations of two bodies with central dipole moments μ_i and μ_j as a function of the angle θ between the two bodies at a fixed separation of r_{ij}. The angle θ is increasing ongoing from left to right. The configurations at 0 and 180 degrees are equivalent, head to tail configuration, and have an attractive energy U which is twice the magnitude of that obtained for the repulsive configurations at 90 and 270 degrees, the parallel configuration.*

The figure illustrates the two configurations, the head-tail and the parallel orientations that occur at angles of 0 and 180 degrees and angles of 90 and 270 degrees respectively. The head-tail orientation is an attractive configuration that is twice the magnitude of the repulsive parallel orientation. The energy difference between these two configurations is in fact three times that observed for the parallel orientation. The are other configurations which can be examined between two bodies with dipoles at fixed separations apart if one considers a further angle ψ between the dipoles to account for the relative orientations of the dipole moments between the two bodies (Figure 108).

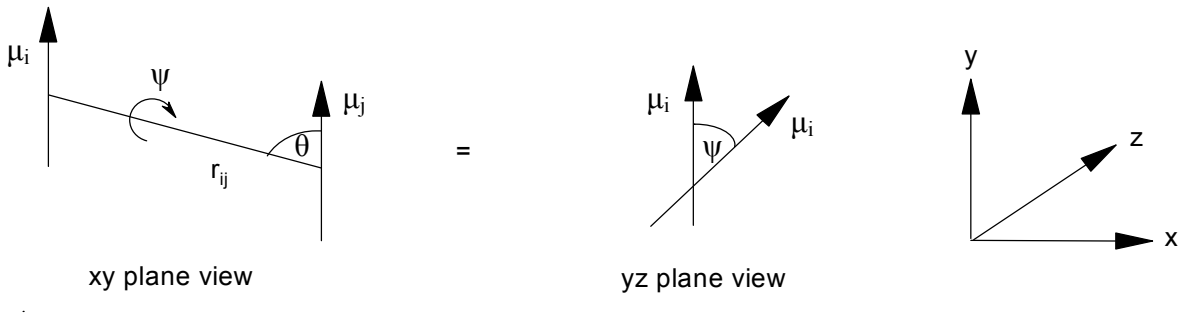

Figure 108 - *The rotation angle ψ between the dipole moments. This angle ψ is shown from the xy plane and yz planes, in addition it should not be confused with the angle θ between the dipoles i and j at a fixed separation of r_{ij}.*

The introduced angle ψ can be used to determine the Y component of the dipole moment, when one of the dipoles for instance μ_i is fixed to point only in the Y direction, so that any rotation of the μ_j about an angle ψ can be used to determine its Y component by using a similar cosine function encountered in Figure 105 and hence the dipole-dipole interaction energy at a fixed separation r_{ij} with angles θ and ψ (Equation 32). This leads to a subtle modification of the previously encountered Equation 31.

$$U(dd) = \mu_i \mu_j \frac{1 - 3\cos^2\theta}{r_{ij}^3} \qquad \text{as; } \mu_{jy} = \mu_j \cos\varphi \text{ , then}$$

$$U(dd) = \mu_i \mu_j \cos\varphi \frac{1 - 3\cos^2\theta}{r_{ij}^3}$$

Equation 32 - *The dipole-dipole interaction energy between two dipoles with rotational angles of θ and ψ. The separation is fixed at r_{ij} between the two dipoles of magnitude μ_i and μ_j.*

This form of the dipole interaction can be used to show the range of attractive and repulsive configurations between dipoles a fixed distance apart, by varying the angle θ between the dipoles so that a plot of $1\text{-}3\cos^2\theta$ vs. θ can be made similar to that observed in Figure 106. On this occasion the angle ψ will be set to 180 degrees, cos(180) = -1, in order to achieve a starting configuration that is the exact opposite of the head-tail configuration, the head-head configuration (Figure 109).

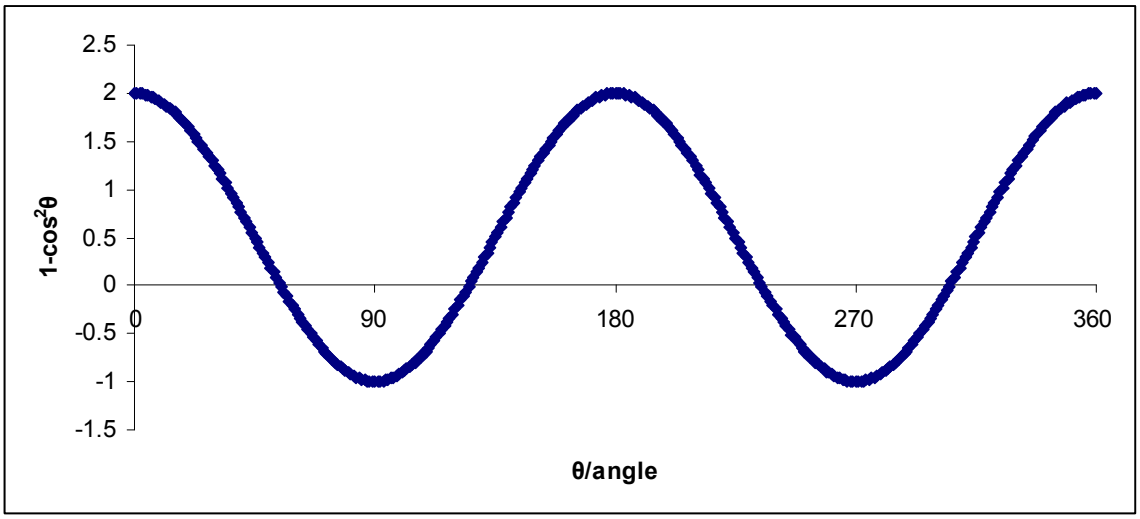

Figure 109 - *The plot of $1\text{-}3\cos^2\theta$ vs. θ. This graph essentially shows the variation of energy independent of the dipole moments on the bodies and separation between them. This particular graph has the angle ψ set at 180 degrees. There are maxima at 0 and 180 degrees, these are the head-head and tail-tail orientations respectively. The minima at 90 and 270 degrees are attributed to the ant-parallel orientation.*

The graph illustrates there are minima at 90 and 270 degrees of the angle θ and similarly there are maxima at 0 and 180 degrees of the angle θ when ψ is set to 180 degrees. These minima and maxima are the result of two configurations for the dipoles, the anti-parallel and head-head (tail-tail) orientations respectively. These configurations are shown with their respective energies independent of the fixed separation r_{ij} and dipole moments on each body (Figure 110).

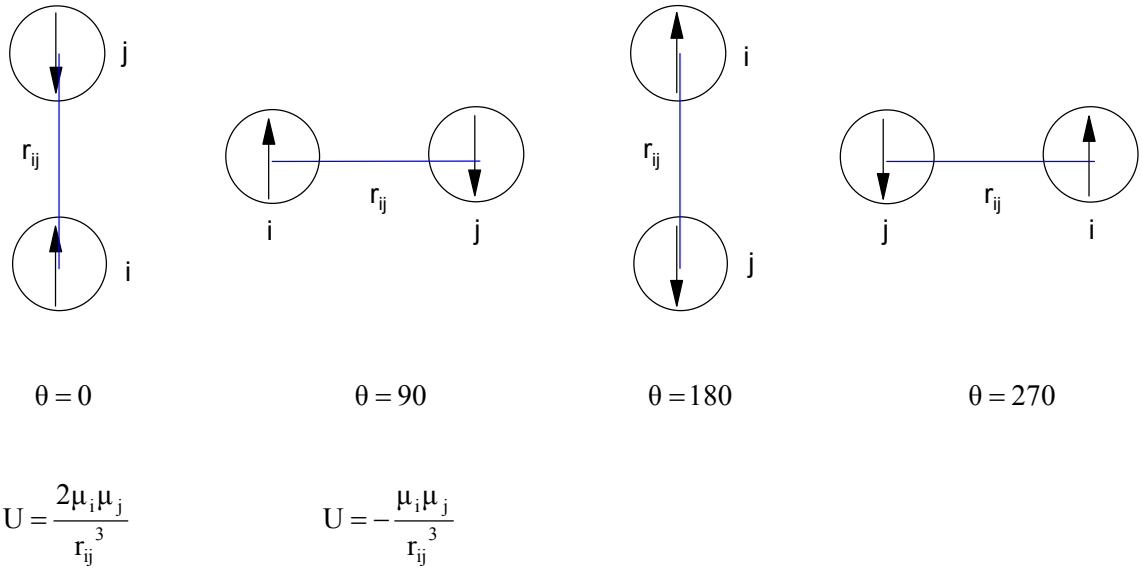

Figure 110 - *The different orientations of two bodies with central dipole moments μ_i and μ_j as a function of the angle θ between the two bodies at a fixed separation of r_{ij}. The angle θ is increasing ongoing from left to right. The configurations at 0 and 180 degrees are equivalent, head-head and tail-tail configurations respectively, and they have a repulsive energy U which is twice the magnitude of that obtained for the attractive configurations at 90 and 270 degrees, the anti- parallel configuration.*

The figure illustrates the two configurations, the head-head (tail-tail) and the anti-parallel orientations that occur at angles of 0 and 180 degrees and angles of 90 and 270 degrees respectively. The head-head orientation is a repulsive configuration that is twice the magnitude of the attractive anti-parallel orientation. The energy difference between these two configurations is three times that observed for the anti-parallel orientation, similar to those encountered for the previous head-tail and parallel orientations. The energies of the different dipole-dipole orientations discussed previously are all summarized (Figure 111). The figure shows that the head-tail configuration is the lowest energy followed by the anti-parallel configuration, which is half the energy of the former. There is a similar pattern for the head-head (tail-tail) and parallel configurations, the former is highest in energy and is twice the energy of the parallel orientation.

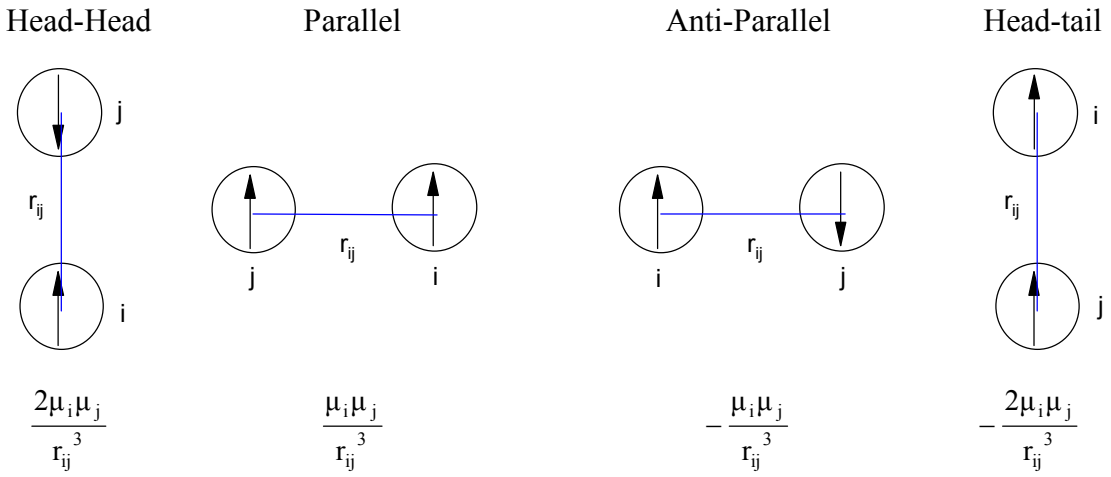

Figure 111 - *The range of dipole-dipole interactions listed in terms of decreasing energy. The various dipole configurations are listed in decreasing energy ongoing from left to right, with their respective energies listed below in terms of the separation r_{ij} between the dipoles and the magnitudes of the dipole moments μ_i & μ_j.*

5.2 Stockmayer fluid simulations

The previous sections show the head to tail alignment of dipoles to be the most energetically favourable. How does this translate to the condensed phase in terms of the structures formed by the Stockmayer fluid? The formation of chain structures was first discussed by de Gennes and Pincus in their theoretical study of ferromagnetic colloids[177]. The magnetic properties of the colloids were described by the dipole-dipole interaction discussed previously (Equation 27). The particles or grains formed linear chain structures in the presence and direction of high external magnetic fields. There were also shorter chain structures and ring structures in the absence of the external magnetic field[177]. The structures adopted by a few magnetic particles were modelled, essentially using dipolar hard sphere (DHS) potential, in both the presence and absence of an applied magnetic field[178]. The work showed similar results in terms of the magnetic particles forming ring structures in the absence of the magnetic field and hence no resultant magnetic moment. The same magnetic particles subjected to an applied magnetic field produce chain structures with a resultant magnetic moment[179] (Figure 112).

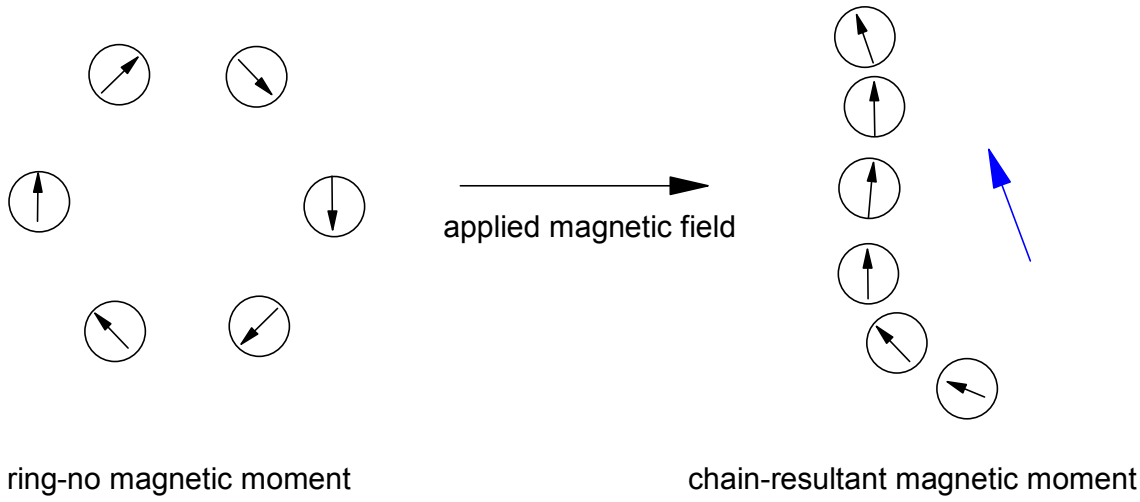

Figure 112 - *The structures of a few magnetic particles in varying applied magnetic fields. The left figure show the magnetic particles adopting a ring structure in the absence of an applied magnetic field. The right figure shows the result of an applied magnetic field resulting in a chain structure with a resultant magnetic moment indicated by the blue arrow.*

They, de Gennes and Pincus[177], also predicted the presence of a conventional phase diagram, containing a gas, liquid and solid phases, for these particles. The phase diagram for these dipolar type systems was investigated using the dipolar hard sphere (DHS) fluid, which encompasses a hard repulsive core with dipole interaction, and the Stockmayer fluid model. These early simulations[176,180,181] showed that phase coexistence curves were present only if there were sufficiently strong dispersive interactions (λ>0.3) present when using the Stockmayer fluid model and in the absence of or weak dispersive forces, DHS fluid, there was living chain like polymers formed that did not show phase separation into liquid or vapour phases. The vapour-liquid equilibria for the Stockmayer fluid has been thoroughly investigated by a number of groups also showing the presence of a dispersive force is necessary to obtain vapour and liquids phases[182,183]. The work of Wei and Patey in simulating dipolar soft spheres (DSS) revealed the transition from an isotropic system at low densities to a ferroelectric ordered phase at higher densities[184,185] (Figure 113). The work of Weis and Levesque with dipolar hard spheres also showed agreement with presence of ferroelectric phases[186]. In addition, however they found at very high densities that the dipolar hard spheres split into two domains of ferroelectric ordering

in opposite directions resulting in no overall polarization or magnetic moment. They also showed the formation of large chain structures at low temperatures and densities and that it was possible to obtain ferroelectric phases at these low densities and temperatures[187]. It should be noted that the ferroelectric ordering in dipolar hard spheres can be affected by the polydispersity in both the relative size of the particles and the dipole moments[171]. The dipolar hard spheres also appear to exhibit isotropic liquid phase transitions at low temperatures[188].

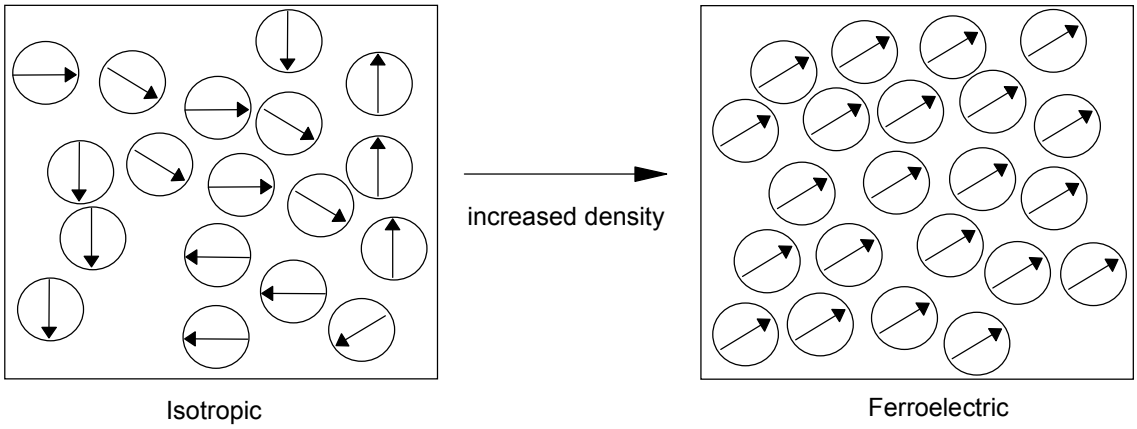

Figure 113 - *The Isotropic and ferroelectric phases in a 2D depiction. The left figure shows the isotropic phase found for many simulations at low density for DHS or DSS fluids. The right figure shows the ferroelectric phase, which is characterised by the fact that dipoles align in a single direction.*

The formation of ferroelectric phases is also observed to occur in the extended dipole model. In this model the point dipoles used in previous simulations are replaced by placing two opposite charges symmetrically with respect to the centre of the spherical body[189], the separation d between the two charges q give rise to the dipole moment $\mu=qd$. In the first instance it is found that varying the ratio d/σ whilst keeping the overall dipole moment constant, by varying the magnitude of the charges, can have a profound effect on the Stockmayer fluid. When the ratio of d/σ is greater than 0.6 the formation of the ferroelectric phase occurs, and this phase is observed at lower dipole moments than previous point dipole models[190]. It has also been shown that with the use of this extended dipole model, orientationally ordered phases also occur at a range of densities[191].

The extended dipole model is similar to an earlier model employed by Camp and Patey in which the spheres contain two point dipoles equally distant from the centre of the sphere (Figure 114). This two point dipole model also showed the formation of ferroelectric phases with increasing densities from an isotropic phase, when the ratio between the separation of the dipoles and the diameter of the sphere d/σ was less than 0.3. When the ratio of d/σ was set to 0.3, the model showed that the formation of antiferroelectric phases was favoured over the formation of ferroelectric phases[192].

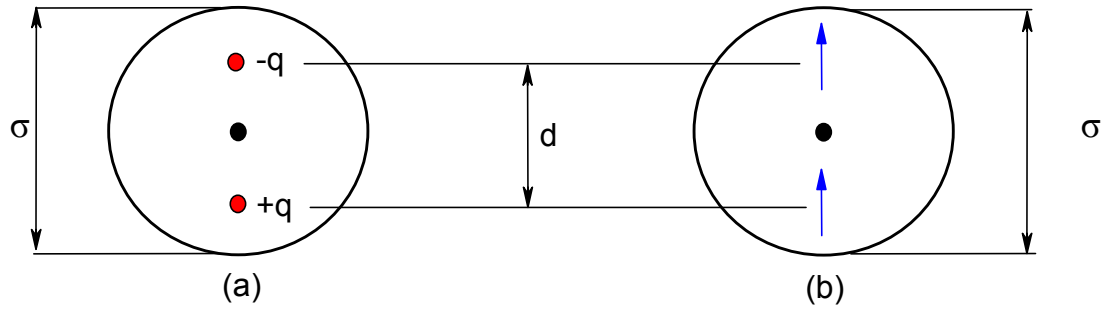

Figure 114 - *The extended dipole and the two point dipole models. The left figure (a) is the extended dipole model with the two charges +q and –q placed an equal distant from the centre of the sphere, with the separation between the charges being d. The right figure (b) is the two point dipole model with two dipoles an equal distant from the centre of the sphere, with the separation between the dipoles is also d. The spheres have diameters σ.*

The work of Xu and co-workers[193] investigated the formation of chains and ring structures in dipolar fluids and the effect of having varying size of surfactant coatings on the dipolar particles (Figure 115); the surfactant coatings only interact with one another when in direct contact and have an infinite repulsive energy in this situation. There is no energy interaction between the surfactant coatings when not in contact. The formation of chain and ring structures has been shown to be prevalent at low densities and temperatures for dipolar fluids[194,195]. The research of Xu and co-workers also shows a significant energy barrier to the formation of rings from the bending of preformed chains; this implies that the formation of rings only occurs through aggregation. In addition an almost linear relationship is obtained between the transition from ring and chain region to chain only region with relation to the

surfactant coating layer size and dipole moment squared. This implies that small coating or no layers on the dipolar fluid particles favour the formation a mixed region of rings and chains, whilst large coating layers favour chain only structures[193].

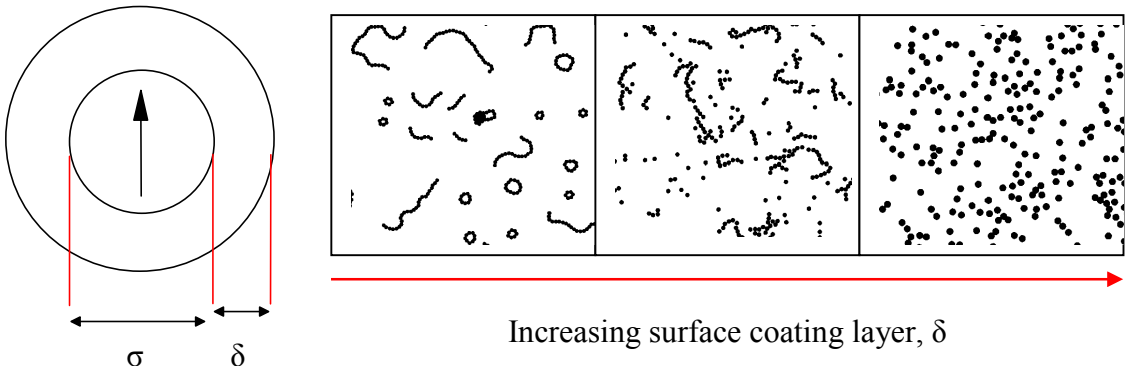

Figure 115 - *The formation of ring and chain structures using a dipole fluid model with additional surface coating layer. The left figure shows a conventional dipolar fluid particle of diameter σ with a central point dipole. The diameter is increased by an amount δ to signify the surfactant coating. The right figure shows the effect of increasing the value of δ, on going from left to right, resulting in a transition from ring & chain region to chain only and no aggregated structures*[193].

The specific examples of cobalt nanoparticles of approximate diameter 32 nm with a small silca coated shell of approximately 4 nm displays the formation of pearl necklace style chains that are aggregated to form loops and chain structures; Salgueirino-Maceira and co-workers[196] also attribute the formation of such structures to the magnetic dipole-dipole interactions between the cobalt nanoparticles. Loop structures of cobalt are reproduced by the simulation work of Hucht and co-workers[197] using the dipolar hard sphere model with the ratio between the surface coating and magnetic cobalt diameter set to $\delta/\sigma = 0.12$ (Figure 116).

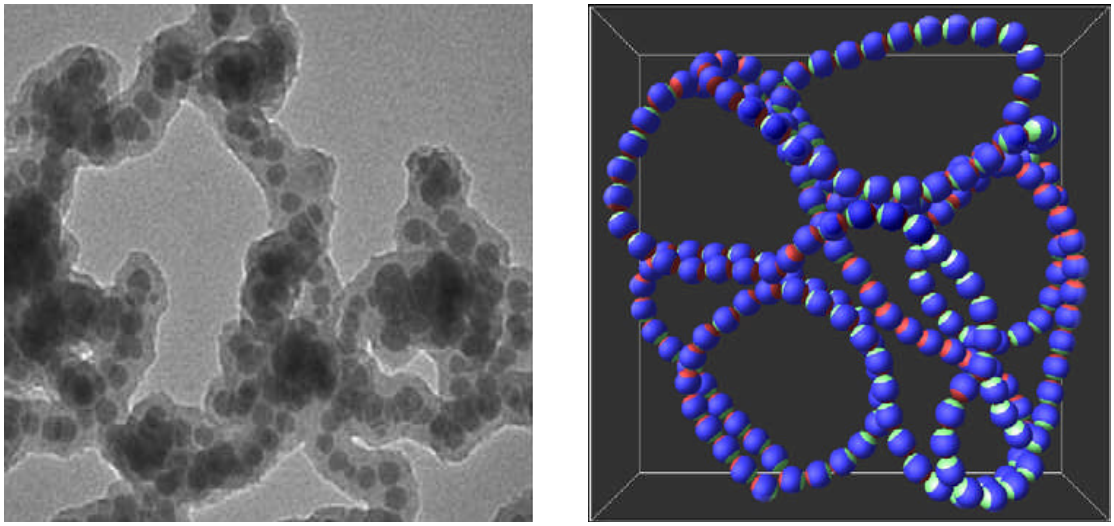

Figure 116 - *The formation of chain loop structures in the synthesis of cobalt nanoparticles coated with silca shell. The left figure shows the experimental transmission electron microscopy image of the cobalt nanoparticle with a silca shell in loop looking structures. The right figure shows the simulation results of Hucht and co-workers for cobalt nanoparticles using a dipolar hard sphere potential*[196].

The investigations of Stevens and Grest initially using dipolar soft spheres showed that the phase coexistence did not occur in zero fields, though it did occur in an applied field. The chain structures of the dipolar soft spheres can be seen to align in the direction of the applied field[198] (Figure 117). The difference between the dipolar soft sphere and Stockmayer fluid potential is also highlighted with the latter forming spherical droplet structures at the coexistence point; these droplet structures were also shown to elongate when in the presence of an applied field[199] (Figure 118). The dipolar soft sphere shows no clustering of the particles under exactly the same conditions as the Stockmayer fluid spheres in the absence of a field. The application of a field on the Stockmayer particles results in the clustered structures extending in the direction of the applied field. Their work also shows that ferroelectric ordered phases also occur at high densities for the Stockmayer fluid as do more recent investigations[200,201].

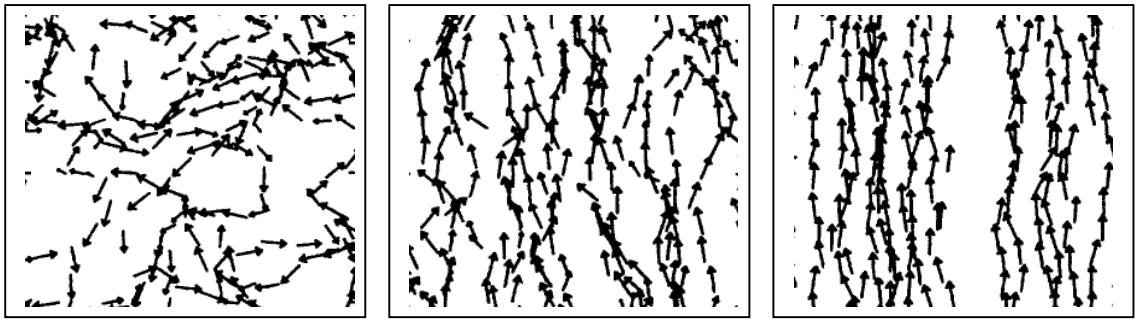

Figure 117 - *The chain structures formed by dipolar soft spheres in the absence and presence of an applied field. The left figure is in the absence of an applied, the other figures are in the presence of an applied field, with the magnitude of the field increasing on going from left to right. The arrows represent the dipolar soft sphere particles and simultaneously the direction of the dipoles*[198].

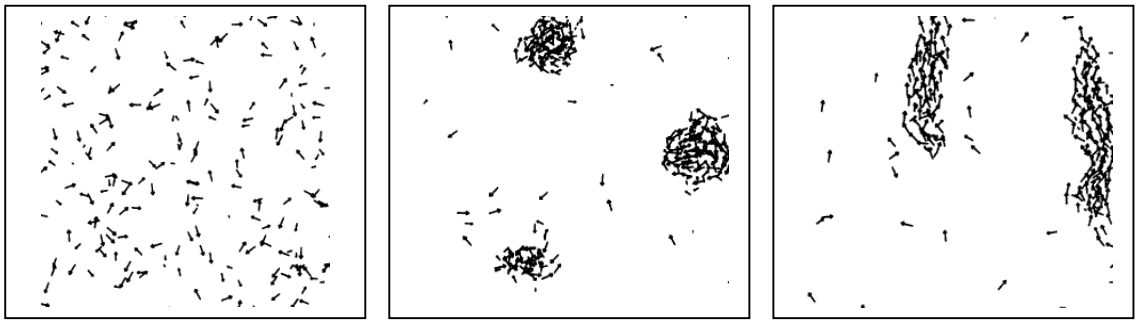

Dipole soft sphere | Stockmayer fluid | Stockmayer fluid in a field

Figure 118 - *The difference in the structures adopted by the dipolar soft sphere and Stockmayer particles. The left figure shows the dipole soft sphere structure, the central figure shows the Stockmayer fluid under the same conditions. The final figure on the right is the Stockmayer fluid under an applied field. The arrows simultaneously present the dipolar particles and the direction of the dipoles*[199].

The work of Hentschke and co-workers involved simulations of the Stockmayer fluid with larger magnitude of dipole moments, not considered in previous Stockmayer fluid simulations[202]. The results of these simulations showed the vapour-liquid transition to still occur using these larger dipole moments[203]. The relatively small contribution of the Lennard-Jones energy in these simulations compared to the dipolar energy lead Ivanov and co-workers to conjecture that the vapour-liquid phase separation was possible in dipolar systems[204]. The original authors however disagreed

with this conclusion and they were able to demonstrate this by showing the gas-liquid critical temperature T_c had a linear relationship with the dipole moment squared for the Stockmayer fluid, in agreement with previous studies[205], and crucially the gas-liquid critical temperature did not approach zero in the absence of or small dipole moments in the Stockmayer fluid. The dependence of the gas-liquid critical temperature T_c with the relative strength of the dispersion force λ of the Lennard-Jones potential was also plotted alongside that for the critical density ρ_c with the relative strength of the dispersion force λ (Figure 119). These results showed that as the strength of the Lennard-Jones dispersion force λ approached zero both the gas-liquid critical temperature and the critical density also reached zero. This indicated the results were in agreement with previous studies that showed in the absence of the dispersion force meant the dipolar soft and hard spheres did not display a vapour-liquid transition[206].

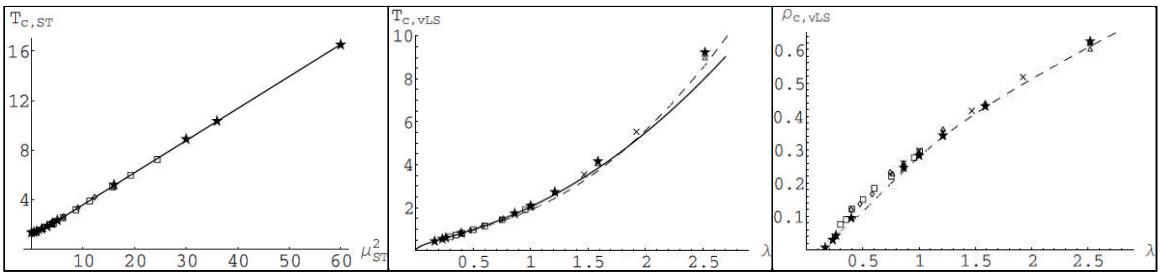

T_c vs μ^2 T_c vs λ ρ_c vs λ

Figure 119 - *The results of Hentschke and co-workers are presented. The left figure shows the critical temperature T_c vs the dipole moment squared μ^2. The central figure shows the critical temperature T_c vs the Lennard-Jones dispersion force strength λ. The right figure shows the critical density ρ_c vs the Lennard-Jones dispersion force strength λ*[206].

The formation of chain structures is prevalent throughout the three dipolar sphere models, the Stockmayer fluid, dipolar soft spheres and dipolar hard spheres[207,208]. The formation of a network of chains is often observed at low temperatures and densities[209], and there are a number of Y junctions present in such networks[210] (Figure 120). The average chain length of a system of dipolar hard spheres at equilibrium has been shown to increase with increasing dipole moments, whilst the diameter of the

spheres is kept constant[211,212]. The chain length also increases when decreasing the density, while the dipole moment is maintained[213].

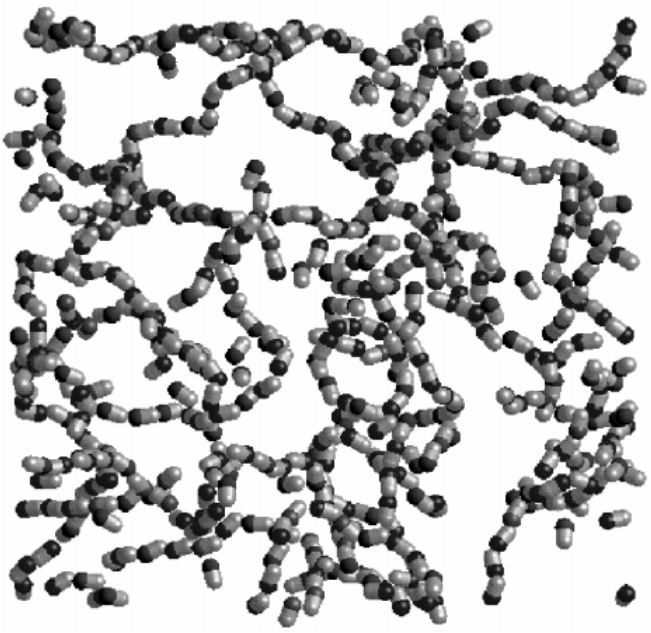

Figure 120 - *The equilibrium structure of 500 dipolar hard spheres at low temperature and density. The formation of a network of chain structures is visible. The dipolar hard spheres are represented as rod structures with the direction of the dipoles indicated by the black tips in the rods[209].*

5.3 The Stockmayer fluid and polar solvents

5.3.1 Solvation of ions

In the early 1990's the Stockmayer fluid model was used in trying to understand the process of solvation of ions in polar solvents, where the polar solvent molecules were represented by the Stockmayer fluid model, as it was considered important in understanding reactions[214]. The initial work evolved around solvation dynamics, examining the effect of rotational and translational solvent motions on the solvation process. It was found in general that the Stockmayer fluid model is a very a good model for describing the two regime relaxation behaviour, initially short-time followed by long time relaxation, of polar solvent in the solvation process[215-217]. This description matched well with previous theoretical studies specific to water[218],

acetonitrile[219], methanol[220], methyl-chloride[221] and with experimental work[222]. The short time relaxation was attributed to the rotational movements of the Stockmayer particles to realign into favourable orientations about ions. The long time relaxation was ascribed to the translational movements of the Stockmayer particles. In addition the response times of the Stockmayer particles to the presence of ions and changing charges was found to strongly affect Stockmayer particles closest to the ions, considered to be in the first shell. Subsequent shells of Stockmayer particles showed ever decreasing response times as the distance from the ions increased in the so called inward outward mechanism (Figure 121).

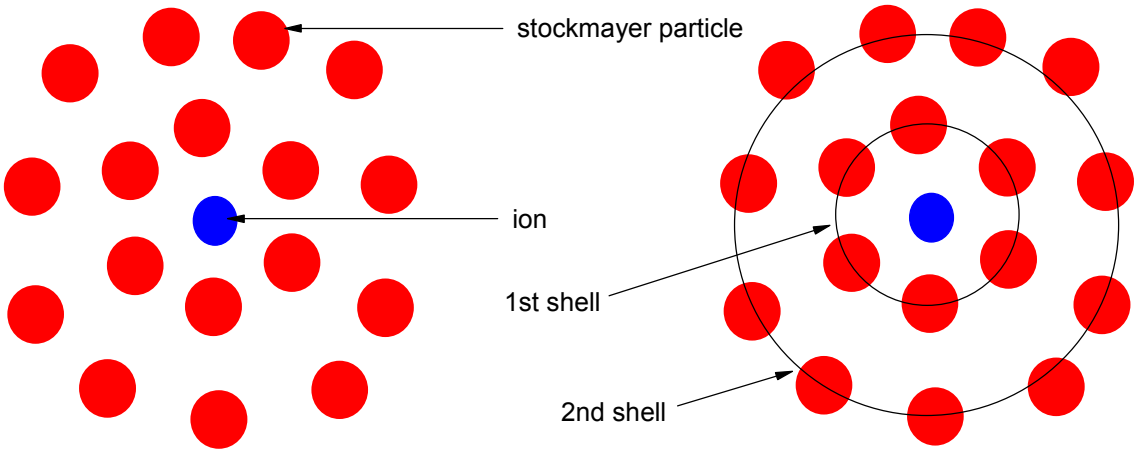

Figure 121 - *The solvation of ions by stockmayer particles. The figure left shows the central ion surrounded by polar fluid particles, represented by the stockmayer fluid potential, these surrounding polar particles can be divided in terms of shells. The polar particles directly surrounding the ion are considered to in the first shell, with subsequent layers of polar particles being labelled in ascending order with increasing separation from the central ion.*

5.3.2 Polar and non polar fluid mixtures

Other aspects of chemical processes were examined using the Stockmayer fluid model, such as mimicking mixtures of polar and non polar fluids. The polar fluids were again described by the Stockmayer fluid potential while the non-polar molecules were described by the Lennard–Jones potential. The main conclusion from this theoretical work was that low concentrations of Stockmayer particles or Lennard-

Jones particles meant a tendency for like molecules to cluster, although the effect was clearly more pronounced for Stockmayer particles. The low concentrations of Stockmayer particles meant Stockmayer particles were aligned head to tail, while at high concentrations the Stockmayer particles showed a decrease in orientational ordering (Figure 122). This decrease of orientational ordering was attributed to a frustration effect arising from the impossibility to achieve energetically favourable configurations when more than two dipoles were close to one another[223,224]. It was also found that highly polar Stockmayer particles caused demixing forming a phase pure in Stockmayer particles and a phase pure in Lennard-Jones particles; this has also been observed in previous work[225].

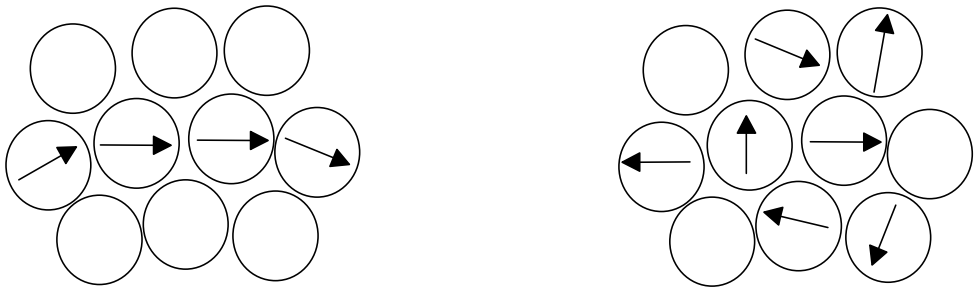

Low concentration of Stockmayer particles

High concentration of Stockmayer particles

Figure 122 - *The orientational ordering of the Stockmayer particles at different concentrations. The left figure illustrates the formation of head-tail orientations of the Stockmayer particles at low concentrations. The right figure shows the Stockmayer particles at high concentrations, the particles are in more disordered configurations.*

This model was subsequently modified to include polarizable Lennard-Jones particles. This work reveals that at sufficiently high polarizability there is no longer a phase separation occurring at high polarity of the Stockmayer particles[226]. The reasons for this lie in the ability of Stockmayer particles to induce a dipole in the Lennard Jones particles, the effect being stronger for higher polarizabilities, and as such the tendency of Stockmayer particles to align observed previously decreases. This is due to an increase in the alignment of permanent dipoles with induced dipoles (Figure 123). It is visible from the pair radial distribution functions that correlations between Stockmayer particles decrease with increasing polarizability of Lennard-Jones

molecules, while correlations between Stockmayer and polarized Lennard-Jones molecules increase[227].

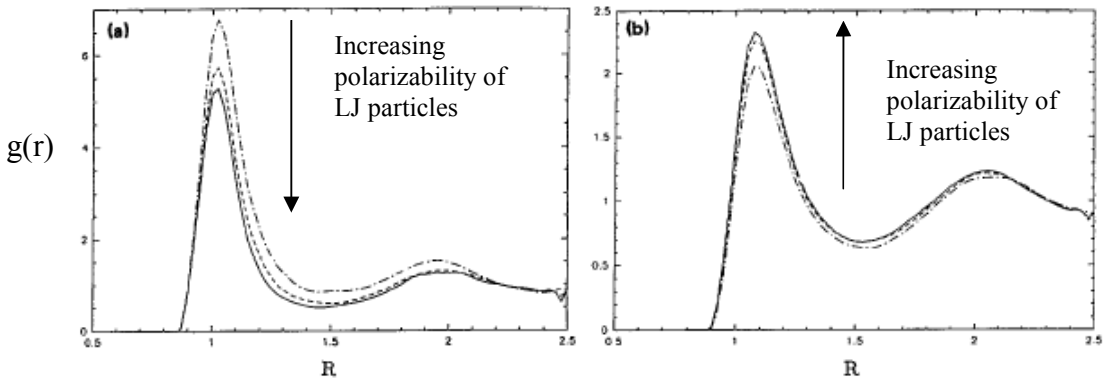

Figure 123 - *The effect of increasing polarizability of Lennard-Jones particles (LJ). The left figure (a) shows the Stockmayer pair radial distribution function with increasing polarizability of the LJ particles. The figure on the right (b) shows the polarizable LJ-Stockmayer pair radial distribution function, with increasing LJ polarizability resulting in an increase in the LJ-Stockmayer pair radial distribution function*[226].

5.3.3 Structural properties of the Stockmayer fluid

Once this general behaviour of Stockmayer fluid had been established a more detailed analysis of the types of ground state configurations formed by the Stockmayer fluid particles was examined. Clusters ranging from 3-20 particles in size were examined by Clarke and Patey. It was found that for small clusters of 3 or 4 particles tended to form chains, while clusters of 5-13 particles tended to form rings and clusters of greater than 13 particles tended to form double rings[228] (Figure 124). In part this work was trying to produce a simple model for simulating structures that are known to form rings or chains, such as hydrogen fluoride which have been simulated with more detailed model interactions[229,230].

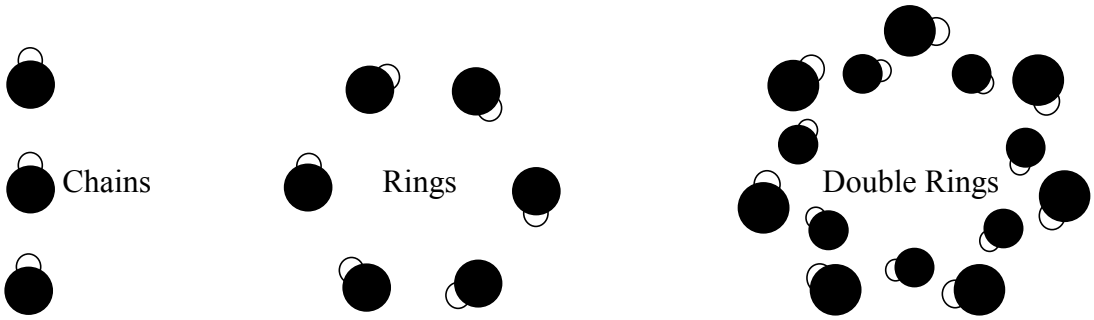

Figure 124 - *The formation of different dipolar structures as the number of particles increases. The left figure illustrates the formation of chains for less than 5 Stockmayer particles. The middle figure shows the formation of rings for more than 4 and less than 14 Stockmayer particles is preferred. The right figure shows the formation of double rings, where one ring layer is stacked on top of another, this occurs for more than 13 Stockmayer particles. The smaller white spheres attached to the black spheres indicated the direction of the dipole moments of the Stockmayer particles.*

The effect of polarizability on the Stockmayer fluid was also examined by Clarke and Patey for a cluster of six polarizable dipolar hard sphere particles. The effect of polarizability was to initially change the ground state structure from a ring to a bent chain and further increasing of the polarizability lead to the formation of a linear chain structure (Figure 125).

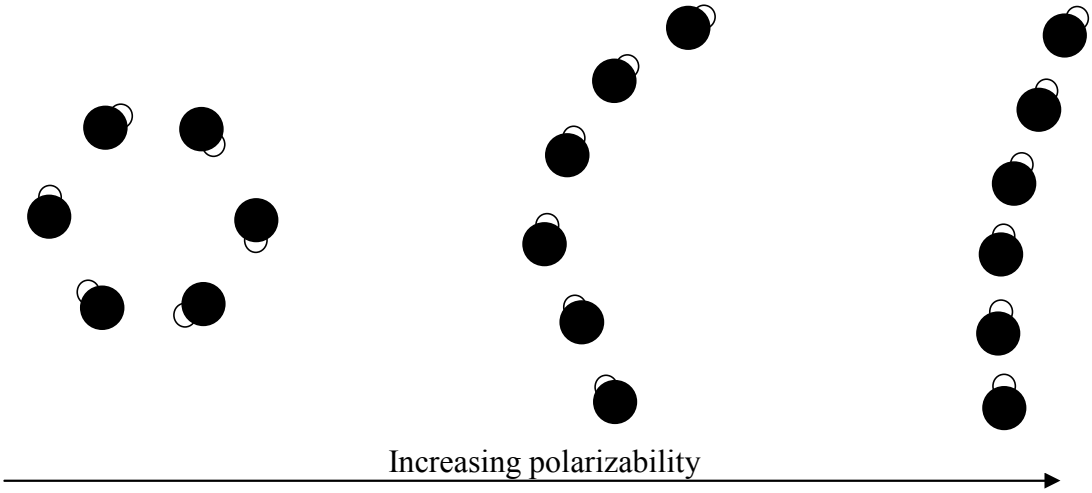

Figure 125 - *The effect of increasing polarizability on a six particle cluster. The left figure shows the cluster forms a ring structure in the absence of polarizability. The effect of adding polarizability to the cluster results in a breakage of the ring structure and the formations of chains are favoured.*

This work was followed up by further investigations into the zero temperature clusters of Stockmayer fluid particles. The rational for this is that in order to understand ion solvation in polar clusters the energetics of this process requires prior knowledge of the cluster before and after introduction of the ion. The results produced by Lavender and co-workers are similar in pattern to those of Clarke and Patey. However, they produce a more detailed analysis of the ground state structures and subsequently observed the formation of rings is favoured over simple chains. Furthermore the formations of double rings are favoured over rings for clusters greater than 13 particles. There are two double ring structures examined in this research the staggered and eclipsed ring[231] (Figure 126).

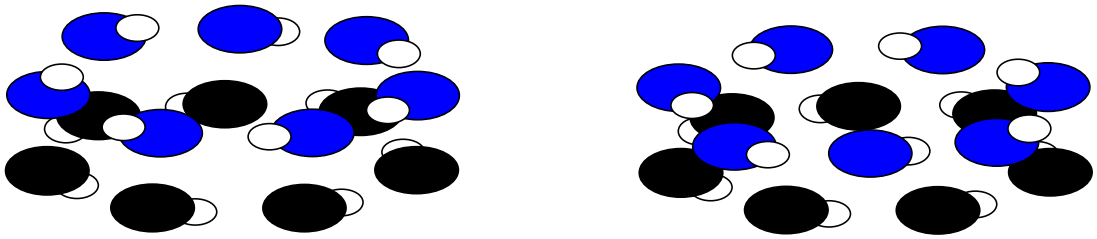

Eclipsed rings Staggered rings

Figure 126 - *The different double ring structures that form in simulations. The left figure shows two rings of particles, highlighted in black and blue respectively, which are stacked in phase with one another to yield the eclipsed ring structure. The two rings have dipole anti-parallel interactions between them to stabilize this eclipsed ring structure. The right figure shows two rings of particles stacked slightly out of phase from one another to yield the staggered ring structure. The individual rings have dipoles pointing in the same direction. The white spheres indicate the direction of the dipoles on the individual particles.*

The staggered double rings are always energetically more favourable for the Stockmayer particles ranging from 13-50 particles relative to the eclipsed double ring and single ring structures possible. The eclipsed ring structure is only energetically favourable relative to single rings when 24 or more particles are present in the structure. This is rather an odd result when one considers the fact that the eclipsed rings have anti-parallel dipole interactions between the stacked rings, however on the other hand the Lennard-Jones potential repulsion between the particles may account for the staggered rings being more stable. Further investigations by Lu and Singer also

show that there is global orientational ordering of Stockmayer particles that persists to high temperatures[232]. It is found for a cluster of 13 and 50 Stockmayer particles that a slightly distorted icosahedron structure exists for low dipole moment values[233]; this is also observed in a model related to the Stockmayer potential involving quadrupole-quadrupole interactions instead of dipole-dipole interactions[234]. These structures clearly show a global circular orientation of head to tail alignment of dipoles. These structures are very similar to those observed by Miller and Wales and as such these global minima structures could actually be construed as a number of individual rings that form knots and coil with one another[235] (Figure 127).

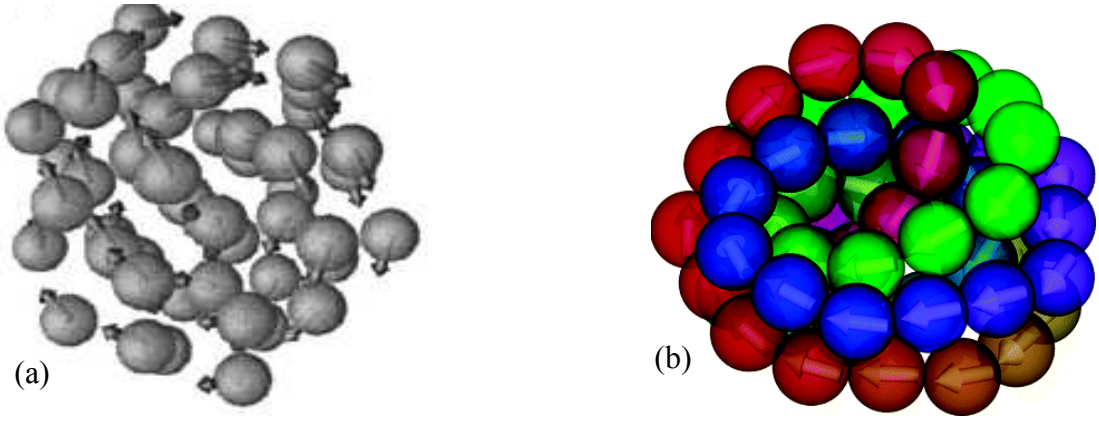

Figure 127 - *The global minimum energy structures for Stockmayer particles at low dipoles. The left figure (a) is the minimum structure for fifty Stockmayer particles observed by Lu and Singer[232]. The right figure (b) is the same structure construed as a number of overlapping individual rings forming knots and coils; this structure is remarkably like that observed in figure (a). The different colours indicate individual rings.*

The presence of higher dipole moments leads to minimum energy structure that resemble in part the eclipsed ring structures observed in previous work (Figure 128). However on this occasion the interaction between the eclipsed rings is alternating with a larger ring layer in between separating the eclipsed rings. The result of this is that the eclipsed rings in this structure are not anti-parallel relative to each other; instead they are parallel to one another. Figure 128 also clearly shows two larger staggered rings separating the three smaller eclipsed rings in the structure; in addition there is a further ring orthogonal to all the other rings that passes through the centre of all the other rings forming a knot[232].

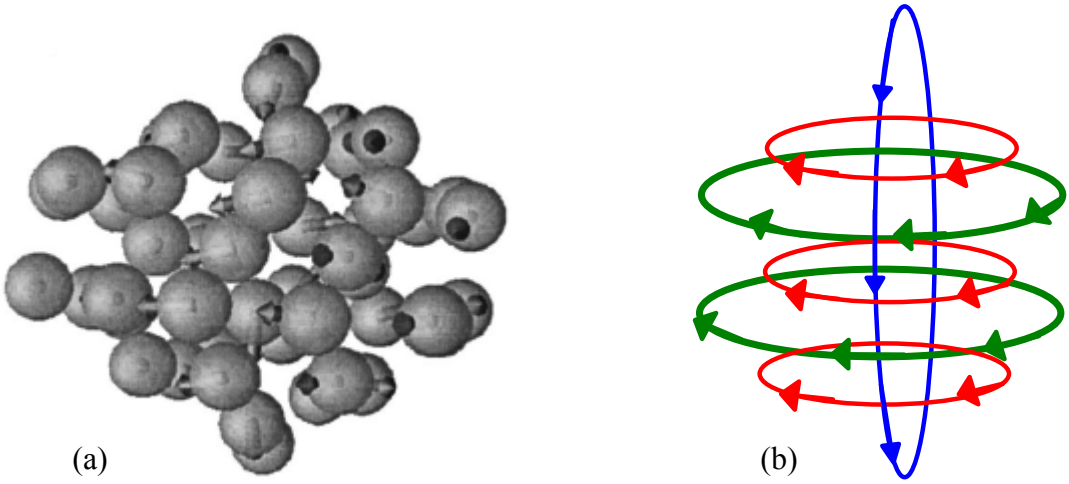

Figure 128 - *The minimum energy structure for fifty Stockmayer particles at high dipoles. The left figure (a) shows the Stockmayer particle structure obtained by Lu and Singer*[232]*. The right figure (b) illustrates the structure in terms of rings; the larger staggered rings are represented in green and the smaller eclipsed rings are represented in red. The orthogonal ring passing through the other rings to form a knot is shown in blue.*

Following on from this work, which establishes the types of structures adopted by a polar solvent and in essence shows the global circular orientational order in the Stockmayer fluid particles, the effect of having an ion present within a polar environment is examined more closely. Initially looking at small clusters Lu and Singer show the formation of a radial cluster of Stockmayer particles, the Stockmayer particles can be seen to emanate away from the ion, surrounding an ion is favoured over the expected circular cluster seen without the presence of an ion[236] (Figure 129) . The simulated results for a larger cluster of 100 Stockmayer particles reveal that there is tendency for the particles closest to the ion to form a radial cluster as described previously, the first solvated shell of the ion. The subsequent shells tend to form the circular pattern found in the ion free polar solvent, however this is dependent on the relative strength of the dipole moment on the Stockmayer particles. Considering the two extremes situations a low charge ion and strong dipole moment favours the first solvated shell of the ion to be radial and subsequent shells to be circular, while in the second scenario with a high charged ion and low dipole moment favours the first and subsequent shells to be radial with the effect decreasing with increasing distance

(Figure 130). The results from the simulation work are also represented for the two extreme situations.

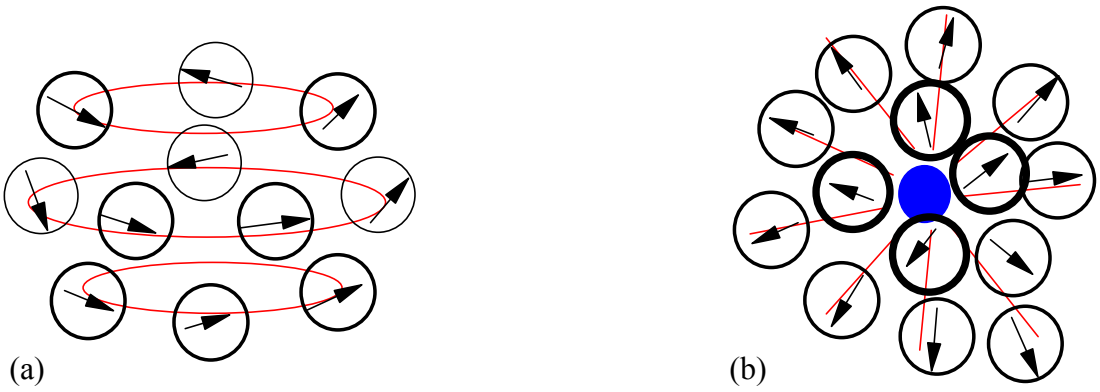

Figure 129 - *The different structures adopted by the Stockmayer particles in the presence and absence of ions. The figure on the left (a) is the Stockmayer particles without the ion; they form head to tail spherical structures. The figure on the right (b) is the Stockmayer particles in the presence of an ion, highlighted in blue; this causes the surrounding Stockmayer particles to emanate outwards from the ion.*

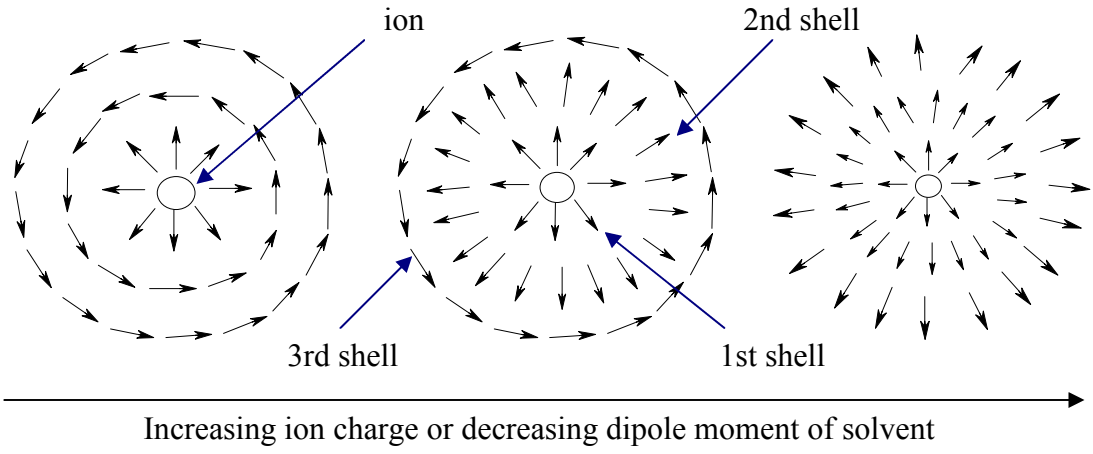

Figure 130 - *The variation in the polar solvent shells around an ion. The left figure describes the situation with low charge ion or Stockmayer particle with a large dipole moment. The right figure illustrates the situation of a high charge ion or Stockmayer particles with a low dipole moment. The central figure is a cross between the two extreme situations.*

The Stockmayer potential has been utilized in forming a simple model that describes the behaviour of water molecules. The work of Muller and Gubbins uses the Stockmayer potential to account for the long range and short range interactions of water; in addition to these interactions, there are four square well sites placed on the stockmayer particle in a tetrahedral arrangement to mimic the short range hydrogen bonding capability of water molecules. This model is able to form a network of chains as well as a few individual particles in this network being either three or four coordinated, though this only at high densities[237] (Figure 25).

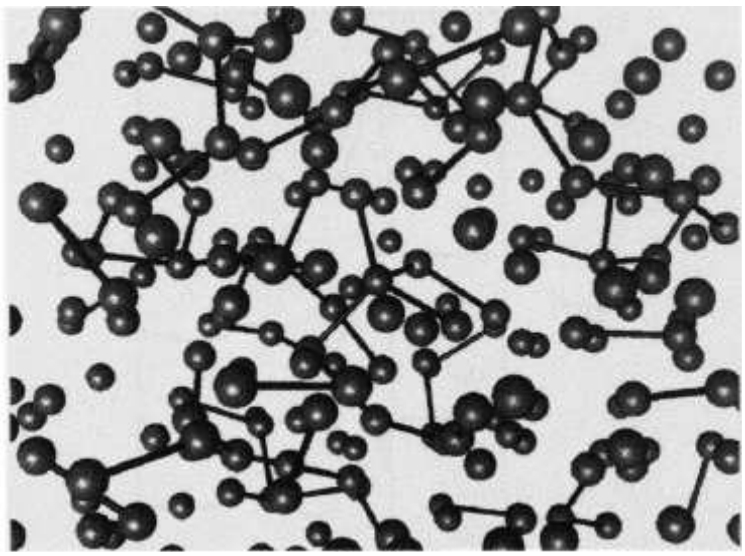

Figure 131 - *The network of water molecules being formed at high densities using a Stockmayer fluid potential with additional square well potential to account for hydrogen bonding. The figure has a central particle that is four coordinated, whilst the majority are either two coordinated or uncoordinated*[237].

5.4 Dipole interactions in nanoparticle simulations

The inclusion of the dipole-dipole interactions in the simulation of nanoparticle self-assemblies has been utilised by Sinyagin and co-workers[238]. Their model treats the nanoparticles as spherical bodies which contain a central dipole moment and a charge, with additional van der Waals interactions. The simulation work showed that the presence of dipole-dipole interactions was important in leading to the formation of

chain like structures, resembling the pearl necklace structures observed in experimental nanowire synthesis, as the absence of dipole-dipole interactions in the simulations lead to the formation of nanoparticle cluster aggregates. In addition, the increasing of the dipole moments or reduction in the charges of the particles in the simulation leads to a transition from the nanoparticle cluster aggregates to more linear chain like structures[239] (Figure 132). There are similar models using dipole-dipole interactions that also result in the formation of wire and sheet structures[240,241].

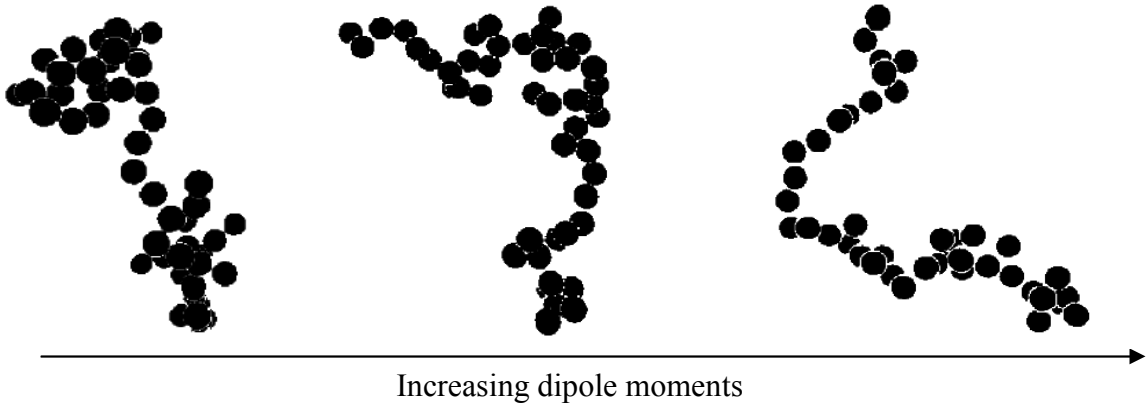

Figure 132 - *The formations of different nanoparticle structures in simulations by Sinyagin and co-workers. The left hand figure shows the effect of having low dipole moments in the spheres resulting in cluster aggregate structures. The middle figure shows the same spheres with a 4-fold increase in the dipole moment, producing less cluster aggregation. The right figure shows a further 4-fold increase in the dipole moment of the spheres resulting in a pearl-necklace type structure observed experimentally*[239].

The self-assembly of nanocubes is also examined using a dipole-dipole interaction by Zhang and co-workers. They additionally include a square well potential to account for attractive forces between facets of the cubes[242]. This simulation was inspired by the experimental work of Cho and co-workers which deduced there were two types of nanocubes produced in the synthesis of lead selenide nanocrystals resulting in the formation of unqiue nanoring and nanowires structures. The nanocubes either had a dipole moment pointing directly through a single face of the nanocube or it had a dipole moment that dissects two of the faces (Figure 133).

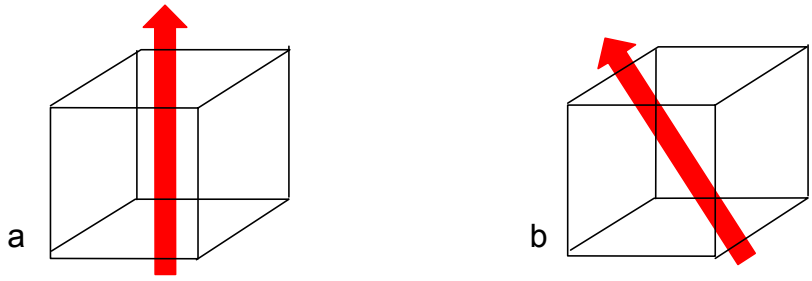

Figure 133 - *The nanocubes with different dipole directions thought to be responsible for the unique structures observed for lead selenide. The nanocube-a on the left depicts the nanocube with dipole moment through a single face. The nanocube-b on the right depicts the nanocube with dipole moment cutting between two faces.*

This was explicitly modelled in the work by Zhang and co-workers and they found linear nanowire like structures to form as a result of simulating nanocube-a structures in Figure 133. In addition, they found sheet structures to occur as the square-well potential was increased for these nanocubes. The simulation of mixtures of the nanocubes illustrated in Figure 133 was found to give rise to the ring structures observed experimentally with the nanocube-b acting as the linker between chains of nanocube-a structure[242] (Figure 134).

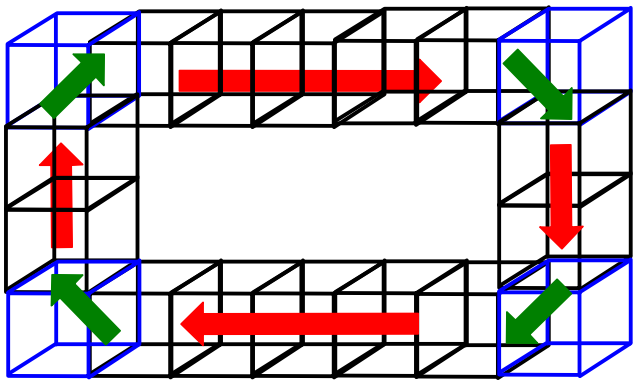

Figure 134 - *The formation of lead selenide nanorings is the result of two types of nanocubes combining. The two types of nanocubes are highlighted; the black nanocubes are the ones with the dipole moment pointing through a single face and the blue nanocubes have the dipole moments (green arrows) pointing between two faces of the cubes. The red arrows indicate the resultant dipole of the black nanocubes as they aggregate to form chains; these individual chains are linked together by the blue nanocubes to form the nanorings.*

Chapter 6 Polydisperse dipolar fluids

6.1 Introduction

This chapter examines the effects of having polydispersity present in the Stockmayer fluid. The Stockmayer fluid in the simulation cell is composed of an equimolar mixture, with Stockmayer fluid particles A and particles B. The size distribution of this two component system is simply measured in terms of a size ratio α, where the diameter σ_A of the larger particles A is divided by the diameter σ_B of the smaller particles B (Equation 33). There are in total 256 particles present in the simulations, such that $N_A = N_B = 128$ particles. The reduced dipole moment is constant for both the components, $\mu_a^* = \mu_b^* = 3.0$ (see section 2.4). The reduced temperature of the simulations is also constant, $T^* = 1.0$.

$$\alpha = \frac{\sigma_A}{\sigma_B}$$

Equation 33 - *The size ratio of the Stockmayer fluid. The size ratio is calculated by dividing the diameter of Stockmayer particles A with the diameter of Stockmayer particles B.*

6.2 Radial distribution function

The radial distribution function of the Stockmayer fluid at size ratios of 1.0, 2.1 and 4.0 are shown and compared at all four reduced densities $\rho^* = 0.1$, 0.2, 0.4 and 0.8 (in terms of volume fraction these are 5, 10, 20 and 40%, respectively) examined in the simulations. These results are contrasted with their Lennard-Jones radial distribution function counterparts at the same size ratios and reduced densities (Figure 135). The results indicate that at all sizes ratios there are greater peaks in g(r) for the Stockmayer fluid compared to the counterpart Lennard-Jones potential. This essentially means there is greater frequency of bonds, defined in this case when the A and B particles are in contact, between the particles. This indicates the formation of chains in the Stockmayer fluid simulations. The effect of density in the Stockmayer fluid simulations is to cause a decrease in the peaks with increasing density, as the

probability of finding particles close to one another at higher density increases. This effect is negligible in the Lennard-Jones simulations at all size ratios shown. The different bonds, A-A, A-B and B-B, formed between different sized A and B particles are highlighted in each of the radial distribution function figures.

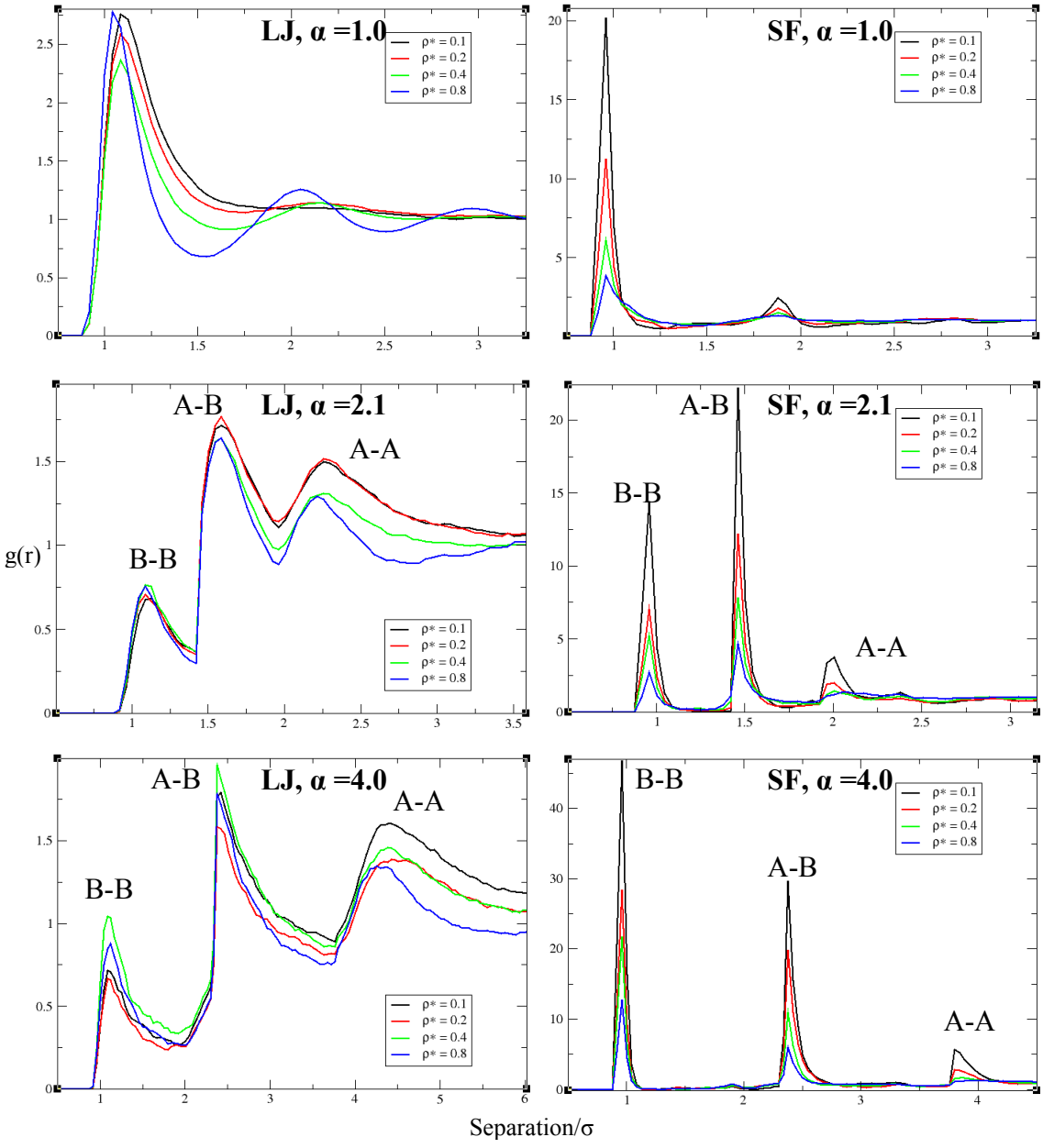

Figure 135 - *The radial distribution function of two component Lennard-Jones (LJ) and Stockmayer fluid (SF) potentials. The left figures are all 6-12 Lennard-Jones only rdf's, whilst the right figures are all Stockmayer fluid potential rdf's. The size ratio α can be seen to increase on going from the top (1.0), to the middle (2.1) and finally the bottom (4.0) figures. There are four reduced densities ρ* shown in each individual figure as indicated by the figure legends. The length scale is represented in terms of σ.*

6.3 Local coordination enviroment

The coordination data gives information regarding the number of connections or bonds to each particle in the simulations. The mean coordination number of the Stockmayer fluid particles at different size ratios is plotted for all four reduced densities ρ* = 0.1, 0.2, 0.4 and 0.8 (Figure 136).

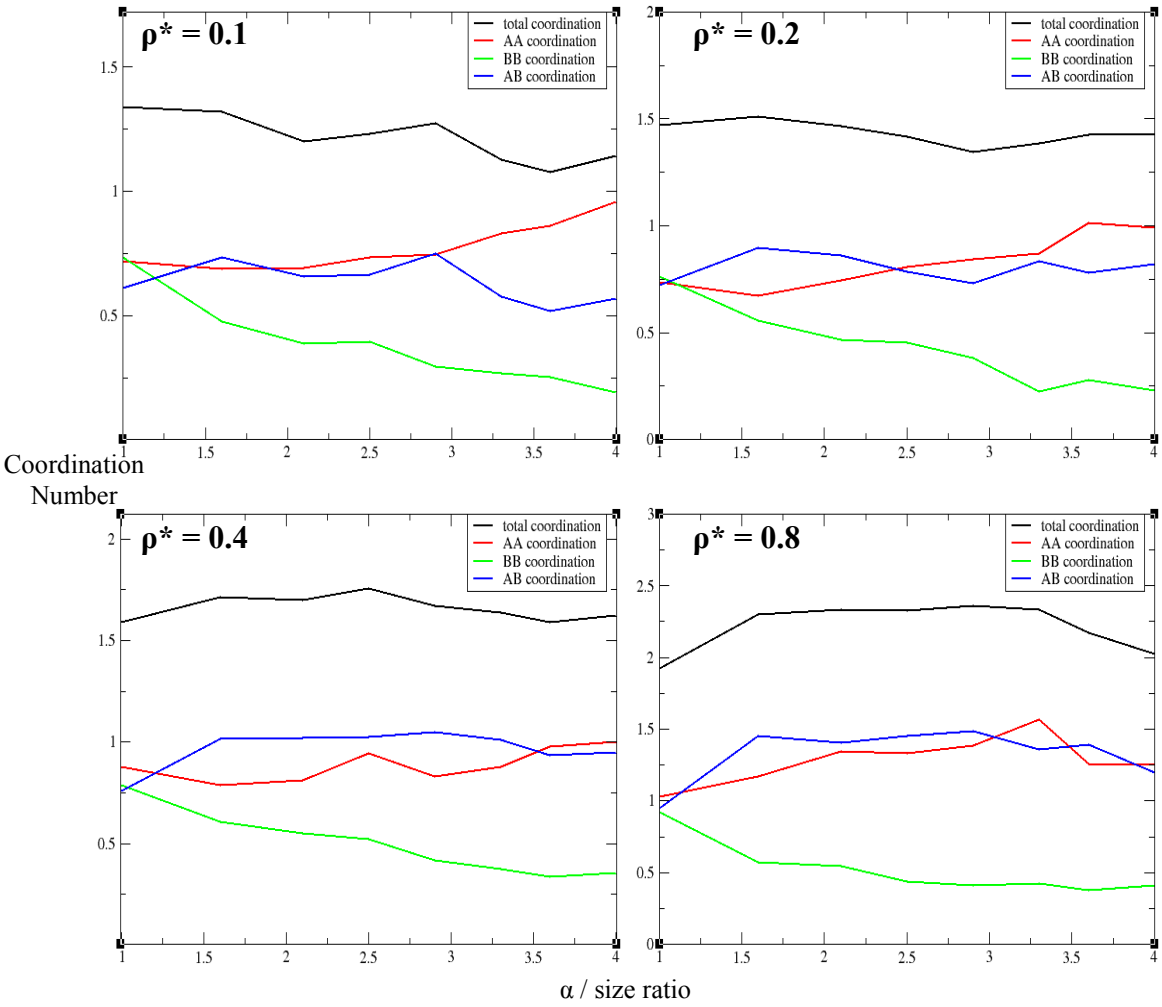

Figure 136 - *The mean coordination number for different sized Stockmayer fluid particle mixtures at different densities. The mean coordination number is plotted as a function of the mixtures (particles A and B) size ratio* α *for the total, AA, BB and AB coordination numbers. There are four plots showing the result of simulation under different densities* ρ* *as indicated in the figure inset.*

The mean coordination data shows that with the full range of size ratios α between the mixture of A and B Stockmayer particles at any given density ρ*, the results show essentially in no change in the total coordination numbers. Though there is no overall change in the coordination numbers at different densities there are however fundamental changes that seem to occur to the mean coordination numbers of AA, AB and BB. The B Stockmayer particles, the smallest particles in the mixture, shows a rapid decrease in the coordination numbers as the size ratio α is constantly increased. This means there are fewer chains or connections forming between the B-B particles as the size of the A particles in the mixture increase. Conversely there is a general trend of increasing A-A connections as the size ratio α increases and similar trend emerges for the A-B connections. The data tends to indicate the increase in A-A and A-B connections occurs in the system as a consequence of losing B-B disconnections in the system. This can be further clarified be viewing the individual coordination numbers for the B-B associations at different size ratios α at the specific reduced density ρ* = 0.2 (Figure 137).

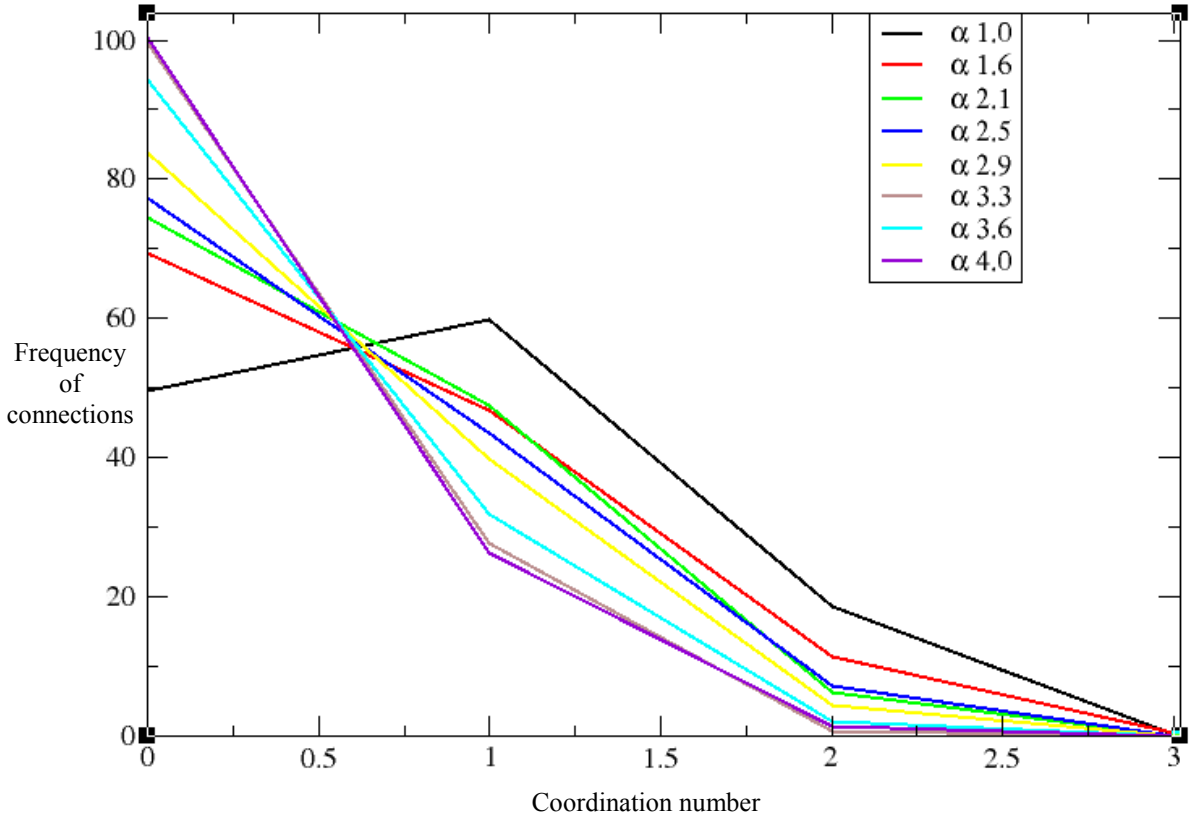

Figure 137 - *The frequency of coordination numbers for the B-B connections in the simulations at different size ratios. The coordination numbers for B-B connections for*

the different size ratios α are shown; the figure legend indicates the size ratios examined.

The coordination data for the B-B connections in the different, size ratio α, mixtures reveals a striking pattern in that there is a clear decrease in the coordination of B-B associations that are one coordinated and two coordinated. Indeed there is further evidence of size ratios in mixtures of Stockmayer particles having an important role as there is a step wise decrease in the one and two coordinated B-B associations with increasing size ratio α. The data show approximately twenty two-coordinated particles when the size ratio α is 1.0 and when this value reaches 4.0 there are essentially no more two-coordinated atoms. There is also corresponding increase in the number of zero coordinated atoms with respect to B-B connections in the system as the size ratio increases. The number of zero coordinated particles is approximately fifty when the size ratio α is 1.0 and when the size ratio is increased to 4.0 there are approximately twice as many uncoordinated particles in the system. The pattern emerging from these data alone indicates that increasingt the size of the A particles in the system results in the break up of the B chains to free monomers or very small number of connections, with respect to B-B associations. The data can be summarised in a simple diagram of the system, shown in Figure 138.

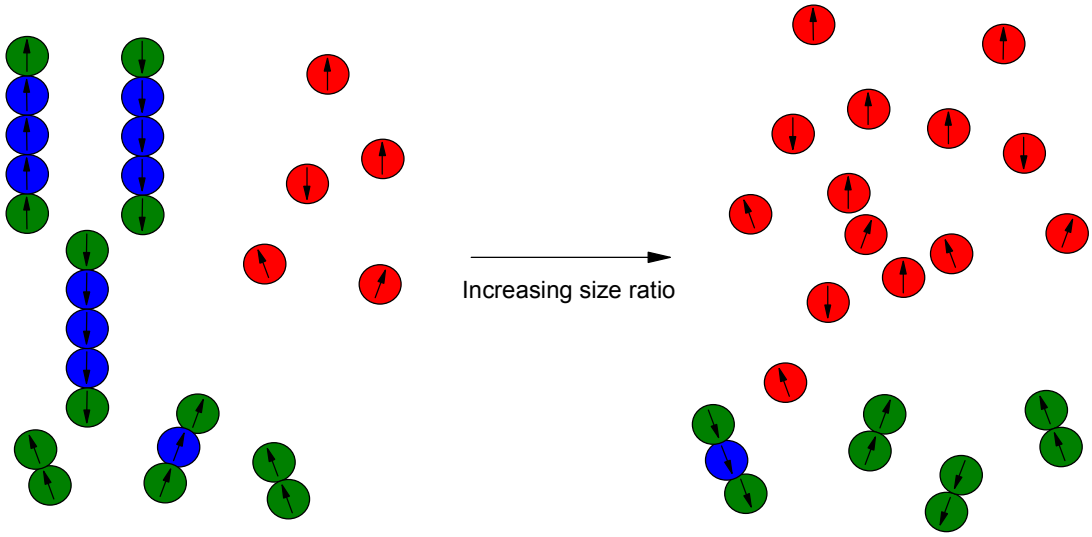

Figure 138 - *The summary of the connection data between B particles only in presence of different sized A particles. The left figure shows the scenario when A and B particles are of equal size and the right figure shows the scenario of A particles*

being larger than B particles. The blue particles show two coordinated particles, the green one coordinated particles and the red uncoordinated particles.

The coordination data for the A-A connections only is examined at the same reduced density of ρ* = 0.2 as that for the B-B connections at different size ratios of the Stockmayer fluid mixture (Figure 139).

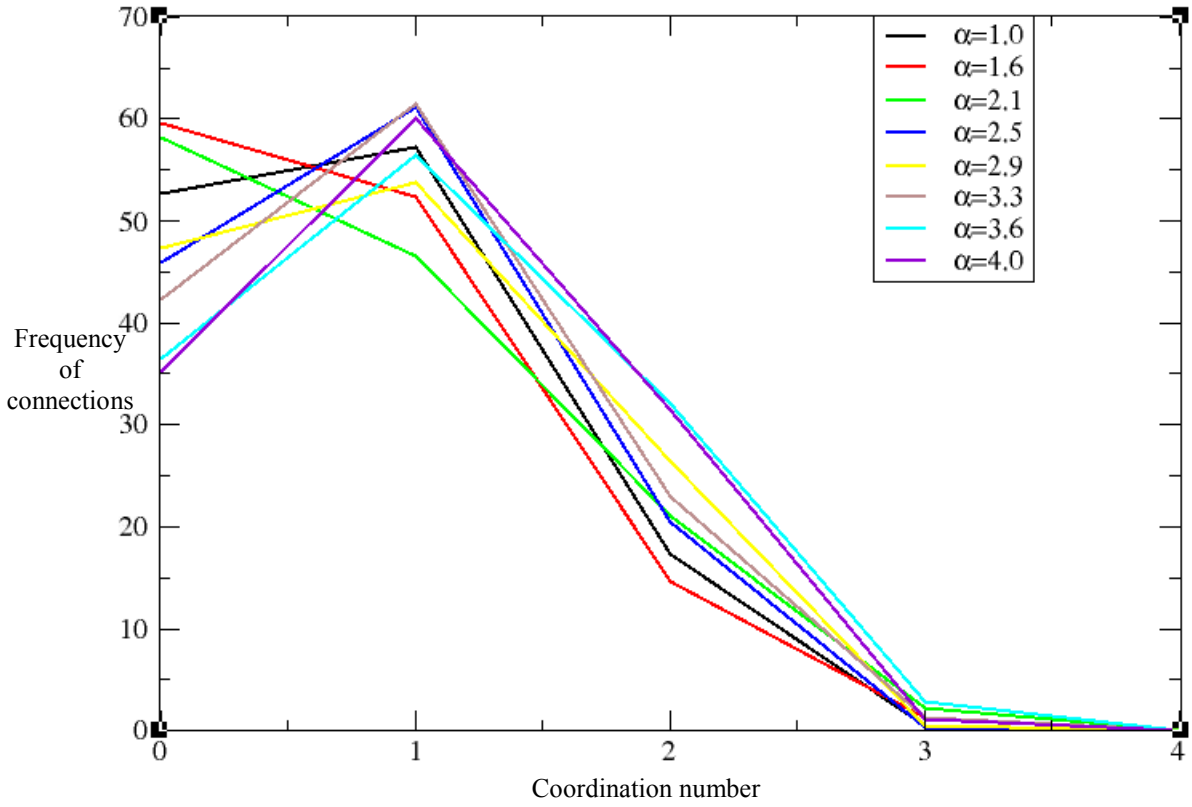

Figure 139 - *The frequency of coordination numbers for the A-A connections in the simulations at different size ratios. The coordination numbers for A-A connections for the different size ratios α are shown; the figure legend indicates the size ratios examined.*

The coordination data for the A-A connections only illustrates that increasing the size of the A particles leads to a greater number of two coordinated particles, for example when the A particles are of equal size to the B particles there are approximately seventeen A particles that are two coordinated. When the A particles are four times the size of the B particles, size ratio α = 4.0, there are approximately double the number of two-coordinated particles in the simulation. The number of one coordinated atoms in the different size ratio simulations remains approximately the

same throughout. The number of uncoordinated particles in the simulations decreases with increasing size of the A particles; there are fifty three uncoordinated A particles in the absence of any size difference between A and B particles. When the size of the A particles is four times that of the B particles there are only thirty five uncoordinated A particles in the simulations. The simulation data tend to indicate that a significant proportion of the uncoordinated A particles at low size ratios are shifted to the higher one or two coordinated particles. The fact that there is approximately the same number of one coordinated particles in all the different size ratio simulations indicates that the chain length of the A-A connected chains must be increasing rather than greater number of smaller chains forming at high size ratios (Figure 140).

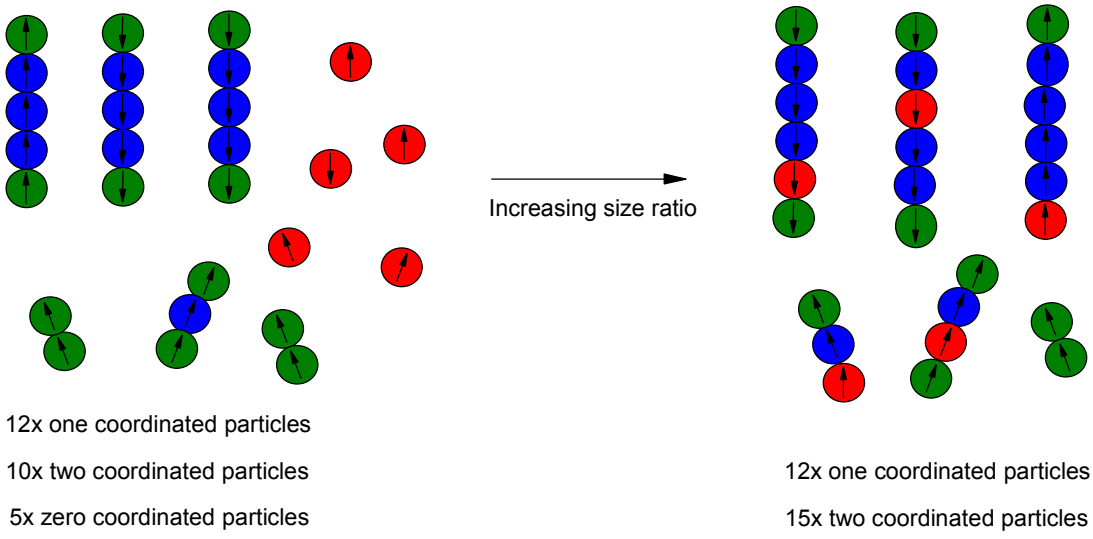

Figure 140 - *The change in coordination of the A particles only with increasing size ratio of the mixture. The left figure illustrates the A particles when the size ratio* α *is 1.0, there are two (blue), one (green) and zero (red) coordinated particles present in the system. The right figure illustrates the mixture with larger A particles relative to B particles, under these conditions the free A monomers become integrated into existing A chains structures resulting in a decrease in the zero coordinated particles. The number of two coordinated particles increases, however the number of one coordinated particles in the system remain constant when the free monomer A particles attach to existing chain structures. There are a total of twenty seven A particles in this depiction with their coordination's indicated in the figure inset.*

The coordination data for the A-B connections only is examined at the same reduced density of ρ* = 0.2 as that for the B-B and A-A connections at different size ratios of the Stockmayer fluid mixture (Figure 141).

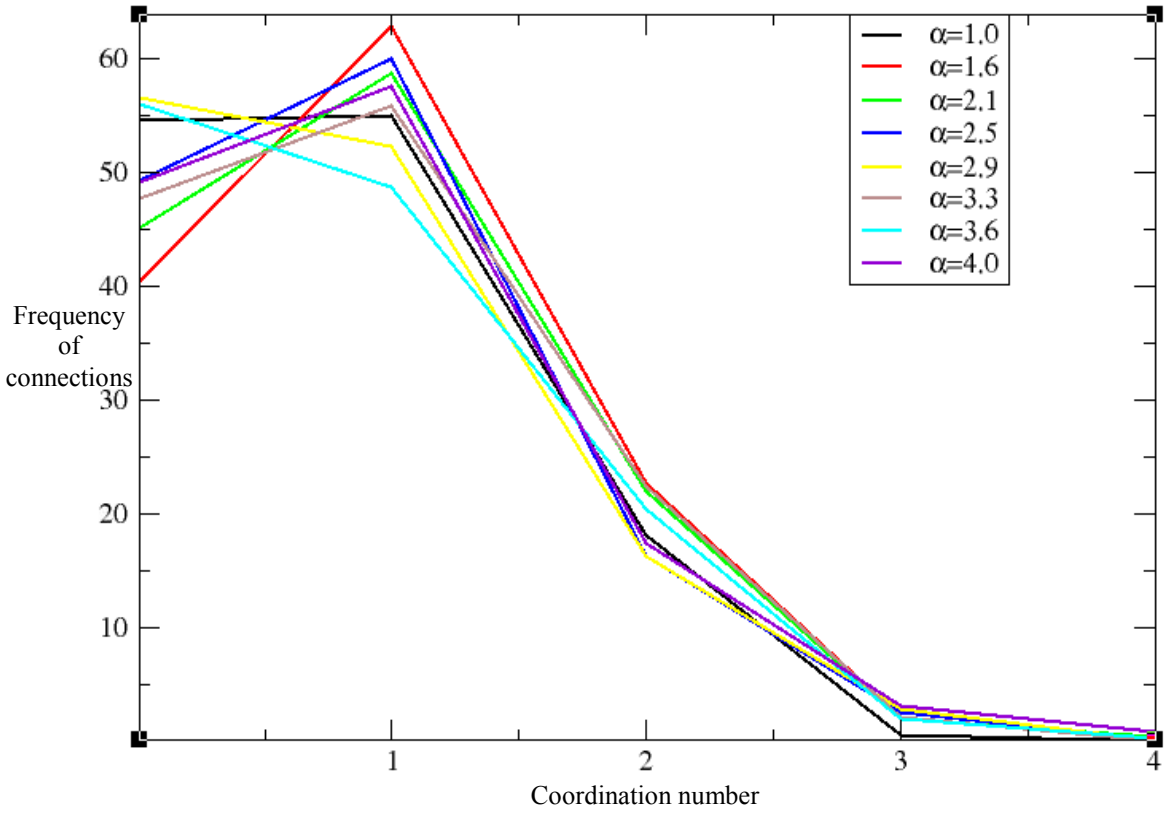

Figure 141 - *The frequency of coordination numbers for the A-B connections, with respect to A, in the simulations at different size ratios. The coordination numbers of A particles in A-B connections for the different size ratios* α *are shown; the figure legend indicates the size ratios examined.*

The coordination results for the A-B connections with respect to A particles takes into account only A-B bonds, so connections such as A-A-B are ignored, but connections such as A-B and B-A-B are taken into account. This is exemplified by a fictitious chain composed of A and B particles, with the coordination of the A particles with respect to A-B connections highlighted (Figure 142). The coordination data for the A-B connections indicates that in general there are no significant increases observed in two-coordinated A particles, but there is a subtle increase in the number of three coordinated particles with increases size ratio. There is a small decrease in the number of zero coordinated A particles, and conversely there is a small increase in one

coordinated A particles, with increasing size ratio. The results essentially show little change occuring to the coordination of A particles with B particles with increasing size ratio in the mixture. The coordination data for the A-B connections with respect to B particles only is also examined (Figure 143).

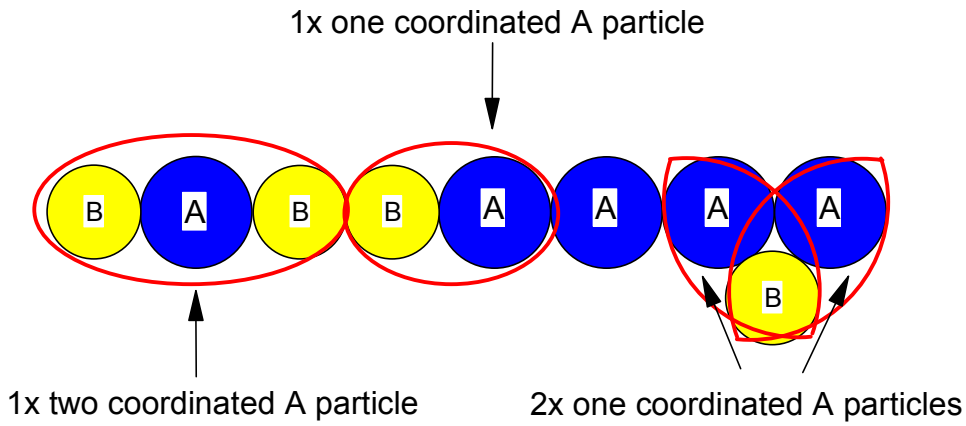

Figure 142 - *The A-B connections taken into account when observing the coordination of A particles. The fictitious chain figure illustrates how the coordination data for A-B connections with respect to the coordination of A particles is put together. The left side of the chain shows a single two coordinated A particle, whilst the right side shows two, one coordinated A particles. The figure also shows any A-A, A-B-B and A-A-B connections are ignored.*

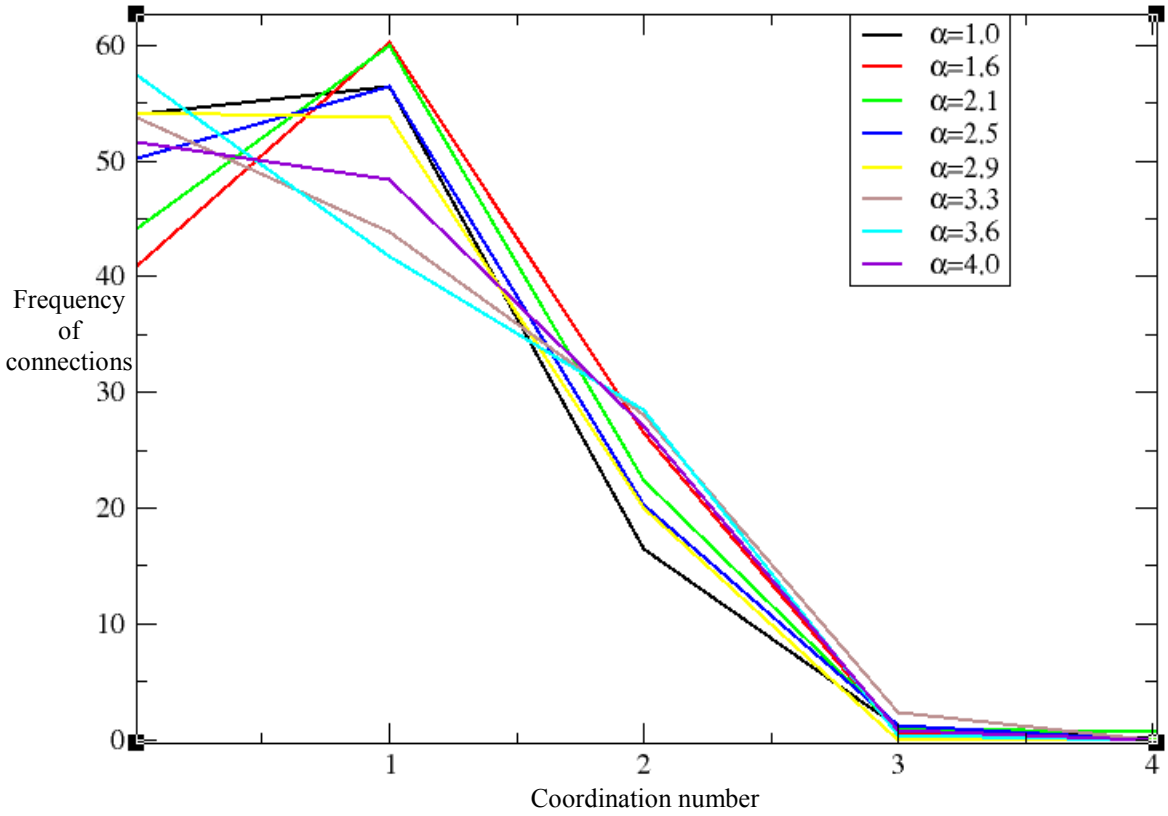

Figure 143 - *The frequency of coordination numbers for the A-B connections, with respect to B, in the simulations at different size ratios. The coordination numbers of B particles in A-B connections for the different size ratios* α *are shown; the figure legend indicates the size ratios examined.*

The coordination data for the A-B connections with respect to the B particles shows more prominent changes in the coordination numbers with increasing size ratio than the previous data with respect to the A particles. The number of zero coordinated B particles in fact remains reasonably constant throughout with different size ratios, while the number of one coordinated atoms is observed to decrease from fifty six, when the size ratio α is 1.0, to forty two when the size ratio α reaches 3.6. The decrease in one coordinated B particles is linked to an increase in the number of two coordinated B particles; the number of two coordinated B particles is approximately sixteen when the size ratio between A and B particles is 1.0. This shifts to approximately thirty two-coordinated B particles when the size ratio α is 3.6 or 4.0. The data initially seem contradictory as the distribution of A-particle coordination numbers with respect to A-B connections only, remains essentially constant. This is not the case for the distribution of the B-particle coordination numbers, which show a

shift towards more two-coordinated B particles. These differing distributions suggest an asymmetrical chain structure must be responsible for the observed data. The number of two coordinated A particles is outweighed by approximately twice the amount two coordinated B particles, with respect to A-B connections only, when the size of A particles is four times that of the B particles. The data are rationalised by examining different model chain structures shown in Figure 144.

The figure illustrates two possible scenarios, in the first idealised case the different sized particles could be thought to mix equally when forming chains. This would result in approximately equal numbers of two and one coordinated A and B particles with respect to A-B connections; In reality there are more two coordinated B particles relative to A with respect to A-B connections only. The previous A-A connection data suggest that increasing two-coordinated A particles, but the B-B connection data suggests substantial decreasing of two coordinated B particles. The accumulation of all this data suggests the formation of long A chains surrounded by B particles. The attachment of smaller particles to the ends of larger chains has been previously observed[243-245]. However, the effect is to decrease the mean chain length of the larger particles, which is the converse of the work presented in this thesis.

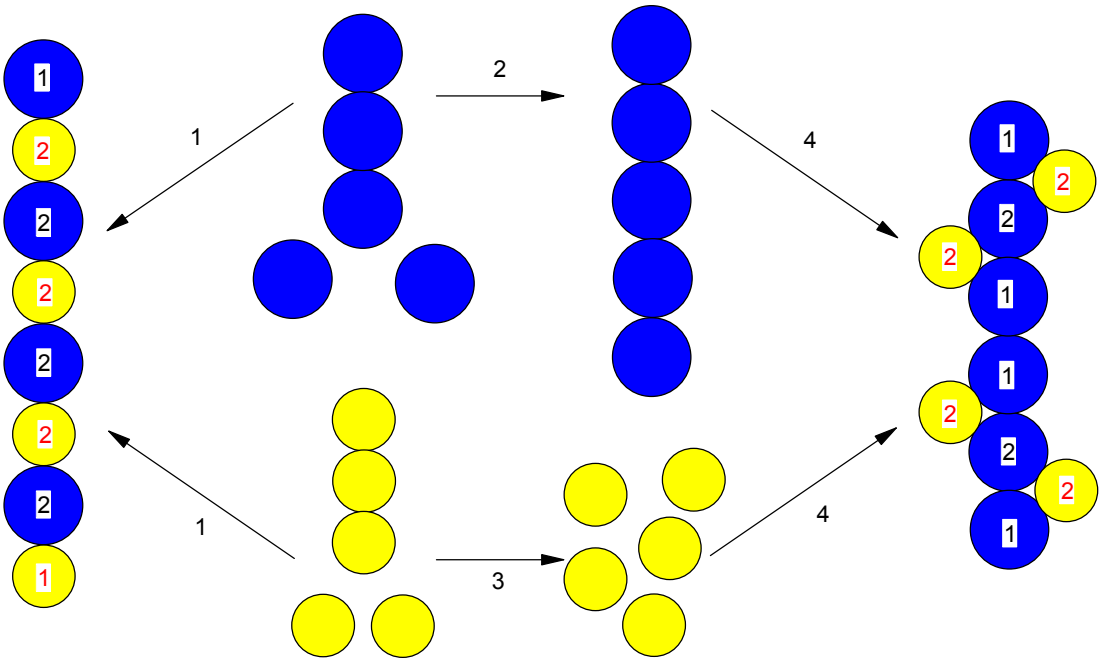

Figure 144 - *The interpretation of the coordination data leading to a possible explanation of the types of structures formed in polydisperse Stockmayer fluid*

particles. The first pathway represents possible product of equal mixing of two particle sets in solution resulting in equal number of two and one coordinated A and B particles. The second pathway shows the interpretation of the A-A coordinate data leading to increased chains with increasing size ratio. The third pathway shows how the B-B connections dissipate with increasing size ratio. The fourth pathway shows mixing of the A and B particles to yield a chain primarily composed of A particles with additional B particles attached. The blue spheres are A particles and the yellow spheres are B particles, the coordination of particles with respect to A-B connections is shown.

6.4 Chain length analysis

The mean chain length data can be examined to see whether they support the previous data in terms of the chain structures that are forming. The mean chain length includes chains composed of only two particles, even though these are not normally considered chains due the absence of any two coordinated particles in this structure. The chain lengths of the total, A-A, B-B and A-B connections are all calculated. The particles are considered to have connections when each particle is touching another particle only (Figure 145). The figure illustrate that there are two possible combinations of A and B particles to yield A-B chains in the chain length of three It should be noted that chain counting of A-B chains will not differentiate between these two structures. These different numbers of A and B particles only occur for odd number of chain lengths, as there has to be more of one type of the particles, however in the case of even chain length there are equal number of A and B particles and hence no different A-B chains exist.

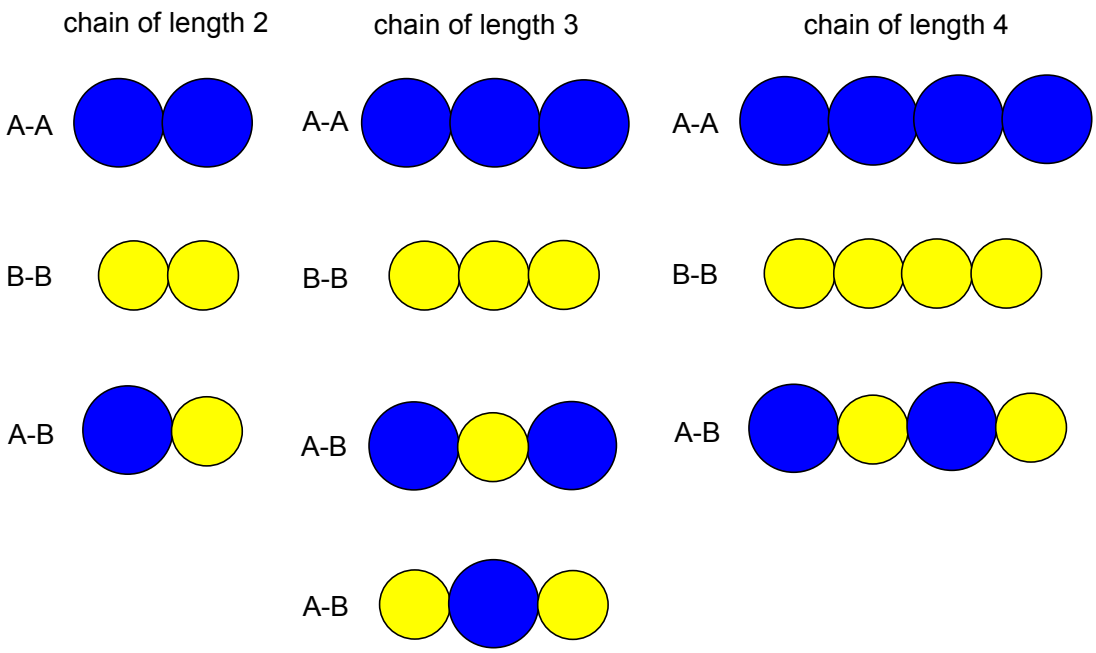

Figure 145 - *The calculation of chain lengths in the Stockmayer fluid simulations. The A and B particles can combine in a number of ways to achieve different chain lengths. The chains of length two for different combinations of the A and B particles are shown. The chains of length three also show that there are two possible combinations of the A and B particle combining to yield A-B chains, in one case there are two A and one B particles and in the alternative case there are two B and one A particles. The chains of length four are also shown for each combination of A and B particles. The A particles are yellow whilst the B particles are blue in the figure.*

The determination of whether particles constitute part of any chain structure, total, A-A, B-B or A-B, is also summarized diagrammatically in order to illustrate how the chain counting process occurs for a larger chain structure composed of both A and B particles (Figure 146).

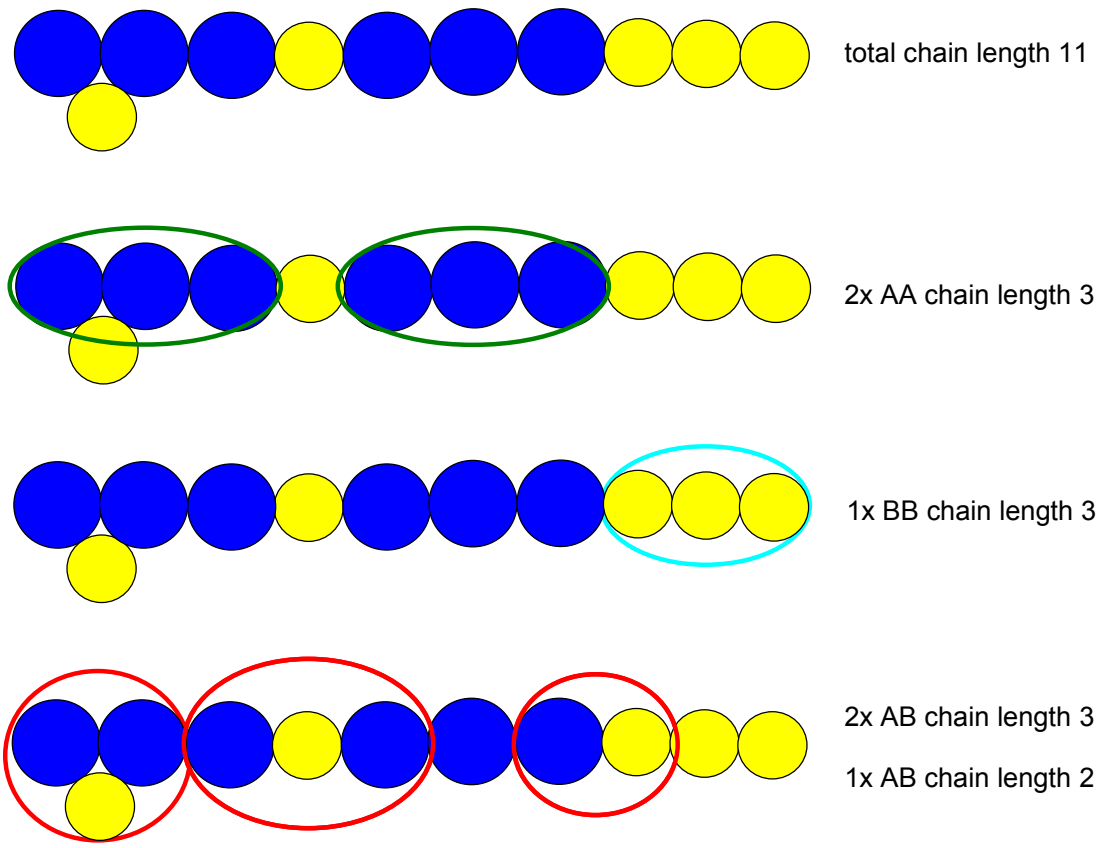

Figure 146 - *The chain counting of chains with respect to A-A, B-B and A-B connections. The top figure shows a hypothetical chain structure composed of both A and B particles, in total there are eleven particles. The subsequent figure shows the same chain structure analysed in terms of A-A chains only (green rings). The next figure illustrates B-B chains present within the larger chain structure (cyan ring). The final figure highlights A-B chains present in the larger chain structure (red rings).*

The mean chain lengths for the total, A-A, B-B and A-B connections, in the mixture of the different sized Stockmayer fluid particles as a function of the size ratio is plotted for all four densities investigated in Figure 147. The results of these chain-length data are similar to the pattern observed in the coordination data previously shown in Figure 136. There are increases in the mean chain lengths of the A-A and A-B chains with increasing size ratio of the system at each particular density shown. The mean chain length of the B-B chains can be seen to fall rapidly with increasing size ratio. The mean B-B chain length can be seen to tend towards a chain length of two when the size ratio α is four. This indicates a likelihood of B particles only associating with one another sporadically, forming essentially only a single connection and hence the coordination of a B-B chain length of two is one for each of the B particles. This

agrees well with the coordination data for B-B connections only where there are simply zero and one coordinated B particles at a size ratio α of four. The total chain length is also observed to increase with the increasing density; there are particularly large mean total chain lengths at the density ρ* = 0.8. These are attributed to the high density of the system resulting in the particles being extremely close to one another and on occasions the majority of particles in the system can be seen to be connected. Snapshots of equilibrium structures of the system when the reduced density ρ* = 0.8 and the size ratio α is 1.0, 2.1, 3.3 and 4.0 are shown (Figure 148).

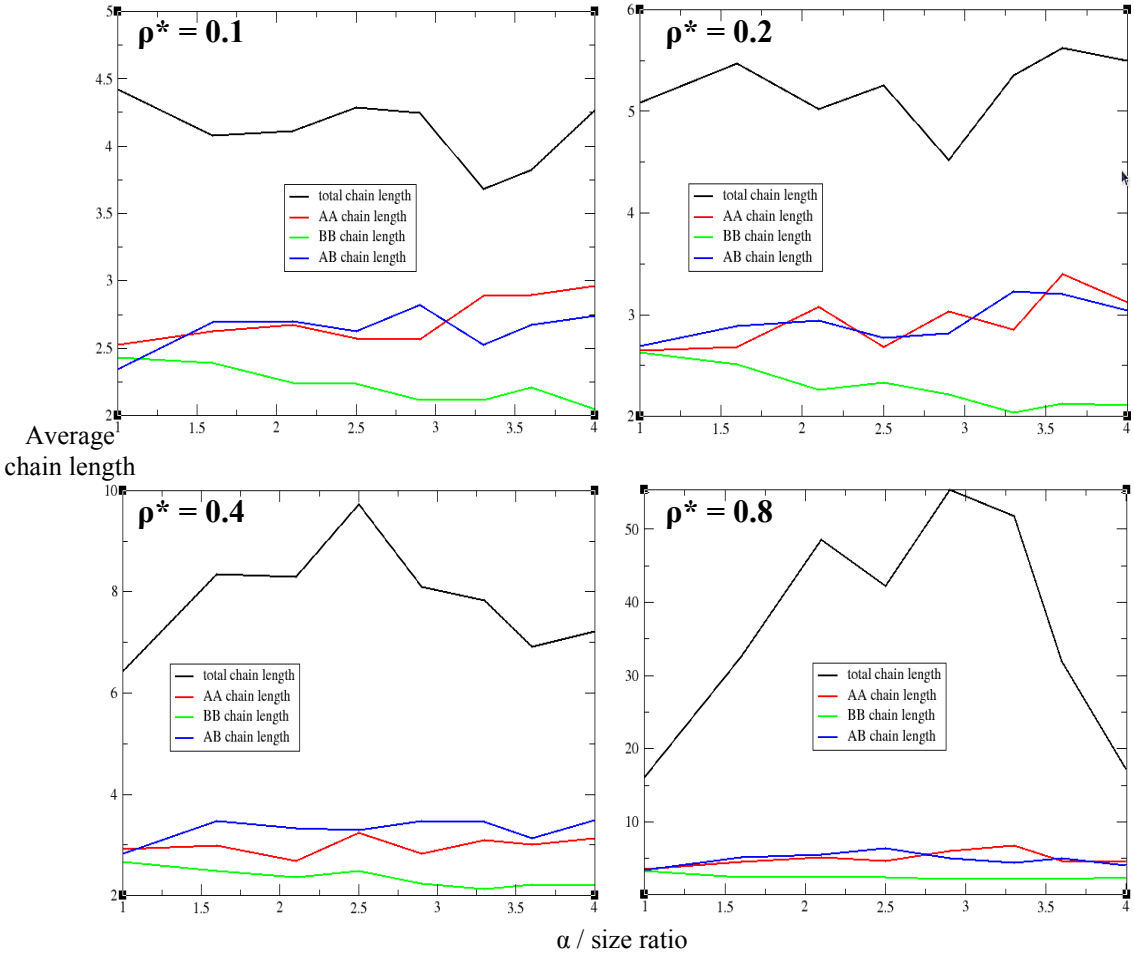

Figure 147 - *The mean chain lengths for different sized Stockmayer fluid particle mixtures at different densities. The mean chain length is plotted as a function of the mixtures (particles A and B) size ratio* α *for the total, AA, BB and AB chain lengths. There are four plots showing the result of simulation under different densities* ρ* *as indicated in the figure inset.*

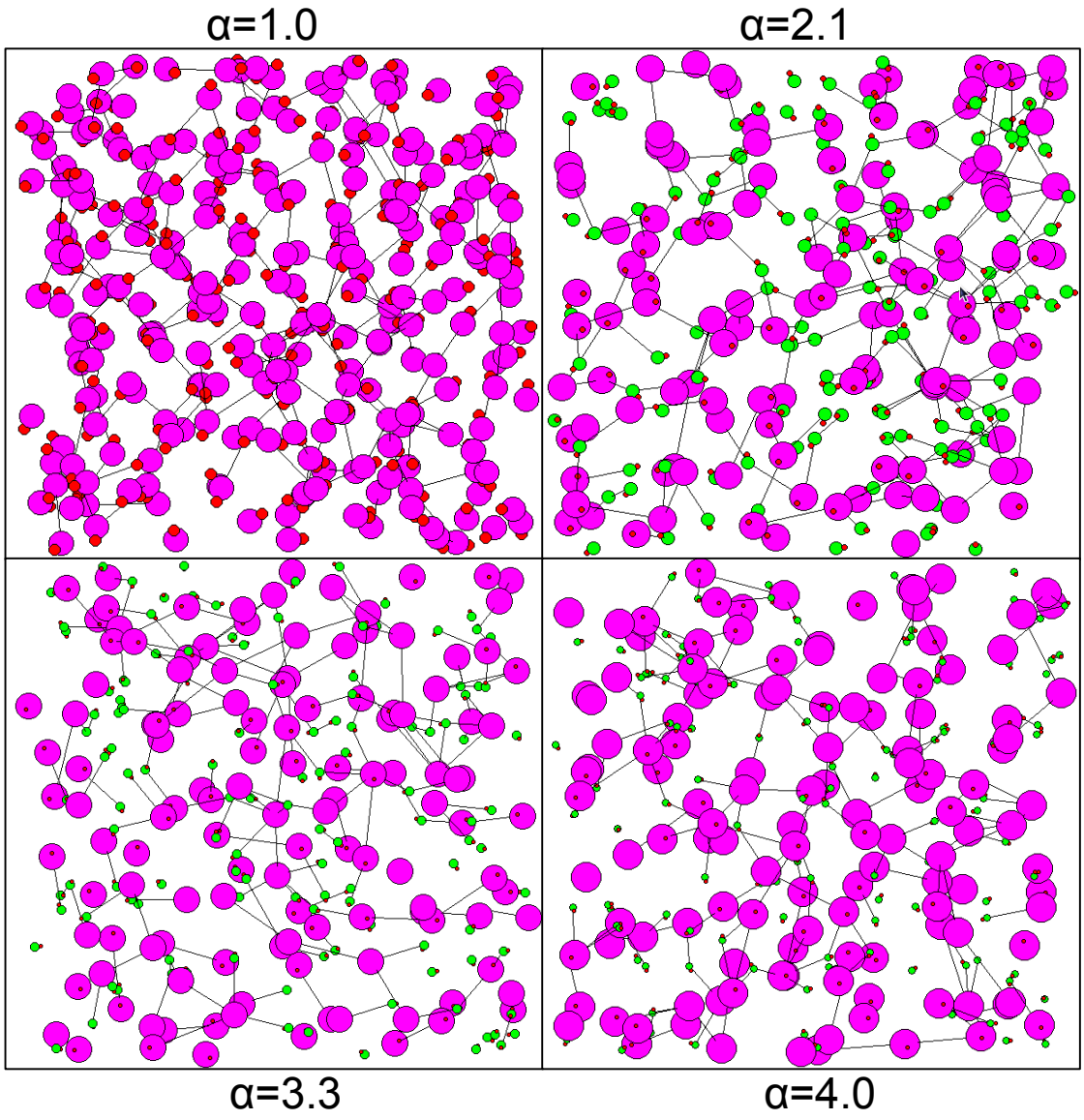

Figure 148 - *Snapshots of the equilibrium structure of the Stockmayer fluid at different size ratios. The figure contains the equilibrium structure achieved in the density ρ* = 0.8, the different size ratios shown are indicated adjacent to the figures. The purple particles, representing A particles, are larger relative to the green particles, representing B particles. The red particles indicate the direction of the dipole moments within each particle. The relative sizes of the purple and green particles are in accordance with the size ratios α indicated. The black line indicates connections or bonds between particles.*

6.5 Bond angle distribution

The bond angle data can be used to shed further light on to the types of structures being adopted by the Stockmayer fluids with different size ratios. The bond angle data for the Stockmayer fluid particles when there is a size ratio α of one are shown at four different reduced densities ρ*, which are 0.1, 0.2, 0.4 and 0.8 (Figure 149).

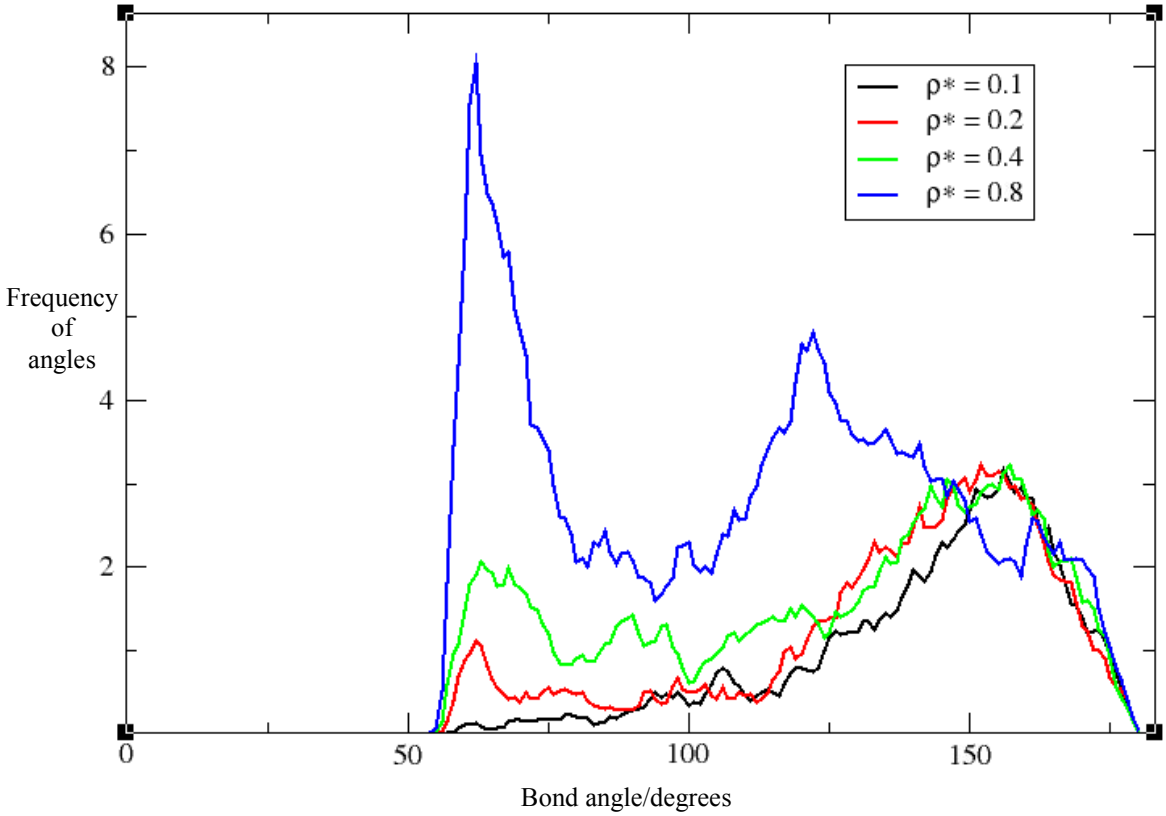

Figure 149 - *The bond angle data at different densities for a size ratio of one. The data inset shows the bond angles for the same Stockmayer fluid particles under varying densities ρ*. The data shows an ever-increasing peak at sixty degrees with increased density.*

The bond angle data show that the Stockmayer particles tend to form connections with a range of bond angles varying approximately between 55 and 180 degrees. The lower density of ρ* = 0.1 shows a peak at approximately 155 degrees, which indicates the presence of almost linear chain structures. The increasing of the density leads to a transformation of the bond angle data with the emergence of a peak at 60 degrees and a general increase in the distribution of bond angles below 155 degrees. The 60 degree

bond angle indicates the formations of a triangular unit of Stockmayer particles and this is particularly strong at the highest simulation reduced density of $\rho^* = 0.8$. The range of structures that are adopted by the Stockmayer particles along with the associated bond angles are represented in a simple diagram (Figure 150).

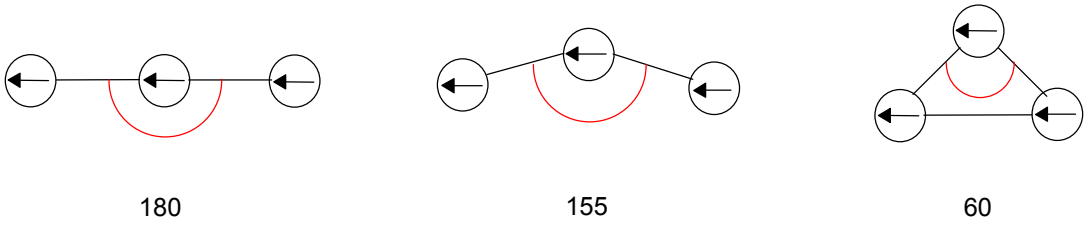

Figure 150 - *The range of Stockmayer particle structures adopted and their associated bond angles. The left figure shows a linear chain structure, with its highlighted angle also shown. The central figure shows the chain structure adopted on average in the simulations with a central angle of 155 degrees. The right figure shows the formation of a triangular unit with its associated bond angle of 60 degrees. The angles of interest are indicated by red.*

The examination of the Stockmayer fluid system composed of equally sized particles is contrasted with the extreme example, where the size ratio α between the particles is four. This means half the particles in the simulations are four times the size of the other component. The bond angle results of this simulation at all the reduced densities investigated, $\rho^* = 0.1$, 0.2, 0.4 and 0.8, in addition the total, A-A, A-B and B-B bond angle data are shown concurrently in Figure 151.

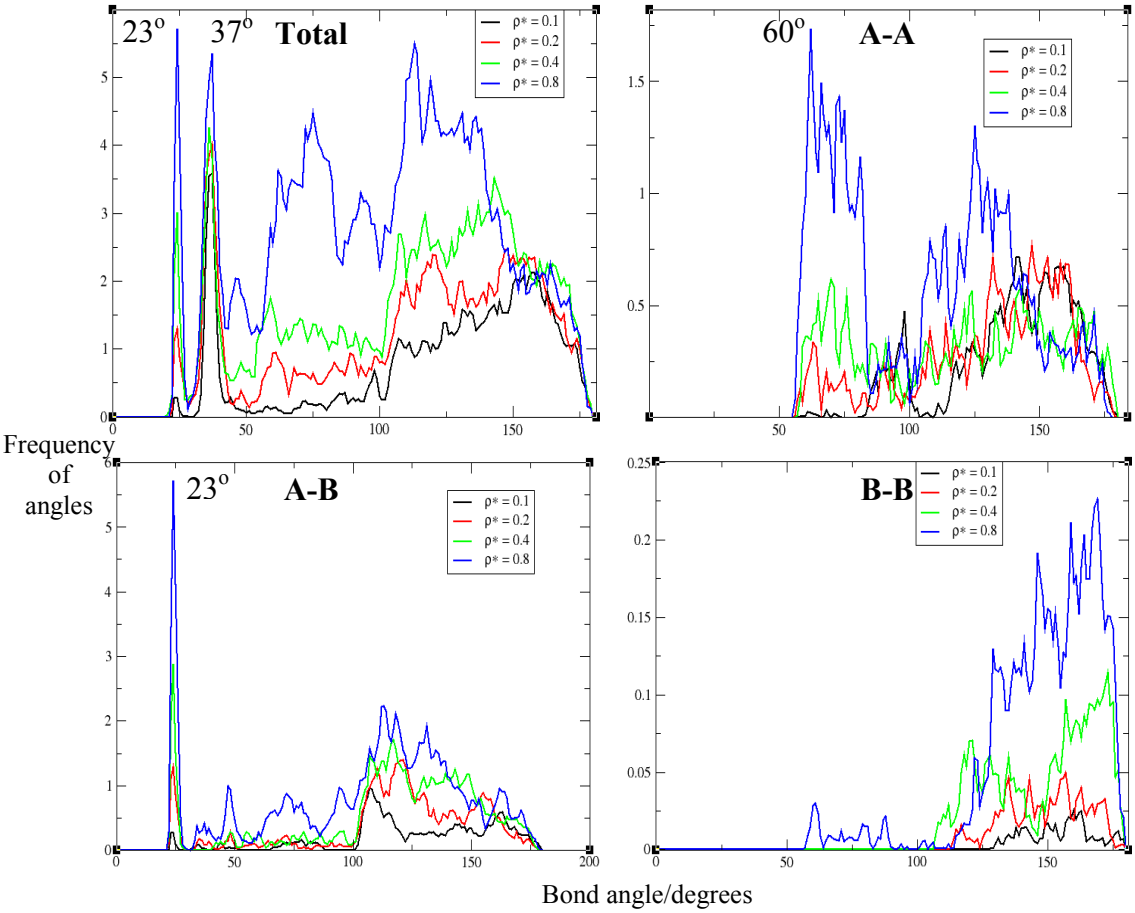

Figure 151 - *The Bond angle data for the Stockmayer fluid at varying densities when the size ratio α is four. The top left figure shows the total bond angle data, the top right figure shows the A-A bond angle data only. The bottom left figure represents the A-B bond angle data only and the bottom right figure shows the B-B bond angle data only. The particular densities used densities are listed in the figure legends. The potentially important peaks are highlight in each figure.*

The total bond angle data reveals the presence of the 155 degree peak observed previously for the equally sized Stockmayer fluid particles. The 60 degree peak is no longer prominent as there are strong peaks observed at approximately 23 and 38 degrees in the total bond angle data. The peak at 38 degrees is relatively unaffected by the variation in the densities, but the maximum at 23 degrees increases with increasing density. The A-A bond angle data shows that the larger Stockmayer particles only associate between the angles of 55 and 180 degrees. There is also a peak at 60 degrees, which increases with increasing density, similar to that observed previously in Figure 149 indicating that the same sized Stockmayer particles continue to form triangular units. The effect of increased density is to increase the frequency of

angles between 55 and 150 degrees for the A-A bond angle data. The A-B bond angle data reveals that the previously observed peak at 23 degrees in the total bond angle data is entirely due to the interaction between A and B Stockmayer particles. This is confirmed by the fact that the frequency in the A-B data matches that of the total bond angle data for the 23 degree peak. The A-B bond angle data also show increasing peaks between 100 and 110 degrees with increasing density similar to the 23 degree peak. The B-B bond angle data firstly shows very small frequency scale indicating few connections between the B-B atoms, and the bond angles vary primarily between 100 and 180 degrees. The frequency of the B-B bond angles increases with increasing density. The whole bond angle data set, A-A, A-B and B-B, can be seen to account for the bond angles observed in the total bond angle data except for the peak observed at 38 degrees which is not accounted for in any data set. This can only be the result of fragments such as AAB or BBA which are not picked up by the A-B bond angle data as they do not fulfil the requirements of being ABA or BAB fragments.

The bond angle data for the A-A connections indicated the presence of the triangular units of Stockmayer particles, due to the 60 degree angle peak, and so it is speculated that similar structures exist for the A-B connections. There are two possible combinations of differently sized Stockmayer fluid particles that can lead to triangular units. The most obvious is the ABA structure, and the second possible configuration is the BAB structure (Figure 152).

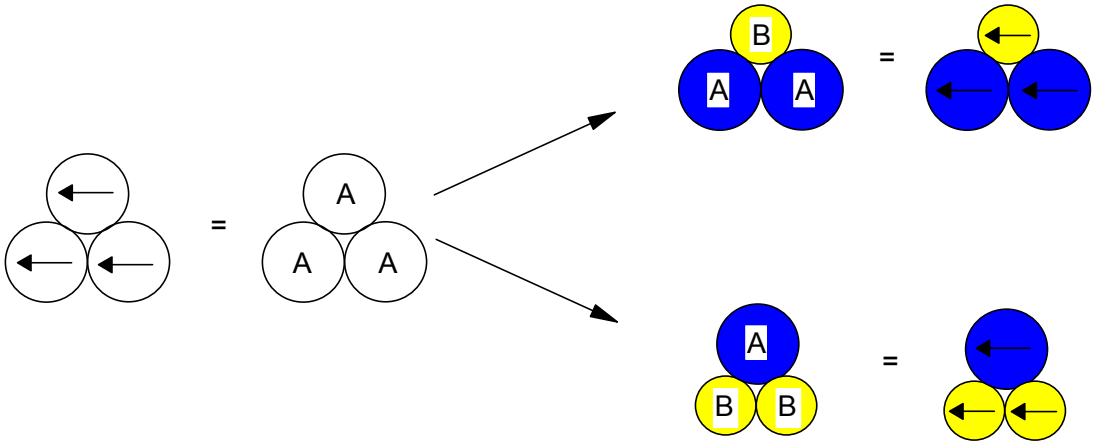

Figure 152 - *The two possible combinations of different sized Stockmayer fluid particles in forming triangular units. The left figure shows the triangular unit of equal sized Stockmayer particles. The right hand figures show the possible Stockmayer particle structures for differently sized particles. The top right figures show the ABA*

structure of Stockmayer particles, whilst the bottom right figures show the BAB structure. The A particles are larger than the B particles.

The theoretical bond angles of these triangular units can be calculated using the cosine function; this is exemplified by the calculation of the bond angles of the ABA structure when the size ratio α is four. The separations between the particles are based on the separations from the centre of each Stockmayer fluid particle (Figure 153).

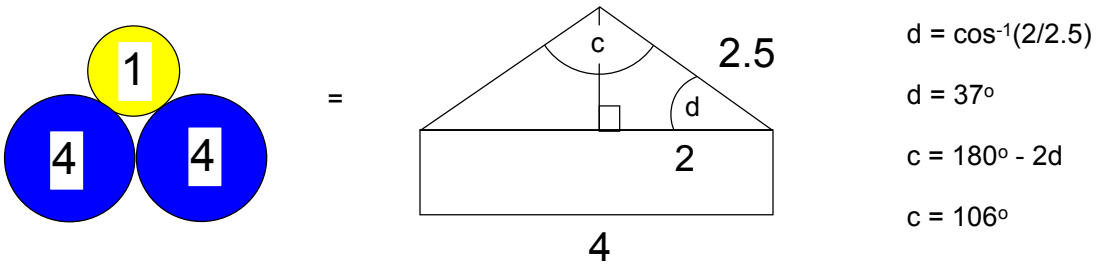

Figure 153 - *The calculations of bond angles in triangular units of different sized Stockmayer particles. In this example the ABA structure is composed of two larger A particles of diameter four, whilst the smaller B particles are of size one. This gives a size ratio of four. The separations between the centres of the Stockmayer particles are used to calculate the angles (c & d) in the triangular unit, as shown in the right hand side of the figure.*

The theoretical bond angle calculations for the size ratio of four indicates that two bond angles should be present in the total bond angle data, if indeed these triangular units exist. The bond angles at 37 and 106 degrees should appear strongly in the total bond angle data shown in Figure 151; in the case of the 37 degree angle this appears strongly. The larger 106 degree angle also appears in the range between 100 and 110 degrees, though not as strongly as the associated 37 degree angle as there are two 37 degree angles in the triangular unit as opposed to only one 106 degree angle. This analysis also accounts for the absence of the 37 degree angle from the A-B bond angle data as it is a BAA or AAB angle, and so it can not appear in the A-B data which require an alternating ABA or BAB patterns. The theoretical bond angles of the alternative triangular unit BAB can also be calculated (Figure 154).

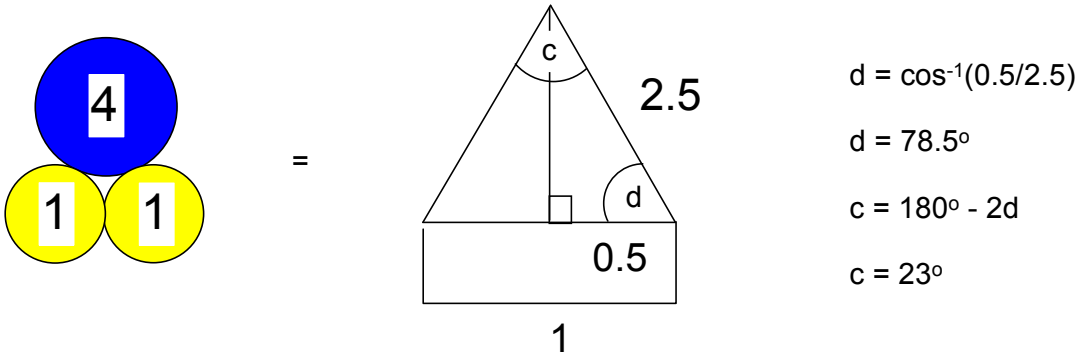

Figure 154 - *The calculations of bond angles in triangular units of different sized Stockmayer particles. In this example the BAB structure is composed of a larger A particles of diameter four, whilst the two smaller B particles are of size one. This gives a size ratio of four. The separations between the centres of the Stockmayer particles are used to calculate the angles (c & d) in the triangular unit, as shown on the right of the figure.*

The theoretical bond angle calculation for the BAB triangular unit gives a BAB angle of 23 degrees. This angle is observed in both the total and A-B connection bond angle data Figure 151 , and so this indicates that this BAB triangular unit becomes more prevalent with increasing density. This is opposed to the relatively constant ABA triangular unit which seems unaffected by density. The theoretical bond angle data also indicates the BAB triangular unit should have a BBA associative bond angle of approximately 78.5 degrees. This is not as clearly observed in the total bond angle data as the 23 degrees angle; however there is an extremely large increase at approximately 78 degrees when the density ρ* of the system is 0.8. This adds weight to the formation of these BAB triangular units at high density. To further understand the energetics to the formation of these ABA and BAB triangular units, their respective dipolar energies at different size ratios are calculated, assuming the reduced dipole moment and reduced temperature used in the simulations (Figure 155).

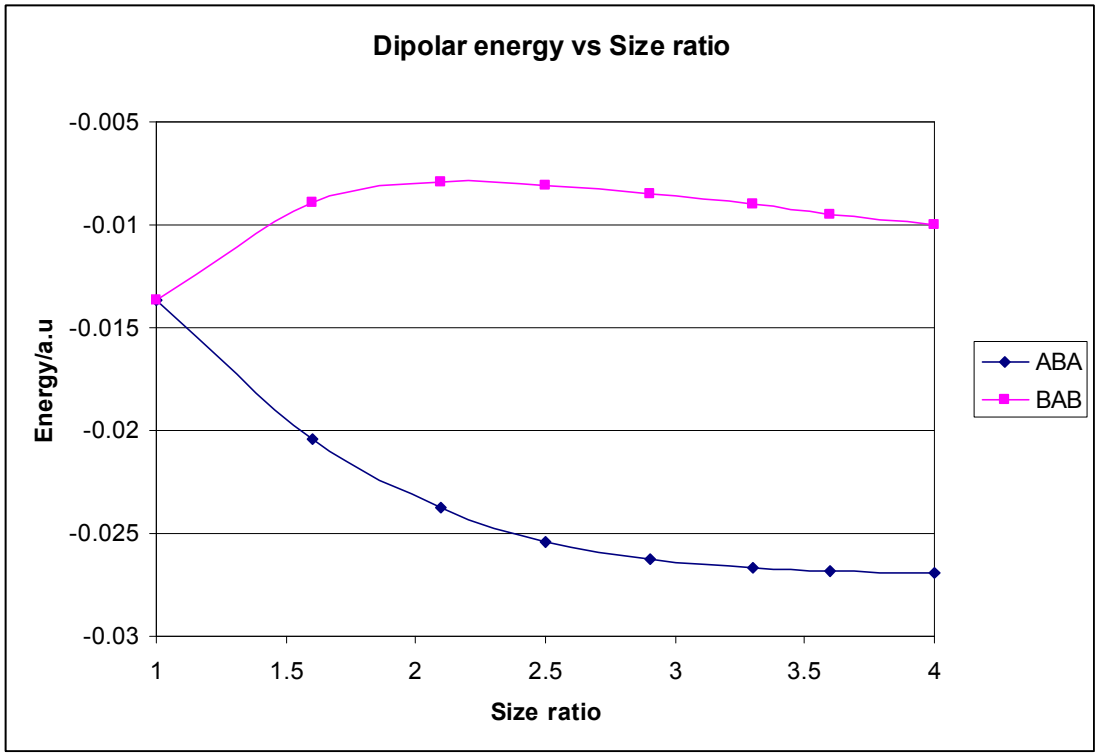

Figure 155 - *The dipole energy of the triangular ABA and BAB units at different size ratios of Stockmayer fluid particles. The ABA triangular unit energies at different size ratios are indicated in blue, whilst the BAB energies are indicated in red.*

The results of the energy calculations of the triangular units with different size ratios rather curiously reveal that it is in fact unfavourable to form the BAB triangular units relative to ABA units. They become increasingly energetically unfavourable to form with increasing size ratio, until approximately a size ratio of 2.3 after which the energy of the BAB units begins to slowly decrease with increasing size ratio. The energy of the BAB unit at a size ratio of four is still greater than that of triangular unit composed of equally sized Stockmayer particles, a size ratio of one. This is in stark contrast to the ABA triangular units which are energetically favourable to form with increasing size ratio. The energy of the ABA units at a size ratio of four is twice that for the triangular units at a size ratio of one. The results tend to suggest there is only a small energetic reason for formation of BAB units at high size ratios. The BAB units only increase in frequency with increasing density according to the total bond angle data in Figure 151, where the size ratio α is four. To further understand the formation of the BAB units in the Stockmayer fluid one can imagine a Stockmayer fluid where

there is a 1:1 ratio of ABA and BAB triangular units. The energy of such a system will then be dependent on the sum of the energies between a single ABA and BAB units, the energies at each size ratio in Figure 155 are summed, providing an overall energy that accounts for the equal presence of ABA and BAB units (Figure 156).

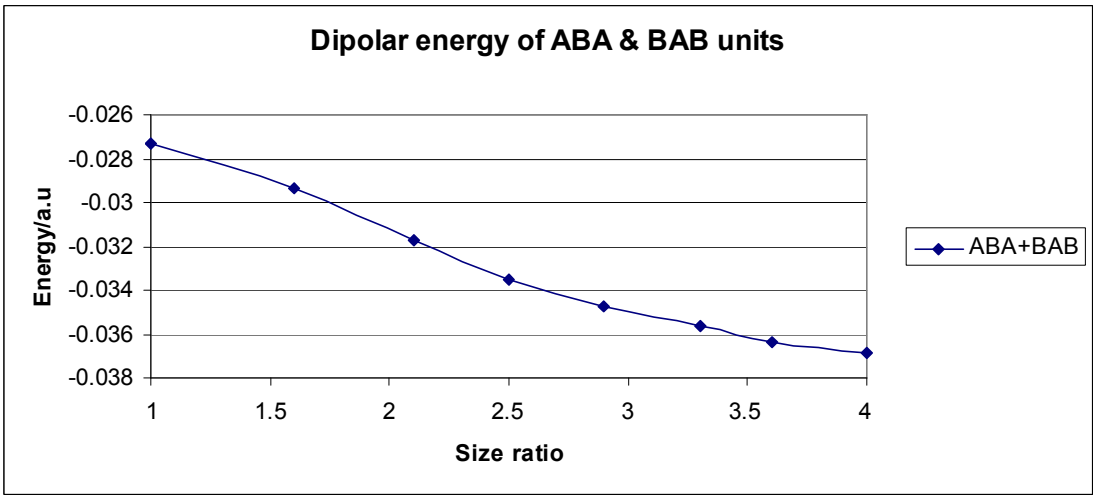

Figure 156 - *The summed dipole energy of the triangular ABA and BAB units at different size ratios of Stockmayer fluid particles. The figure illustrates the energy of having a 1:1 ratio of ABA and BAB units.*

The energy calculations show that linking the formation of the BAB units with that of the ABA units means that all size ratios greater than one, results in a favourable decrease in energy. The results indicate that the formation of the favourable ABA unit is able to compensate for the relatively unfavourable BAB unit at all size ratios greater than one in this idealised example of having equal quantities of the two configurations. There is an approximately 40% drop in energy from a size ratio of one to four. The results tend to provide the explanation behind why the BAB units can form in Stockmayer fluid. The results also raise the interesting question of how the energies of ABA and BAB triangular units compare to those of ABA, BAB, AAA and BBB chain structures (Figure 157). The dipolar energy of the AAA, BBB, ABA and BBB chain energies are calculated and compared (Figure 158).

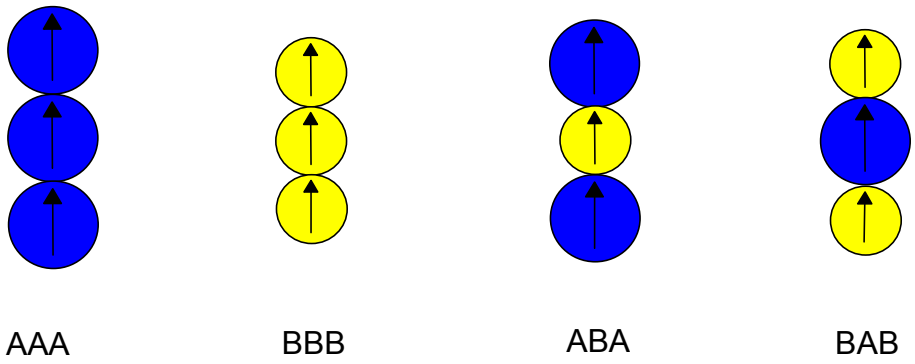

Figure 157 - *The different chain structures that can possibly form in the Stockmayer fluid. The figure above shows the basic chain structures that can be formed, with the homogenous AAA and BBB chains on the left and the heterogeneous ABA and BAB chains on the right of the figure.*

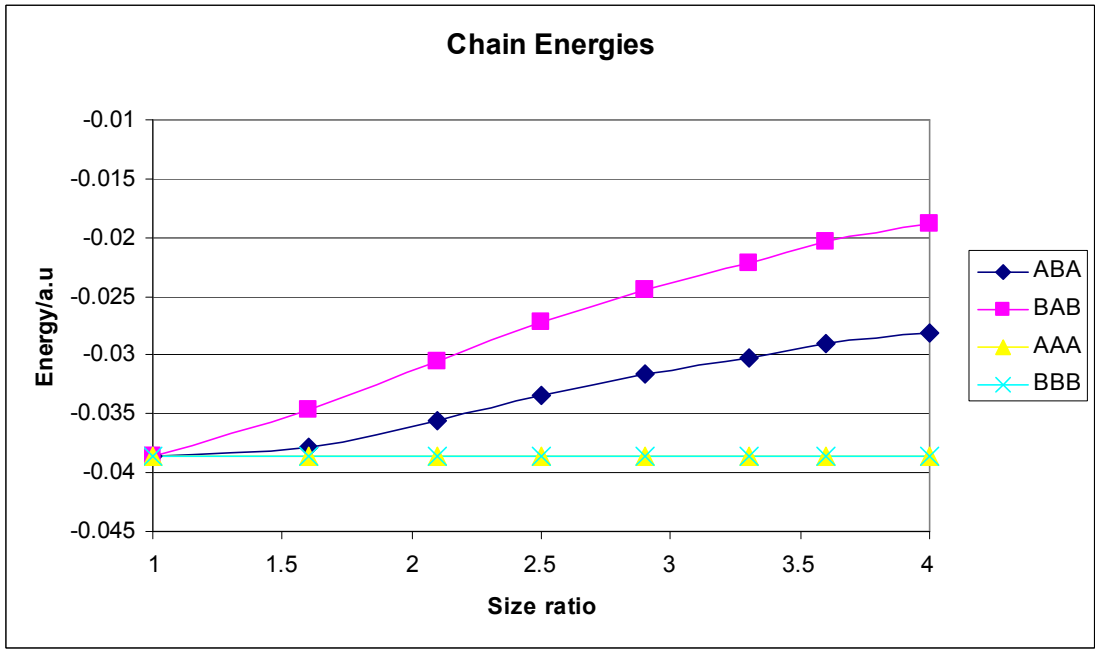

Figure 158 - *The dipolar chain energies of varying size ratio of Stockmayer fluid particles. The energies of the chain structures, AAA, BBB, ABA and BAB, are shown in the figure at different size ratios. The figure legend inset indicates each particular chain.*

The energy of the different chain structures indicate increasing the size ratio of the Stockmayer fluid has no effect on the energy of the AAA or BBB chains, which have the same energy at all sizes ratios. The energy of both the ABA and BAB chains

increase with increasing size ratio, though the BAB chains are more unfavourable than the ABA chains. The interesting thing to note from the data is that BBB chain energy is far more favourable than that of the ABA or BAB chains. This implies that homogeneous A-A and B-B chains should coexist in the Stockmayer fluid in energy terms rather than the formation A-B chains, however the presence of the larger A-A chains is likely to be preventing the association of the smaller B-B chains simply as a result of their size and steric hindrance. The data also suggests it is more favourable to form A-A chains surrounded by B particles, formation of ABA triangle units, than to form B-B chains surrounded by A particles giving rise to less favourable BAB triangle units (Figure 159). The ABA/BAB chains or triangular units are hence probable artefacts of the smaller B-B chain fragments associating with the larger A-A chains. The ABA and BAB chain and triangular unit dipolar energies are compared directly (Figure 160).

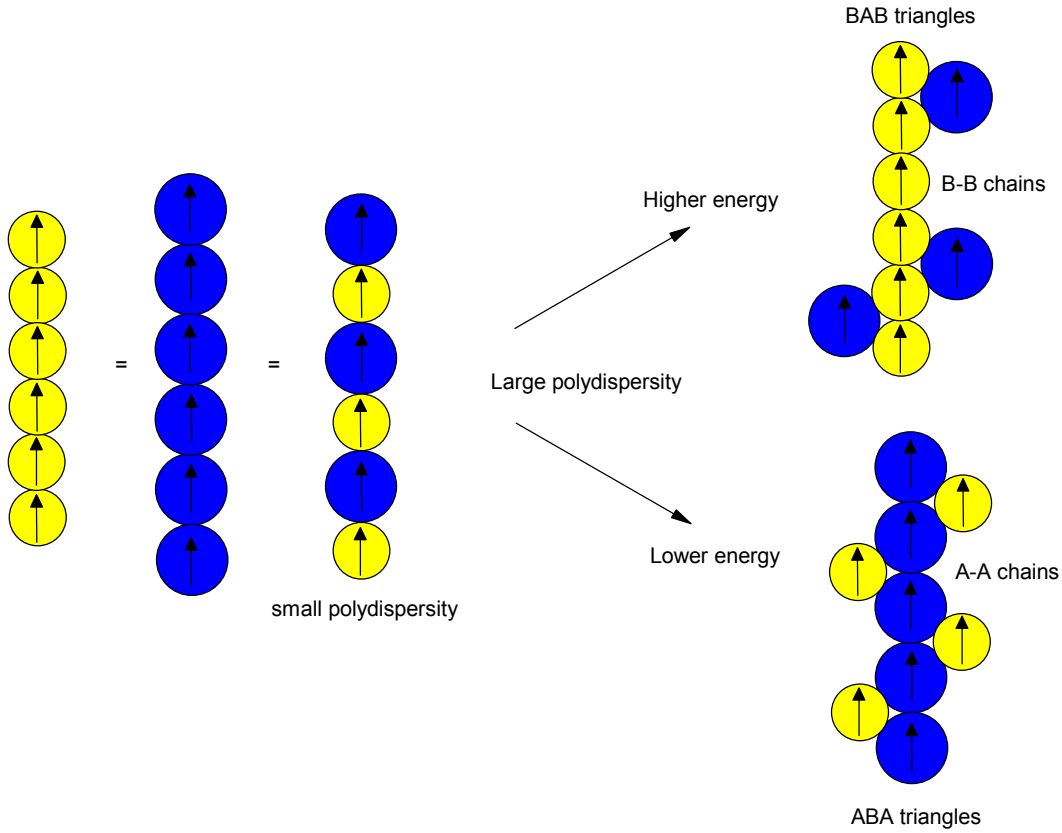

Figure 159 - *The information from the energy chain data summarized in a simple diagram. The left figures show that at small polydispersity the energy of the A-A, B-B and A-B chains are approximately the same. The situation at higher polydispersity makes the formation of linear A-A chains surrounded by smaller B particles (bottom right figure) more favourable than the formation of B-B chains surrounded by larger*

A particles (upper right figure). The former gives rise to ABA triangles whilst the latter gives rise to BAB triangles. The A particles are yellow and B particles blue.

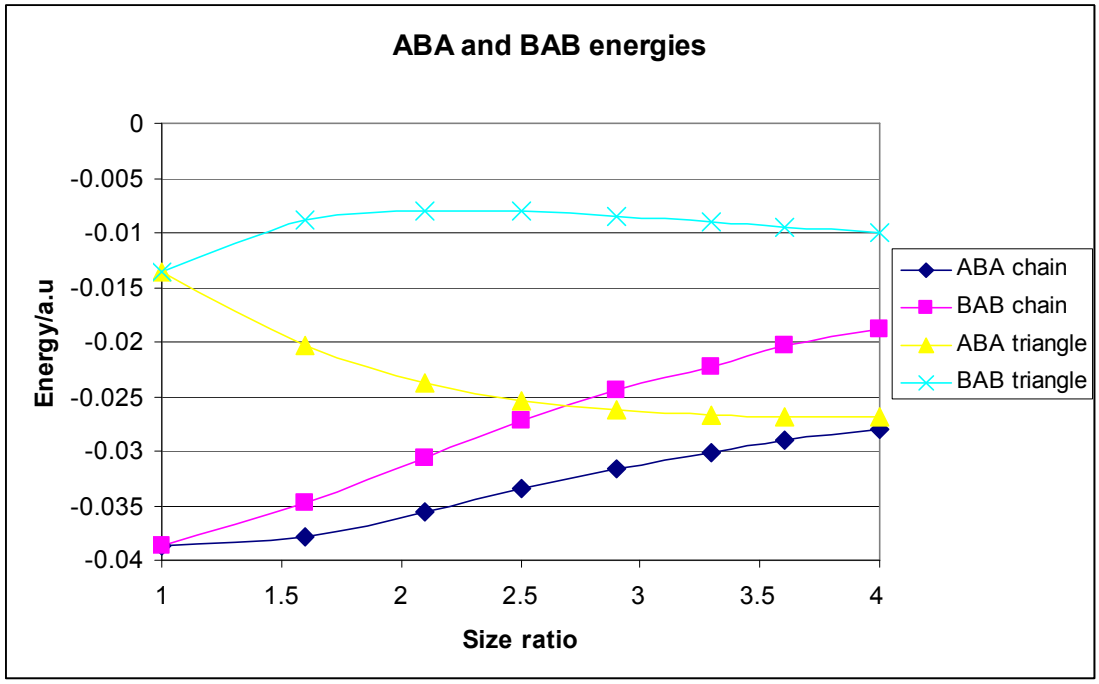

Figure 160 - *The comparison of dipolar energies of the ABA & BAB chain and triangular units. The figure legend indicates the ABA and BAB chain and triangular unit energies.*

The direct comparison of the ABA/BAB chain and triangular unit energies shows the respective chain and triangle energies converging at high size ratios. The ABA chain and triangle unit energies in fact converge at a size ratio of four: both structures are energetically equally favoured. The BAB chain and triangle unit energies also seem to be converging, however both the ABA chain and triangle units remain energetically more favourable than their BAB counterparts at all sizes ratios. The energies of the ABA triangles maybe greater than both A-A and B-B chains, however the efficient packing of the Stockmayer particles in the triangle ABA unit make them more attractive at higher densities. This can be confirmed if the bond angles between 20 and 110 degrees increase at higher densities, as angles in this range are indicative of the formation of triangular units. The total bond angles for all size ratios at the four different densities $\rho^* = 0.1$, 0.2, 0.4 and 0.8 are shown (Figure 161).

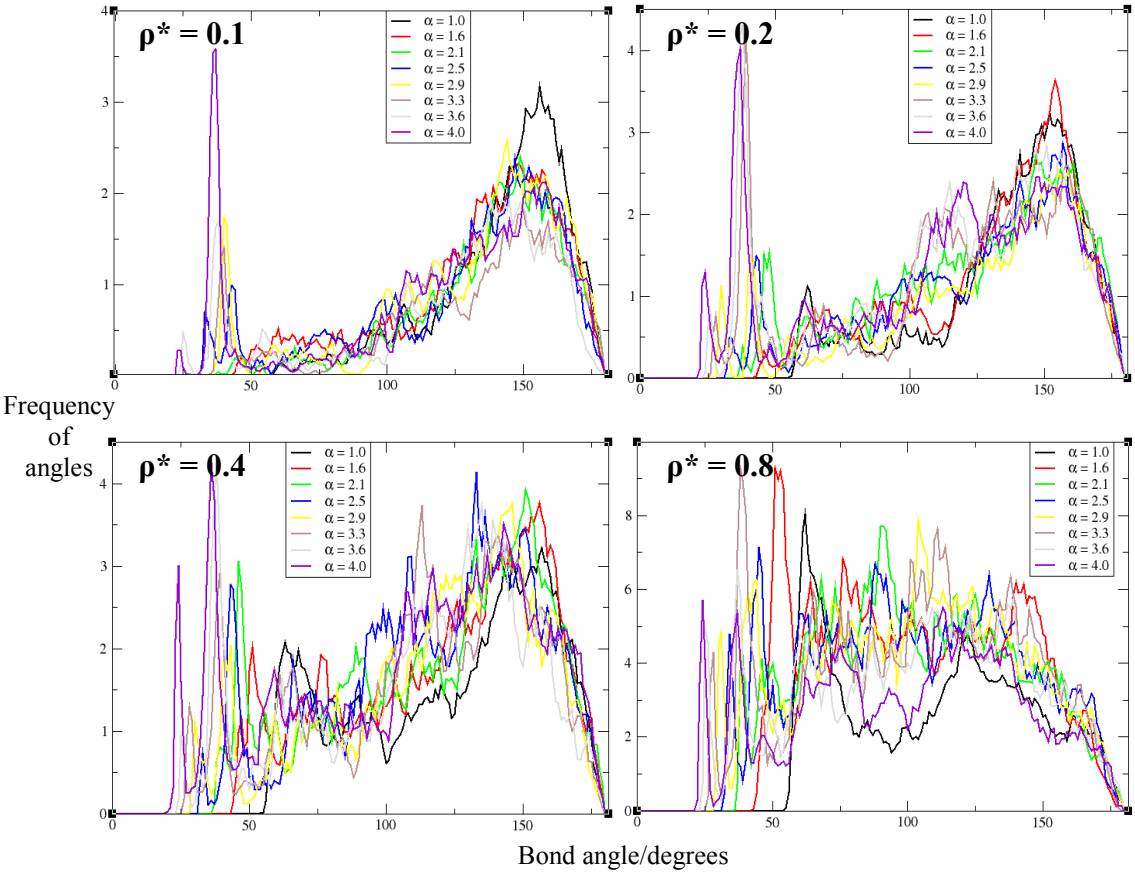

Figure 161 - *The total bond angle data for the Stockmayer fluid at varying densities with size ratio α one to four. The different densities are indicated in each figure inset. The size ratios are also indicated by the figure legends.*

The results of the total bond angles at different densities does indeed show an increase with rising density in the frequency of bond angles between 20 and 110 degrees which are indicative of the triangular ABA and BAB units. The interesting thing to note in the lowest density of ρ* = 0.1 is that the angles below 50 degrees only occur at high size ratios and especially for the highest size ratio of four. This fits well with the energy data which point to the energy of ABA chains and ABA triangular being equal at a size ratio of four, hence greater number of triangular units should be expected with increasing size ratio as the total bond angle data indicates.

6.6 Summary

The results all of the Stockmayer fluid simulations indicate that polydisperse dipolar fluids result in the mixing of the polydisperse particles to yield mixed chains even when the relative difference in sizes between particles is small. The presence of large polydispersity in the system results in the larger particles, with greater dipole moments associating in a chain like fashion. These larger particles prevent the formation of chains of smaller particles due to their steric hindrance; however the large voids between these larger particles allow the smaller particles to associate at the edges forming an extended chain structure. The formation of ABA and BAB triangular units occur more readily at both high size ratios and densities. This is due to the energy of the ABA triangular units being in parity with the ABA chain units at a size ratio four. These ABA and BAB fragments are shown from actual simulation at high density and size ratio (Figure 162).

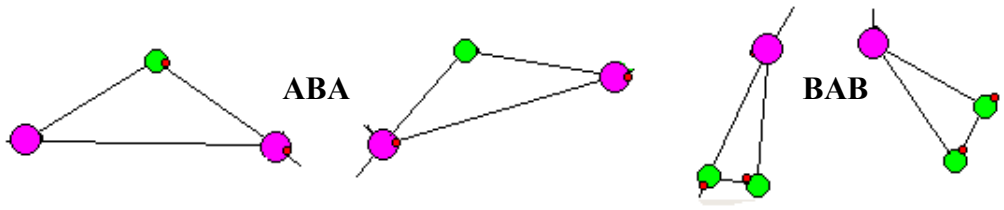

Figure 162 - *The presence of ABA and BAB units in Stockmayer fluid simulations at high density and size ratios. The A particles are represented by pink particles while the B particles are represented by green particles.*

Chapter 7 Simulations of tetrapods

7.1 Model details for zinc blende nanocrystals

The central aim of this chapter is to extend the Stockmayer fluid model, introduced previously, in an attempt to model the formation of bipod, tripod and tetrapod structures which are observed in the chemical synthesis of chalcogenide nanostructures. The standard Stockmayer fluid potential consisting of spherical particles described by the Lennard-Jones potential and a central dipole-dipole interaction is insufficient to model the formation of the aforementioned nanostructures. This is evident by having not observed the tetrapod structures previously in chapter 5. The wide variety of pod structures is essentially the result of the central core nanocrystals in these structures being of a zinc blende tetrahedrally faceted nature. Thus, in its simplest form the core nanocrystals can be considered to have four surfaces in a tetrahedral arrangement (Figure 163).

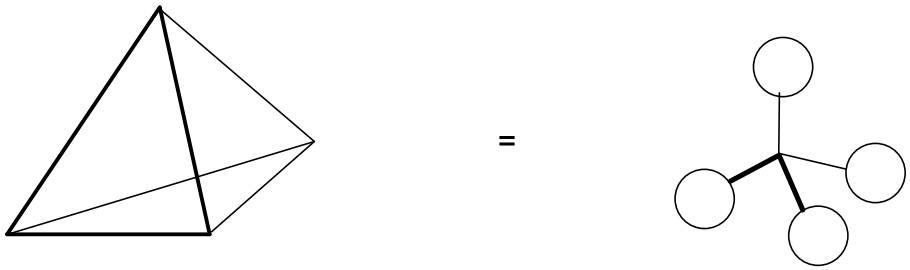

Figure 163 - *The core nanocrystals in pod structures can be represented as tetrahedral nanocrystals. The left figure shows a simple zinc blende nanocrystal with its four surfaces represented in tetrahedral arrangement. In the right figure, each of the spheres represent one of the four vertices of the tetrahedral nanocrystal.*

The primary reason, as discussed previously, for the presence of dipole moments in nanocrystals of this type is the result of opposite surfaces in nanocrystals being composed of contrasting anions or cations. Thus in the case of the core tetrahedral zinc blende nanocrystals there are four surfaces of which two can be composed of anions, whilst the remaining two can be composed of cations. This arrangement of the four surfaces, when each surface is considered as an independent entity, can result in four separate dipole moments which combine to give the overall resultant dipole moment found in the nanocrystal (Figure 164).

Figure 164 - *The tetrahedral arrangement of the four surfaces resulting in dipole moments. The left figure shows the zinc blende nanocrystal with its four surfaces, the black spheres represent the cation surfaces and the white spheres represent the anion surfaces. The right figure treats each sphere as a separate entity with the result of the different combinations of cation and anion surfaces being four separate dipole moments. These four separate dipole moments combine to give the overall dipole moment in the nanocrystals***.**

The four individual dipole moments of the tetrahedral nanocrystals all have a centre of mass, and the tetrahedral nanocrystals can now be represented in terms of four Stockmayer particles each with its own central dipole moment (Figure 165).

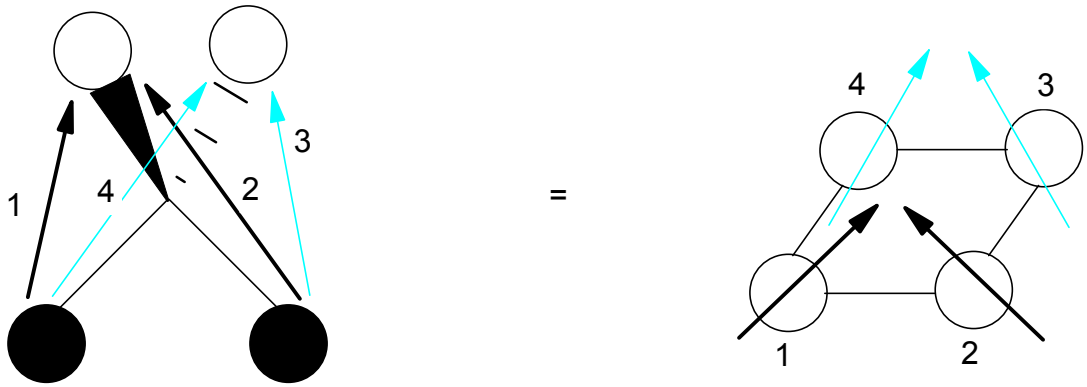

Figure 165 - *The tetrahedral nanocrystal represented in terms of Stockmayer particles. The left figure illustrates the origin of the four dipole moments in tetrahedral nanocrystals, whilst the right figure depicts the cluster of Stockmayer particles that can potentially model these tetrahedral nanocrystals.*

The four Stockmayer particles clustered together to describe the tetrahedral zinc blende nanocrystals found in pod structures has every nearest pair of particles with the dipoles pointing or merging together and this should theoretically lead to the formation of tetrahedral, tetrapod, structures. The standard Stockmayer particle can be considered to represent the wurtzite nanocrystals whilst the four clustered Stockmayer particles can be thought of as the zinc blende nanocrystals (Figure 166).

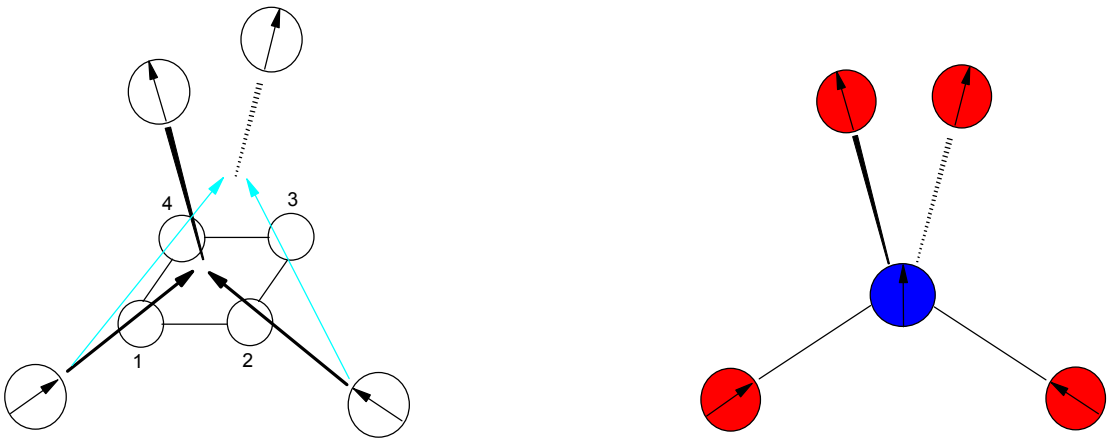

Figure 166 - *The theoretical formation of tetrapod structures using zinc blende and wurtzite nanocrystal representations. The left figure show the explicit representation of the zinc blende nanocrystal as four clustered Stockmayer particles, in addition isolated Stockmayer particles representing wurtzite nanocrystals are shown to be associating in an idealised manner with the zinc blende nanocrystal. The right figure shows the zinc blende Stockmayer cluster represented by a single blue Stockmayer particle and the wurtzite red Stockmayer particles associating around it.*

7.2 Lennard-Jones energy of zinc blende representations

In order to have continuity with previous simulation work the newly structured zinc blende nanocrystals representation must in some way relate back to a single idealised Lennard-Jones particle with diameter σ. The average 2D size of the zinc blende nanocrystals, 2σ*, can be used to calculate the size of the individual Lennard-Jones particles, σ*, making up the cluster (Figure 167). This means that the size of the smaller Lennard-Jones particles in the zinc blende cluster are simply related to a single Lennard-Jones particle by $\sigma^* = \sigma/2$.

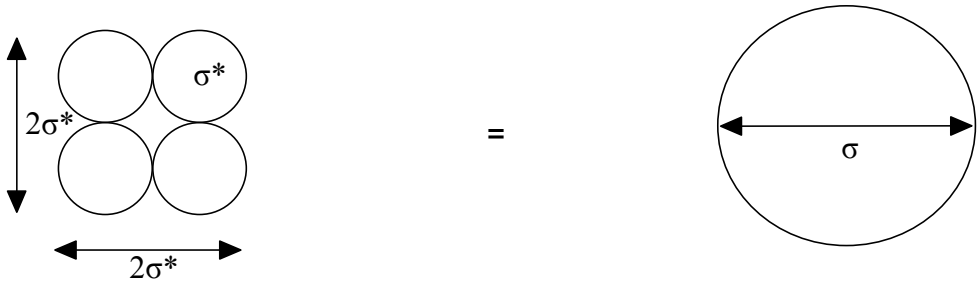

Figure 167 - *The constructed zinc blende cluster related to a single Lennard-Jones particle. The left figure shows the zinc blende cluster in terms of 4 Lennard-Jones particles each with diameter σ*. The average two-dimensional diameter of the zinc blende cluster is 2σ* and this must be the equivalent to a single Lennard-jones particle, right figure, with diameter σ.*

The interaction energy of the constructed zinc blende nanocrystals must have similar energy profiles to the interaction between two Lennard-Jones particles of diameter σ. This must be true for both the interaction between zinc blende nanocrystals themselves and between the zinc blende and wurtzite nanocrystals (Figure 168).

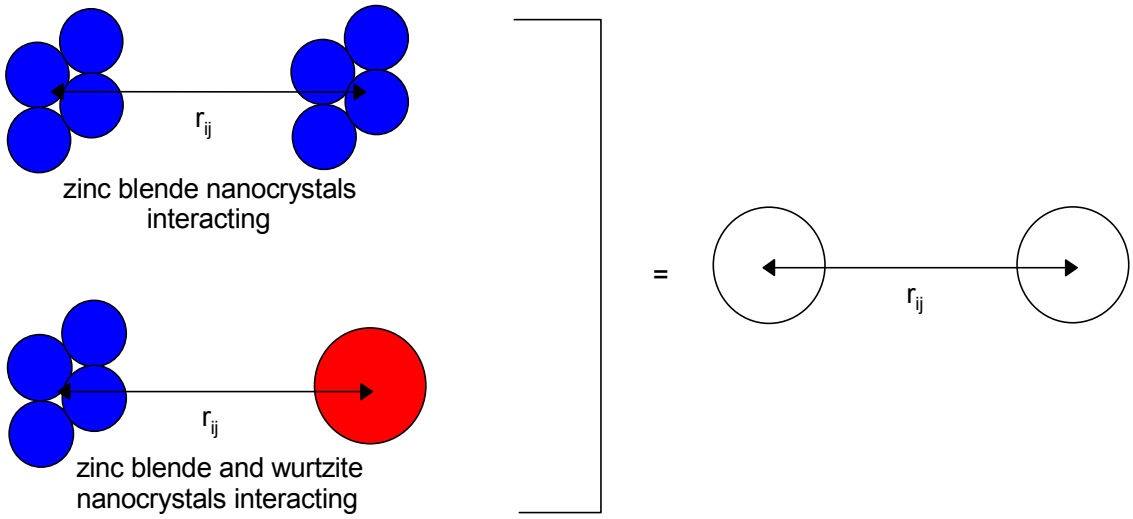

Figure 168 - *The constructed zinc blende nanocrystals representations interacting. The top left figure shows the zinc blende nanocrystals interacting amongst themselves. The bottom left figure shows the zinc blende nanocrystals interacting with wurtzite nanocrystals (Stockmayer fluid particle). The Lennard-Jones interaction energies of these two interactions must be approximately the same as two Lennard-Jones particles, right figure, to maintain continuity with previous simulation work.*

The interaction between pairs of zinc blende nanocrystals will require the calculation of sixteen Lennard-Jones interactions, the attractive and repulsive components of which can be treated separately in order to arrive at the effective potential energy well-depths for the attractive (ε_{za}) and repulsive (ε_{zr}) components. To achieve this, the assumption is made that separation, $r_{ij,}$ between all the possible combinations of interactions is the same as between the centres of mass of the two zinc blende nanocrystals (ie that the length-scales within the zinc blende nanocrystals are small compared with typical separations) (Equation 34).

Repulsive component:

$$\varepsilon\left(\frac{\sigma^{12}}{r_{ij}^{12}}\right) = \varepsilon_{zr}16\left(\frac{\sigma^{*12}}{r_{ij}^{12}}\right) \Rightarrow \varepsilon\sigma^{12} = \varepsilon_{zr}16\sigma^{*12} \Rightarrow \varepsilon_{zr} = \frac{\varepsilon\sigma^{12}}{16\sigma^{*12}}$$

Attractive component:

$$\varepsilon\left(\frac{\sigma^{6}}{r_{ij}^{6}}\right) = \varepsilon_{za}16\left(\frac{\sigma^{*6}}{r_{ij}^{6}}\right) \Rightarrow \varepsilon\sigma^{6} = \varepsilon_{za}16\sigma^{*6} \Rightarrow \varepsilon_{za} = \frac{\varepsilon\sigma^{6}}{16\sigma^{*6}}$$

Equation 34 - *The derivation of epsilon between two zinc blende nanocrystals. The value of epsilon is derived by comparing the interaction energy of the zinc blende nanocrystals with that of similarly sized Lennard-Jones particles and setting them to be of the same energy at the same separation. The top equation shows the derivation of the repulsive epsilon* (ε_{zr}) *whilst the bottom equation shows that for the attractive epsilon* (ε_{za})*. It should be noted that* $\varepsilon_{zr/}\ \varepsilon_{za} = (\sigma/\sigma^{*})^{6}_{.} = 64$.

The interaction between the zinc blende and wurtzite nanocrystals comprises of four Lennard-Jones interactions, and the repulsive and attractive components can be treated independently to attain analgous values of the effective potential energy well-depth for the attractive (ε_{zwa}) and repulsive (ε_{zwr}) interactions. Again, the separation between all inter-particle interactions is assumed to be the same separation, r_{ij}, between the zinc blende and wurtzite nanocrystals representations (Equation 35).

Repulsive component:

$$\varepsilon\left(\frac{\sigma^{12}}{r_{ij}^{12}}\right) = \varepsilon_{zwr} 4\left(\frac{\sigma^{*12}}{r_{ij}^{12}}\right) \Rightarrow \varepsilon\sigma^{12} = \varepsilon_{zwr} 4\sigma^{*12} \Rightarrow \varepsilon_{zwr} = \frac{\varepsilon\sigma^{12}}{4\sigma^{*12}}$$

Attractive component:

$$\varepsilon\left(\frac{\sigma^{6}}{r_{ij}^{6}}\right) = \varepsilon_{zwa} 4\left(\frac{\sigma^{*6}}{r_{ij}^{6}}\right) \Rightarrow \varepsilon\sigma^{6} = \varepsilon_{zwa} 4\sigma^{*6} \Rightarrow \varepsilon_{zwa} = \frac{\varepsilon\sigma^{6}}{4\sigma^{*6}}$$

Equation 35 - *The derivation of epsilon between a zinc blende and wurtzite nanocrystals. The value of epsilon is derived by comparing the interaction energy of the zinc blende and wurtzite nanocrystals with that of similarly sized Lennard-Jones particles and setting them to be of the same energy at the same separation. The top equation shows the derivation of the repulsive epsilon* (ε_{zwr}) *whilst the bottom equation shows that for the attractive epsilon* (ε_{zwa}). *Note* $\varepsilon_{zwr/}\ \varepsilon_{zwa} = (\sigma/\sigma^*)^6 = 64$.

The energy of interaction between two zinc blende nanocrystal representations can be directly compared to that of two similarly sized Lennard-Jones particles with the parameters listed in Table 1. The value of the repulsive (ε_{zr}) and attractive (ε_{za}) energy parameters are calculated as indicated by Equation 34. The Lennard-Jones interaction energy for the zinc blende nanocrystal is shown for three different configurations as it is an asymmetrical structure (Figure 169).

σ	6.00 a.u
ε	0.10 a.u

σ*	3.00 a.u
ε_{zr}	25.60 a.u
ε_{za}	0.40 a.u

Table 1 - *The parameters used in the calculation of the Lennard-Jones potential. The left table shows the parameters used to calculate the standard Lennard-Jones potential, whilst the right table shows the parameters used in calculating the energy between the zinc blende nanocrystals.*

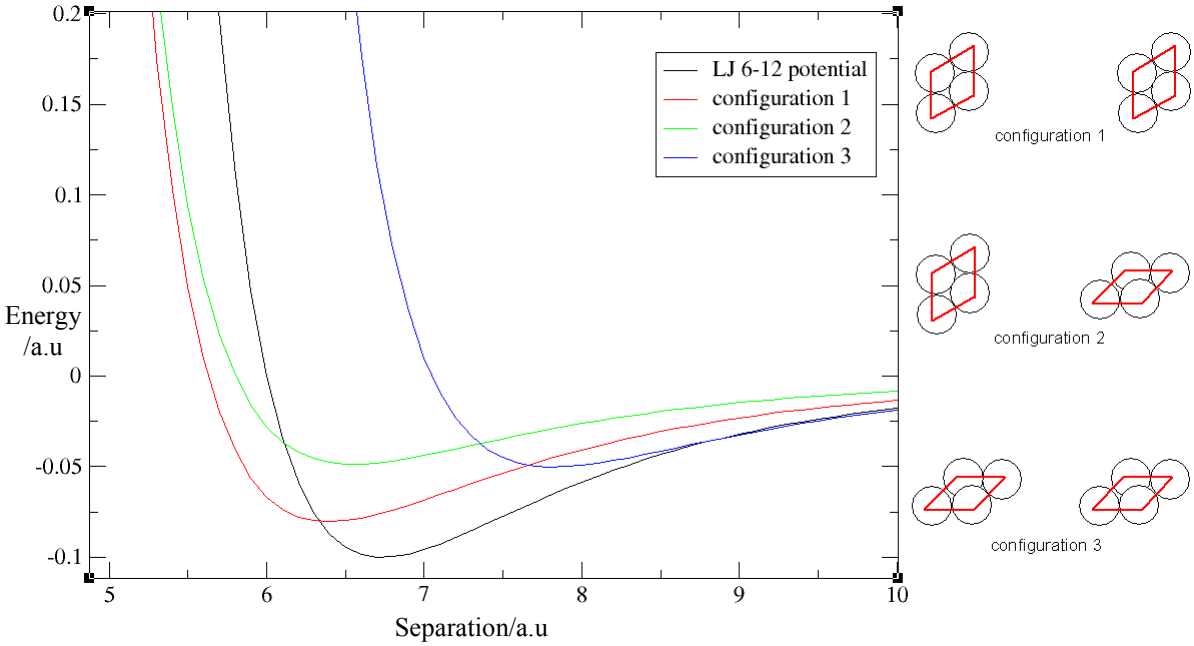

Figure 169 - *The Lennard-Jones potential between two zinc blende nanocrystals. The energy of the zinc blende nanocrystals in three different configurations is calculated and compared to the idealised energy of two Lennard-Jones particles in the graph with the configurations of the nanocrystals illustrated in the right of the figure.*

The first configuration presented has a minimum that occurs at 6.4 a.u, the second configuration of the zinc blende nanocrystals, which are orthogonal to one another, has a minimum at approximately at 6.5 a.u. These two results compare favourably with the Lennard-Jones potential which has a minimum at 6.75 a.u. The third configuration has a minimum at 7.8 a.u, though the minima for all three configurations varies greatly the energy interaction compares reasonably with the standard Lennard-Jones potential for a collection of four smaller particles forming an asymmetrically shaped cluster.

The energy of interaction between zinc blende and wurtzite nanocrystal representations can be directly compared to that of two similarly sized Lennard-Jones particles with the parameters used listed (Table 2). The value of the repulsive (ε_{zwr}) and attractive (ε_{zwa}) epsilon are calculated as indicated by Equation 35. The Lennard-Jones interaction energy between zinc blende and wurtzite nanocrystals is shown for three different configurations due to the asymmetrical structure of the zinc blende nanocrystal in Figure 170.

σ	6.00 a.u
ε	0.10 a.u

σ*	3.00 a.u
ε_{zwr}	102.4 a.u
ε_{zwa}	1.60 a.u

Table 2 - *The parameters used in the calculation of the Lennard-Jones potential. The left table shows the parameters used to calculate the standard Lennard-Jones potential, whilst the right table shows the parameters used in calculating the energy between the zinc blende and wurtzite nanocrystals.*

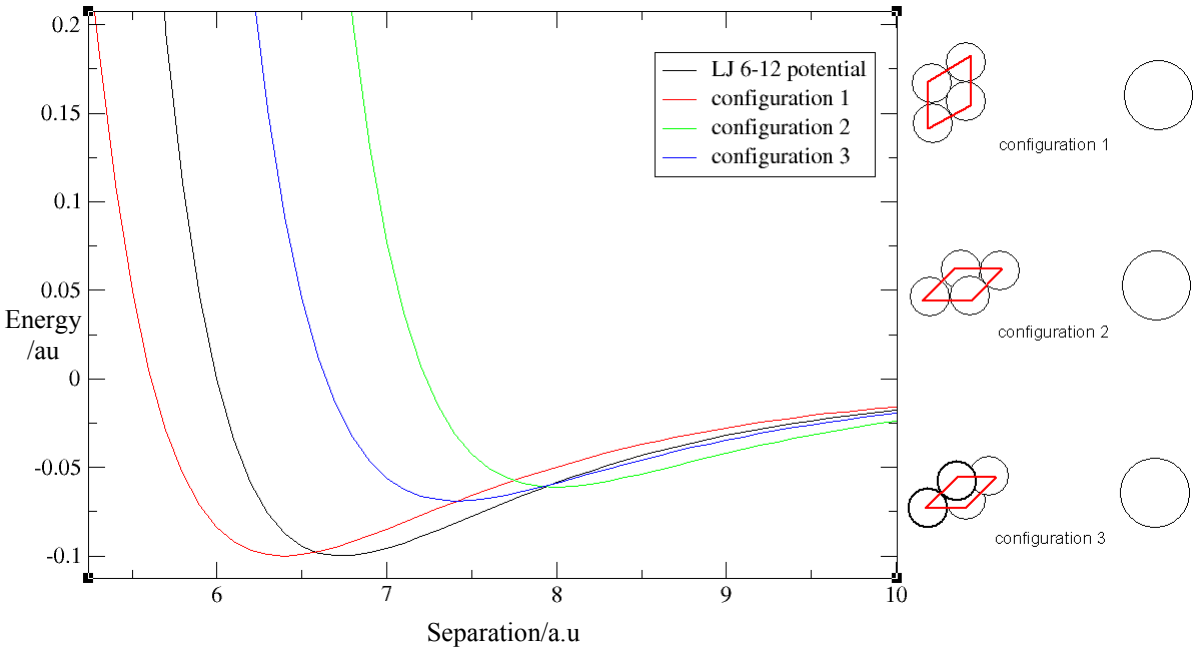

Figure 170 - *The Lennard-Jones potential between zinc blende and wurtzite nanocrystals. The energy of the nanocrystals in three different configurations is calculated and compared to the energy of two Lennard-Jones particles in the graph with the configurations of the nanocrystals illustrated in the right of the figure.*

The first configuration between the zinc blende and wurtzite nanocrystals has a minimum that occurs at 6.4 a.u, the second configuration has a minimum at approximately 8.0 a.u. The third configuration, in which the zinc blende nanocrystal is at 45 degree angle, has a minimum at 7.4 a.u, The minima for all three configurations varies greatly and is similar to the results observed in Figure 169. The Lennard-Jones idealised potential is closest in energy to the first configuration.

7.3 Zinc blende representations and their dipole moments

The dipole moments in the zinc blende nanocrystal are assigned essentially according to the ratio of the separations between the anion and cation surfaces. In the perfect tetrahedral case the angle between the surfaces is 109.5 degrees; this can be used to determine the ratio of the separation between the anion and cation surfaces in the x, y and z directions (Figure 171).

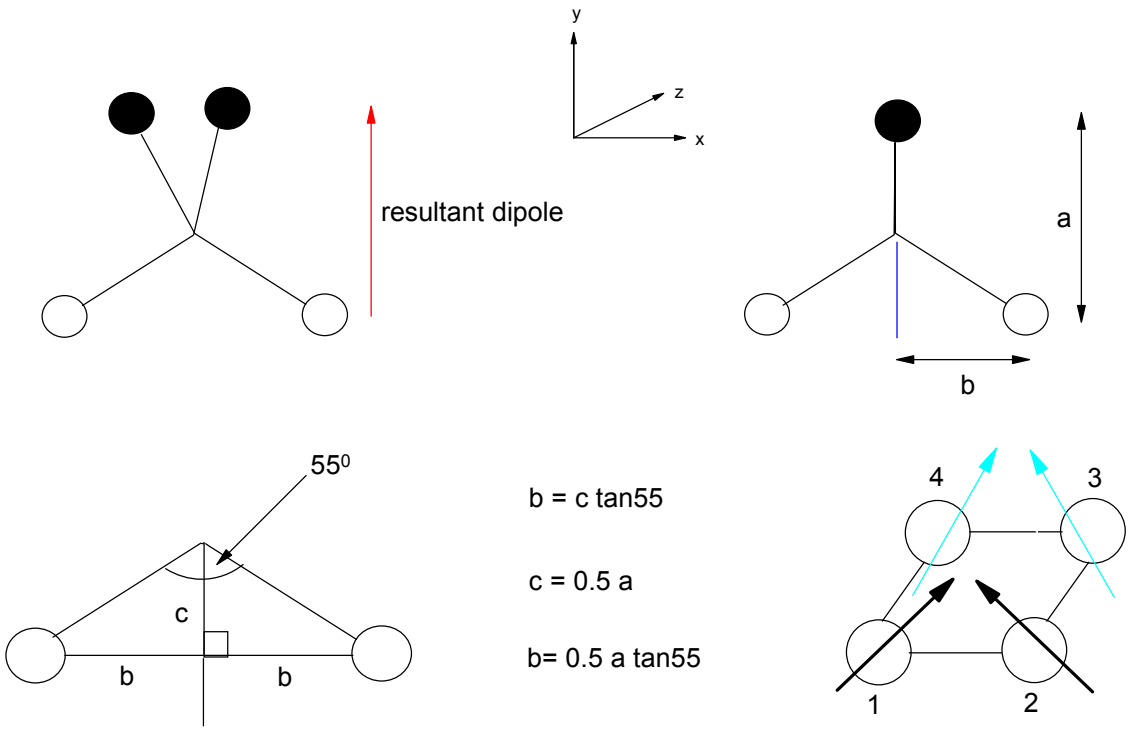

Figure 171 - *The calculation of the separation between the anion, black spheres, and cation, white spheres, surfaces. The top left figure show a tetrahedral arrangement of surfaces with the resultant dipole in the y direction. The top right figure shows the tetrahedral arrangement from a different angle. The resultant dipole is proportional to the separation a, the separation b is calculated according to the bottom left figure in terms of the separation a. This separation ratio can be used to assign the dipole components of each Lennard-Jones particle in the zinc blende nanocrystals depicted, bottom right figure.*

The figure illustrates how the dipole components of each particle in the zinc blende nanocrystals are assigned. This can be proven by a simple example in which the zinc blende nanocrystals are supposed to have a resultant dipole moment of μ=1 a.u. In this

case the four individual particles must have a μ_y component that is 1/4, 0.25 a.u, as this y component dipole is related to the separations according to Figure 171. The x and z components can be calculated for each particle making up the zinc blende nanocrystals, this is shown for the first two particles in the zinc blende nanocrystal (Figure 172).

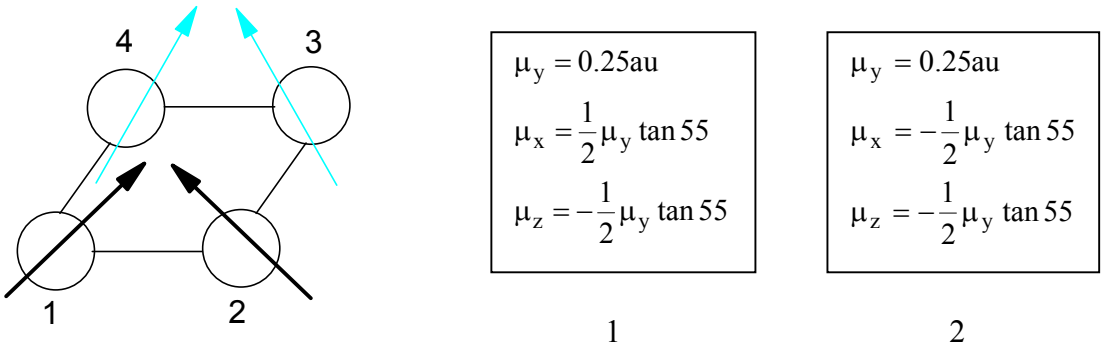

Figure 172 - *The dipole components of the zinc blende nanocrystals. The figure left shows the zinc blende nanocrystals made up of four particles. The dipole components, in the y, x and z directions, of the first and second particles are assigned according to the equations on the right for each particle respectively.*

7.4 Dipole-dipole energies of zinc blende representations

The Lennard-Jones interactions between these exotic looking zinc-blende nanocrystals and the standard Stockmayer particle, which can represent the wurtzite nanocrystals, have been calculated and their effects illustrated. The next stage is to examine the dipole-dipole interaction energies between the zinc-blende (zb) wurtzite (wz) nanocrystals. In the following examples the resultant moments in both of the zinc blende and wurtzite representations are 1.0 a.u and the diameters σ = 6.0 a.u, which corresponds to σ^* = 3.0 for the zinc blende nanocrystals. The dipole-dipole energy profile is built up by rotating one nanocrystal j about another i at a fixed separation, these are $r_{ij} = \sigma$, 1.5σ, 2σ and 3σ, through various angles θ (Figure 173). The results of these energy profiles are shown at the four separations listed previously (Figure 174).

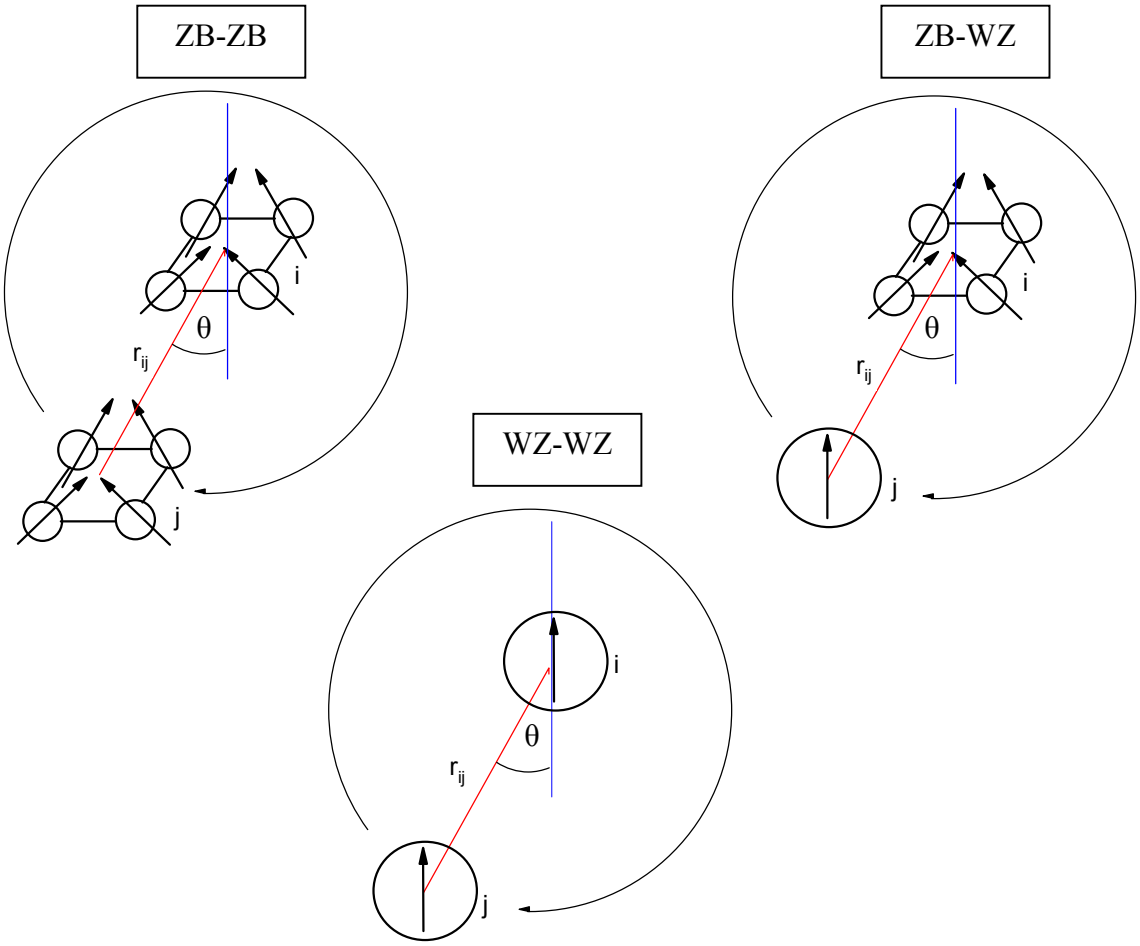

Figure 173 - *The dipole-dipole energy profile being built up for the zinc blende and wurtzite nanocrystals. The top left figure shows the zinc blende nanocrystal profile, the top right figure illustrates the zinc blende and wurtzite energy profile being built up and the bottom figure shows the wurtzite or idealised Stockmayer fluid particle energy profile being built up.*

The result of the energy profiles in Figure 174 for the various interactions, zb-zb, wz-wz and zb-wz, reveal that at separations that are three times the diameters of the nanocrystals there is good agreement as the energy profiles overlap well. This indicates that the structural detail of the zinc blende nanocrystals is effectively lost at these large separations. There is subtle departure from the overlapping energy profiles when the separation is reduced to twice the diameter, the zb-zb interactions show the greatest departure from the idealised dipolar model with respect to the wz-wz interaction. This departure from overlapping energy profiles continues at one and half times the diameter of the nanocrystal, however the zb-zb and zb-wz profiles still show

good agreement with the wz-wz interactions with regards to the positions of minima and maxima energies in the profiles. This analysis is similarly true for when the separation is equal to the diameter, the spheres or nanocrystal representations are in zcontact, though in the case of the zb-wz profile there is an emergence of a new minima at an angle θ is equal to 35 degrees. These deviations at short separations are the result of the zinc blende nanocrystal with the effect of the four individual dipole moments becoming more prominent, the new minima at 35 degrees could potentially be construed as the formation of the tetrahedral connection predicted in the inception of this model. This can be investigated further by carrying out the zb-wz calculations again at a separation of σ; however on this occasion the relative angle between dipoles is set to 45 degrees, to mimic a preferential angle of association, for the wz nanocrystal j (Figure 175).

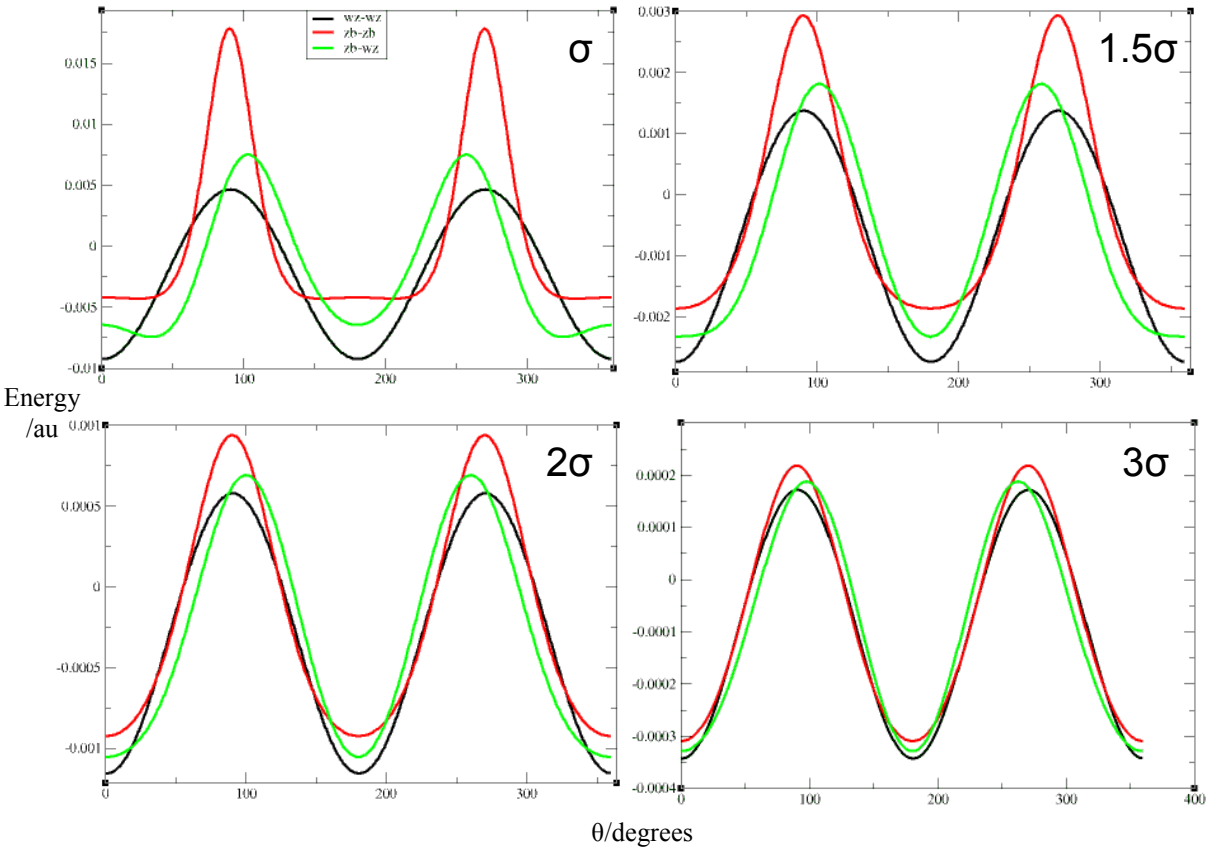

Figure 174 - *The energy profiles of the zinc blende (zb) and wurtzite (wz) nanocrystals at fixed separations. The figures above show the wz-wz interaction profiles in black, the zb-zb interaction profiles in red and the zb-wz interaction profiles in green. The different separations at which the energy profiles are built up for the different interactions are listed in the individual figures.*

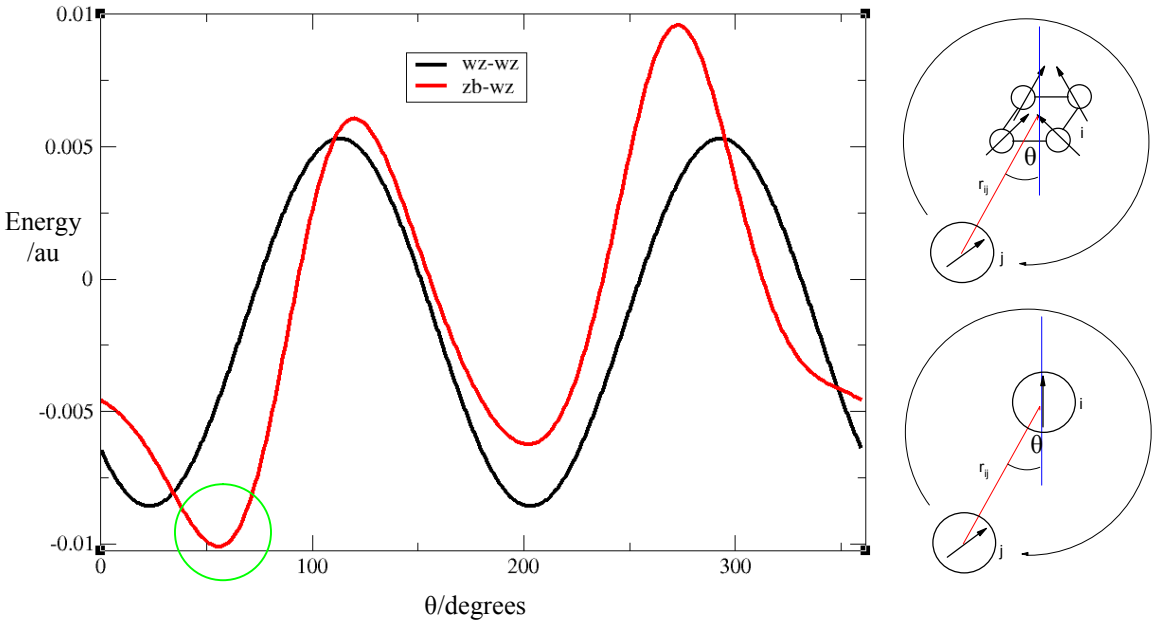

Figure 175 - *The dipole-dipole energy profile of the zinc blende (zb) and wurtzite (wz) nanocrystal representations. The right figures show the rotating spheres j having their respective dipoles at a 45 degree angle relative to the dipoles in i. The energies of the wz-wz are shown in black and that of the zb-wz are shown in red. The minimum at 55 degrees of angle θ is highlighted in green.*

The results from energy profile show that there is indeed a minimum at 55 degrees. This is the result of the wz nanocrystals representation interacting with the zb nanocrystals representation in a tetrahedral manner as the angle is 55 degrees between the zb and wz nanocrystals. The interaction energy of this tetrahedral interaction is greater, by approximately 7%, than that observed for the head-tail interaction between the wz-wz nanocrystals at an angle of 0/360 or 180 degrees of θ in Figure 174 at exactly the same separation of σ.

7.5 Introduction to simulations

The simulations in this chapter also examine the effect of polydispersity similar to that observed in the previous chapter 6. However unlike previously, where the binary mixture of particles were homogenous with respect to their basic structure, the zinc blende and the wurtzite representations are structurally heterogeneous. This means the size ratio parameter between the two is slightly modified to the one encountered previously, A particles can be considered the wurtzite representations and the zinc blende representations are B particles (Equation 36). There are 216 particles in total present in the simulations, such that $N_A = N_B = 108$ particles. The reduced dipole moment is constant for both the components, $\mu_a^* = \mu_b^* = 3.0$. The reduced temperature of the simulations is also constant, $T^* = 1.0$.

If $\sigma_A > \sigma_B$ then: $\alpha = \frac{\sigma_A}{\sigma_B}$

If $\sigma_A < \sigma_B$ then: $\alpha = -\frac{\sigma_B}{\sigma_A}$

Equation 36 - *The size ratio between the zinc blende and wurtzite representations. The top equation shows the size ratio calculated when the size of A particles is greater than B particles. The bottom equation shows the size ratio calculated when the size of B particles is greater than A particles.*

7.6 Radial distribution function

The radial distribution function offers an insight into the spatial arrangements of particles in a system. However the radial distribution functions are not ideal in helping to discern the presence of any tetrahedral structure in the system. The radial distribution functions of the Lennard-Jones and Stockmayer fluids involving zinc blende and wurtzite representations are shown for size ratios of 1.0, 2.1 and -2.1 at three reduced densities $\rho^* = 0.1$, 0.2 and 0.4 in each case (Figure 176).

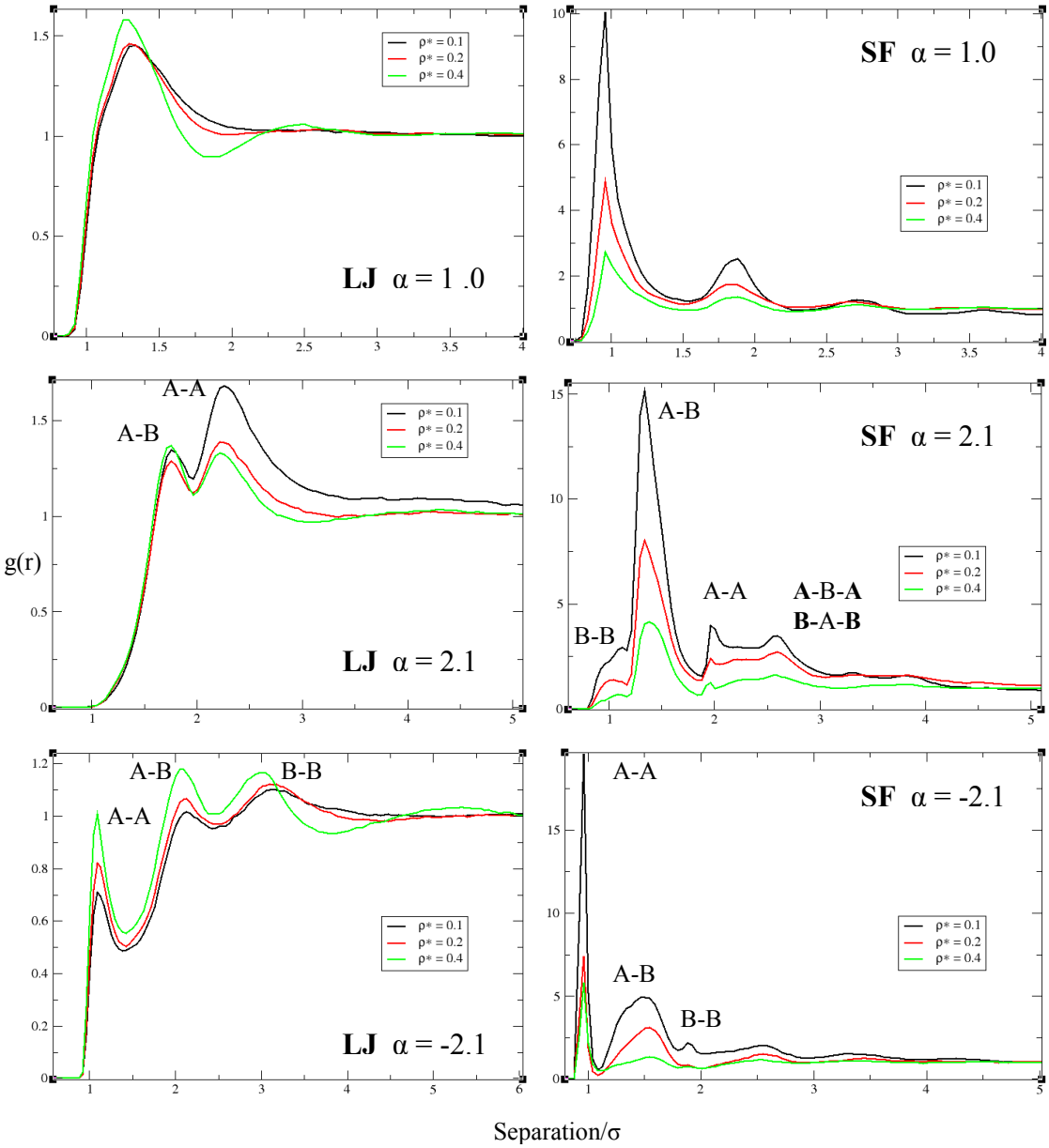

Figure 176 - *The radial distribution functions for both the Lennard-Jones and Stockmayer fluid potentials with zinc blende and wurtzite representation. The left figures all show the Lennard-Jones (LJ) radial distributions functions at different size ratios, indicated in each individual figure. The right figures all show the Stockmayer fluid (SF) radial distribution functions at different size ratios, indicated in each individual figure. The reduced density examined is shown by each figures legend.*

The radial distribution data for the Lennard-Jones potential at a size ratio of 1.0 shows peaks at separations of approximately 1.25σ and 2.5σ. This compares with the Stockmayer fluid at a size ratio of 1.0, which shows strong peaks at separations of approximately 1.0σ and 1.9σ. The high frequency of the peaks in the Stockmayer fluid

at a size ratio of 1.0 indicates the formation of significant chain structure. These chains are the result of A particles (wurtzite representations) interacting with B particles (zinc blende representations) and the other possible combinations of interactions A-A and B-B. The radial distribution data for the Lennard-Jones potential at a size ratio of 2.1 (A particles larger than B particles) has a first peak at a separation of 1.7σ. This first peak indicates A-B interactions; the absence of the normal first peak at approximately 1.0σ means that nearest neighbour B-B interactions do not tend to be observed. There are A-A interactions visible in the radial distribution data at a size ratio of 2.1 with a peak at approximately 2.3σ. The Stockmayer fluid results at the same size ratio of 2.1 do have a peak at a separation of 1.0σ; however this peak is dwarfed by the A-B interaction peak at approximately 1.4σ. This high peak indicates significant interactions between A-B particles. There is further conformation of this through another peak at approximately 2.7σ, which is the result of A-B-A and B-A-B interactions. The radial distribution data for the Lennard-Jones potential at a size ratio of -2.1 (B particles larger than A particles) has a first peak at approximately 1.1σ, which indicates A-A interactions. The second peak that occurs at approximately 2.0σ is the result of A-B interactions and the final peak at 3.0σ is the result of B-B interactions. The Stockmayer fluid results at the size ratio of -2.1 shows a significant first peak at 1.0σ, the result of A-A interactions, which is far greater than the broad A-B peak at approximately 1.5σ and the B-B peak at 1.9σ. The data has highlighted that positive size ratios show greater A-B frequency peaks relative to the negative size ratio results at the same size ratio. The aim of this chapter is to examine the Stockmayer fluid for tetrahedral structures, through A-B interactions, the data suggests positive size ratios are the probable place to find them.

7.7 Local coordination enviroment

The coordination data will provide possible clues as to the presence of any tetrahedral structures, by way of seeing an increase in four coordinate particles and subsequently an increase in the mean coordination. The mean coordination number of the Stockmayer fluid particles at a range of size ratios, -2.9 to +2.9, is plotted for all four reduced densities $\rho^* = 0.1, 0.2, 0.4$ & 0.8 (Figure 177). The negative size ratio at the highest density of $\rho^* = 0.8$ are not investigated at this stage.

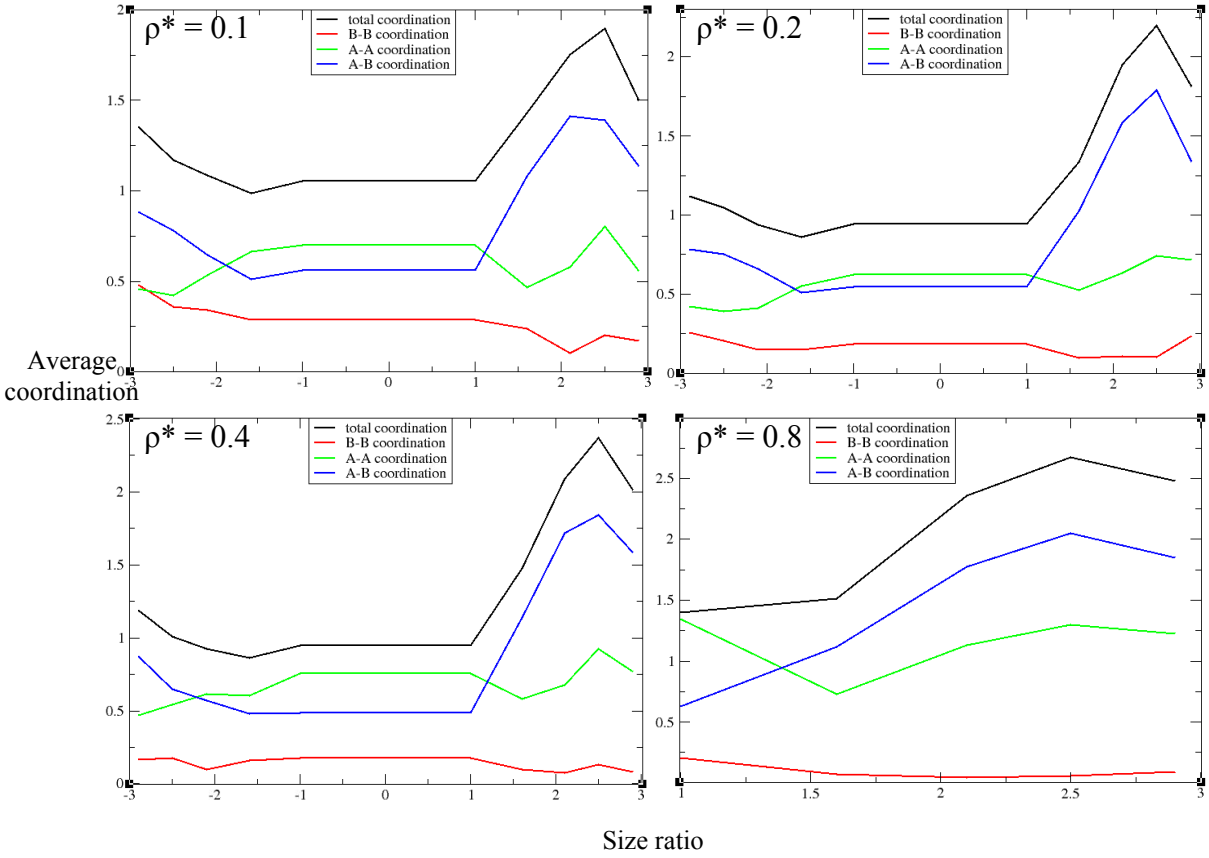

Figure 177 - *The mean coordination's of the Stockmayer fluid simulations at different size ratios and reduced densities. The top left figure highlights the coordination data at a reduced density ρ* = 0.1, the top right figure is at a reduced density ρ* = 0.2, the bottom left figure is at a reduced density ρ* = 0.4 and the botto right figure is at reduced density ρ* = 0.8. The figure legends indicate the total, A-A, B-B and A-B coordination data.*

The mean coordination data shows an increase in the total coordination of the Stockmayer fluids for both the increasing size ratios from α = 1 and decreasing size ratios from α = -1. This increase in the total coordination data is most prominent for positive size ratios, with the size ratio α of 2.5 producing the greatest peak in the data at all reduced densities. The B-B particles (zinc blende representations) data shows the general trend of decreasing coordination with increasing size ratio from α = -2.9. This means as the B particles decrease in diameter relative to the A particles their coordination drops as well. This has been previously observed in chapter 5, where smaller particles tend show the trend of decreasing coordination in the binary Stockmayer fluid. The A-A (wurtzite representation) particle data is essentially constant at different size ratios at all reduced densities, though it also has a subtle

increase in coordination at a size ratio of 2.5. The A-B particle data shows an increase in the coordination as the difference in diameters of the binary Stockmayer particles increase, though the greatest increase in coordination occurs with positive size ratios. There is once again a peak at size ratio of 2.5 at all reduced densities, this indicates there maybe something structurally important occurring at this specific size ratio. The next size ratio of 2.9 shows both a drop in the total and A-B coordination data, however this is not true for negative size ratio, where there is an increase in coordination for both on going from -2.5 to -2.9. The data suggests the greatest mean coordination occurs in the positive size ratios range with the most prominent being at a size ratio of 2.5. This suggests the greatest probability of finding four coordinate tetrahedral structures are most likely to occur at this size ratio of 2.5. Thus the coordination data, total, A-A, B-B and A-B connections, at a size ratio of 2.5 are shown at all four reduced densities ρ* = 0.1, 0.2, 0.4 & 0.8 (Figure 178).

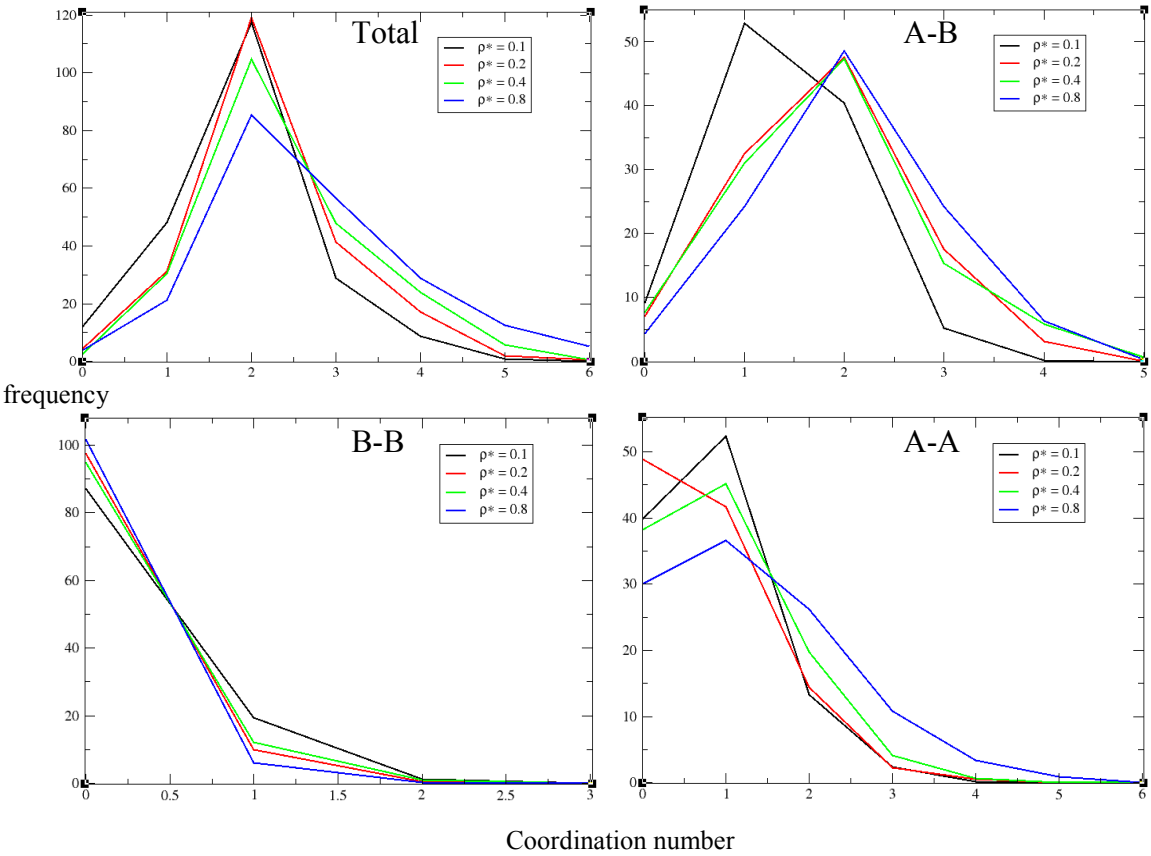

Figure 178 - *The coordination data for the binary Stockmayer fluid at a size ratio of 2.5. The top left figure highlights the total coordination data, the top right figure the A-B coordination data with respect to A particles, the bottom left figure shows the B-*

B coordination data and the bottom right figure shows the A-A coordination data. The reduced densities examined are indicated by the figure legends.

The total coordination data at a size ratio of 2.5 illustrates that two coordinated particles are the most abundant at all densities, suggesting the formation of chains. The increasing of the density in the total coordination data shows a corresponding fall in the number of two coordinated particles, additionally there is a greater number of three and higher coordinated particles present. The A-B coordination data, with respect to the coordination of A particles (wurtzite representations), has a relatively constant number of two coordinated A particles at all densities. There is an increase in the number of three or more coordinated A particles with increasing density at the expense of decreasing zero or one coordinated A particles in the system. The B-B coordination data suggests no chain formation as there are no two coordinated B particles in the system, there are however some one coordinated B particles. These one coordinated particles decrease with increasing density and this also results in increasing number of zero coordinated B particles. The A-A coordination data shows a general shifting of the A coordinated particles to higher coordination, two or more coordinated, with increasing density at the expense of decreasing one and zero A coordinated particles. The coordination data results are similar to those observed in chapter 5 where the smaller B particles, with respect to B-B connections, have a lower coordination relative to both the A-A and A-B coordination data. The primary interest of this chapter is to see whether the B particles associate with the A particles to form four coordinate, with respect to B particles, tetrahedral structures. This is examined by looking at the B-A coordination data, with respect to B particles at all the reduced densities $\rho^* = 0.1, 0.2, 0.4$ & 0.8 (Figure 179).

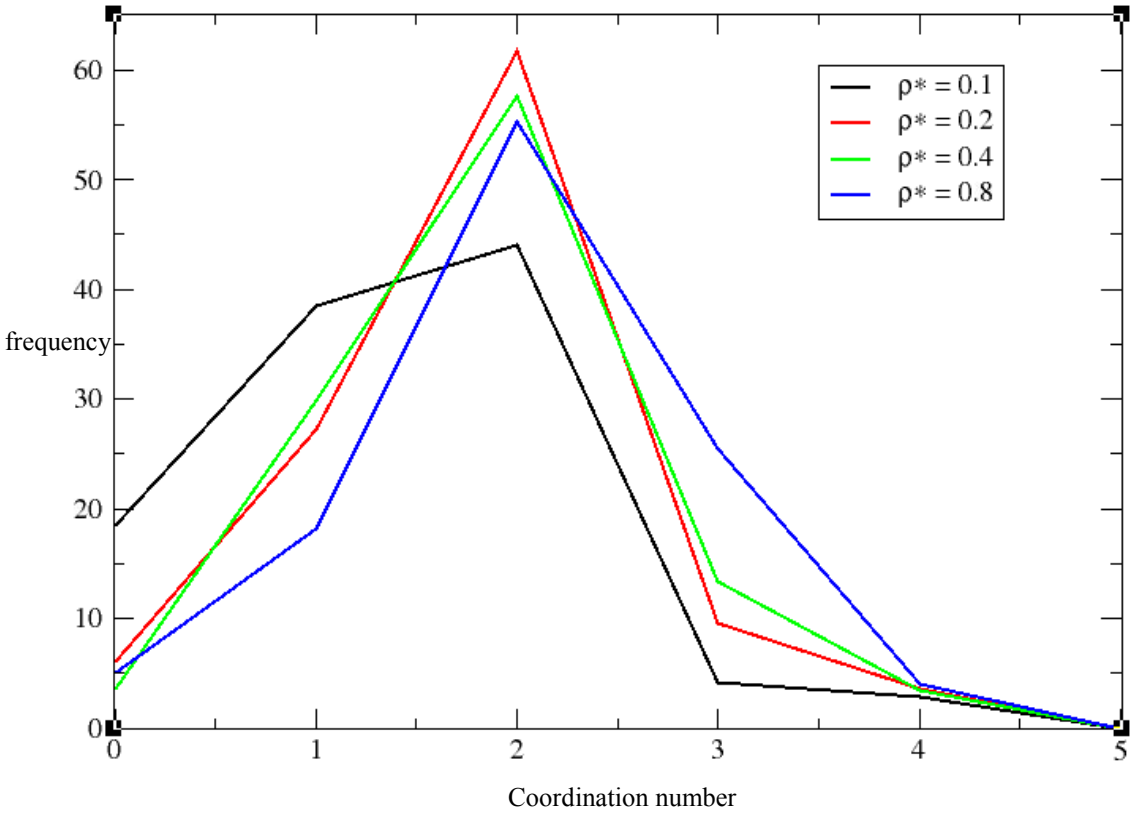

Figure 179 - *The coordination of B particles with respect to A-B connections in the Stockmayer fluid at a size ratio of 2.5. The figure legend indicates the reduced densities examined.*

The coordination data for the B-A connections, with respect to B particles (zinc blende representations), shows a similar pattern to the A-B connections in terms of relatively constant number of two coordinated particles in the system at different densities. There is also a decrease in the number of one and zero coordinated B particles with increasing density which yield increasing number of three coordinated B particles in then system. The difference between the A-B and B-A connection data lies in the number of four coordinated particles at different densities, in the case of the A-B coordination data the number of four coordinated A particles increases with increasing density. This is not true for the B-A coordination data where there is generally constant number of four coordinated B particles in the system at all densities examined. This is a rather odd result as at higher densities the particles are forced into smaller box and as such in general terms there should be an increase in the coordination numbers with increasing densities. This suggests something specific is happening with B particles when they are surrounded by A particles.

7.8 Chain length analysis

The chain length data gives information on the length of chain structures within the Stockmayer fluid simulations. The chain length data should in essence be very similar to the coordination data as the two are linked, with higher coordination only being possible with more connections in the systems and more connections in turn means greater chain lengths. The mean chain length data, the total, B-B, A-A and A-B, for the range of size ratios, -2.9 to +2.9, are shown for all the reduced densities ρ* = 0.1, 0.2, 0.4 & 0.8 (Figure 180).

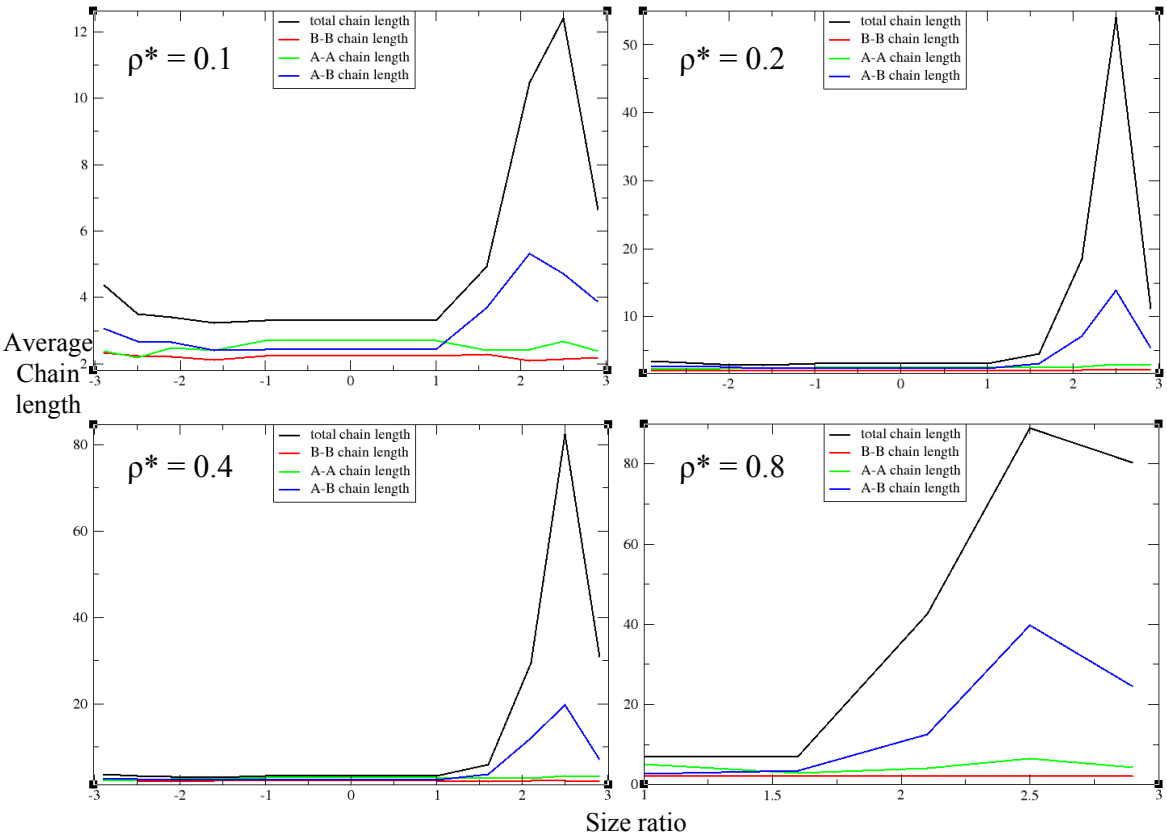

Figure 180 - *The mean chain length data for the range of size ratios at different reduced densities in the Stockmayer fluid. The top left figure shows the mean chain length at a reduced density ρ* = 0.1, the top right figure shows the mean chain length at a reduced density ρ* = 0.2, the bottom left figure highlights the average chain length at a reduced density ρ* = 0.4 and the bottom right figure highlights the mean chain length at a reduced density ρ* = 0.8. The figure legends indicate the mean chain lengths of the total, A-A, B-B and the A-B chain lengths.*

The chain length data does indeed mirror the results of the mean coordination results as the greatest total mean chain lengths occur at positive size ratios and the highest again occurring at the specific size ratio of 2.5 at reduced densities. There are very small increases in the total chain length data in the negative size ratio regime, which are dwarfed in terms on the results in the positive size ratio. The A-B chain length data suggests it is the primary cause for the increase in the total chain length data in both the positive and negative size ratios, while the B-B chain length data points to decreasing B-B chains with increasing positive size ratios. There is a subtle increase in the B-B chains with decreasing negative size ratios, where the sizes of B particles are increasing in size relative to A particles. The A-A chain length data stays relatively constant at all size ratios including both negative and positive size ratios. This suggests A-A chains remain unaffected at all size ratios, with the breakup of B particles and their consequential associations to A particles being responsible for the increase in the A-B chain length data in the positive size ratio. The chain length data does not provide any clues to the presence of tetrahedral structures or any structural information that will help to determine whether any pod structures are present in the Stockmayer fluid simulations; as such no further analysis is done on the chain length data.

7.9 Bond angle distributions

The bond angle distributions can help to determine if any pod structures, bipods, tripods and tetrapods, are present in the Stockmayer fluid simulations by seeing if there is an increase in bond angles around 110 degrees. That would potentially indicate the presence of tetrahedral structures in the Stockmayer fluid. The bond angle distributions for positive size ratios only are shown for the different reduced densities ρ* = 0.1, 0.2, 0.4 and 0.8 (Figure 181).

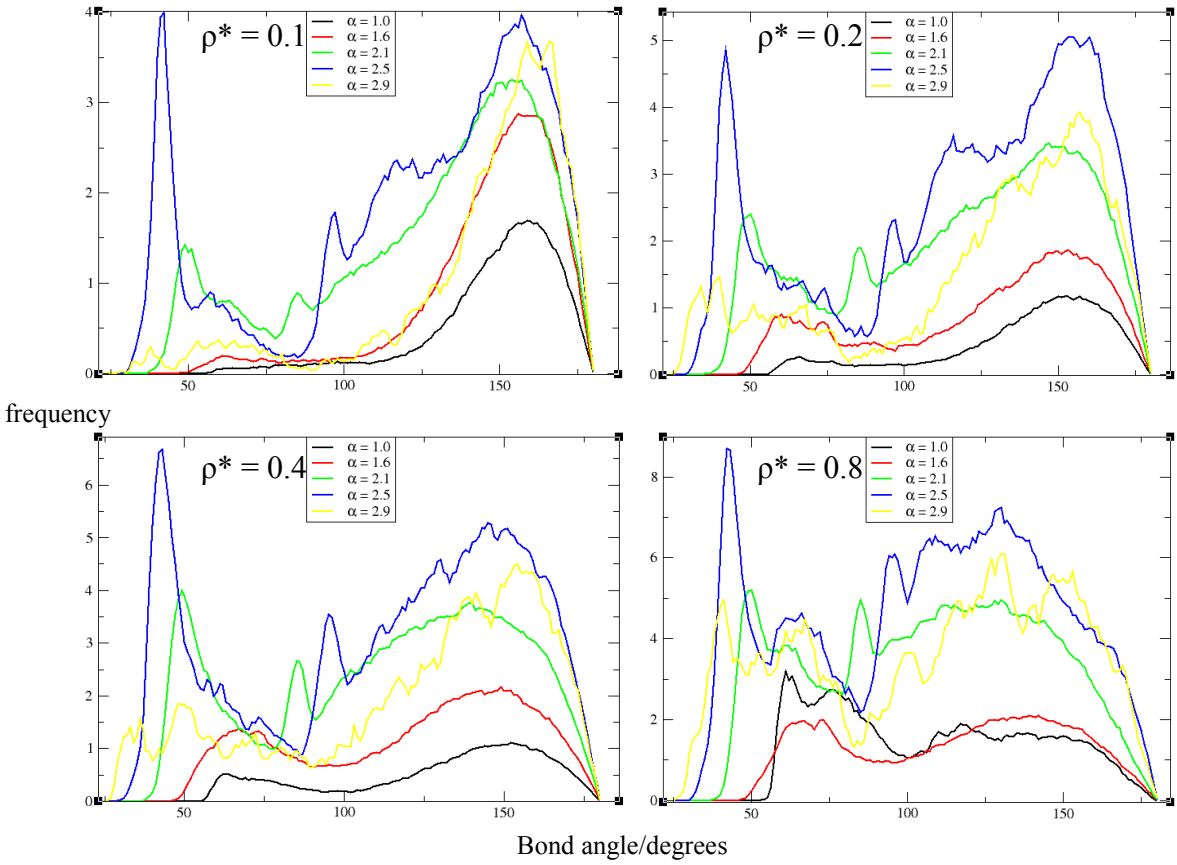

Figure 181 - *The bond angle distribution data for all size ratios for different reduced densities. The top left figure shows the bond angle data at a reduced density ρ* = 0.1 and the top right figure shows the bond angle data at a reduced density ρ* = 0.2. The bottom left figure highlights the bond angle data at a reduced density ρ* = 0.4 and the bottom right figure highlights the bond angle data at a reduced density ρ* = 0.8. The figure legends inset indicate the size ratios examined.*

The bond angle data reveal a general pattern of increasing bond angle frequency with increasing size ratio at all reduced densities examined. There is also the general pattern of the bond angles shifting from high angles between 120 and 180 degrees to lower angles below 120 degrees, also observed in chapter 5, with increasing reduced density for each specific size ratio. The main purpose of looking at the bond angle data is to observe whether there are any peaks present at approximately 110 degrees, which potentially signifies the formation of tetrahedral structures. The lower reduced densities of $\rho^* = 0.1$ and 0.2 do indeed show an increased number of bond angles between 100 and 120 degrees, specifically for the size ratio of 2.1 and 2.5 data. The data shows that for other size ratios, other than 2.1 and 2.5, there is a generally dip in the frequency of bond angles between 100 and 120 degrees and as such the broad peak in the size ratio of 2.5 data is particularly easy to spot. This broad peak becomes increasingly difficult to spot at higher densities, $\rho^* = 0.4$ and 0.8, due to the general trend of shifting bond angles to below 120 degrees. The size ratios of 2.1 and 2.5 bond angle data at all reduced densities examined also have significant peaks visible at approximately 50 and 45 degrees respectively. These peaks have been previously encountered in chapter 5 and are attributed to the formation of ABA triangular units, this can be confirmed by showing the theoretical angles expected for ABA triangular units at a size ratio of 2.5 (Figure 182).

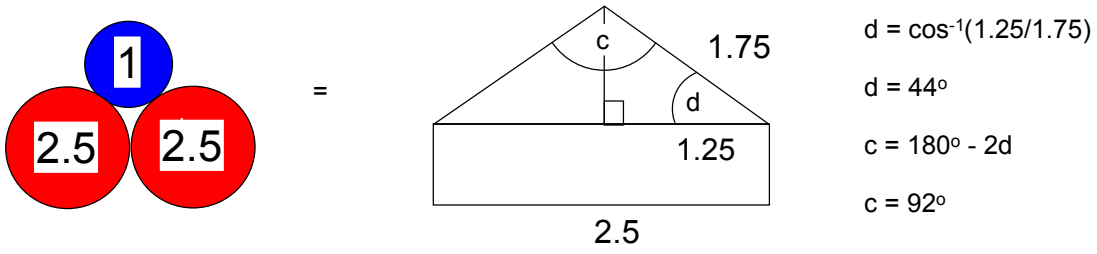

Figure 182 - *The bond angles produced by triangular ABA units in the Stockmayer fluid. The figure shows the ABA unit at a size ratio of 2.5 with its expectant angles. The d angle is calculated using cosine function indicated in the right hand side of the figure. This d angle can be used to workout the c angle. The A particles are highlighted in red and B particles in blue.*

The bond angles expected at a size ratio for ABA triangular units are either the ABA angle of 92 degrees or the AAB angle of 44 degrees, the former ABA angle is also

clearly visible in the bond angle data at all reduced densities, hence confirming the presence of these triangular units in the Stockmayer fluid. The most significant frequency of bond angles occurring between 100 and 120 degrees is at a size ratio of 2.5, hence the breakdown of the bond angle distribution data, in terms of the total, A-B, B-B and A-A contributions, for this size ratio of 2.5 are shown (Figure 183).

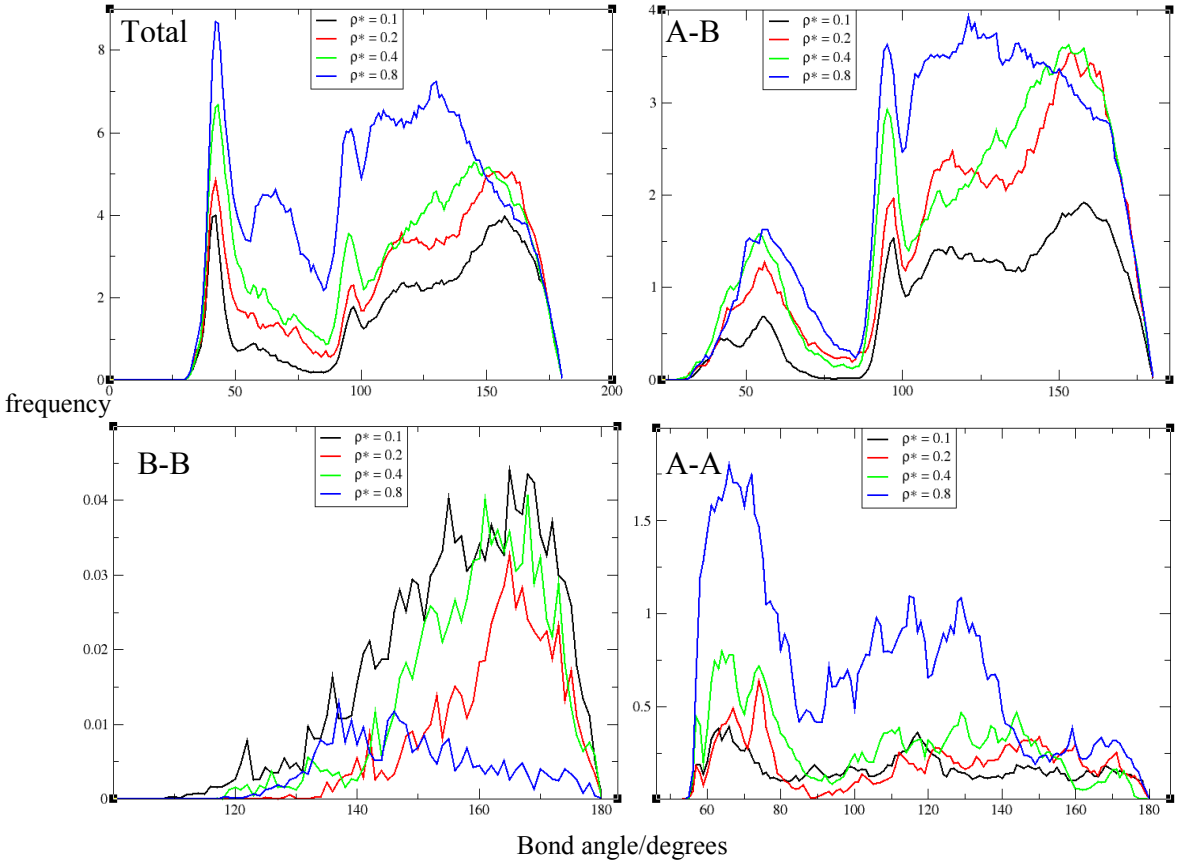

Figure 183 - *The bond angle distribution data for a size ratio of 2.5 only for different reduced densities. The top left figure shows the total bond angle data and the top right figure shows the bond angle data for A-B connections only. The bottom left figure highlights the bond angle data for B-B connections only and the bottom right figure highlights the bond angle data for A-A connections. The figure legends inset indicate reduced densities examined.*

The bond angle distribution breakdown at a size ratio of 2.5 reveals the most significant contribution to the angles of interest between 100 and 120 degrees occur most prominently in the A-B bond angle data. This A-B bond angle data includes both angles where A particles are connected to B particles only and from B particles being

connected to A particles only. The B-B (zinc blende representations) bond angle data has a very small contribution to the total bond angle data and it also shows a decrease in the frequency of angles with increased reduced density. The bond angles for B-B connections are approximately restricted to only angles between 120 and 180 degrees. The A-A (wurtzite representations) bond angle data shows a distribution of angles between 55 and 180 degrees, there are significant peaks occurring at approximately 60 degrees. These peaks tend to increase with increasing density; the 60 degree peak has previously been attributed to particles of the same size forming triangular units. The contribution of bond angles from A-A connections only is relatively small when compared to the A-B bond angle data. This modified Stockmayer model is meant to mimic the formation of pod structures, which should have approximate angles of 110 degrees, but the angles need to be the results ABA connections and not BAB connections in order to prove the model is working as theoretically hypothesised. This can be achieved by splitting the A-B bond angle distribution in terms of whether central particle is A or B (Figure 184).

Figure 184 - *The representation of ABA and BAB units that are possibly responsible for bond angles at 110 degrees. The left figure shows the ABA unit with the centrally coordinated B particle (zinc blende representation) and the right figure shows the BAB unit with the centrally coordinated A particle (representation). The angle θ of interest are also highlighted.*

The bond angle distribution for A-B data is split according to the central particle being either A or B particles for all reduced densities ρ* = 0.1, 0.2, 0.4 and 0.8 (Figure 185).

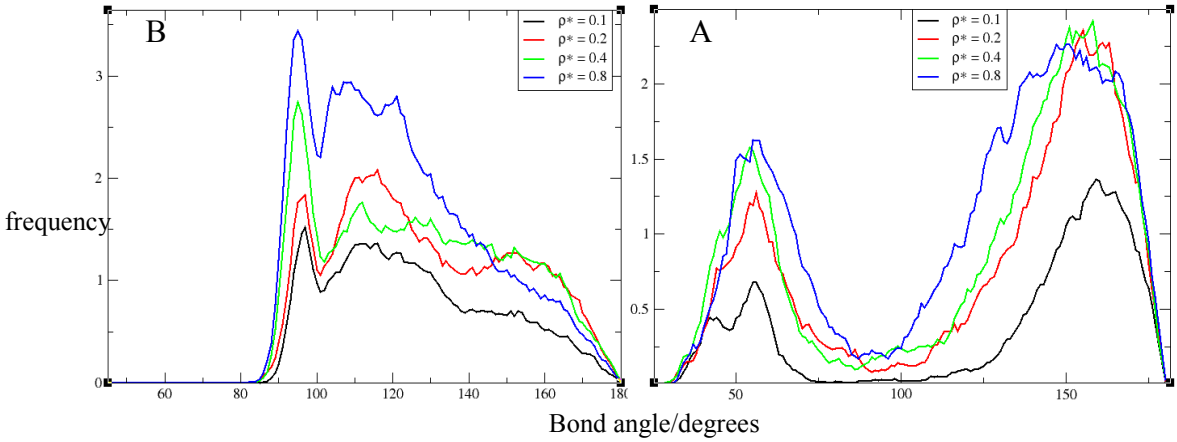

Figure 185 - *The bond angle distribution for A-B connections at a size ratio of 2.5 with respect to both central A and B particles. The left figure highlights the bond angle data with respect to B particles being the central coordinated particle. The right figure highlights the bond angle data with respect to A particles being the centrally coordinated particle.*

The A-B bond angle distribution in terms of the centrally coordinated particle being either A or B particles highlights that the most significant contribution to bond angles at approximately 110 degrees comes when the centrally coordinated particle is B (zinc blende representations). The bond angle data also shows when the centrally coordinated particle is the B particle the distribution of the angles is narrowly concentrated between 90 and 120 degrees. This is in stark contrast to the bond angle data when the central particle is A (wurtzite representation) where there is in fact a massive dip between the angles of 80 and 120 degrees. However the distribution of bond angles with centrally coordinated A particles is concentrated at angles greater than 120 and less than 80 degrees. The higher angles, greater than 120 degrees, present with central A particles suggest the formation of more linear BAB structures alongside the formation of BAB triangular units which account for the lower angles between 30 and 70 degrees. The bond angle peaks between 90 and 100 degrees with central B particles in the data also suggest the formation of ABA triangular units alongside the pod ABA structures with angles close to 110 degrees. The results for A-B connections with respect to both the centrally coordinated particle being A or B are summarized in a simple structure diagram (Figure 186).

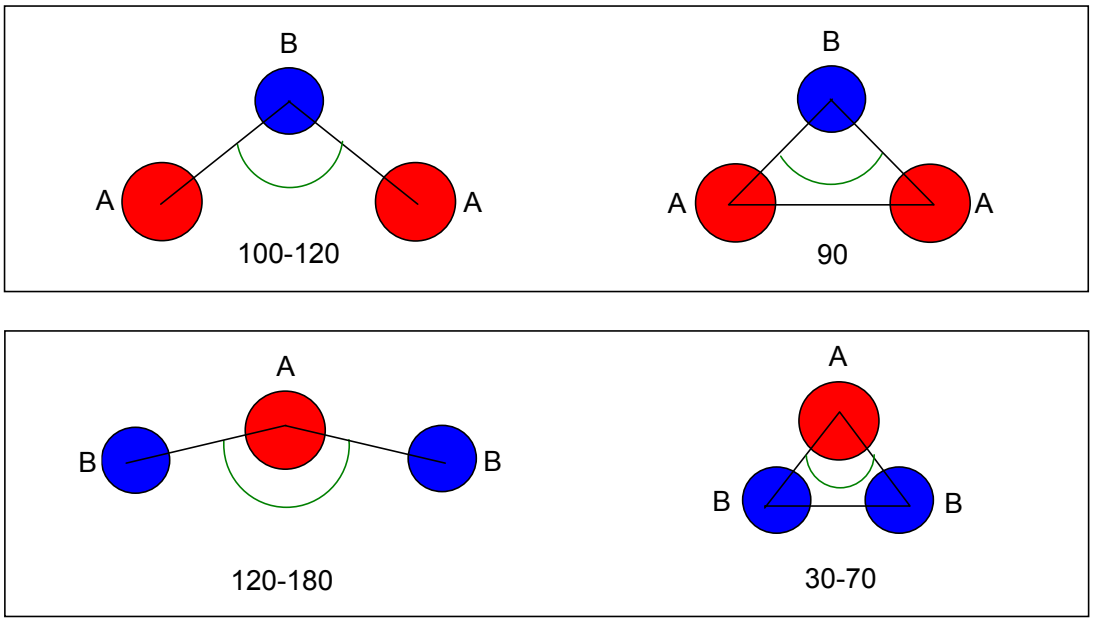

Figure 186 - *The types of structures adopted in the Stockmayer fluid according to bond angle distributions. The top figure shows the two distinct ABA structures adopted when B is the central coordinating particle. The bottom figure highlights two distinct BAB structures adopted when A is the central coordinating particle. A particles are shown in red and B particles in blue.*

7.10 Molecular graphics

The above analysis indicates that the richest structural changes occur at a size ratio of 2.5. The equilibrium snapshots of the Stockmayer fluid simulations involving zinc blende and wurtzite representations for a size ratio of 2.5 at all reduced densities $\rho^* =$ 0.1, 0.2, 0.4 and 0.8 are shown (Figure 187). The snapshots shown are where structures present resemble tetrapod or tetrahedral shapes with the central four coordinate particle being zinc blende representations and the four particles connected to it being wurtzite representations.

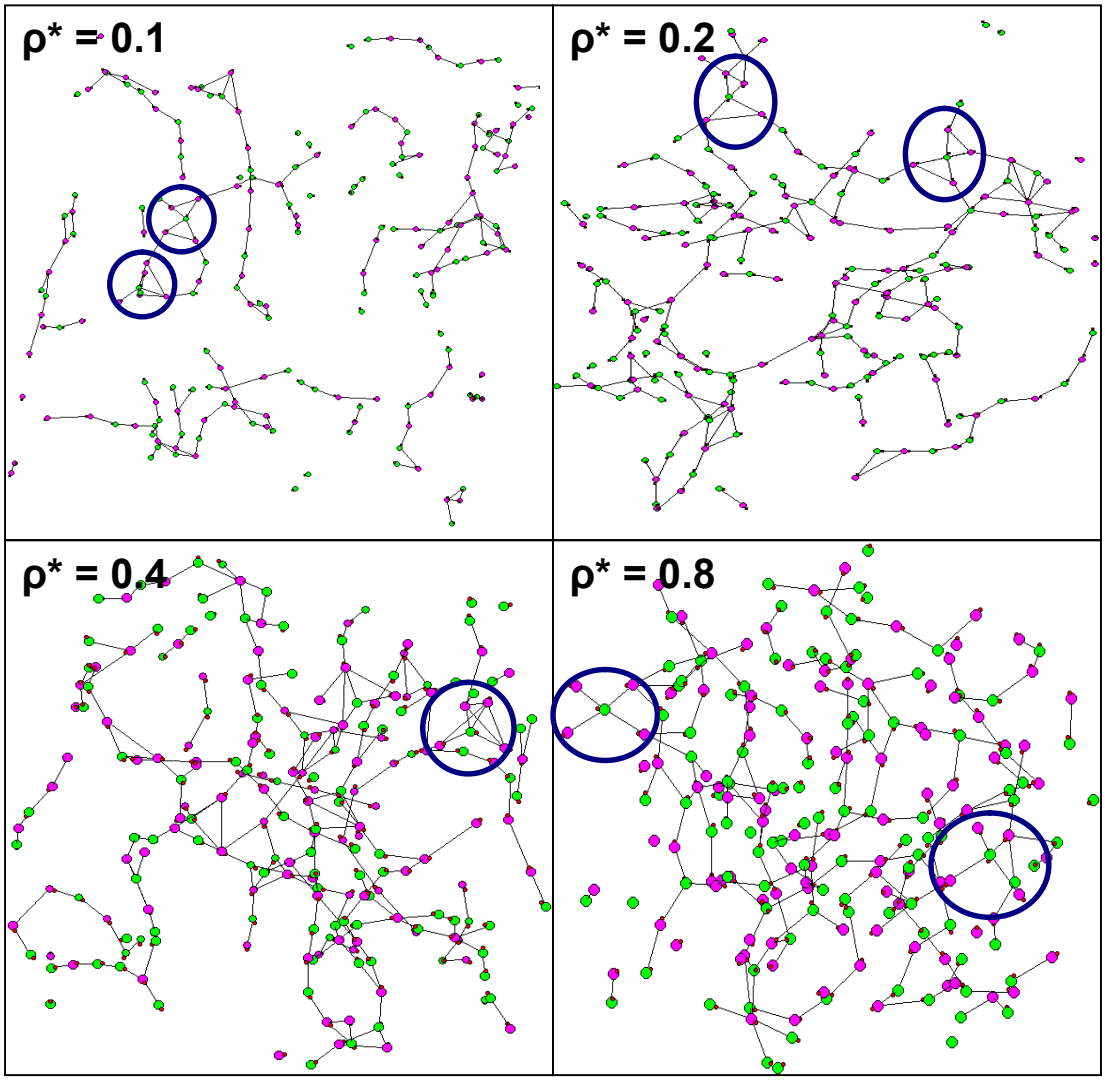

Figure 187 - *The equilibrium snapshots of the binary Stockmayer fluid simulations when the size ratio between particles is 2.5. The top left figure is the snapshot at a reduced density ρ* = 0.1, the top right figure at a reduced density ρ* = 0.2, the bottom left figure at a reduced density ρ* = 0.4 and the bottom right figure at a reduced density ρ* = 0.8. The green particles are zinc blende representations and the purple particles are wurtzite representations. The red particles indicate the direction of resultant dipole moments. The potential tetrapod structures are highlighted in blue.*

7.11 Tetrahedricity

The determination of the tetrahedral nature of the local coordination in the Stockmayer fluid is an important factor in learning whether this simple model can produce the tetrapod type structures, observed in actual synthesis of nanostructures. To achieve this, the Delaunay equation is used to determine the tetrahedricity (T) of simplices close in shape to a regular tetrahedron in the Stockmayer fluid[246] (Equation 37).

$$T = \sum_{i>j} \frac{(l_i - l_j)^2}{15\underline{l}^2}$$

Equation 37 - *The Delaunay equation for determining the tetrahedricity in a liquid. The tetrahedricity T is calculated by finding the length of the i*th *edge* l_i*. The* $\underline{l}$ *is the mean edge length of the simplex.*

The Delaunay equation is utilized to work out the tetrahedricity of four coordinated particles in the Stockmayer fluid simulations involving zinc blende and wurtzite representations. The Delaunay equation relies on working out the edge lengths of the four particles surrounding a four coordinated particle, only those four particles which have edges of equal length can give a perfect tetrahedron structure (Figure 188). This means low values of T represent good tetrahedral structures, whilst high values of T are considered bad tetrahedral structures. This means a value of T must be chosen to differentiate good and bad structures, for the subsequent analysis this is arbitrarily set to a T value of 0.02, thus $T \leq 0.02$ are considered to be good tetrahedral structures[247].

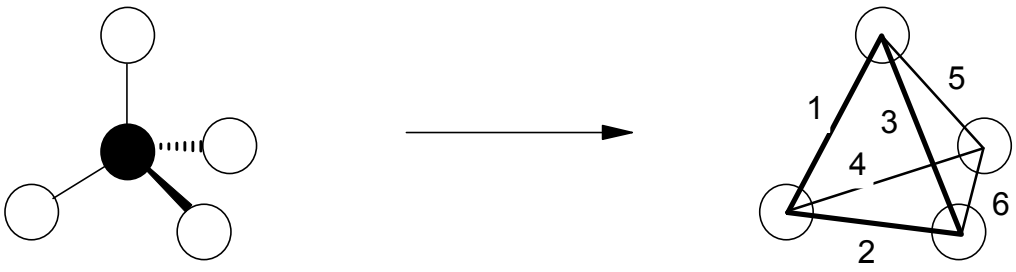

Figure 188 - *The tetrahedricity from a four coordinated Stockmayer particle. The left figure shows a central particle (black) that is four coordinated. The four particles*

(white) are only used in the calculation of tetrahedricity. The right figure shows the edges that are worked out in order to find the tetrahedricity of this simplex. The right figure also highlights there are six edges of equal length in a perfect tetrahedron.

The coordination and chain length data have indicated the most interesting events occur with positive size ratios, as such the tetrahedricity will only be calculated for positive size ratios. The results for the tetrahedricity at positive sizes ratios for reduced densities ρ* = 0.1, 0.2, 0.4 and 0.8 are shown (Figure 189).

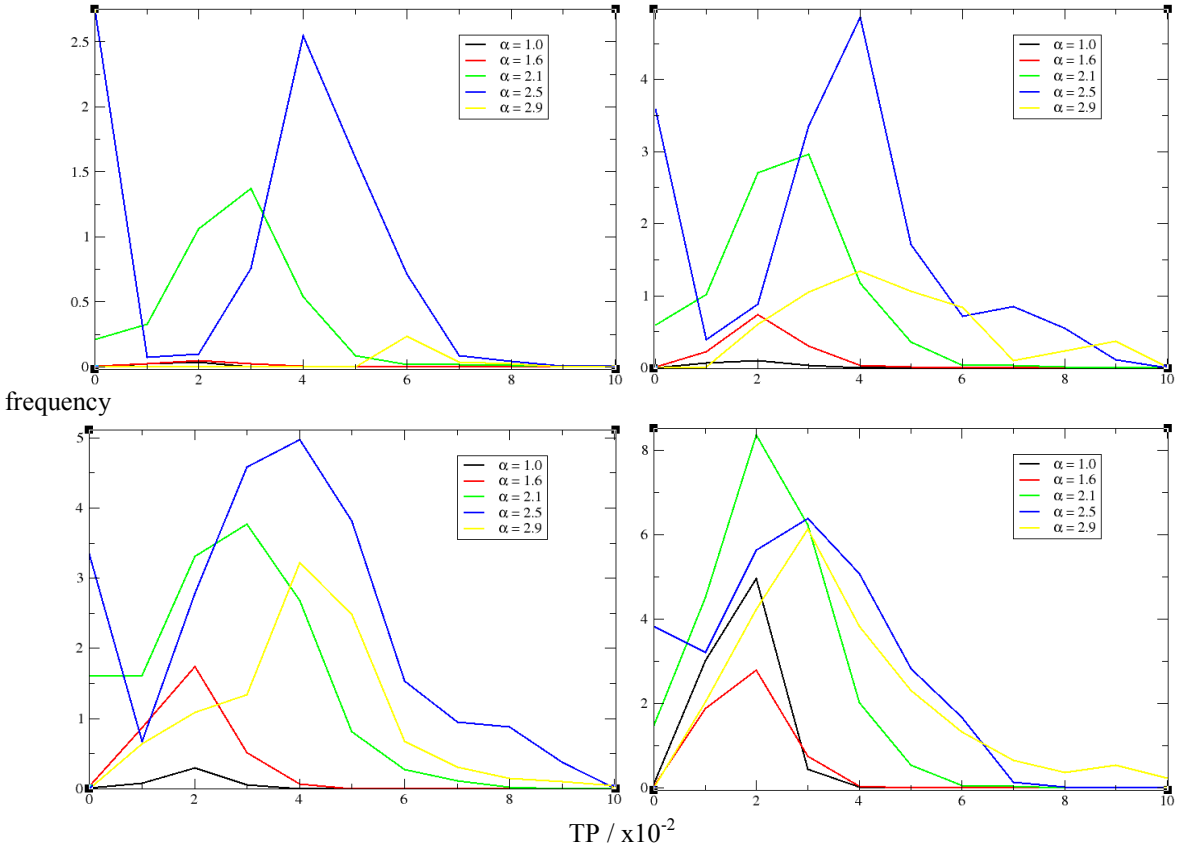

Figure 189 - *The tetrahedricity of the binary Stockmayer fluid at different size ratios. The top left figure is the tetrahedricity results for reduced density ρ* = 0.1, the top right figure is at a reduced density ρ* = 0.2. The bottom left figure shows the tetrahedricity results for a reduced density ρ* = 0.4 and the bottom right figure highlights the results at a reduced density of ρ* = 0.8. The size ratios examined are shown in each of the figure legends.*

The tetrahedricity data indicates a general increase in the tetrahedricity with increasing size ratio, up to a size ratio of 2.5, after which there is a fall in the

frequency of tetrahedricity at a size ratio of 2.9. This pattern is observed at all reduced densities, however good tetrahedricity in which the T values are low is only consistently observed at all reduced densities for a size ratio of 2.5. The size ratio at 2.5 results stand out compared to others because of the significant frequency of T values at 0.00 that are present in all the densities shown. There are also a reasonable number of good tetrahedrons, $T \leq 0.02$, according to the data for a size ratio of 2.1, though they are not as consistent at all the reduced densities examined, when compared to the results at a size ratio of 2.5. The tetrahedricity results for a size ratio of 2.5 are examined more closely, with the results of the total, A-A, A-B and B-A shown at reduced densities $\rho^* = 0.1$, 0.2, 0.4 and 0.8 (Figure 190).

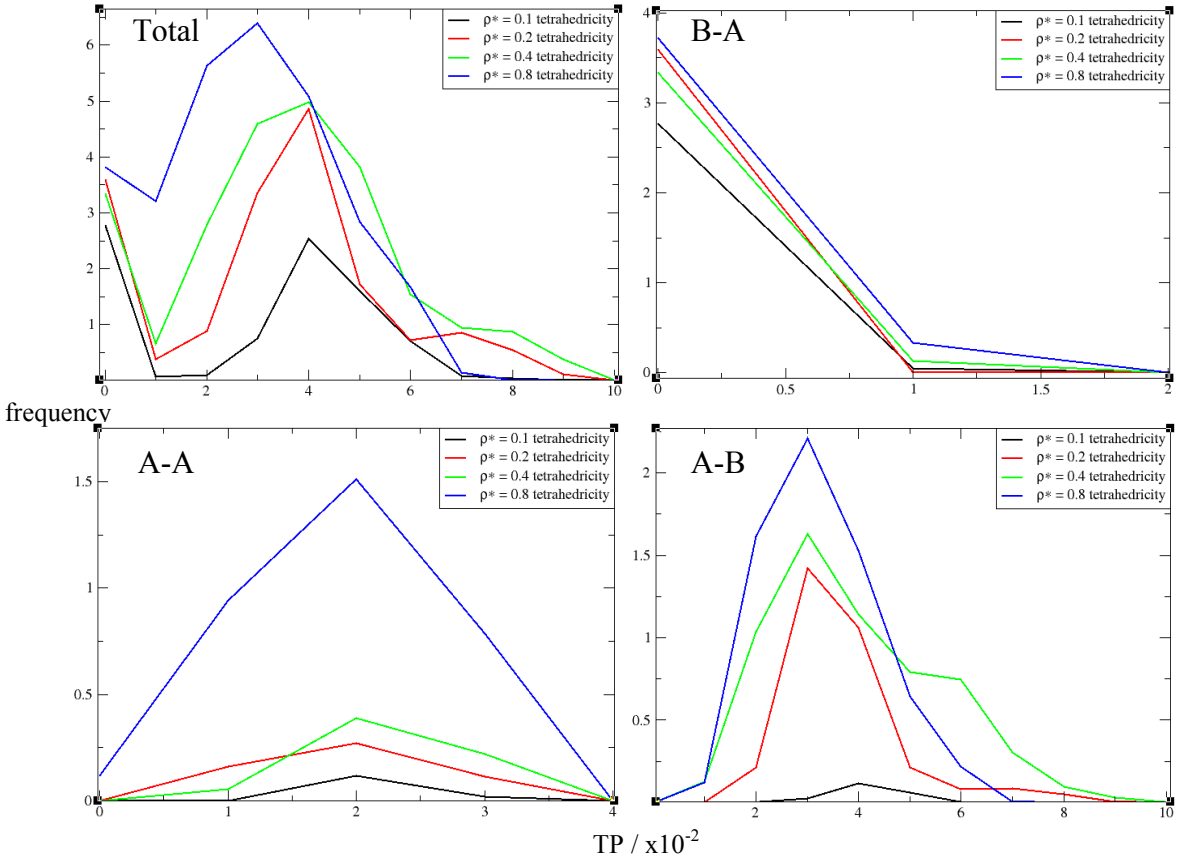

Figure 190 - *The tetrahedricity of the Stockmayer fluid at a size ratio of 2.5 for different reduced densities. The top left figure shows the total tetrahedricity, the bottom left figure shows the A-A connection tetrahedricity. The top right figure shows the B-A connection tetrahedricity and bottom right figure highlights the A-B connection tetrahedricity. The different reduced densities used are indicated in the figure legends inset.*

The results show that the total data has a wide distribution of T values, 0.00 to 0.10, however there are perfect tetrahedrons present in the total data. This is indicated by peaks in the data at T value of 0.00 for all reduced densities shown. Interestingly the number of perfect tetrahedrons is approximately three at all the reduced densities. The B-A connection data, which means the B particle (zinc blende representation) is the central four coordinated particle surrounded by four A particles (wurtzite representations), has a very narrow distribution of T values between 0.00 and 0.02. The data also reveals that the perfect tetrahedrons, indicated by a T value of 0.00, observed in the total data are almost entirely the result of the B particles being surrounded by A particles to form a tetrahedral structure. There is an insignificant amount of tetrahedrons above T values of 0.00 in the B-A data, this tends to indicates that the B particle is very good at controlling or directing the A particles to form a tetrahedral structure. The A-B connection data, which means the A particle is the central four coordinated particle surrounded by four B particles, in contrast has a much wider distribution of T values from 0.00 to 0.l0. The highest peaks tend to occur at approximate T value of 0.03 in the A-B data. This tends to indicate poor quality tetrahedrons and more significantly the number of good quality tetrahedral structures, T values between 0.00 and 0.02, is far less than in the B-A data. The other thing to note is the increasing frequency of the tetrahedricity values with increasing density, this would tend to support the idea of the A particles ability to direct B particles towards themselves in a tetrahedral arrangement as being poor and that the increase is simply the result of high density packing of particles. The A-A connection data has a distribution of T values between 0.00 and 0.04. The frequency of the A-A data is relatively small when compared to the total and B-A data, indicating few A particles are surrounded by other A particles forming tetrahedral structures. The different densities, except for the highest density of $\rho^* = 0.8$, show essentially insignificant amount of tetrahedral structures forming due to A-A connections. The results at a size ratio of 2.5 clearly suggest that B particles (zinc blende representations) are causing the formations of perfect tetrahedral structures by combining with the A particles (wurtzite representations) very much like that observed experimentally in the formation of tetrapod structures. The actual B-A tetrahedral structures from the different reduced densities at a size ratio of 2.5 are shown (Figure 191).

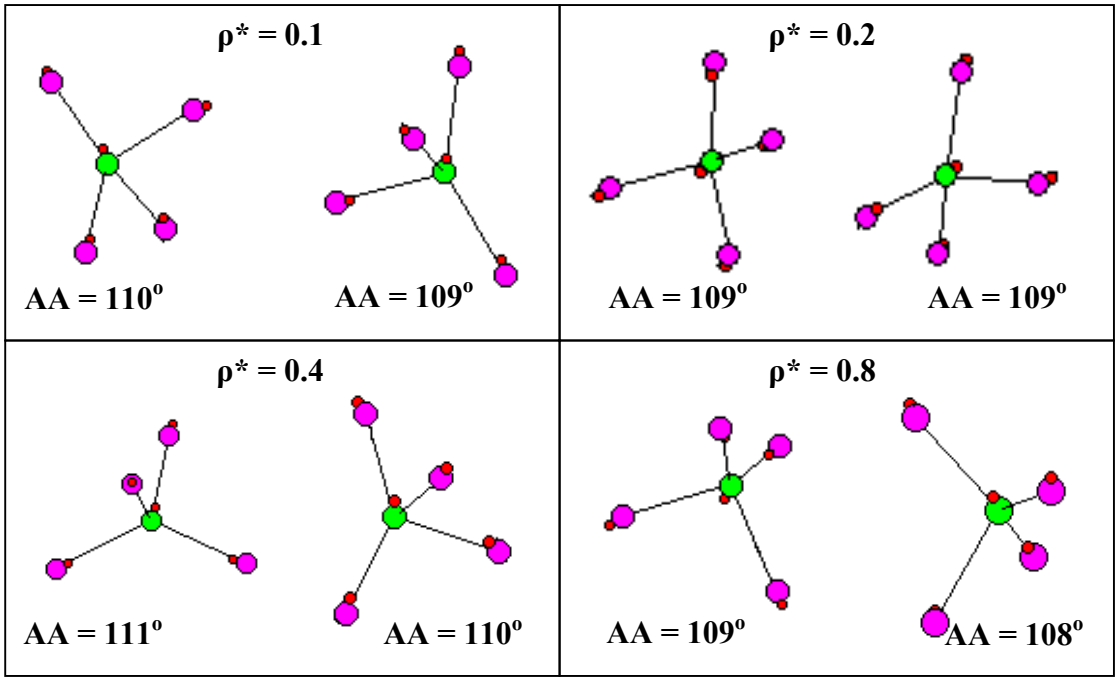

Figure 191 - *The actual tetrahedral structures observed in the Stockmayer fluid simulations at a size ratio of 2.5 involving zinc blende representations. The figure shows the tetrahedral structures formed in the simulations at different densities. The green particles are the zinc blende representations and the purple particles are normal Stockmayer particles representing wurtzite particles. The small red particles indicate the direction of the resultant dipole moment in each particle. The average angles (AA) of each species are also shown.*

7.12 Trigonal Pyramidal structures

This chapter has so far focused on the potential presence of tetrahedral structures in the Stockmayer fluid, however the Stockmayer fluid like real synthesis of nanostructures must be expected to have bipod and tripod structures in addition to tetrapods. The ability to measure bipod structures is particularly difficult as there little to distinguish a bipod structure from a chain or triangular unit in the Stockmayer fluid. The tripod structure has a greater possibility of being measured in the Stockmayer fluid. This can be achieved by using the Delaunay equation to find trigonal pyramidal structures. The first process is to find three coordinated particles in the Stockmayer fluid and then carryout the tetrahedricity calculation described in Equation 37. In the case of the trigonal pyramidal structure it is essentially the tetrahedral structure with a bonded particle missing; hence the edges in a perfect trigonal pyramidal structure must still have the same lengths like the tetrahedral structure. The problem that arises with simply using the original Delaunay equation is that it can not distinguish between trigonal pyramidal and trigonal planar structures (Figure 192).

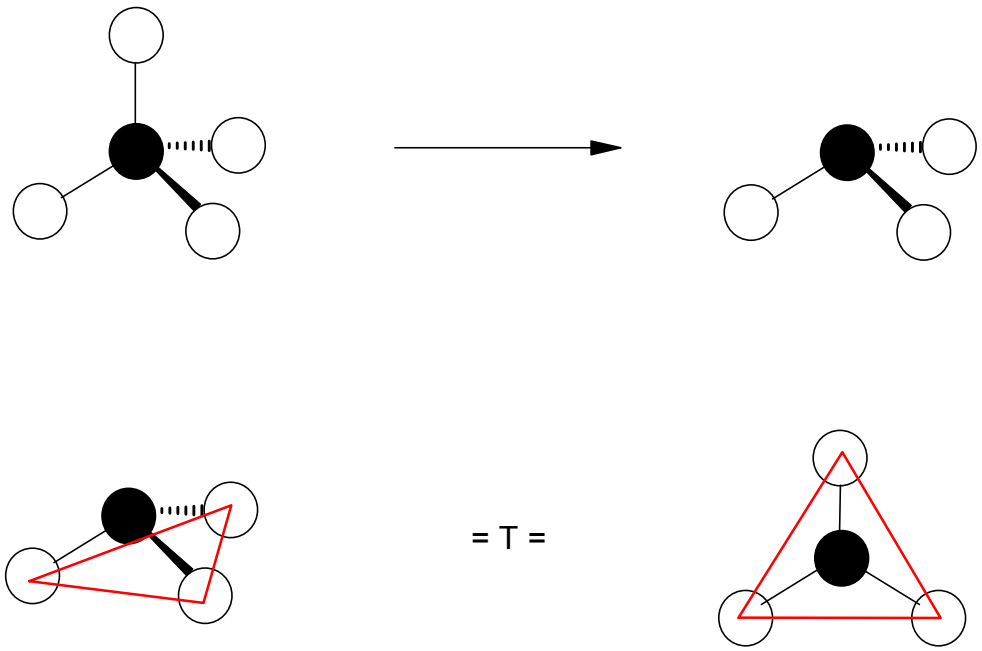

Figure 192 - *The trigonal pyramidal structure and the trigonal planar structures. The top figure highlights the trigonal pyramidal structure (right) is essentially the tetrahedral structure with a missing connection. The bottom figure shows the problem of the edges (red) in both the trigonal planar (right) and pyramidal (left) structures having the same length in each case respectively, thus leading to the same T value.*

The trigonal pyramidal and planar structures can be distinguished by including the centrally coordinated particle, normally excluded from the Delaunay calculation, and hence the three bond lengths. These particles together form a distorted tetrahedron in the case of the trigonal pyramidal structure, as described before the Delaunay equation relies on working out the edges of the simplex. The ratio between the bond lengths and edges in both the tetrahedral and trigonal pyramidal structures are the same (assuming the same bond angles) and can be worked out (Figure 193), this is crucially not true for the trigonal planar structure.

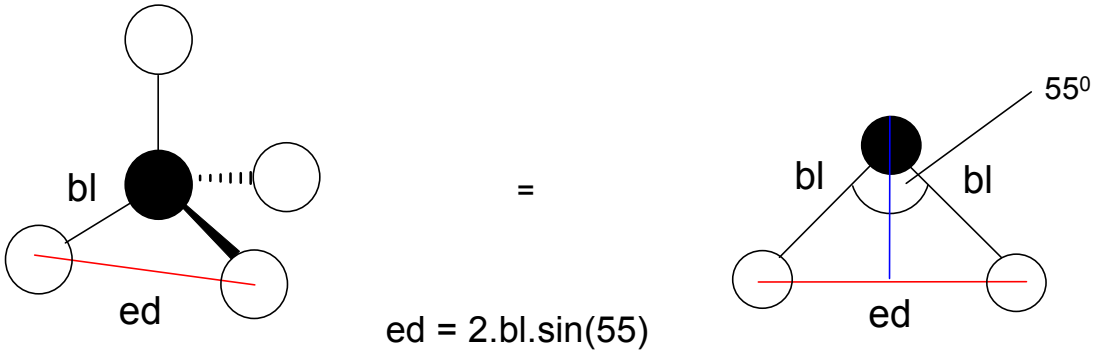

Figure 193 - *The ratio between the bond lengths and edges in tetrahedral and trigonal pyramidal structures. The left figure shows the tetrahedral structure with bond length (bl) and edge length (ed), the bond angle between the bond lengths is approximately 110 degrees. The right figure shows the edge length can be determined from the bond length. The ratio between edge and bond length is 2sin(55).*

The ratio between edge length and the bond length can be used to give rise to three fictitious edge lengths from the bond lengths alone, which can be used to determine the degree of trigonal pyramidicity (TP) in Stockmayer fluid (Equation 38).

$$TP = T + \sum_{i>j} \frac{(l_i^f - l_j^f)^2}{15\underline{l}^{f\,2}}$$

Equation 38 - *The Delaunay equation modified to find trigonal pyramidal structures in a liquid. The equation requires the use of the original Delaunay equation (T) in addition to the modified part, which uses both actual edge lengths and fictitious edge lengths, determined from the bond lengths, $\underline{l}_i^f$ and the mean edge length $\underline{l}_i^f$.*

The measure of good and bad trigonal pyramidicity is based on that utilized in the tetrahedricity measurement, where good tetrahedral structures were considered to occur at $T \leq 0.02$. In the case of the pyramidicity the TP value is also set to the same value $TP \leq 0.02$, with values above this being considered poor trigonal pyramidal structures. The results for the trigonal pyramidicity at positive sizes ratios for reduced densities $\rho^* = 0.1$, 0.2, 0.4 and 0.8 are shown for different size ratios (Figure 194).

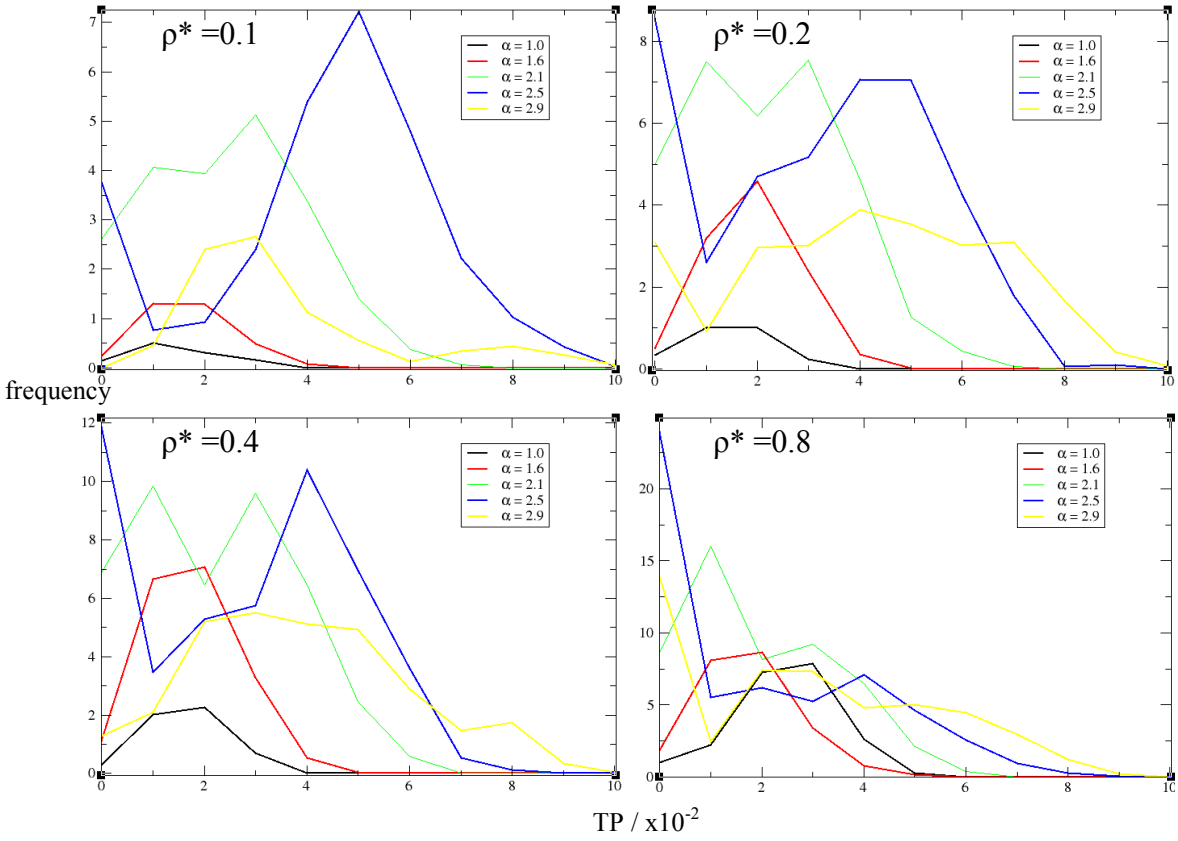

Figure 194 - *The trigonal pyramidicity at all size ratios for different reduced densities. The top left figure shows the pyramidicity at a reduced density $\rho^* = 0.1$, the top right figure shows the pyramidicity at a reduced density $\rho^* = 0.2$. The bottom left figure shows the pyramidicity at a reduced density $\rho^* = 0.4$ and the bottom right figure shows the pyramidicity at a reduced density $\rho^* = 0.8$. The size ratios examined at each density are indicated in the figure legends.*

The trigonal pyramidicity data reveals the general pattern of increasing pyramidicity with increasing size ratio at all reduced densities examined, though there is a decrease in the pyramidicity at a size ratio of 2.9 for all the densities. The pyramidicity, much like the tetrahedricity, also shows an increase in individual size ratio results with

increasing density. This can be simply observed by seeing the increase in the frequency scale with increasing reduced density. The size ratios of 2.1 and 2.5 standout in the data as they consistently have the highest frequency of trigonal pyramidicity, they also have the greatest number of good quality trigonal pyramidal structures with TP values at 0.02 or less. The size ratio of 2.1 actually shows a subtly greater frequency of pyramidicity at TP $\leq$ 0.02 relative to the size ratio of 2.5 data, however the size ratio of 2.5 results have the highest frequency of TP values at 0.00. This indicates there are extremely good quality trigonal pyramidal structures present in the size ratio of 2.5 results at all reduced densities. The trigonal pyramidicity results for the total, A-A, B-A and A-B connections at a size ratio of 2.5 are shown for different reduced densities ρ* = 0.1, 0.2, 0.4 and 0.8 (Figure 195).

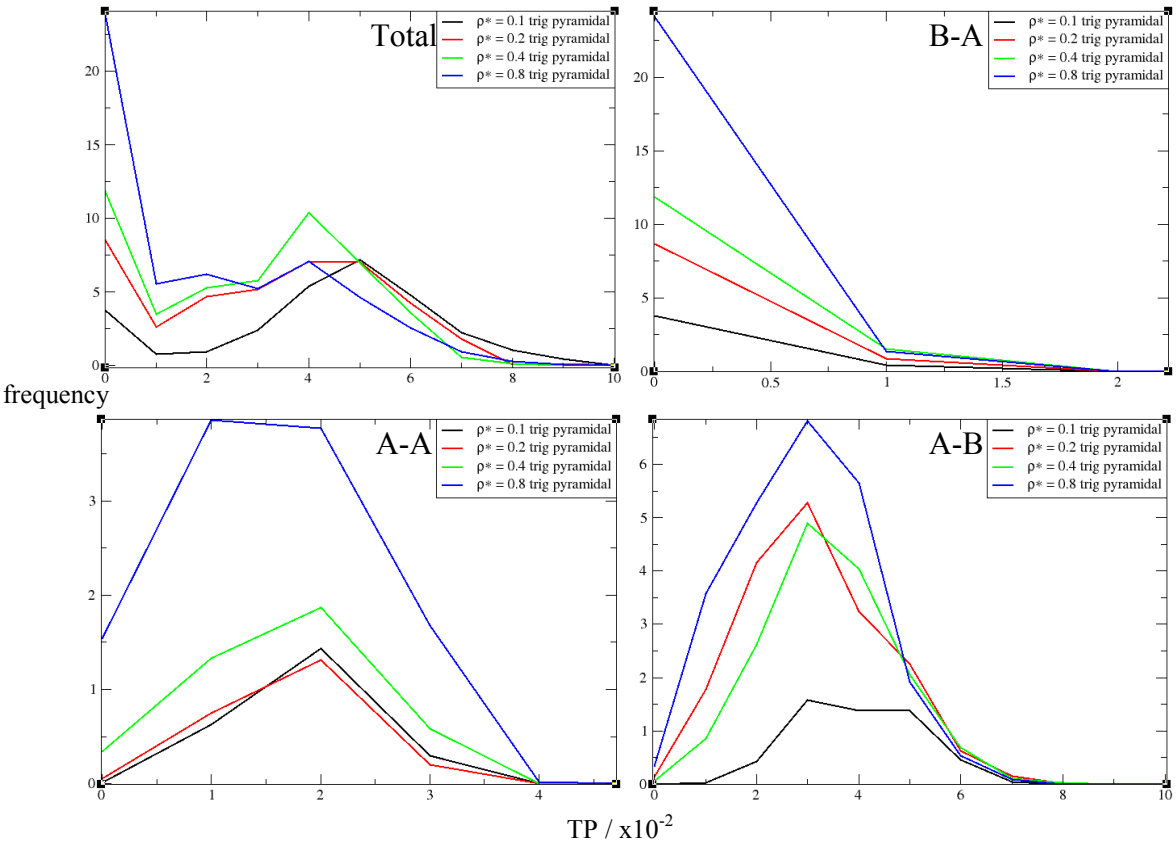

Figure 195 - *The trigonal pyramidicity at a size ratio of 2.5 for different reduced densities. The top left figure shows the total pyramidicity, the bottom left figure shows the A-A connection pyramidicity. The top right figure shows the pyramidicity for B-A connections, this means a three coordinate B particle surrounded by three A particles. This is reversed in the A-B connections data, where three B particles surround an A particle (bottom right).*

The results indicate there is indeed a significant amount of trigonal pyramidal structures at size ratio of 2.5, the total data shows an increase of trigonal pyramidal structures with increasing density. There are a considerable number of good quality trigonal pyramidal structures present as there are strong peaks at TP = 0.00 visible in the total data at different densities. The B-A data reveals that not only a significant amount are due to the A particles (wurtzite representations) surrounding B particles (zinc blende representations) to form trigonal pyramidal strucutures, but also they are very narrowly distributed between TP values of 0.00 to.0.02. This indicates the majority of these trigonal pyramidal structures are both good quality and the most abundant as their frequencies are very high relative to the other breakdown data sets. The A-B data has a much wider distribution of TP values varying from 0.00 to 0.10 and with major peaks in the data occurring at approximately 0.03. This points to poor trigonal pyramidal structures when B particles surround A particles and furthermore the frequency of the peaks at each density shown being approximately a third of that observed for the B-A data. There is a maximum frequency of five or less for TP $\leq$ 0.02 visible in the A-B data for all reduced densities. This can be contrasted with the B-A data which has a frequency of at least three and rising to twenty three from the lowest to the highest density result at the same range of TP values. The A-A data also shows a wider distribution with TP values varying from 0.00 to 0.04, in addition the frequency scale is approximately five times smaller than that of the B-A data. This again indicates very few trigonal pyramidal structures resulting from A particles surrounding a central A particle. The results for B-B particles have not been shown as there are no three coordinated B particles with respect to B-B connections, hence no trigonal pyramidicity can not be determined. To further highlight the propensity of the B (zinc blende representations) particles to associate with A (wurtzite representations) particles to form tripod structures the total results in Figure 195 are shown in terms of whether the central three coordinated particle is either the B particle or the A particle (Figure 196).

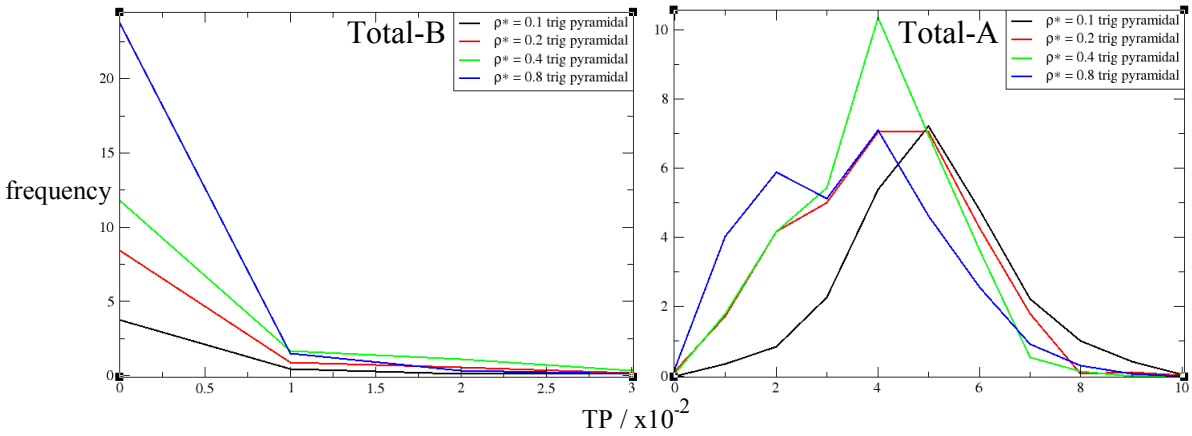

Figure 196 - *The breakdown of the trigonal pyramidicity at a size ratio of 2.5 in terms of the centrally coordinated particle being zinc blende or wurtzite representations. The left figure shows the total trigonal pyramidicity in terms of the central coordinated particle being B particles (zinc blende representations) The right figure also shows the total trigonal pyramidicity in terms of the central coordinated particle being A particles (wurtzite representation).*

The results of the total trigonal pyramidicity illustrate firmly that the majority of good quality trigonal pyramidal structures in the Stockmayer fluid at a size ratio of 2.5 are the result of A (wurtzite representations) particles coordinating around B (zinc blende representations) particles. There is a narrow distribution for the total data with respect to central B particles, TP values 0.00 to 0.03 and the fact that this data is almost completely identical to that of the B-A data in Figure 195 means that the B particles tend to only coordinate with A particles to form trigonal pyramidal structures and not with a mixture of B and A particles. The opposite is true for the total data with respect to A particles as it has a wider distribution, TP values 0.01 to 0.10, and it is not identical to the A-B data in Figure 195 indicating that the A particles coordinate with both B and A indiscriminately to form poor quality trigonal pyramidal structures. The data at a size ratio of 2.5 for both Figure 195 and Figure 196 is summarised by way of a simple diagram showing the types of trigonal pyramidal structures formed when the central coordinating particle is either A or B (Figure 197). It should be noted this summary does not take into account the quality of the trigonal pyramidal structures, as has already been shown the good quality trigonal pyramidal structures tend to only occur when A particles exclusively surround B particles (B particles are the centrally coordinating particle).

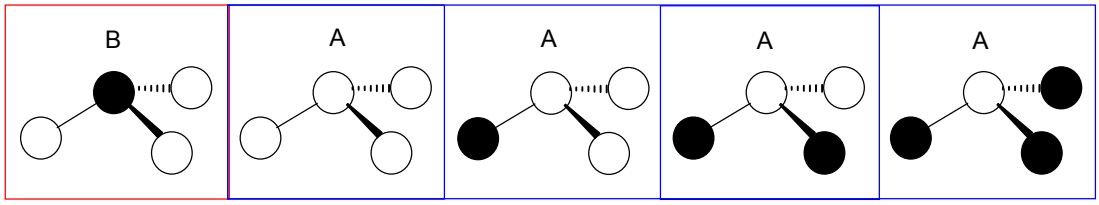

Figure 197 - *The diagrammatic representations of the structures forming in the Stockmayer fluid according to the trigonal pyramidicity data. The left diagram highlighted in red shows the only structure formed when the central coordinating particle is a B particle. The right diagrams highlighted in blue show the many structures that can be adopted when the central three coordinate particle is an A particle. The A particles are represented as white and B particles as black.*

7.13 Summary

The Stockmayer fluid simulations involving zinc blende and wurtzite representations have shown that the zinc blende representations are able to form tetrahedral and trigonal pyramidal structures which resemble the tripod and tetrapod structures encountered in the chalcogenide experimental synthesis of nanostructures. The Stockmayer fluid simulations show the greatest formation of good quality tetrahedral structures occurs at the specific size ratio of 2.5, where the wurtzite representations are 2.5 times the size of the zinc blende representations. In addition there are also good quality trigonal pyramidal structures present at this size ratio. The production of the good quality tetrahedral structures seems to be independent of the density of the system, as there are relatively constant numbers at all of the densities investigated. The trigonal pyramidal structures seem to be linked more closely to the density, with the number of good quality trigonal pyramidal structures tending to increase with increasing density. The data in this chapter point to the formation of nanostructures, ranging from simple chains to complex tetrapods, as being the result of dipolar interactions between nanocrystals.

Chapter 8 Summary & Conclusions

In this thesis the formation of potentially complex nanostructures from seemingly simple nanoparticles has been investigated. The Monte Carlo simulation method has been employed throughout. The resultant structures range from simple nanowires to more complex pod structures. The nanoparticles have been modelled as soft spheres with additional dipole moments, also known as the Stockmayer fluid potential. In addition the Stockmayer fluid model was modified to represent more complex nanoparticles in order to model the formation of tetrapod structures observed experimentally.

In chapter 3 clusters of the ideal zinc blende crystal were constructed and their resultant dipole moments calculated. Effective energy profiles for each cluster were generated by rotating a secondary image about the first cluster at a fixed separation. The subsequent analysis of the cluster-cluster interaction energies revealed good agreement with dipole pair energy profiles at large separations. They also resemble dipole pairs at short separations; however deviations in the cluster energy profile from the dipole pair energy profile tended to occur as a result of the atomistic detailing of the surface. These deviations in the energy profile increased with the size of the clusters as there were more atoms on the surface of the clusters.

In chapter 4 ideal wurtzite clusters were constructed and their resultant dipole and quadrupole moments calculated. The energy profiles were built up in the same manner as in chapter 3, however on this occasion the presence of quadrupole-quadrupole interactions between clusters lead to a diverse range of energy profiles. The presence of the nanocluster quadrupoles was observed to complicate the underlying energy profiles with respect to purely dipolar interactions. The most favourable configuration possible is still essentially the head to tail interaction, but with additional quadrupole interactions that augment the dipole interactions. The atomistic energy profiles of both the zinc blende and wurtzite crystal structures showed reasonably good agreement with the dipole-pair and multipole-pair profiles, respectively.

The Stockmayer fluid potential was used as a model to mimic the chalcogenide nanocrystals and the effects of having a binary polydisperse distribution of particles was examined in chapter 6. The binary Stockmayer fluid simulations revealed that increasing the density of the system translated into an increase of both the chain length and the mean coordination number of the resulting nanostructures. The simulations also showed the presence of triangular units; at a size ratio of 1.0, the bond angle distribution had peaks at 60 degrees. The frequency of the triangular units tended to increase with larger system densities. The frequency of the triangular units also increased with increasing size ratio of the system; this was attributed to the fact that energy of ABA triangular units and ABA chains converged at high size ratios. This meant ABA chains and ABA triangular units were equally favoured in the system. The same was not true for BAB triangular units and chains, in which triangular units only tended to occur at very high reduced densities. The binary Stockmayer fluid simulations also highlighted that the increasing size ratio of the system led to a slight increase in larger particles associating amongst themselves to form chains; conversely the length of smaller particle chains tended to decrease with increasing size ratio. However chains made up of a mixture of alternating large and small particles also tended to increase with increasing size ratio.

In chapter 7 the Stockmayer fluid model was altered such that zinc blende representations were constructed from four Stockmayer particles. These would act as mimics of the dipoles of zinc blende cores found in tetrapod structures encountered in nanoparticle synthesis. These zinc blende representations were combined with wurtzite representations (standard Stockmayer particles) in order to try and simulate tetrapod formation. The simulations showed that good quality tetrapod structures, signified by a zinc blende representation surrounded by four wurtzite representations in a tetrahedral fashion, occurred at a particular size ratio of 2.5. These tetrapod structures seemed to be unaffected by changes in density as the frequency of tetrapod structures remained constant. There were also significant trigonal pyramidal structures present in these simulations, which were most frequently present between a size ratio of 2.0 and 2.5. The trigonal pyramidal structures, unlike the tetrahedral tetrapod structures, did show an increase in frequency with increasing density.

8.1 Future work

The atomistic energy calculations of the ideal clusters with the wurtzite morphology have indicated that they possess both a dipole moment and a quadrupole moment. The ideal zinc blende clusters have been shown to only have a dipole moment, and so there is the possibility that dipole-quadrupole interaction between the zinc blende and wurtzite clusters may also play a significant role alongside dipole-dipole interactions. This requires further investigation, and if confirmed this would imply that tetrapod Stockmayer fluid simulations could be further modified to take into account the dipole-quadrupole interactions between the zinc blende and wurtzite representations. This may help to further increase the formation of pod structures in the Stockmayer fluid simulations.

The current simulations have been narrowly focused at certain reduced dipole moments, temperatures and densities. Therefore a more vigorous examination of different parameters for these reduced units needs to be explored. The simulations carried out in this thesis are a very small sample size and in a sense not optimized for tetrapod formation. When one considers that in order to form a tetrapod structure there is a ratio of one zinc blende representation to four wurtzite representations, and the current simulations encompass 216 particles of which half are zinc blende and the other half wurtzite representations. This means that the wurtzite particles are a limiting factor, with the number of maximum possible tetrapods structures in the simulations being 108/4 = 27. The simulations hence need to be carried out with the ratio of 1:4 between zinc blende and wurtzite representations to achieve a greater understanding of tetrapod formation.

Appendix

A.1 Simulation details

The initial simulation configurations for the Stockmayer fluid simulations encountered in chapter 5 and chapter 6 are achieved by randomly generating coordinates and dipoles for the particles. To avoid any unexpected or biased results, due to overlapping particles in the initially generated configurations, the initial configurations are allowed to equilibriate according to the soft sphere potential only Equation 26. This ensures the particles are as evenly spread in the simulation cell as possible, before the start of the Stockmayer fluid simulations. Approximately fifteen million steps were needed to reach equilibrium. The equilibrium run length for the simulations was one million steps.

A.2 Simulation parameters

The parameters utilized in the Stockmayer simulations encountered in both chapters five and six are listed (Table 3). The temperature is constant in all simulations with the value set at 320 K.

Reduced T	Reduced dipole	ε (a.u)	Size ratio	Dipole of A (a.u)	σ of A (a.u)	Dipole of B (a.u)	σ of B (a.u)
1.00	3.00	0.001	1.00	1.00	4.80	1.00	4.80
1.00	3.00	0.001	1.60	1.00	4.80	2.00	7.70
1.00	3.00	0.001	2.10	1.00	4.80	3.00	10.00
1.00	3.00	0.001	2.50	1.00	4.80	4.00	12.00
1.00	3.00	0.001	2.90	1.00	4.80	5.00	13.90
1.00	3.00	0.001	3.30	1.00	4.80	6.00	15.80
1.00	3.00	0.001	3.60	1.00	4.80	7.00	17.30
1.00	3.00	0.001	4.00	1.00	4.80	8.00	19.20

Table 3 - *The parameters used in simulations of the Stockmayer fluid. The dipole moments and size of the binary mixture of Stockmayer fluid particles are listed.*

A.3 Atomic units

In this thesis we refer to length, energy and temperature in atomic units. The conversion to SI units is listed (Table 4).

Length	1 α_o	5.29×10^{-11} m
Energy	1 E_h	4.36×10^{-18} J
Temperature	1 a.u	3.16×10^{5} K

Table 4 - *The Atomic unit conversions.*

References

(1) Alivisatos, A. P.; Barbara, P. F.; Castleman, A. W.; Chang, J.; Dixon, D. A.; Klein, M. L.; McLendon, G. L.; Miller, J. S.; Ratner, M. A.; Rossky, P. J.; Stupp, S. I.; Thompson, M. E. "From molecules to materials: Current trends and future directions"; Workshop on From Molecules to Materials, 1997, Austin, Texas.

(2) Goldstein, A. N.; Echer, C. M.; Alivisatos, A. P. *Science* **1992**, *256*, 1425.

(3) Li, L. S.; Hu, J. T.; Yang, W. D.; Alivisatos, A. P. *Nano Letters* **2001**, *1*, 349.

(4) Sonvico, F.; Dubernet, C.; Colombo, P.; Couvreur, P. *Current Pharmaceutical Design* **2005**, *11*, 2091.

(5) Laurent, S.; Forge, D.; Port, M.; Roch, A.; Robic, C.; Elst, L. V.; Muller, R. N. *Chemical Reviews* **2008**, *108*, 2064.

(6) Cui, Y.; Banin, U.; Bjork, M. T.; Alivisatos, A. P. *Nano Letters* **2005**, *5*, 1519.

(7) Liu, B.; Song, Z. T.; Feng, S. L.; Chen, B. M. *Microelectronic Engineering* **2005**, *82*, 168.

(8) Huynh, W. U.; Dittmer, J. J.; Alivisatos, A. P. *Science* **2002**, *295*, 2425.

(9) Subramanian, V.; Wolf, E. E.; Kamat, P. V. *Journal of Physical Chemistry B* **2003**, *107*, 7479.

(10) Parak, W. J.; Boudreau, R.; Le Gros, M.; Gerion, D.; Zanchet, D.; Micheel, C. M.; Williams, S. C.; Alivisatos, A. P.; Larabell, C. *Advanced Materials* **2002**, *14*, 882.

(11) Wang, Z. L. *Materials Science & Engineering R-Reports* **2009**, *64*, 33.

(12) Krahne, R.; Yacoby, A.; Shtrikman, H.; Bar-Joseph, I.; Dadosh, T.; Sperling, J. *Applied Physics Letters* **2002**, *81*, 730.

(13) Sinha, A. K.; Seelan, S.; Tsubota, S.; Haruta, M. "Catalysis by gold nanoparticles: epoxidation of propene"; 16th National Meeting of the Catalysis-Society-of-India/1st Indo-German Conference on Catalysis, 2003, Hyderabad, INDIA.

(14) Jin, R. C.; Cao, Y. W.; Mirkin, C. A.; Kelly, K. L.; Schatz, G. C.; Zheng, J. G. *Science* **2001**, *294*, 1901.

(15) Alivisatos, A. P. *Journal Of Physical Chemistry* **1996**, *100*, 13226.

(16) Greenwood, G. W. *Acta Metallurgica* **1956**, *4*, 243.

(17) Lifshitz, I. M.; Slyozov, V. V. *Journal of Physics and Chemistry of Solids* **1961**, *19*, 35.

(18) Speight, M. V. *Acta Metallurgica* **1968**, *16*, 133.

(19) Law, M.; Goldberger, J.; Yang, P. D. *Annual Review of Materials Research* **2004**, *34*, 83.

(20) Duan, X. F.; Lieber, C. M. *Advanced Materials* **2000**, *12*, 298.

(21) Zhang, Y. J.; Wang, N. L.; Gao, S. P.; He, R. R.; Miao, S.; Liu, J.; Zhu, J.; Zhang, X. *Chemistry of Materials* **2002**, *14*, 3564.

(22) Pan, Z. W.; Dai, Z. R.; Xu, L.; Lee, S. T.; Wang, Z. L. *Journal of Physical Chemistry B* **2001**, *105*, 2507.

(23) Kuno, M. *Physical Chemistry Chemical Physics* **2008**, *10*, 620.

(24) Jun, Y. W.; Seo, J. W.; Oh, S. J.; Cheon, J. *Coordination Chemistry Reviews* **2005**, *249*, 1766.

(25) Kumar, S.; Nann, T. *Small* **2006**, *2*, 316.

(26) Jun, Y. W.; Choi, J. S.; Cheon, J. *Angewandte Chemie-International Edition* **2006**, *45*, 3414.

(27) Kudera, S.; Carbone, L.; Zanella, M.; Cingolani, R.; Parak, W. J.; Manna, L. "Synthesis and perspectives of complex crystalline nano-structures"; International Conference on Trends in Nanotechnology, 2005, Oviedo, SPAIN.

(28) Yang, S. W.; Gao, L. *Journal Of The American Chemical Society* **2006**, *128*, 9330.

(29) Kang, C. C.; Lai, C. W.; Peng, H. C.; Shyue, J. J.; Chou, P. T. *Small* **2007**, *3*, 1882.

(30) Ribeiro, C.; Barrado, C. M.; de Camargo, E. R.; Longo, E.; Leite, E. R. *Chemistry-a European Journal* **2009**, *15*, 2217.

(31) Sun, L. L.; Wang, L.; Song, Y. H.; Guo, C. L.; Sun, Y. J.; Peng, C. Y.; Liu, Z. L.; Li, Z. *Applied Surface Science* **2008**, *254*, 2581.

(32) Li, J.; Liu, B.; Li, J. H. *Langmuir* **2006**, *22*, 528.

(33) Chen, M. H.; Gao, L. *Journal of the American Ceramic Society* **2005**, *88*, 1643.

(34) Sathyamoorthy, R.; Manjuladevi, V.; Sudhagar, P.; Senthilarasu, S.; Pal, U. *Materials Chemistry and Physics* **2007**, *105*, 20.

(35) Martin, C. R. *Science* **1994**, *266*, 1961.

(36) Enculescu, I.; Sima, M.; Enculescu, M.; Enache, M.; Ion, L.; Antohe, S.; Neumann, R. "Deposition and properties of CdTe nanowires prepared by template replication"; Symposium on Wide Band Gap II-VI Semiconductors - Growth, Characterization and Applications held at the 2006 E-MRS Fall Meeting, 2006, Warsaw, POLAND.

(37) Chen, C. C.; Chao, C. Y.; Lang, Z. H. *Chemistry of Materials* **2000**, *12*, 1516.

(38) Grebinski, J. W.; Hull, K. L.; Zhang, J.; Kosel, T. H.; Kuno, M. *Chemistry of Materials* **2004**, *16*, 5260.

(39) Kan, S. H.; Aharoni, A.; Mokari, T.; Banin, U. "Shape control of III-V semiconductor nanocrystals: Synthesis and properties of InAs quantum rods"; Nanoparticle Assemblies Meeting, 2003, Liverpool, England.

(40) Cheng, C. D.; Haynie, D. T. *Applied Physics Letters* **2005**, *87*, 3.

(41) Wang, J.; Chen, Q. W.; Zeng, C.; Hou, B. Y. *Advanced Materials* **2004**, *16*, 137.

(42) Zeng, J.; Huang, J. L.; Lu, W.; Wang, X. P.; Wang, B.; Zhang, S. Y.; Hou, J. G. *Advanced Materials* **2007**, *19*, 2172.

(43) Jun, Y. W.; Jang, J. T.; Cheon, J. *Bulletin of the Korean Chemical Society* **2006**, *27*, 961.

(44) Tang, Z. Y.; Kotov, N. A. *Advanced Materials* **2005**, *17*, 951.

(45) Xia, Y. N.; Yang, P. D.; Sun, Y. G.; Wu, Y. Y.; Mayers, B.; Gates, B.; Yin, Y. D.; Kim, F.; Yan, Y. Q. *Advanced Materials* **2003**, *15*, 353.

(46) Larsen, T. H.; Sigman, M.; Ghezelbash, A.; Doty, R. C.; Korgel, B. A. *Journal of the American Chemical Society* **2003**, *125*, 5638.

(47) Cheon, J. W.; Kang, N. J.; Lee, S. M.; Lee, J. H.; Yoon, J. H.; Oh, S. J. *Journal of the American Chemical Society* **2004**, *126*, 1950.

(48) Lee, S. M.; Jun, Y. W.; Cho, S. N.; Cheon, J. *Journal of the American Chemical Society* **2002**, *124*, 11244.

(49) Jun, Y. W.; Jung, Y. Y.; Cheon, J. *Journal of the American Chemical Society* **2002**, *124*, 615.

(50) Cozzoli, P. D.; Manna, L.; Curri, M. L.; Kudera, S.; Giannini, C.; Striccoli, M.; Agostiano, A. *Chemistry of Materials* **2005**, *17*, 1296.

(51) Kitano, M.; Hamabe, T.; Maeda, S.; Okabe, T. *Journal of Crystal Growth* **1991**, *108*, 277.

(52) Murray, C. B.; Norris, D. J.; Bawendi, M. G. *Journal of the American Chemical Society* **1993**, *115*, 8706.

(53) Boyle, T. J.; Bunge, S. D.; Alam, T. M.; Holland, G. P.; Headley, T. J.; Avilucea, G. *Inorganic Chemistry* **2005**, *44*, 1309.

(54) Green, M.; Wakefield, G.; Dobson, P. J. *Journal of Materials Chemistry* **2003**, *13*, 1076.

(55) Panda, A. B.; Acharya, S.; Efrima, S.; Golan, Y. *Langmuir* **2007**, *23*, 765.

(56) Yin, M.; O'Brien, S. *Journal of the American Chemical Society* **2003**, *125*, 10180.

(57) Jana, N. R.; Chen, Y. F.; Peng, X. G. *Chemistry of Materials* **2004**, *16*, 3931.

(58) Hyeon, T.; Lee, S. S.; Park, J.; Chung, Y.; Bin Na, H. *Journal of the American Chemical Society* **2001**, *123*, 12798.

(59) Park, J.; Kang, E. A.; Bae, C. J.; Park, J. G.; Noh, H. J.; Kim, J. Y.; Park, J. H.; Park, J. H.; Hyeon, T. *Journal of Physical Chemistry B* **2004**, *108*, 13594.

(60) Hyeon, T.; Chung, Y.; Park, J.; Lee, S. S.; Kim, Y. W.; Park, B. H. *Journal of Physical Chemistry B* **2002**, *106*, 6831.

(61) de Silva, R. M.; Palshin, V.; de Silva, K. M. N.; Henry, L. L.; Kumar, C. *Journal of Materials Chemistry* **2008**, *18*, 738.

(62) Kang, E.; Park, J.; Hwang, Y.; Kang, M.; Park, J. G.; Hyeon, T. *Journal of Physical Chemistry B* **2004**, *108*, 13932.

(63) Nelmes, R. J.; McMahon, M. I.; Wright, N. G.; Allan, D. R.; Liu, H.; Loveday, J. S. "STRUCTURAL STUDIES OF III-V AND GROUP-IV SEMICONDUCTORS AT HIGH-PRESSURE"; 6th International Conference on High Pressure Semiconductor Physics (HPSP VI), 1994, Vancouver, Canada.

(64) Nelmes, R. J.; McMahon, M. I.; Wright, N. G.; Allan, D. R. "STRUCTURAL STUDIES OF II-VI SEMICONDUCTORS AT HIGH-PRESSURE"; 6th International Conference on High Pressure Semiconductor Physics (HPSP VI), 1994, Vancouver, Canada.

(65) Xia, H.; Xia, Q.; Ruoff, A. L. *Physical Review B* **1993**, *47*, 12925.

(66) Desgreniers, S.; Beaulieu, L.; Lepage, I. *Physical Review B* **2000**, *61*, 8726.

(67) Ueno, M.; Yoshida, M.; Onodera, A.; Shimomura, O.; Takemura, K. *Physical Review B* **1994**, *49*, 14.

(68) Tolbert, S. H.; Alivisatos, A. P. *Journal of Chemical Physics* **1995**, *102*, 4642.

(69) Wilson, M.; Madden, P. A. *Journal of Physics-Condensed Matter* **2002**, *14*, 4629.

(70) San-Miguel, A. *Chemical Society Reviews* **2006**, *35*, 876.

(71) Jacobs, K.; Wickham, J.; Alivisatos, A. P. *Journal of Physical Chemistry B* **2002**, *106*, 3759.

(72) Tolbert, S. H.; Alivisatos, A. P. *Annual Review of Physical Chemistry* **1995**, *46*, 595.

(73) Tolbert, S. H.; Alivisatos, A. P. *Science* **1994**, *265*, 373.

(74) Tolbert, S. H.; Alivisatos, A. P. “SIZE DEPENDENCE OF THE SOLID-SOLID PHASE-TRANSITION IN CDSE NANOCRYSTALS”; 6th International Symp on Small Particles and Inorganic Clusters (Isspic 6), 1992, Chicago, Il.

(75) Tolbert, S. H.; Herhold, A. B.; Brus, L. E.; Alivisatos, A. P. *Physical Review Letters* **1996**, *76*, 4384.

(76) Hines, M. A.; Guyot-Sionnest, P. *Journal of Physical Chemistry* **1996**, *100*, 468.

(77) Revaprasadu, N.; Malik, M. A.; O'Brien, P.; Wakefield, G. *Chemical Communications* **1999**, 1573.

(78) Schlamp, M. C.; Peng, X. G.; Alivisatos, A. P. *Journal of Applied Physics* **1997**, *82*, 5837.

(79) Casavola, M.; Buonsanti, R.; Caputo, G.; Cozzoli, P. D. *European Journal of Inorganic Chemistry* **2008**, 837.

(80) Cozzoli, P. D.; Pellegrino, T.; Manna, L. *Chemical Society Reviews* **2006**, *35*, 1195.

(81) Liang, D. S.; Shen, L.; Wang, Z. B.; Cui, Y. P.; Zhang, J. Y.; Ye, Y. H. *Chinese Physics Letters* **2008**, *25*, 4431.

(82) Chistyakov, A. A.; Martynov, I. L.; Mochalov, K. E.; Oleinikov, V. A.; Sizova, S. V.; Ustinovich, E. A.; Zakharchenko, K. V. *Laser Physics* **2006**, *16*, 1625.

(83) Zhu, C. Q.; Wang, P.; Wang, X.; Li, Y. *Nanoscale Research Letters* **2008**, *3*, 213.

(84) Hwang, C. S.; Cho, I. H. *Bulletin of the Korean Chemical Society* **2005**, *26*, 1776.

(85) Cao, Y. W.; Banin, U. *Journal of the American Chemical Society* **2000**, *122*, 9692.

(86) Tomlinson, I. D.; Grey, J. L.; Rosenthal, S. J. *Molecules* **2002**, *7*, 777.

(87) Kim, S.; Fisher, B.; Eisler, H. J.; Bawendi, M. *Journal of the American Chemical Society* **2003**, *125*, 11466.

(88) Seo, H.; Kim, S. W. *Chemistry of Materials* **2007**, *19*, 2715.

(89) Zeng, R. S.; Zhang, T. T.; Liu, J. C.; Hu, S.; Wan, Q.; Liu, X. M.; Peng, Z. W.; Zou, B. S. *Nanotechnology* **2009**, *20*, 8.

(90) Kim, S. W.; Zimmer, J. P.; Ohnishi, S.; Tracy, J. B.; Frangioni, J. V.; Bawendi, M. G. *Journal of the American Chemical Society* **2005**, *127*, 10526.

(91) Zimmer, J. P.; Kim, S. W.; Ohnishi, S.; Tanaka, E.; Frangioni, J. V.; Bawendi, M. G. *Journal of the American Chemical Society* **2006**, *128*, 2526.

(92) Pons, T.; Lequeux, N.; Mahler, B.; Sasnouski, S.; Fragola, A.; Dubertret, B. *Chemistry of Materials* **2009**, *21*, 1418.

(93) Cheng, C. T.; Chen, C. Y.; Lai, C. W.; Liu, W. H.; Pu, S. C.; Chou, P. T.; Chou, Y. H.; Chiu, H. T. *Journal of Materials Chemistry* **2005**, *15*, 3409.

(94) Carbone, L.; Nobile, C.; De Giorgi, M.; Sala, F. D.; Morello, G.; Pompa, P.; Hytch, M.; Snoeck, E.; Fiore, A.; Franchini, I. R.; Nadasan, M.; Silvestre, A. F.; Chiodo, L.; Kudera, S.; Cingolani, R.; Krahne, R.; Manna, L. *Nano Letters* **2007**, *7*, 2942.

(95) Kudera, S.; Carbone, L.; Casula, M. F.; Cingolani, R.; Falqui, A.; Snoeck, E.; Parak, W. J.; Manna, L. *Nano Letters* **2005**, *5*, 445.

(96) Saunders, A. E.; Popov, I.; Banin, U. *Journal of Physical Chemistry B* **2006**, *110*, 25421.

(97) Fiore, A.; Mastria, R.; Lupo, M. G.; Lanzani, G.; Giannini, C.; Carlino, E.; Morello, G.; De Giorgi, M.; Li, Y.; Cingolani, R.; Manna, L. *Journal of the American Chemical Society* **2009**, *131*, 2274.

(98) Lee, H.; Yoon, S. W.; Ahn, J. P.; Suh, Y. D.; Lee, J. S.; Lim, H.; Kim, D. "Synthesis of type II CdTe/CdSe heterostructure tetrapod nanocrystals for PV applications"; 17th International Photovoltaic Science and Engineering Conference, 2007, Fukuoka, JAPAN.

(99) Zhong, H. Z.; Zhou, Y.; Yang, Y.; Yang, C. H.; Li, Y. F. *Journal of Physical Chemistry C* **2007**, *111*, 6538.

(100) Milliron, D. J.; Hughes, S. M.; Cui, Y.; Manna, L.; Li, J. B.; Wang, L. W.; Alivisatos, A. P. *Nature* **2004**, *430*, 190.

(101) Manna, L.; Milliron, D. J.; Meisel, A.; Scher, E. C.; Alivisatos, A. P. *Nature Materials* **2003**, *2*, 382.

(102) Jun, Y. W.; Lee, S. M.; Kang, N. J.; Cheon, J. *Journal of the American Chemical Society* **2001**, *123*, 5150.

(103) Lee, S. M.; Cho, S. N.; Cheon, J. *Advanced Materials* **2003**, *15*, 441.

(104) Greyson, E. C.; Barton, J. E.; Odom, T. W. *Small* **2006**, *2*, 368.

(105) Catlow, C. R. A.; Bromley, S. T.; Hamad, S.; Mora-Fonz, M.; Sokol, A. A.; Woodley, S. M. *Phys Chem Chem Phys* **2009**, *12*, 786.

(106) Zhang, H. Z.; Huang, F.; Gilbert, B.; Banfield, J. F. *Journal of Physical Chemistry B* **2003**, *107*, 13051.

(107) Schmelzer, J. W. P. *Nucleation Theory and Applications* **2005**, *Wiley-VCH*.

(108) Peng, Z. A.; Peng, X. G. *Journal of the American Chemical Society* **2001**, *123*, 1389.

(109) Saunders, A. E.; Ghezelbash, A.; Sood, P.; Korgel, B. A. *Langmuir* **2008**, *24*, 9043.

(110) Yong, K. T.; Sahoo, Y.; Swihart, M. T.; Prasad, P. N. *Journal of Physical Chemistry C* **2007**, *111*, 2447.

(111) Manna, L.; Scher, E. C.; Alivisatos, A. P. *Journal of the American Chemical Society* **2000**, *122*, 12700.

(112) Peng, X. G.; Manna, L.; Yang, W. D.; Wickham, J.; Scher, E.; Kadavanich, A.; Alivisatos, A. P. *Nature* **2000**, *404*, 59.

(113) Hanrath, T.; Veldman, D.; Choi, J. J.; Christova, C. G.; Wienk, M. M.; Janssen, R. A. J. *Acs Applied Materials & Interfaces* **2009**, *1*, 244.

(114) Murray, C. B.; Sun, S. H.; Gaschler, W.; Doyle, H.; Betley, T. A.; Kagan, C. R. *Ibm Journal of Research and Development* **2001**, *45*, 47.

(115) Houtepen, A. J.; Koole, R.; Vanmaekelbergh, D. L.; Meeldijk, J.; Hickey, S. G. *Journal of the American Chemical Society* **2006**, *128*, 6792.

(116) Wang, F. D.; Tang, R.; Buhro, W. E. *Nano Letters* **2008**, *8*, 3521.

(117) Wang, F.; Tang, R.; Kao, J. L. F.; Dingman, S. D.; Buhro, W. E. *Journal of the American Chemical Society* **2009**, *131*, 4983.

(118) Kim, Y. H.; Jun, Y. W.; Jun, B. H.; Lee, S. M.; Cheon, J. W. *Journal of the American Chemical Society* **2002**, *124*, 13656.

(119) Yeh, C. Y.; Lu, Z. W.; Froyen, S.; Zunger, A. *Physical Review B* **1992**, *46*, 10086.

(120) Cho, J. W.; Kim, H. S.; Kim, Y. J.; Jang, S. Y.; Park, J.; Kim, J. G.; Kim, Y. J.; Cha, E. H. *Chemistry of Materials* **2008**, *20*, 5600.

(121) Jun, Y. W.; Casula, M. F.; Sim, J. H.; Kim, S. Y.; Cheon, J.; Alivisatos, A. P. *Journal of the American Chemical Society* **2003**, *125*, 15981.

(122) Whitesides, G. M.; Grzybowski, B. *Science* **2002**, *295*, 2418.
(123) Penn, R. L.; Banfield, J. F. *American Mineralogist* **1998**, *83*, 1077.
(124) Penn, R. L.; Banfield, J. F. *Geochimica Et Cosmochimica Acta* **1999**, *63*, 1549.
(125) Chemseddine, A.; Moritz, T. *European Journal of Inorganic Chemistry* **1999**, 235.
(126) Pacholski, C.; Kornowski, A.; Weller, H. *Angewandte Chemie-International Edition* **2002**, *41*, 1188.
(127) Liu, B.; Zeng, H. C. *Journal of the American Chemical Society* **2003**, *125*, 4430.
(128) Zhang, Z. P.; Sun, H. P.; Shao, X. Q.; Li, D. F.; Yu, H. D.; Han, M. Y. *Advanced Materials* **2005**, *17*, 42.
(129) Xu, H. L.; Wang, W. Z.; Zhu, W. *Chemistry Letters* **2006**, *35*, 264.
(130) Tang, Z. Y.; Kotov, N. A.; Giersig, M. *Science* **2002**, *297*, 237.
(131) Yu, J. H.; Joo, J.; Park, H. M.; Baik, S. I.; Kim, Y. W.; Kim, S. C.; Hyeon, T. *Journal of the American Chemical Society* **2005**, *127*, 5662.
(132) Huang, F.; Zhang, H. Z.; Banfield, J. F. *Journal of Physical Chemistry B* **2003**, *107*, 10470.
(133) Thangadurai, P.; Balaji, S.; Manoharan, P. T. *Materials Chemistry and Physics* **2009**, *114*, 420.
(134) Colvin, V. L.; Alivisatos, A. P. *Journal of Chemical Physics* **1992**, *97*, 730.
(135) Colvin, V. L.; Cunningham, K. L.; Alivisatos, A. P. *Journal of Chemical Physics* **1994**, *101*, 7122.
(136) Blanton, S. A.; Leheny, R. L.; Hines, M. A.; GuyotSionnest, P. *Physical Review Letters* **1997**, *79*, 865.
(137) Schmidt, M. E.; Blanton, S. A.; Hines, M. A.; GuyotSionnest, P. *Journal of Chemical Physics* **1997**, *106*, 5254.
(138) Rabani, E.; Hetenyi, B.; Berne, B. J.; Brus, L. E. *Journal of Chemical Physics* **1999**, *110*, 5355.
(139) Shiang, J. J.; Kadavanich, A. V.; Grubbs, R. K.; Alivisatos, A. P. *Journal of Physical Chemistry* **1995**, *99*, 17417.
(140) Nann, T.; Schneider, J. *Chemical Physics Letters* **2004**, *384*, 150.
(141) Blanton, S. A.; Leheny, R. L.; Hines, M. A.; Guyot-Sionnest, P. *Physical Review Letters* **1997**, *79*, 865.
(142) Shim, M.; Guyot-Sionnest, P. *Journal Of Chemical Physics* **1999**, *111*, 6955.
(143) Huong, N. Q.; Birman, J. L. *Journal of Chemical Physics* **1998**, *108*, 1769.
(144) Cho, K. S.; Talapin, D. V.; Gaschler, W.; Murray, C. B. *Journal Of The American Chemical Society* **2005**, *127*, 7140.
(145) Li, L. S.; Alivisatos, A. P. *Physical Review Letters* **2003**, *90*.
(146) Talapin, D. V.; Shevchenko, E. V.; Murray, C. B.; Kornowski, A.; Forster, S.; Weller, H. *Journal Of The American Chemical Society* **2004**, *126*, 12984.
(147) An, K.; Lee, N.; Park, J.; Kim, S. C.; Hwang, Y.; Park, J. G.; Kim, J. Y.; Park, J. H.; Han, M. J.; Yu, J. J.; Hyeon, T. *Journal of the American Chemical Society* **2006**, *128*, 9753.
(148) McGrother, S. C.; Gil-Villegas, A.; Jackson, G. *Molecular Physics* **1998**, *95*, 657.

(149) Dagtepe, P.; Chikan, V.; Jasinski, J.; Leppert, V. J. *Journal of Physical Chemistry C* **2007**, *111*, 14977.

(150) Dagtepe, P.; Chikan, V. *Journal of Physical Chemistry A* **2008**, *112*, 9304.

(151) Klokkenburg, M.; Houtepen, A. J.; Koole, R.; de Folter, J. W. J.; Erne, B. H.; van Faassen, E.; Vanmaekelbergh, D. *Nano Letters* **2007**, *7*, 2931.

(152) Gao, J. H.; Zhang, B.; Zhang, X. X.; Xu, B. *Angewandte Chemie-International Edition* **2006**, *45*, 1220.

(153) Chang, J. Y.; Chang, J. J.; Lo, B.; Tzing, S. H.; Ling, Y. C. *Chemical Physics Letters* **2003**, *379*, 261.

(154) Bao, Y. P.; Beerman, M.; Krishnan, K. M. *Journal Of Magnetism And Magnetic Materials* **2003**, *266*, L245.

(155) Feng, C. H.; Guo, L.; Shen, Z. G.; Gong, J. M.; Li, X. Y.; Liu, C. M.; Yang, S. H. *Solid State Sciences* **2008**, *10*, 1327.

(156) Liu, C. M.; Guo, L.; Wang, R. M.; Deng, Y.; Xu, H. B.; Yang, S. H. *Chemical Communications* **2004**, 2726.

(157) Zhang, F.; Wang, C. C. *Journal of Physical Chemistry C* **2008**, *112*, 15151.

(158) Wang, H.; Chen, Q. W.; Sun, L. X.; Qi, H. P.; Yang, X.; Zhou, S.; Xiong, J. *Langmuir* **2009**, *25*, 7135.

(159) Klokkenburg, M.; Vonk, C.; Claesson, E. M.; Meeldijk, J. D.; Erne, B. H.; Philipse, A. P. *Journal Of The American Chemical Society* **2004**, *126*, 16706.

(160) Liao, J. H.; Chen, K. J.; Xu, L. N.; Ge, C. W.; Wang, J.; Huang, L.; Gu, N. *Applied Physics A-Materials Science & Processing* **2003**, *76*, 541.

(161) Handley, D. A. *Colloidal Gold Principles, Methods and Applications*, *1*, 1989.

(162) Sylvestre, J. P.; Poulin, S.; Kabashin, A. V.; Sacher, E.; Meunier, M.; Luong, J. H. T. *Journal of Physical Chemistry B* **2004**, *108*, 16864.

(163) Liao, J. H.; Zhang, Y.; Yu, W.; Xu, L. N.; Ge, C. W.; Liu, J. H.; Gu, N. *Colloids And Surfaces A-Physicochemical And Engineering Aspects* **2003**, *223*, 177.

(164) Taratula, O.; Chen, A. M.; Zhang, J. M.; Chaudry, J.; Nagahara, L.; Banerjee, I.; He, H. X. *Journal of Physical Chemistry C* **2007**, *111*, 7666.

(165) Tong, H.; Zhu, Y. J.; Yang, L. X.; Li, L.; Zhang, L. *Angewandte Chemie-International Edition* **2006**, *45*, 7739.

(166) Tai, G. A.; Guo, W. L.; Zhang, Z. H. *Crystal Growth & Design* **2008**, *8*, 2906.

(167) Du, G. X.; Feng, S. A.; Zhao, J. H.; Song, C.; Bai, S. L.; Zhu, Z. P. *Journal of the American Chemical Society* **2006**, *128*, 15405.

(168) Leach, A. R. *Molecular Modelling Principles and Applications* **2001**, Pearson Education.

(169) Hognas, G.; Mukherjea, A. *Probability Measures on Semigroups* **1995**, Plenum Press.

(170) Aguado, A.; Madden, P. A. *Journal of Chemical Physics* **2003**, *119*, 7471.

(171) Cabral, B. J. C. *Journal Of Chemical Physics* **2000**, *112*, 4351.

(172) West, A. R. *Solid State Chemistry and Its Applications* **1990**, John Wiley & Sons Ltd.

(173) Allen, M. P.; Tildesley, D. J. *Computer simulation of liquids* **1996**, Oxford Science Publications.

(174) Stockmayer, W. H. *The Journal of Chemical Physics* **1941**, *9*, 398.

(175) Jones, J. E. *Proceedings of the Royal Society of London. Series A, Containing Papers of a Mathematical and Physical Character* **1924**, *106*, 463.
(176) Vanleeuwen, M. E.; Smit, B. *Physical Review Letters* **1993**, *71*, 3991.
(177) Degennes, P. G.; Pincus, P. A. *Physik Der Kondensiterten Materie* **1970**, *11*, 189.
(178) Jund, P.; Kim, S. G.; Tomanek, D.; Hetherington, J. *Physical Review Letters* **1995**, *74*, 3049.
(179) Tomanek, D.; Kim, S. G.; Jund, P.; Borrmann, P.; Stamerjohanns, H.; Hilf, E. R. "Self-assembly of magnetic nanostructures"; 8th International Symposium on Small Particles and Inorganic Clusters (ISSPIC 8), 1996, Copenhagen, Denmark.
(180) Caillol, J. M. *Journal of Chemical Physics* **1993**, *98*, 9835.
(181) Tavares, J. M.; da Gama, M. M. T.; Osipov, M. A. *Physical Review E* **1997**, *56*, R6252.
(182) Smit, B.; Williams, C. P.; Hendriks, E. M.; Deleeuw, S. W. *Molecular Physics* **1989**, *68*, 765.
(183) Smit, B. "Molecular simulations of fluid phase equilibria"; 7th International Conference on Fluid Properties and Phase Equilibria for Chemical Process Design, 1995, Snowmass Village, Co.
(184) Wei, D. Q.; Patey, G. N. *Physical Review Letters* **1992**, *68*, 2043.
(185) Wei, D. Q.; Patey, G. N. *Physical Review A* **1992**, *46*, 7783.
(186) Weis, J. J.; Levesque, D. *Physical Review E* **1993**, *48*, 3728.
(187) Weis, J. J.; Levesque, D. *Physical Review Letters* **1993**, *71*, 2729.
(188) Camp, P. J.; Shelley, J. C.; Patey, G. N. *Physical Review Letters* **2000**, *84*, 115.
(189) Goyal, A.; Hall, C. K.; Velev, O. D. *Physical Review E* **2008**, *77*.
(190) Ballenegger, V.; Hansen, J. P. *Molecular Physics* **2004**, *102*, 599.
(191) Wei, D. Q.; Wang, Y. J.; Wang, L.; Hu, J. H.; Gong, Z. Z.; Guo, Y. X.; Zhu, Y. S. *Physical Review E* **2007**, *75*, 5.
(192) Camp, P. J.; Patey, G. N. *Physical Review E* **1999**, *60*, 4280.
(193) Xu, C.; Ma, Y. Q.; Hui, P. M.; Tong, F. Q. *Chinese Physics Letters* **2005**, *22*, 485.
(194) Camp, P. J.; Patey, G. N. *Physical Review E* **2000**, *62*, 5403.
(195) Van Workum, K.; Douglas, J. F. *Physical Review E* **2005**, *71*.
(196) Salgueirino-Maceira, V.; Correa-Duarte, M. A.; Hucht, A.; Farle, M. *Journal of Magnetism and Magnetic Materials* **2006**, *303*, 163.
(197) Hucht, A.; Buschmann, S.; Entel, P. *Epl* **2007**, *77*, 6.
(198) Stevens, M. J.; Grest, G. S. *Physical Review Letters* **1994**, *72*, 3686.
(199) Stevens, M. J.; Grest, G. S. *Physical Review E* **1995**, *51*, 5976.
(200) Stevens, M. J.; Grest, G. S. *Physical Review E* **1995**, *51*, 5962.
(201) Bartke, J.; Hentschke, R. *Molecular Physics* **2006**, *104*, 3057.
(202) Hentschke, R.; Bartke, J.; Pesth, F. *Physical Review E* **2007**, *75*, 8.
(203) Bartke, J.; Hentschke, R. *Physical Review E* **2007**, *75*, 11.
(204) Ivanov, A. O.; Kantorovich, S. S.; Camp, P. J. *Physical Review E* **2008**, *77*, 2.
(205) Dudowicz, J.; Freed, K. F.; Douglas, J. F. *Physical Review Letters* **2004**, *92*, 4.
(206) Hentschke, R.; Bartke, J. *Physical Review E* **2008**, *77*, 2.
(207) Teixeira, P. I. C.; Tavares, J. M.; da Gama, M. M. T. *Journal of Physics-Condensed Matter* **2000**, *12*, R411.
(208) Klapp, S. H. L. *Journal Of Physics-Condensed Matter* **2005**, *17*, R525.

(209) Cabral, B. J. C. “Fluids of strongly interacting dipoles: Monte Carlo sampling using Tsallis statistics”; IUPAP International Conference on New Trends in the Fractal Aspects of Complex Systems, 2000, Maceio Al, Brazil.

(210) Tlusty, T.; Safran, S. A. *Science* **2000**, *290*, 1328.

(211) Tavares, J. M.; Weis, J. J.; da Gama, M. M. T. *Physical Review E* **1999**, *59*, 4388.

(212) Osipov, M. A.; Teixeira, P. I. C.; daGama, M. M. T. *Physical Review E* **1996**, *54*, 2597.

(213) Sear, R. P. *Physical Review Letters* **1996**, *76*, 2310.

(214) Weaver, M. J.; McManis, G. E. *Accounts of Chemical Research* **1990**, *23*, 294.

(215) Perera, L.; Berkowitz, M. L. *Journal of Chemical Physics* **1992**, *97*, 5253.

(216) Perera, L.; Berkowitz, M. L. *Journal of Chemical Physics* **1992**, *96*, 3092.

(217) Neria, E.; Nitzan, A. *Journal of Chemical Physics* **1992**, *96*, 5433.

(218) Maroncelli, M.; Fleming, G. R. *Journal of Chemical Physics* **1988**, *89*, 5044.

(219) Maroncelli, M. *Journal of Chemical Physics* **1991**, *94*, 2084.

(220) Fonseca, T.; Ladanyi, B. M. *Journal of Physical Chemistry* **1991**, *95*, 2116.

(221) Carter, E. A.; Hynes, J. T. *Journal of Chemical Physics* **1991**, *94*, 5961.

(222) Rosenthal, S. J.; Xie, X. L.; Du, M.; Fleming, G. R. *Journal of Chemical Physics* **1991**, *95*, 4715.

(223) Deleeuw, S. W.; Smit, B.; Williams, C. P. *Journal of Chemical Physics* **1990**, *93*, 2704.

(224) Deleeuw, S. W.; Williams, C. P.; Smit, B. *Fluid Phase Equilibria* **1989**, *48*, 99.

(225) Deleeuw, S. W.; Williams, C. P.; Smit, B. *Molecular Physics* **1988**, *65*, 1269.

(226) Mooij, G.; Deleeuw, S. W.; Williams, C. P.; Smit, B. *Molecular Physics* **1990**, *71*, 909.

(227) Mooij, G.; Deleeuw, S. W.; Smit, B.; Williams, C. P. *Journal of Chemical Physics* **1992**, *97*, 5113.

(228) Clarke, A. S.; Patey, G. N. *Journal of Chemical Physics* **1994**, *100*, 2213.

(229) Sun, H.; Watts, R. O.; Buck, U. *Journal of Chemical Physics* **1992**, *96*, 1810.

(230) Zhang, C. Y.; Freeman, D. L.; Doll, J. D. *Journal of Chemical Physics* **1989**, *91*, 2489.

(231) Lavender, H. B.; Iyer, K. A.; Singer, S. J. *Journal of Chemical Physics* **1994**, *101*, 7856.

(232) Lu, D. S.; Singer, S. J. *Journal of Chemical Physics* **1995**, *103*, 1913.

(233) Oppenheimer, C. A.; Curotto, E. *Journal of Chemical Physics* **2004**, *121*, 6226.

(234) Miller, M. A.; Shepherd, J. J.; Wales, D. J. *Molecular Physics* **2008**, *106*, 1655.

(235) Miller, M. A.; Wales, D. J. *Journal of Physical Chemistry B* **2005**, *109*, 23109.

(236) Lu, D. S.; Singer, S. J. *Journal of Chemical Physics* **1996**, *105*, 3700.
(237) Muller, E. A.; Gubbins, K. E. *Industrial & Engineering Chemistry Research* **1995**, *34*, 3662.
(238) Sinyagin, A.; Belov, A.; Kotov, N. *Modelling and Simulation in Materials Science and Engineering* **2005**, *13*, 389.
(239) Sinyagin, A. Y.; Belov, A.; Tang, Z. N.; Kotov, N. A. *Journal of Physical Chemistry B* **2006**, *110*, 7500.
(240) Tang, Z. Y.; Zhang, Z. L.; Wang, Y.; Glotzer, S. C.; Kotov, N. A. *Science* **2006**, *314*, 274.
(241) Zhang; Tang; Kotov, N. A.; Glotzer, S. C. *Nano Letters* **2007**, *7*, 1670.
(242) Zhang, X.; Zhang, Z. L.; Glotzer, S. C. *Journal of Physical Chemistry C* **2007**, *111*, 4132.
(243) Holm, C.; Ivanov, A.; Kantorovich, S.; Pyanzina, E.; Reznikov, E. *Journal of Physics-Condensed Matter* **2006**, *18*, S2737.
(244) Ivanov, A. O.; Kantorovich, S. S. *Physical Review E* **2004**, *70*, 10.
(245) Kantorovich, S. S. *Journal of Magnetism and Magnetic Materials* **2005**, *289*, 203.
(246) Medvedev, N. N.; Naberukhin, Y. I. *Journal of Non-Crystalline Solids* **1987**, *94*, 402.
(247) Medvedev, N. N. *Journal of Physics-Condensed Matter* **1990**, *2*, 9145.